Title
Seismic Earth Pressures on Retaining Structures in Cohesive Soils

Authors
Candia, G
Sitar, N

Publication Date
2013-08-01

Peer reviewed

Seismic Earth Pressures on Retaining Structures in Cohesive Soils

By

Gabriel Candia Agusti
and
Nicholas Sitar

Report submitted to the
California Department of Transportation (Caltrans)
under Contract No. 65A0367
and
NSF-NEES-CR Grant No. CMMI-0936376:
Seismic Earth Pressures on Retaining Structures

August 2013
Report No. UCB GT 13-02

GEOTECHNICAL ENGINEERING

DEPARTMENT OF CIVIL AND ENVIRONMENTAL ENGINEERING

UNIVERSITY OF CALIFORNIA • BERKELEY

STATE OF CALIFORNIA DEPARTMENT OF TRANSPORTATION

TECHNICAL REPORT DOCUMENTATION PAGE

TR0003 (REV. 10/98)

1. REPORT NUMBER	2. GOVERNMENT ASSOCIATION NUMBER	3. RECIPIENT'S CATALOG NUMBER
CA13-2170		

4. TITLE AND SUBTITLE	5. REPORT DATE
Seismic Earth Pressures on Retaining Structures with Cohesive Backfills	August 14, 2013
	6. PERFORMING ORGANIZATION CODE UCB

7. AUTHOR(S)	8. PERFORMING ORGANIZATION REPORT NO.
Gabriel Candia Agusti and Nicholas Sitar	UCB GT 13-02

9. PERFORMING ORGANIZATION NAME AND ADDRESS	10. WORK UNIT NUMBER
Department of Civil and Environmental Engineering University of California, Berkeley 449 Davis Hall Berkeley, CA 94720-1710	11. CONTRACT OR GRANT NUMBER 65A0367

12. SPONSORING AGENCY AND ADDRESS	13. TYPE OF REPORT AND PERIOD COVERED
California Department of Transportation Engineering Service Center 1801 30th Street, MS 9-2/5i Sacramento, California 95816 California Department of Transportation Division of Research and Innovation, MS-83 1227 O Street Sacramento CA 95814	Final Report 6/30/2010 – 6/30/2013 14. SPONSORING AGENCY CODE 913

15. SUPPLEMENTAL NOTES

Prepared in cooperation with the State of California Department of Transportation.

16. ABSTRACT

Observations of the performance of many different types of retaining structures in recent earthquakes show that failures of retaining structures, including braced excavation supports and basement walls, are rare even if the structures were not designed for the actual intensity of the earthquake loading. Therefore, an experimental and analytical study was undertaken to develop a better understanding of the distribution and magnitude of seismic earth pressures on various types of retaining structures.

This report is a second in the series and presents the results of centrifuge model experiments and numerical analyses of seismic response of retaining structures with cohesive backfill. The experimental results show that the static and seismic earth pressures increase linearly with depth and that the resultant acts at 0.35H-0.4H, as opposed to 0.5-0.6H assumed in current engineering practice. In general, the total seismic load can be expressed using Seed and Whitman's (1970) notation as: $P_{ae}= P_a +\Delta P_{ae}$, where P_a is the static load and ΔP_{ae} is the dynamic load increment. In level ground, the dynamic load coefficient can be expressed as $\Delta K_{ae}=½\gamma H^2(0.68PGA_{ff}/g)$ for basement walls and $\Delta K_{ae}=½\gamma H^2(0.42PGA_{ff}/g)$ for cantilever walls. These results are consistent with similar experiments performed in cohesionless soils by Mikola & Sitar (2013). In sloping ground the seismic coefficient is $\Delta K_{ae}=½\gamma H^2(0.7PGA_{ff}/g)$, which is consistent with Okabe's (1926) Coulomb wedge analysis of the problem. However, the numerical simulations and Okabe's (1926) limit state theory suggest that the resultant acts between 0.37H-0.40H for typical values of cohesion. Overall, the results also show that typical retaining walls designed with a static factor of safety of 1.5 have enough strength capacity to resist ground accelerations up to 0.4g.

17. KEY WORDS	18. DISTRIBUTION STATEMENT
Retaining Walls, Seismic Earth Pressure, Cohesive Soil, Earthquake, Mononobe-Okabe, Centrifuge, Numerical Analysis, Design	No restrictions. This document is available to the public through the National Technical Information Service, Springfield, VA 22161

19. SECURITY CLASSIFICATION (of this report)	20. NUMBER OF PAGES	21. PRICE
Unclassified	161	

Abstract

Observations from recent earthquakes show that all types of retaining structures with non-liquefiable backfills perform very well and there is limited evidence of damage or failures related to seismic earth pressures. Even retaining structures designed only for static loading have performed well during strong ground motions suggesting that special seismic design provisions may not be required in some cases. The objective of this study was to characterize the seismic interaction of backfill-wall systems using experimental and numerical models, with emphasis on cohesive soils, and to review the basic assumptions of current design methods.

In the experimental phase of this research, two sets of centrifuge models were conducted at the Center for Geotechnical modeling in UC Davis. The first experiment consisted of a basement wall and a freestanding cantilever wall with level backfill, while the second one consists of a cantilever wall with sloping backfill. The soil used in the experiments was a compacted low plasticity clay. Numerical simulations were performed using FLAC$^{2\text{-D}}$ code, featuring non-linear constitutive relationships for the soil and interface elements. The non-linear hysteretic constitutive UBCHYST was used to model the level ground experiment and Mohr-Coulomb with hysteretic damping was used to model the sloping backfill experiment. The simulations captured the most important aspects of the seismic responses, including the ground motion propagation and the dynamic soil-structure interaction. Special attention was given to the treatment of boundary conditions and the selection of the model parameters.

The results from the experimental and numerical analysis provide information to guide the designers in selecting seismic design loads on retaining structures with cohesive backfills. The experimental results show that the static and seismic earth pressures increase linearly with depth and that the resultant acts at 0.35H-0.4H, as opposed to 0.5-0.6H assumed in current engineering practice. In addition, the observed seismic loads are a function of the ground motion intensity, the wall type and backfill geometry. In general, the total seismic load can be expressed using Seed and Whitman's (1970) notation as: $P_{ae} = P_a + \Delta P_{ae}$, where P_a is the static load and ΔP_{ae} is the dynamic load increment. While the static load is a function of the backfill strength, previous stress history and compaction method, the dynamic load increment is a function of the free field PGA, the wall displacements, and is relatively independent of cohesion. In level ground, the dynamic load coefficient can be expressed as $\Delta K_{ae} = \frac{1}{2}\gamma H^2(0.68\ \mathrm{PGA_{ff}/g})$ for basement walls and $\Delta K_{ae} = \frac{1}{2}\gamma H^2(0.42\ \mathrm{PGA_{ff}/g})$ for cantilever walls; these results are consistent with similar experiments performed in cohesionless soils (Mikola & Sitar, 2013. In the sloping ground experiment the seismic coefficient came out to $\Delta K_{ae} = \frac{1}{2}\gamma H^2(0.7\ \mathrm{PGA_{ff}/g})$, which is consistent with Okabe's (1926) Coulomb wedge analysis of the problem. However, that slope was stable under gravity loads even without the presence of the retaining wall (FS=1.4). Measured slope displacements were very small and in reasonable good agreement with the predictions made with the Bray and Travasarou (2007) semi-empirical method.

The experimental data was not sufficient to determine accurately the point of action of the seismic loads. However, the numerical simulations and Okabe's (1926) limit state theory suggest that the resultant acts between 0.37H-0.40H for typical values of cohesion. While the resultant acts at a point higher than 0.33H with increasing cohesion, the total seismic moment is reduced due to the significant reduction in the total load P_{ae}, particularly for large ground accelerations.

The results also show that typical retaining walls designed with a static factor of safety of 1.5 have enough strength capacity to resist ground accelerations up to 0.4g. This observation is consistent with the field performance of retaining walls as documented by Clough and Fragaszy (1977) and the experimental results by al Atik and Sitar (2010) and Geraili and Sitar (2013).

The evaluation of earth pressures at the wall-backfill interface continues to be a technical challenge. Identified sources of error in the present study include the behavior of pressure sensors, the geometric and mass asymmetry of the model and the dynamic interaction between the model and the container. While these centrifuge experiments reproduced the basic response of prototype models, ultimately, instrumented full-scale structures are most essential to fully characterize the response of tall walls and deep basements with varieties of backfill.

Acknowledgments

The authors acknowledge the assistance of Roozbeh Geraili Mikola, Nathaniel Wagner, and Jeff Zayas from UC Berkeley in the preparation and execution of the centrifuge models. The authors also ackowledge the invaluable input and technical support provided by Dan Wilson, Tom Khonke and staff at the Center for Geotechnical Modeling of UC Davis, and Professors Jonathan Bray, Michael Riemer and Douglas Dreger at UC Berkeley. The DLL version of the constitutive model UBCHYST was generously provided by R. Geraili and used in the numerical phase of this work. This research was funded in part by a grant from the California Geotechnical Engineering Association (CalGeo), the State of California Department of Transportation (Caltrans) Contract No. 65N2170 and NSF-NEES-CR Grant No. CMMI-0936376: Seismic Earth Pressures on Retaining Structures. Gabriel Candia was also supported by a Fulbright-CONICYT fellowship, sponsored by the Chilean Commision of Scientific and Technological Research.

Disclaimer

Table of Contents

List of Figures

List of Tables

1. INTRODUCTION

Earth retaining structures are an essential component of underground facilities and transportation infrastructure, and thus, their study is a matter of great concern for geotechnical engineers, especially in seismic prone countries. One of the earliest solutions to the problem of earth pressures was developed by Coulomb (1776), who introduced the idea of 'critical slip surface' and divided the strength of soils into cohesive and frictional components. Later, Rankine (1857) developed a method based on the frictional stability of a loose granular mass and developed simple equations for the coefficients of active and passive forces on retaining structures. Due to their simplicity and straightforwardness, these theories became a standard analysis tool in engineering practice and the starting point of countless methods of analyzing static and dynamic earth pressures on retaining structures.

The methods of analysis of seismically induced earth pressures were first introduced after the great Kanto earthquake of 1923 when Okabe (1926) developed a general theory of seismic stability of retaining walls as an extension of Coulomb's theory of earth pressures. Then, Mononobe and Matsuo (1929) performed shaking table experiments and validated Okabe's work for cohesionless soils and short gravity walls. The theory developed by these authors is known as the Mononobe-Okabe method (M-O) and is widely used even today in current designs of different types of structures and soil conditions. However, there is a general agreement that the M-O method is a broad simplification of what is actually a very complex soil-structure interaction problem, particularly regarding its use on non-yielding walls, deep underground structures, or in soils that are not truly cohesionless. Moreover, there is a consensus that M-O yields over conservative earth pressures for strong ground motions, and thus, the standard design practice is to use a fraction of the expected peak ground acceleration. Past and recent research (Seed & Whitman, 1970; Clough & Fragaszy 1977; Lew et al., 2010; Sitar et al.; 2012) have addressed these limitations and proposed simple design criteria based on the observed seismic performance of retaining structures.

Much of the past research on the subject of seismic earth pressures has concentrated on cohesionless soils. Thus, the present study was motivated by the lack of experimental data on seismic earth pressures on retaining structures with cohesive backfills. This work consists of three phases: (i) literature review, (ii) experimental analysis and (iii) numerical simulations, and the main objectives are to evaluate the seismic interaction of retaining structures with compacted cohesive backfill on centrifuge experiments, and assess the validity of current design methods and their assumptions.

The study begins with a comprehensive review of existing theories of seismic earth pressures, including limiting equilibrium, linear-elastic and wave propagation methods, with emphasis on cohesive soils. This section continues with a revision of previous experimental results from shaking table and centrifuge tests, and the field performance of retaining structures in recent earthquakes (Chapter 2).

In the experimental phase of this research, two scaled centrifuge tests were conducted at the Center for Geotechnical Modeling of UC Davis (CGM). The first experiment consisted of a braced U-shaped wall or 'basement' and a freestanding cantilever wall on level ground. The second experiment considered a single cantilever wall with a sloping backfill. The cohesive soil used in both tests was a low plasticity clay compacted at 90% and 99% RC, respectively (Chapter 3). Different ground motions were applied at the base of the models and a dense array of instruments allowed monitoring the dynamic interaction between the supporting soil, the retaining structure, and the backfills (Chapters 4, 5).

In the final phase of this research, plain strain simulations of the centrifuge experiments were performed in FLAC. The numerical models were calibrated with the clay properties determined from laboratory tests, simulations of elements in simple shear, and vertical propagation of shear waves in free field (Chapters 6, 7). A thorough discussion of the model results, capabilities, and limitations is also presented. Conclusions and design recommendations are given in Chapter 8.

2. LITERATURE REVIEW

Since the publication of the first paper on the seismic performance of retaining structures by Mononobe and Matsuo (1929) there have been numerous studies of the phenomena. Most of these studies tended to concentrate on the behavior of retaining structures with cohesionless soils (see e.g. Seed & Whitman, 1970; Richards & Elms, 1979; Steedman & Zeng, 1990; Richards 1990; and Mylonakis; 2007). However natural soil deposits, and even 'clean sands', have fines content that contributes to cohesion and may significantly reduce the seismic demands on the retaining system. Hence, the review of previously published work presented in this chapter concentrates on methods used to estimate seismic earth pressures on retaining structures with cohesive backfills. In addition, results from numerical and experimental simulations and field performance of retaining structures during earthquakes are reviewed as well.

2.1. Analytical Methods

The analytical methods used in the study of retaining walls can be classified in three broad categories as limit state, elastic, and elasto-plastic, depending on the soil stress history and the wall displacements (Veletsos & Younan, 1994). The limit state methods are based on the equilibrium of a soil wedge and assume that the wall displaces enough to induce a limit or failure state in the soil. The elastic methods are based on solutions of equilibrium equation on a linear elastic continuum and assume small wall displacements, whereas elasto-plastic methods account for small-to-large displacements and the hysteretic behavior of the soil. The elasto plastic methods are generally implemented using discrete solutions and are discussed in the Section 2.2 of this chapter. Limit state methods and elastic methods are oversimplifications of the true physical problems and have important limitations. Thus, calculated earth pressures are generally conservative unless the underlying assumptions are satisfied. On the other hand, elasto-plastic methods can reproduce experimental data with great accuracy, but their predictive capabilities are limited.

2.1.1. Limit State Methods

The "General Theory of Earth Pressure" proposed by Okabe in 1926 (Okabe, 1926) is an extension of Coulomb's method to include the effects of earthquakes and soil cohesion. This theory was supported by early shaking table experiments with dry cohesionless soils performed by Mononobe and Matsuo (1929) and later became known as the Mononobe and Okabe method (M-O). Okabe's solution for gravity walls is based on the following assumptions:

- The soil satisfies the Mohr-Coulomb criterion and failure occurs along a planar surface that passes through the toe of the wall.

- The wall moves away from the backfill sufficiently to mobilize the shear strength in the soil and produce minimum active earth pressure.
- accelerations are uniform throughout the backfill and the earthquakes are represented as equivalent forces Wk_h and Wk_v applied at the center of gravity of the soil wedge

The forces considered in the Okabe analysis are shown in Figure 2.1(a). The total seismic force acting in the wall can be expressed as $P_{ae} = 1/2\gamma H^2(1-k_v)K_{ae}$, where K_{ae} is the seismic coefficient of lateral earth pressure, given by

$$K_{ae} = \frac{\sin(\alpha-\phi+\theta)\cos(\alpha-\beta)[\cos(\beta-i)+\frac{2q}{\gamma H(1-k_v)}\cos\beta]}{\cos^2\beta\cos\theta\sin(\alpha-i)\cos(\alpha-\beta-\phi-\delta)} - \frac{2c}{\gamma H(1-k_v)}\frac{\cos(\beta-i)\cos\phi}{\cos\beta\sin(\alpha-i)\cos(\alpha-\beta-\phi-\delta)} \tag{2.1}$$

The coefficient K_{ae} is expressed in terms of the wedge angle α that produces the maximum load. A unique failure surface is determined by solving the equation $dK_{ae}/d\alpha = 0$. For the particular case of cohesionless soils and no surcharge, the seismic coefficient simplifies to the well-known M-O equation, given by

$$K_{ae} = \frac{\cos^2(\phi-\theta-\beta)}{\cos\theta\cos^2\beta\cos(\delta+\beta+\theta)\left(1+\sqrt{\frac{\sin(\phi+\delta)\sin(\phi-\theta-i)}{\cos(\delta+\beta+\theta)\cos(i-\beta)}}\right)^2} \tag{2.2}$$

Okabe's model assumes that the earth pressure due to inertial forces are zero at the top and increases linearly with depth, whereas the earth pressure due to surcharge and cohesion are uniform with depth. Thus, with increasing cohesion the point of application of the total seismic load moves up, as shown in Figure 2.1(b), and varies by less than 10% with increasing ground

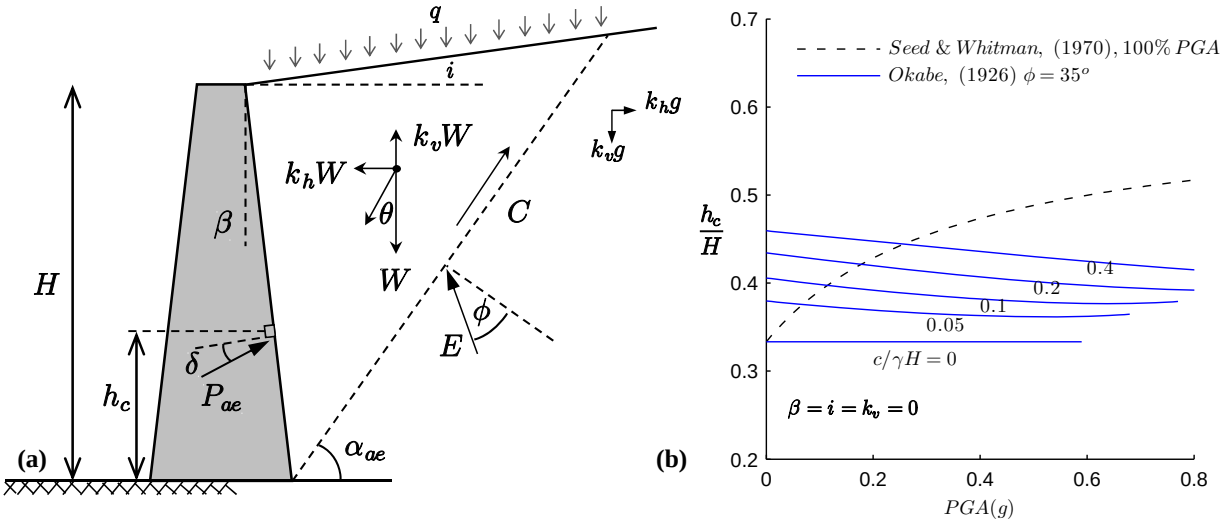

Figure 2.1 (a) Forces diagram used in the Okabe (1926) analysis, and (b) Point of application of total seismic load as a function of cohesion

acceleration. In contrast, engineering practice has adopted 0.6H as the point of action of the dynamic load increments largely based on work of Seed and Whitman (1970), which makes the resultant of the total seismic load to act between 0.33H-0.55H.

For a flat backfill and no vertical acceleration, Equation (2.2) becomes indefinite for $k_h > \tan\varphi + 2c/\gamma H$. A similar restriction is common to other limiting equilibrium solutions (Prakash & Saran 1966; Das 1996; Richards & Shi 1994). Seed and Whitman (1970) proposed a simplified version of equation (2.3) for dry cohesionless soils and separated the total seismic load into a static and dynamic components as

$$P_{ae} = \frac{1}{2}\gamma H^2 (K_a + \Delta K_{ae}) \tag{2.3}$$

where K_a is the Coulomb's coefficient of static earth pressure and $\Delta K_{ae} \approx \frac{3}{4}k_h$ is the dynamic increment for a vertical wall, horizontal backfill slope and ϕ=35°. Based on shaking table experiments by Matsuo (1941), Seed and Whitman (1970) suggested that the seismic load increment acts at 0.5H-0.67H above the footing and that 85% of PGA should be used as the effective acceleration. They concluded that many walls designed adequately for static conditions can resist accelerations on the order of 0.3 g with no special design considerations. For the case of cohesive soils with uniform surcharge, the general form of the seismic coefficient can be written as

$$K_{ae} = N_{a\gamma} + \frac{2q}{\gamma H}N_{aq} + \frac{2c}{\gamma H}N_{ac} \tag{2.4}$$

where $N_{a\gamma}, N_{aq}$ and N_{ac} are dimensionless earth pressure factors that need to be optimized to determine the maximum load. Prakash and Saran (1966) proposed a solution to account for surface cracks and wall adhesion, and Das (1996) further extended this work to include sloping backfills and vertical earthquakes. These two methods imply the existence of multiple failure surfaces, since the coefficients $N_{a\gamma}, N_{aq}$ and N_{ac} are optimized separately. Based on the upper bound limit analysis method, Chen and Liu (1990) computed the seismic earth pressures assuming translational wall movements and a combination of linear and log-spiral failure surfaces, obtaining identical results to Okabe (1926) for the case of cohesionless soils. A comparison of these different approaches is presented in Figure 2.2, where $\tilde{c} = c/\gamma H$ and $k_h = PGA_{ff}/g$. This figure shows that increasing cohesion leads to significant reductions of the total seismic load. Note that for cohesionless soils and medium seismicity ($k_h < 0.4$) these methods converge to Okabe's (1926) solution. Also, note that the Chen and Liu's (1990) solution does not become indefinite at large accelerations and that Das' (1996) solution for the dynamic load increment does not depend on cohesion. An important disadvantage of these methods is the lack of experimental data at high accelerations, and that the computation of the critical coefficient of earth pressure requires a numerical solution. Closed form solutions of Equation (2.4) have been developed recently for the case of smooth vertical walls with flat backfills and no surcharge (Shukla & Gupta; 2009) and flat backfills (Gosh & Sengupta; 2012)

In a somewhat different approach, Richards and Shi (1994) solved the inertial free field equations for a homogeneous c-φ soil and applied them to evaluate the seismic earth pressure at

the wall face. Their solution yields seismic earth pressure coefficients consistent with Okabe's theory and the design recommendations presented in NCHRP 611 (Anderson, Martin, Lam, & Wang, 2008), as seen in Figure 2.3.

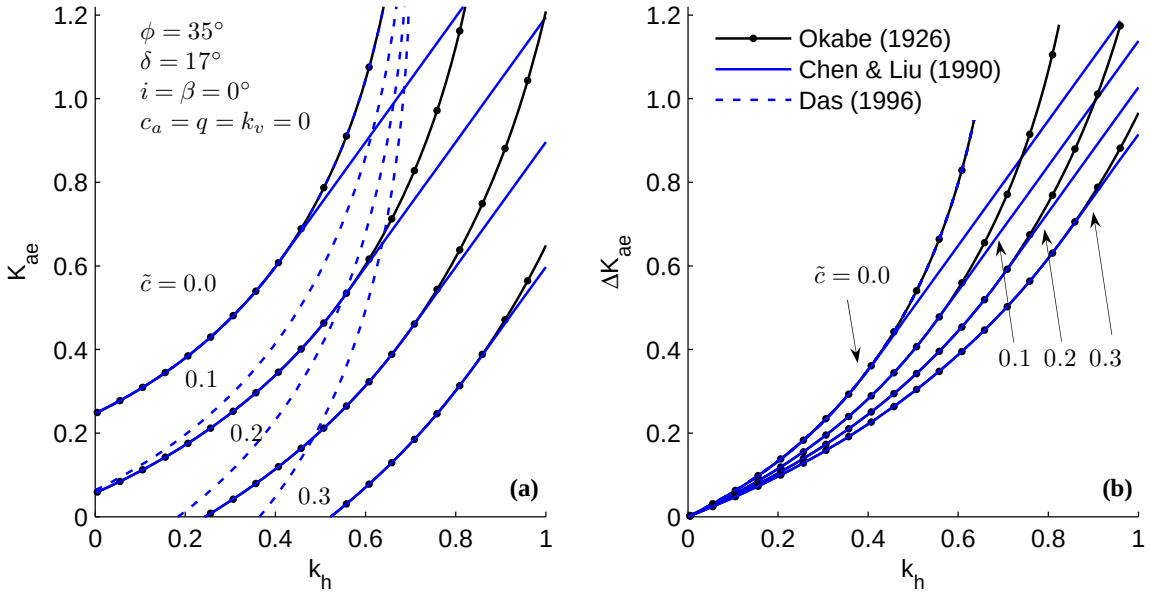

Figure 2.2 Comparison of limit states methods Okabe (1926), Das (1996) and Chen and Liu (1960). (a) Coefficient of total seismic load and (b) coefficient of dynamic load increment.

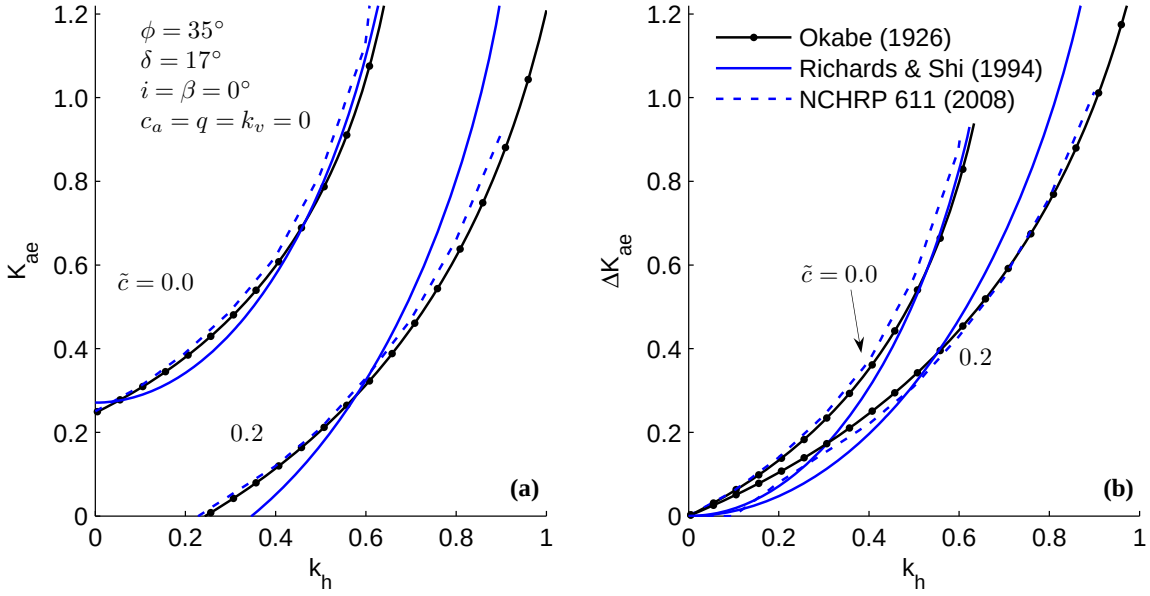

Figure 2.3 Comparison of limit states methods Okabe (1926), Richards and Shi (1994) and design recommendations NCHRP 611 (Anderson et al., 2008). (a) Coefficient of total seismic load and (b) coefficient of dynamic load increment.

In a recent work by Shambabadi et. al (2013), the method of slices was used to compute the earth pressure in retaining structures with Mohr-Coulomb backfill material. Their approach uses a composite logarithmic failure surface and yields active earth pressures consistent with standard trial wedge methods or analytical solutions like Okabe (1926).

As stated earlier, most limit state methods assume that the accelerations in the backfill are uniform, implying that shear waves travel at infinite speed. The effects of a finite shear wave velocity were studied by Steedman and Zeng (1990) for a gravity wall founded on rock. This method is an extension of M-O's (1929) theory and assumes a sinusoidal distribution of the backfill acceleration, as seen in Figure 2.4, in which the input motion is given by $k_h g \sin(\omega t)$.

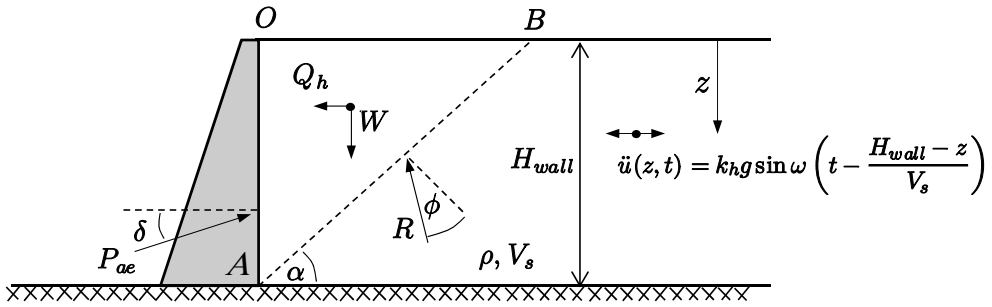

Figure 2.4 Forces diagram used in the Steedman and Zeng (1990) analysis.

Steedman and Zeng (1990) concluded that the induced phase changes have a significant effect of the distribution of dynamic earth pressures, but not in the total seismic load. This solution, however, neglects the energy dissipation in the soil and violates the boundary condition of zero shear stress at the surface. As a result, the coefficient of total earth pressure decreases monotonically with increasing input frequency and important aspects of the dynamic soil response are not well captured. To address these problems, a solution based on the dynamic response of a viscoelastic soil was studied herein. The geometry and boundary conditions of the problem are shown in Figure 2.5, consisting of a gravity wall of height H_{wall} supporting a backfill with total soil depth H_{soil}. The vertically propagating shear waves are assumed to satisfy the wave equation (Schabel, Lysmer, & Seed, 1972), which was solved analytically for the case of a sinusoidal ground acceleration as shown in Appendix A. The resulting acceleration profile is cast in terms of the complex frequency $k^2 = \rho\omega^2/(G + i\omega\eta)$ as

$$\ddot{u}_g(z,t) = k_h g \,\mathbf{Im}\left(\frac{\cos(kz)}{\cos(kH_{soil})} e^{i\omega t}\right) \tag{2.5}$$

A snapshot of the acceleration profile is shown in

Figure 2.6(a) and compared to Steedman and Zeng's (1990) solution. Note that the wave equation predicts an acceleration with decreasing amplitude toward the surface, whereas Steedman and Zeng (1990) assume an acceleration with constant amplitude. In contrast, the M-O (1929) theory assumes a uniform acceleration in the entire soil depth.

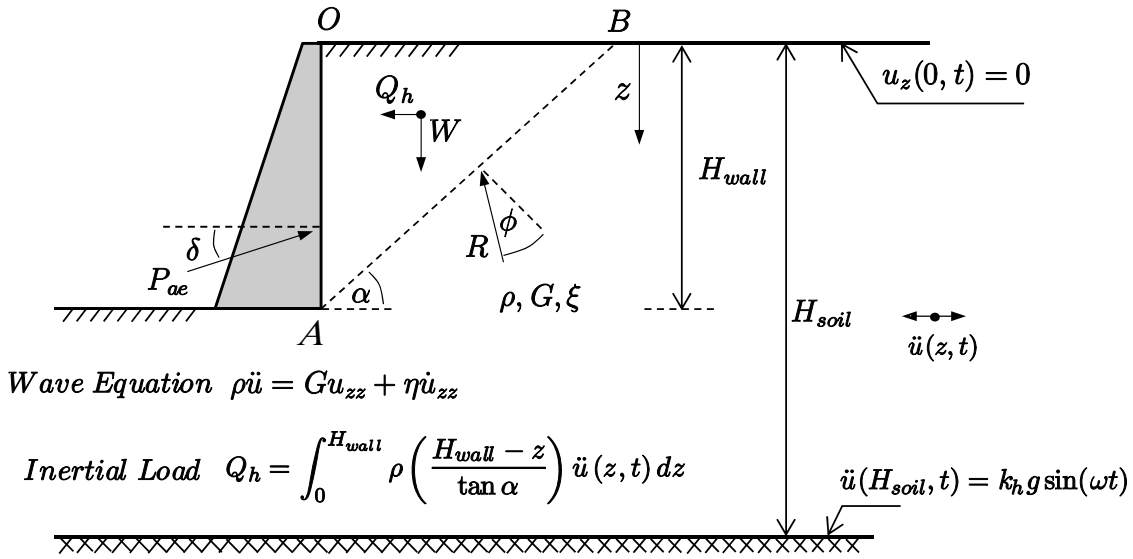

Figure 2.5 Force diagram of a gravity wall founded on a viscoelastic material.

Figure 2.6(b) shows the coefficient of seismic earth pressure for a wall founded on rock as a function of the input frequency normalized by $f_o = V_s/4H_{wall}$, the natural frequency of the retained soil. In this plot, the wave equation approach leads to a significant amplification of earth pressures at the resonant frequencies of the backfill. Likewise, the viscous damping reduces the total earth pressure and has a marked effect on the attenuation of higher frequencies. Note that for static loading, i.e. $f \to 0$, Steedman and Zeng's (1990) theory and the wave equation solution converge to the pseudo-static M-O solution.

The effects of input frequencies and depth to bedrock are shown in Figure 2.7. As discussed earlier, for a wall founded on rock, the maximum earth pressure occurs at the resonance frequency $f/f_0 = 1$. In deeper soil deposits, the natural frequency is smaller and thus, the maximum earth pressure increment occurs at

$$\frac{f}{f_o} = \frac{H_{wall}}{H_{soil}} \tag{2.6}$$

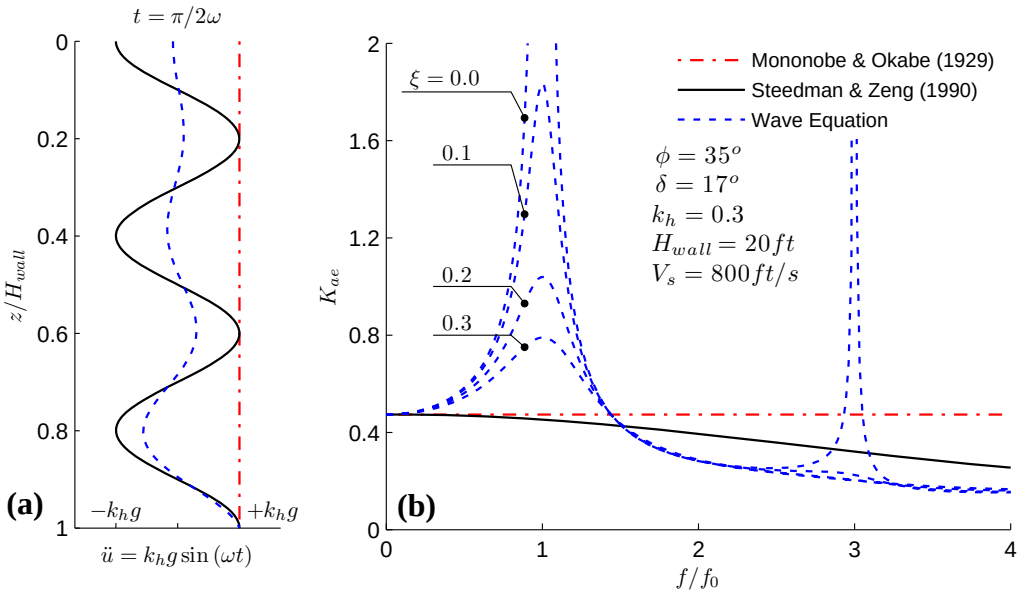

Figure 2.6 (a) Acceleration distribution for ω/ω$_0$=3, k_h=0.3, ξ=0.2 at t=π/2ω, (b) Influence of input frequency and soil damping on the earth pressure coefficient for a gravity wall founded on rock. The frequency independent M-O solution is included as a reference.

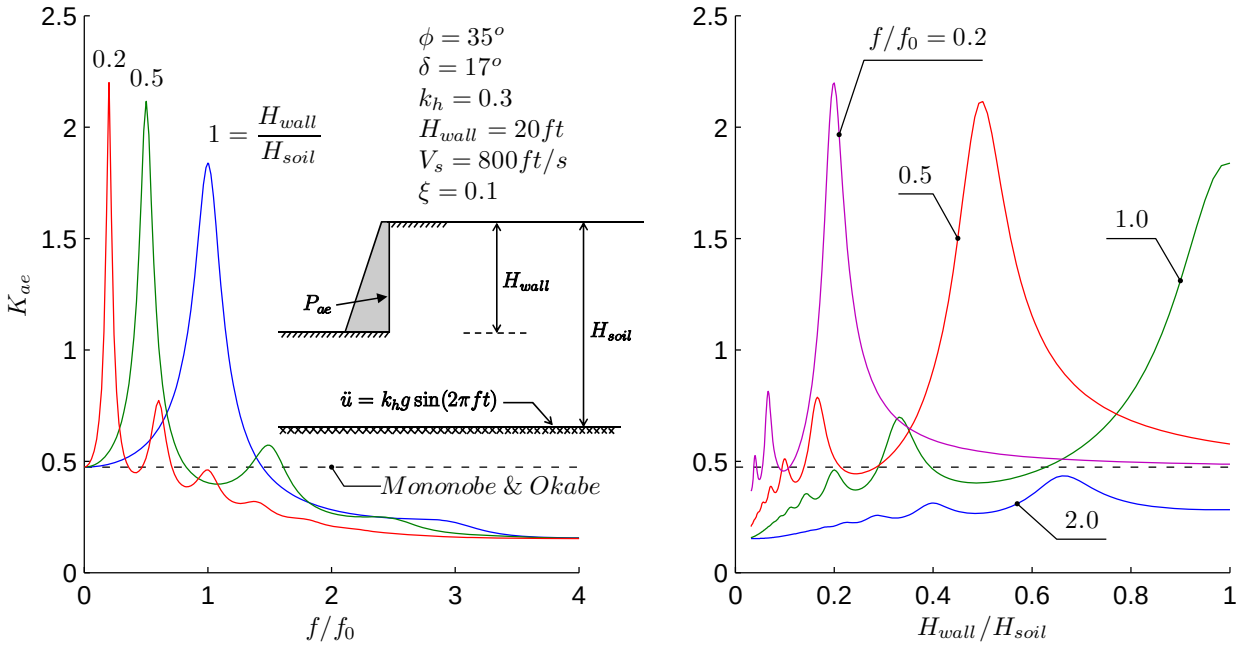

Figure 2.7 Influence of input frequency and depth to bedrock for a gravity wall founded on soil. Input frequency normalized by fo=Vs/4Hwall=10 Hz.

2.1.2. Elastic Methods

An alternative to pure limit equilibrium methods is to use of the theory of elasticity to analyze the dynamic response of non-yielding and yielding walls with a linear elastic backfill. In these solutions, the soil is modeled as a continuum and the interaction with the retaining structures is modeled with appropriate boundary conditions.

Matsuo and O-Hara (1960) developed an upper bound solution to the problem of a semi-infinite elastic soil and a rigid wall excited by a harmonic base acceleration, assuming that vertical displacements are constrained. Later, Scott (1973) developed a simple 1-D shear beam model to evaluate the response of semi-infinite and bounded systems using Winkler springs at the wall interface. Wood's (1973) method - commonly used today for "rigid walls" - provides an exact analytical solution to the problem shown in Figure 2.8(a), where the rigid boundaries represent smooth non-yielding walls and the earthquake-induced loads are modeled as a uniform body force. Wood (1973) showed that the dynamic load on the wall Q_b is a function of the Poisson ratio ν and the aspect ratio L/H, as shown in Figure 2.8(b), applied approximately at 0.55H-0.60H above the base. For rigid walls, this load increment can be as large as twice the load predicted using the Mononobe Okabe method.

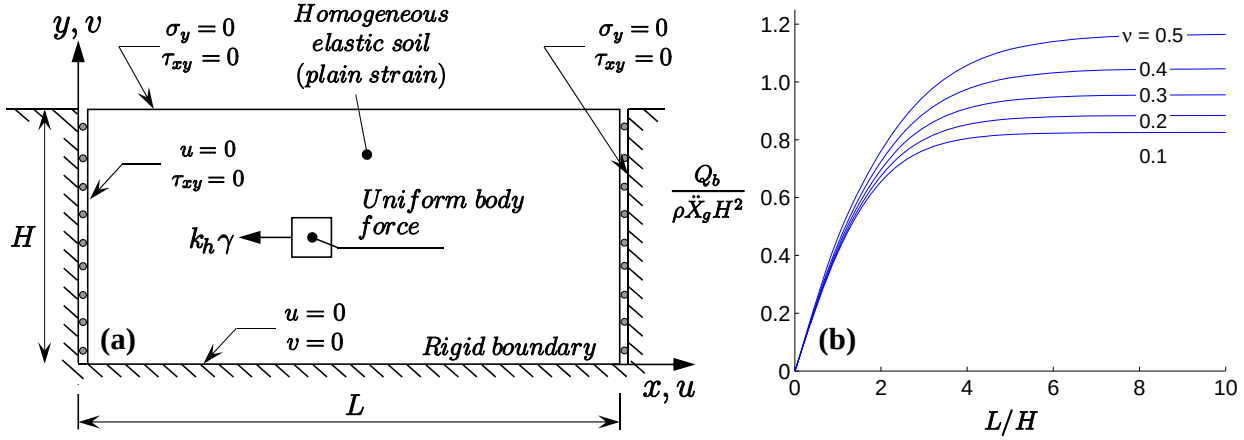

Figure 2.8 (a) Wood's (1973) model for rigid walls and (b) Wood's (1973) dynamic load increment on rigid walls.

Veletsos and Younan (1994[a]) studied the harmonic and earthquake response of a semi-infinite uniform layer of viscoelastic material for rigid straight walls, and expressed the dynamic load increment as given in by the equation

$$Q_b = -\frac{16\psi_\sigma}{\pi^3}\rho\ddot{X}_g H^2\sqrt{1+i\delta}\sum_{n=1,3,5,\ldots}^{\infty}\frac{1}{n^3}\frac{1}{\sqrt{1-\phi_n^2+i\delta}} \tag{2.7}$$

They showed that the solution with no vertical stress is in good agreement with Wood's exact method and that the earth pressure increases monotonically from zero at the base to a maximum value at the top. More recently, Kloukinas and Mylonakis (2012) proposed Equation (2.8), which is a simplified and more general solution to the problem of rigid walls on elastic media using variable separation and Ritz functions.

$$Q_b = -\frac{16\psi_\sigma}{\pi^3}\rho\ddot{X}_g H^2 \tag{2.8}$$

A comparison of these methods is shown in Figure 2.9 for a rigid wall. Note that the dynamic load increments scale linearly with the input acceleration and can be approximated as $Q_b \approx \rho\ddot{X}_g H^2 = k_h g H^2$ applied at 0.6H for typical values of the Poisson ratio.

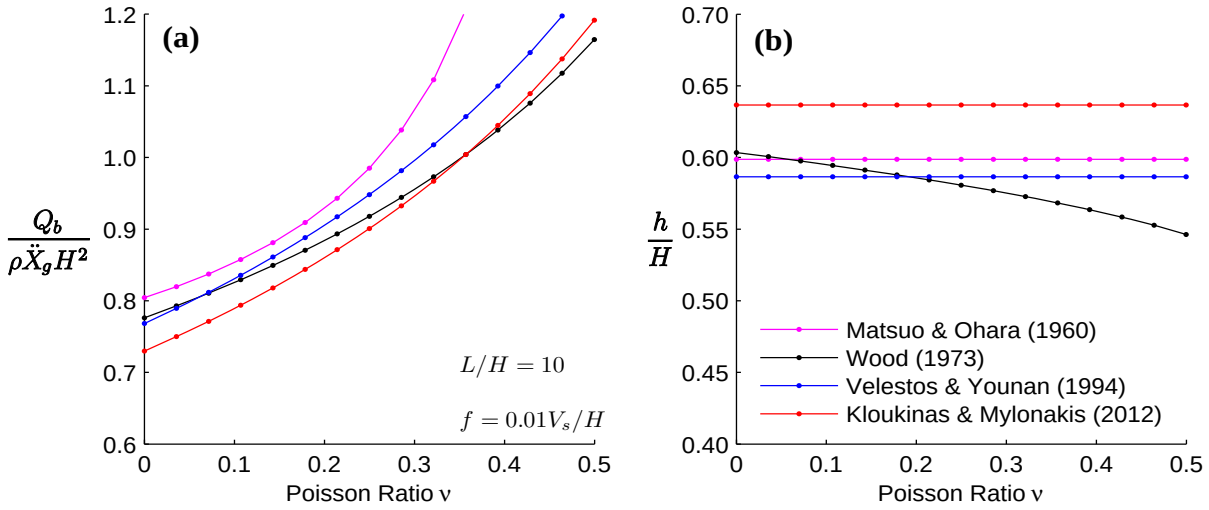

Figure 2.9 Comparison of elastic methods (a) Coefficient of dynamic load increment, and (b) location of the earth pressure resultant.

Elastic methods have also been applied to the study of yielding walls; however their applicability is limited since a small wall deflection can induce a failure state in the soil. Wood (1973) solved the dynamic equations for the problem shown in Figure 2.10(a), consisting of a homogeneous elastic soil retained between a rigid and a rotating wall while Veletsos and Younan (1994[b]) studied the effect of rotations of rigid walls on a semi-infinite backfill, Figure 2.10(b). Later, Veletsos and Younan (1997) included the effects of wall flexibility and computed dynamic loads 50% smaller than those of rigid fixed-based walls and in reasonable agreement limit state solutions like the M-O method.

2.2. Numerical Methods

Numerical methods, Finite Elements (FE) and Finite Differences (FD), have been used extensively in the analysis of retaining structures, and validated against real case histories and experimental data. Nevertheless, the predictive capability of these tools is still debatable, particularly on regions where high accelerations are expected. Clough and Duncan (1971) applied the finite elements method to evaluate the static response of retaining walls, and developed guidelines to represent the soil-structure interface more accurately. They computed active and passive earth pressures in good agreement with classical limit state theory, and residual displacements consistent with the experimental results by Terzaghi (1934).

A comprehensive computer program 'SSCOMP' was developed by Seed and Duncan (1984) for the evaluation of compaction induced earth pressures and deformations, and was validated with several case-studies involving the placement and compaction of fills (Seed & Duncan, 1986). Wood (1973) used finite elements to study the static and dynamic response of non-yielding walls and the effects of bonded walls and non-uniform soil stiffness. He showed that the smooth and bonded wall contacts had no significant influence on the frequency response or the earth pressure distributions.

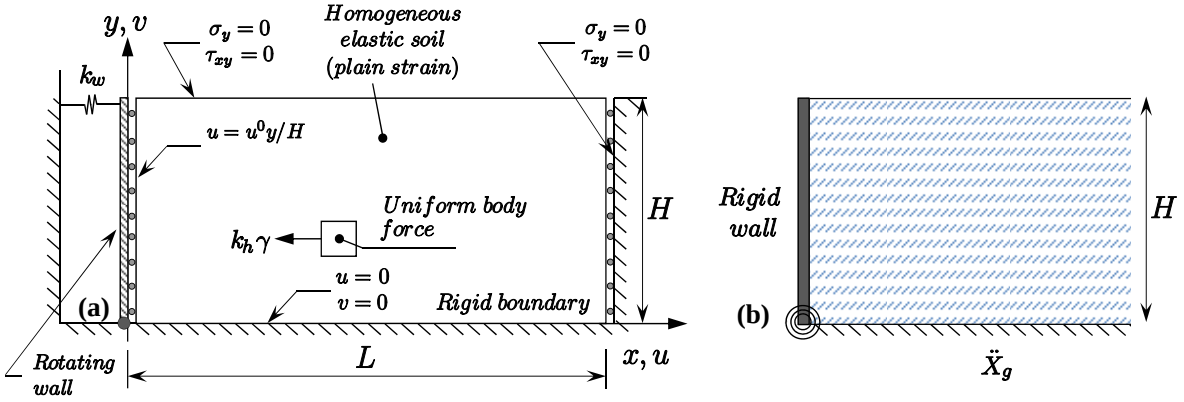

Figure 2.10 Yielding wall models (a) Wood's (1973) and (b) Veletsos and Younan (1994[b]).

The seismic response of gravity retaining walls was studied by Nadim and Whitman (1982) using finite elements. They modeled the soil with a prescribed failure surface and a secant shear modulus to account for large strains, and frictional slip elements at the soil-wall interface. Nadim and Whitman (1982) concluded that the most important factor in the amplification of wall displacements is the ratio between predominant frequency of the earthquake and the natural frequency of the backfill. Siddharthan and Magarakis (1989) studied the response of flexible walls retaining dry sand. The soil model accounted for its non-linear hysteretic behavior, and for increasing lateral stress and volumetric changes as a result of cyclic loading. Siddharthan and Magarakis (1989) concluded that a high relative density and the wall flexibility significantly reduced the maximum moments on the wall. They suggested that the maximum moments computed using the Seed and Whitman method are conservative for flexible walls but not necessarily for stiffer walls.

Green et al. (2002) studied the seismic response of a cantilever retaining wall with cohesionless backfill using the finite difference code FLAC (ITASCA, 2001). For low intensity ground accelerations, they calculated earth pressure coefficient comparable to the M-O method; however, they suggested an upper bound closer to Wood's (1973) solution.

Gazetas et al. (2004) used finite elements to model the earthquake behavior of L-shaped walls and different type of anchored retaining structures, generally obtaining dynamic earth pressures smaller than M-O. More numerical simulations on reinforced soil have been developed by Schmertmann, Chew and Mitchel (1982). They concluded that conventional design methods under predict the reinforcements tension for typical compaction conditions.

Most recently Al Atik and Sitar (2008) and Mikola and Sitar (2013) modeled the earthquake response of yielding and non-yielding walls on medium dense sand, and calibrated their numerical models with centrifuge experiments. They concluded that a well calibrated numerical model captures the essential system responses and can be used as a predictive tool for seismic earth pressures and bending moments, given reliable estimates of the soil properties and a good constitutive model for the soil.

2.3. Experimental Methods

Over the years numerous experimental studies were conducted using both shaking table and centrifuge models. In general, the shaking table models usually had the model walls fixed to the shaking table, whereas the centrifuge models included both, experiments with walls fixed to the base of the container and experiments in which the model structures were founded on soil. The focus of this review is to identify the similarities and the differences in the observed model behavior and to evaluate them in comparison with field observations.

Following the great Kwanto earthquake of 1923, Mononobe and Matsuo (1929) conducted the first experiments of seismic earth pressures on retaining walls. The tests used a shallow sand box filled with relatively loose sand and were subjected to simple harmonic motions. The box dimensions were 4 × 4 × 9 ft and the walls at each end were hinged at the base allowing the wall to tilt outwards, as shown in the experiment set up of Figure 2.11. The seismic loads measured in the experiments were in agreement with Okabe's (1926) analytical work, and thus, Equation (2.2) became the standard for designing retaining walls with dry cohesionless materials.

Similar experiments on sand boxes were performed by Jacobson (1939), Matsuo (1941), Ishi et al. (1960), Matsuo and Ohara (1960), Sherif and Fang (1984), Fang and Ishibashi (1987). More recently, Elgamal and Alampalli (1992) performed a full scale dynamic test of a retaining wall of variable height. Using an impact sledge hammer and simplified numerical models, they identified the resonant patterns and space variability of the wall motion. For yielding walls, all of these experiments report seismic loads similar to the Mononobe-Okabe method, but the general observation was that the earth pressure distribution was non-linear and the resultant was applied at a point much higher than H/3.

An important limitation of scaled shaking table tests performed at 1-g is that the results cannot be scaled to prototype dimensions, since the strength and stiffness of the soil is a function of the confining stress and at the small confining pressures in a scaled experiment at 1-g the soil tends to behave as a rigid-plastic mass under dynamic loading (Ortiz, 1983). However, this kind of behavior is not evident in the field. In addition, the shaking table experiments in rigid boxes cannot adequately simulate typical boundary conditions encountered in prototype settings. An alternative to the 1-g shaking table experiments is to use the centrifuge in order to scale the dimensions of the model and to obtain the correct confining stresses. In a pioneering work, Ortiz (1983) performed centrifuge experiments to study the response of flexible cantilever walls on medium-dense sand, as seen in Figure 2.12. The container was subjected to medium intensity earthquake-like motions, resulting in seismic earth pressures consistent with the M-O theory with the point of application of the dynamic forces at 1/3H.

Bolton and Steedman (1982) and Bolton and Steedman (1984) performed centrifuge experiments of micro concrete cantilever walls retaining a dry cohesionless backfill. The walls were rigidly attached to the loading frame and were subjected to harmonic accelerations up to 0.22g at 0.75 Hz. They also suggested that the dynamic earth pressures acts at H/3 and that the wall inertial forces must be taken into account in addition to M-O earth pressures.

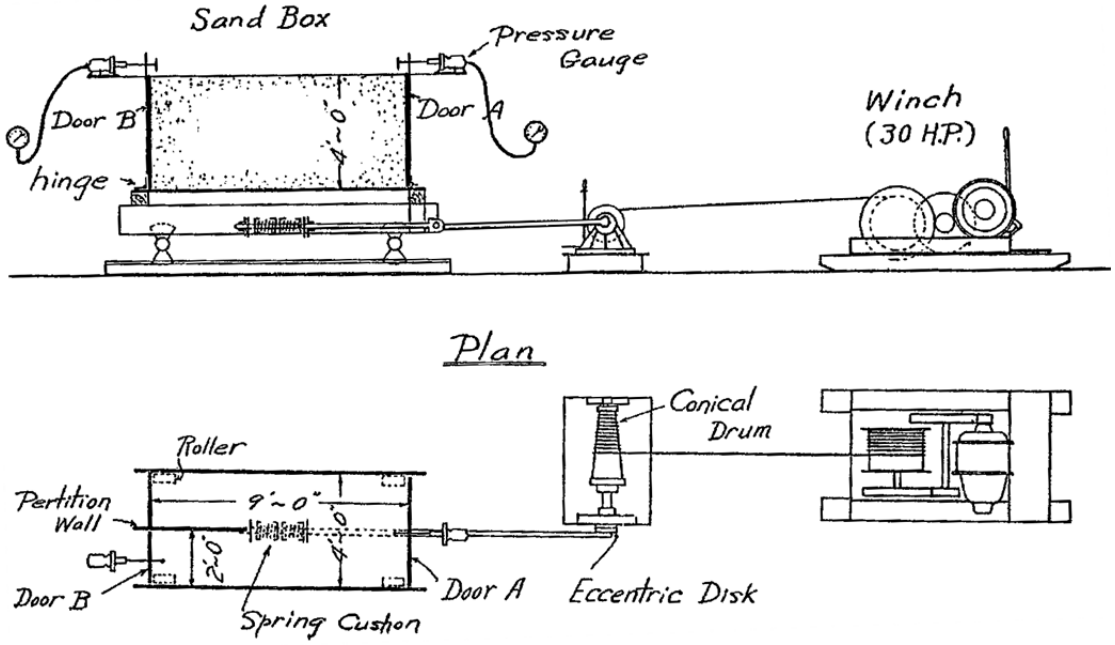

Figure 2.11 Shaking table experiment set up of Mononobe and Matsuo (1929).

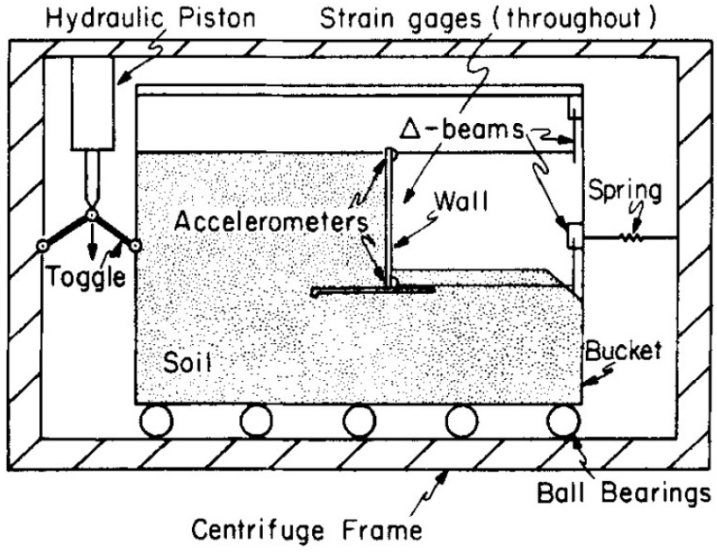

Figure 2.12 Centrifuge experiment set up of Ortiz (1983).

Nakamura (2006) re-examined the M-O theory studying the earthquake response of free standing gravity retaining walls in the centrifuge and concluded that the basic assumptions of the M-O theory are not met. He observed that when the walls are excited in the active direction the ground motion was transmitted instantly to the wall and then to the backfill. Moreover, the distribution of earth pressures was nonlinear and changed with time.

More recently, Al Atik and Sitar (2010) and Mikola and Sitar (2013), used the centrifuge to model the behavior of fixed base U-shaped walls, basement walls and freestanding cantilever walls supported in medium dense sand. The experiments used a flexible shear beam container that deforms horizontally with the soil. They concluded that the M-O method was conservative, especially at high accelerations above 0.4g. They also observed that earth the seismic pressures increase approximately linear with depth, and that the Seed and Whitman method (Seed and Whitman, 1970) with the resultant applied at 0.33H is a reasonable upper bound to the total seismic earth pressure increment.

Dynamic earth pressures on retaining structures with saturated backfill were studied in both,1-g shaking table and centrifuge experiments. Matsuo and Ohara (1965) used a 30 cm deep rigid box filled with saturated and sand subjected to harmonic accelerations. They concluded that the dynamic pore water pressures act at 0.4-0.5H and should be added to the earth induced pressures. Matsuzawa et al. (1985) reviewed the existing experimental results and theories to evaluate the hydrodynamic pressures on rigid retaining walls, and proposed a design method based on the M-O equation that incorporates the effects of permeability, backfill geometry and modes of wall movement. Dewoolkar (2001) performed centrifuge experiments to study the effect of liquefiable backfills on fixed-base cantilever walls under harmonic accelerations and showed that the excess pore pressure and inertial effects contributed significantly to the total seismic lateral pressure.

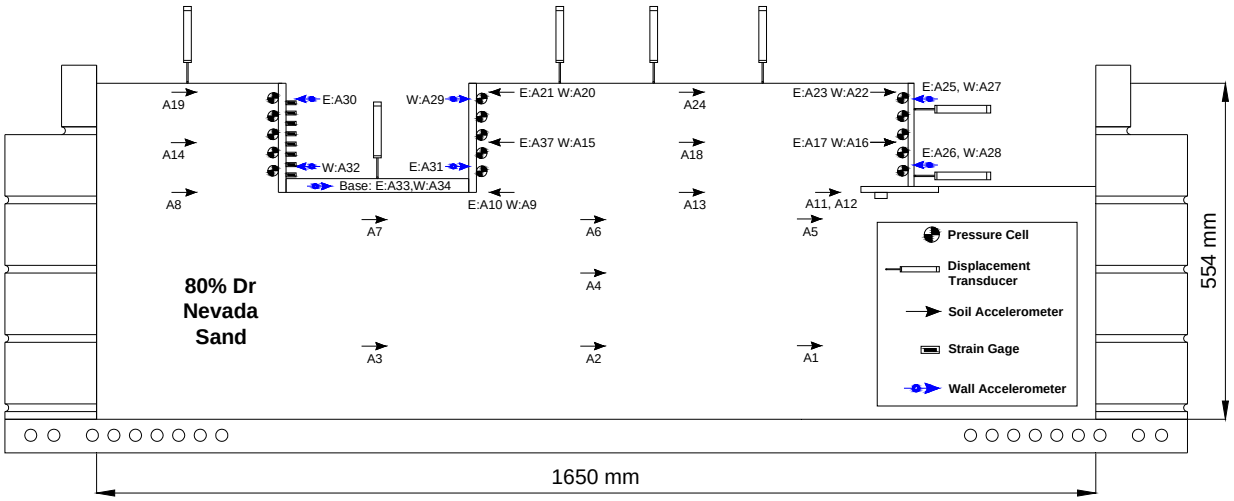

Figure 2.13 Centrifuge experiment set up of Mikola and Sitar (2013).

Overall, the review of past experimental work shows that there is a distinct difference in the behavior observed in 1-g shaking table tests and centrifuge model experiments in which the model retaining structure is fixed to the shaking table or the container, and those of the centrifuge experiments in which the model retaining structures are founded on soil. These are reflected in the different methods of analysis that have been developed over time.

2.4. Field Performance

Several post-earthquake reconnaissance surveys have documented failures of retaining structures. In most cases, the damage is directly caused by the liquefaction of saturated backfills and the supporting soil (Amano et al., 1956; Dukes & Leeds, 1963; Hayashi et al., 1966; Inagaki et al., 1996). Although less frequent, failure cases in which water did not play a role have also been reported in the literature.

According to Seed and Whitman (1970), retaining structures with non-liquefiable backfills have enough strength to withstand earthquakes of significant magnitude even without special design provisions. This has been confirmed in past and recent earthquakes (e.g. 1989 Loma Prieta, 1999 Turkey, 2010 Chile, 2011 Japan (Sitar et al., 2012)), where retaining structures have performed particularly well. Selected cases of failures and good performance of retaining structures with non-liquefiable backfill are reviewed in this section.

Clough and Fragaszy (1977) studied the performance of open floodways channels damaged during in the 1971 San Fernando Earthquake. The channels were designed for Rankine earth pressures with a factor of safety of 1.3. Although no seismic effects were accounted for explicitly, the actual yield strength of the rebar was twice the value used in the static design, which added an important strength reserve for dynamic loads. The increased seismic earth pressure damaged nearly 2 km of the floodway system, mainly in areas with a PGA of 0.5g or higher, as shown in Figure 2.14, causing an inward tilting of the walls and significant yielding of the wall-slab connection. Clough and Fragaszy (1977) concluded that the conventional factors of safety used in the static design of retaining structures provide enough strength to resist seismic loadings with no damage; in this case ground accelerations up to 0.5g. They suggest that the MO method used with 70% of PGA and the dynamic load placed at H/3 from the ground, gives results consistent with the observed performance.

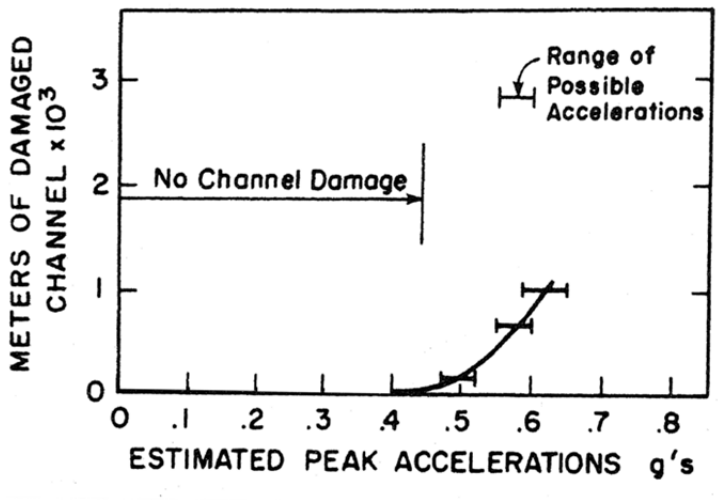

Figure 2.14 Damage to open floodways channels after the 1971 San Fernando Valley earthquake (Clough & Fragaszy, 1977).

Numerous researchers performed reconnaissance after the 1989 Loma Prieta earthquake (Bensuka, 1990; Whitman, 1991) and the 1994 Northridge earthquake (Stewart et al., 1994; Hall 1995; Holmes and Somer, 1996; Lew, Simantob and Judson, 1995). There were no reports of damage to basement structures, mechanically stabilized earth or deep excavation.

The devastating 1995 Kobe earthquake provided evidence of failure in freestanding retaining walls and waterfront structures. No damage to building basements was reported, as cited by Lew et al. (2010). While there was damage to some subway stations, only the Dakai station (Yoshida, 2009) suffered collapse apparently due to a poor structural design and presumably liquefaction of the backfill, but not as a result of dynamic earth pressures (Iida et al. 1996; Yoshida, 2009, Lew et al., 2010).

Most recently, after the 1999 Chi-Chi earthquake, Huang (2000) studied the failure of different types of retaining structures, most of them located on steep slopes. The leaning-type gravity walls, commonly used in Taiwan to support highway embankments, collapsed as a result of low bearing capacity and stress concentration at the footings. Failures of modular block walls retaining soil stabilized with geosynthetics was caused by inadequate design considerations and slope failures in the backfill. Similarly, in the 2010 Chile earthquake different types of retaining structures were subjected to high seismic accelerations. The performance of MSE walls, basements, gravity and cantilever walls was excellent and no significant problems were reported (Bray et al, 2012).

3. PHYSICAL MODELING

3.1. Geotechnical Centrifuge Experiments

Scaled experimental models are essential to geotechnical earthquake engineering because they allow predicting the response of complex systems in a controlled environment. In that sense, centrifuge testing has been used widely in research to study various types of problems including seismic soil-structure interaction (SSI), and particularly, the behavior of earth retaining structures.

Since the behavior of soil is largely controlled by its state of stress, the idea behind centrifuge experiments is to scale the length and acceleration field so that the stresses at any point in the model are identical to the stresses of the corresponding point in the prototype. To accomplish this, a $1/N$-scale model is spun with angular velocity $\Omega = \sqrt{Ng/r}$ at a distance r from the centrifuge spindle, increasing the gravity field N times, as shown schematically in Figure 3.1. The earthquake motions are simulated using a shaking table located below the model container.

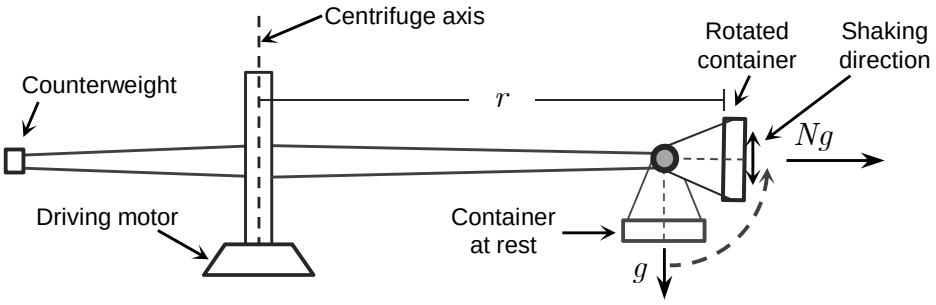

Figure 3.1 Schematic view of the geotechnical centrifuge.

The scaling laws of centrifuge experiments are summarized in Table 3.1 for different physical parameters. For example, at a depth of 20 m a soil with γ=20 kN/m^3 has a vertical stress of 400 kPa. If a scaling factor $N = 40$ is used in the centrifuge, the equivalent depth is 0.5 m and the soil weights 800 kN/m^3, but the vertical stress remains at 400 kPa. Analogously, an earthquake that lasts 40 sec in real time, in the centrifuge takes only 1 sec. For a more throughout discussion of centrifuge scaling principles refer to Kutter (1995).

The main advantage of centrifuge experiments over 1-g shaking tables is that the stresses and strains in the soil can be correctly scaled. As a result it is possible to reproduce complex failure mechanism that would be hard to detect even in full scale prototypes. Different acceleration input can be applied at the base, ranging from simple step waves to complex earthquake-like motions. Centrifuge experiments are also cost effective, repeatable and allow measuring the influence of important factors for evaluating alternative designs (Dobry and Liu, 1994).

Nevertheless, centrifuge modeling is not problem free: the gravitational field increases linearly with the radius which becomes less pronounced with increasing centrifuge radius; highly sensitive instruments are required to capture the frequency content of centrifuge earthquakes; the soil deposit may interact with the container boundary; and rocking and sloshing modes can create undesired high vertical accelerations in the soil and structures.

Table 3.1 Scaling factors (model / prototype) used in 1-g shaking table and centrifuge experiments

Parameter	1-g Shaking Tables	Centrifuge Experiments
Length	1/N	1/N
Mass Density	1	1
Acceleration, Gravity	1	N
Dynamic Time	$1/N^{0.5}$	1/N
Dynamic Frequency	$N^{0.5}$	N
Velocity	$1/N^{0.5}$	1
Stress, Strength	1/N	1
Strain	1	1
Strain Rate	$N^{0.5}$	N
Mass	$1/N^3$	$1/N^3$
Force	$1/N^3$	$1/N^2$
Moment	$1/N^4$	$1/N^3$
Energy	$1/N^4$	$1/N^3$
Bending Stiffness (EI)	$1/N^5$	$1/N^4$
Normal Stiffness (EA)	$1/N^3$	$1/N^2$

3.2. The Large Centrifuge at UC Davis and Model Container

The experiments in this study were conducted at the NEES Center for Geotechnical Modeling of UC Davis, CGM. The centrifuge has a 9.1 m radius from spindle to container floor, and can carry maximum payloads of 4.5 tons to accelerations of 75 g.

A horizontal shaking table is mounted on the centrifuge arm and consists of a loading frame and two parallel servo-hydraulic actuators capable of simulating a broad range of earthquake events. The models can be instrumented with a range of sensors and all the information is collected with a high speed Data Acquisition System (Wilson, 1998). For this research, the models were built in the Flexible Shear Beam container FSB2.1, designed to deform horizontally with the soil during earthquakes. The FSB2.1 container, shown schematically in Figure 3.2, weights 810 kg and is formed by a base plate and five rings stacked between 12 mm neoprene layers. The fixed base natural frequency has been estimated at $0.71N$ (Hz).

3.3. Model Design

Two centrifuge models of earth retaining structures were built at 1/36 scale and tested with a centrifuge acceleration of 36 g. In the following description of the experiment layouts the dimensions are given in prototype scale, unless noted.

The first experiment, named GC01, consisted of a 6 m deep basement wall and cantilever wall, with a horizontal backfill and founded on 13 m of silty clay soil as shown in Figure 3.3 and Figure 3.4. The basement model consisted of aluminum walls with cross bracing at the top and bottom. The individual braces were instrumented with load cells in order to measure the total static and dynamic loads on the two opposing walls. Although this model configuration produced a stiff structure, it did not entirely eliminate racking, as will be discussed later. The 6 m cantilever wall was modeled as a standard AASTHO-LRFD retaining wall per Caltrans specifications, with a 4.5 m wide footing and a shear key to prevent rigid body sliding. A detailed cross section of the prototype wall is shown in Figure B.1.

The second experiment, named GC02, consisted of a 6 m cantilever wall, retaining a 2:1 slope, 8.5 m high in compacted silty clay, as shown schematically in Figures 3.5 and 3.6.

Approximately 80 instruments were used in each experiment to monitor the seismic response, including accelerometers, displacement transducers, load cells, strain gages and pressure cells. The approximate locations of the instruments are shown in the profiles and plan views of the models.

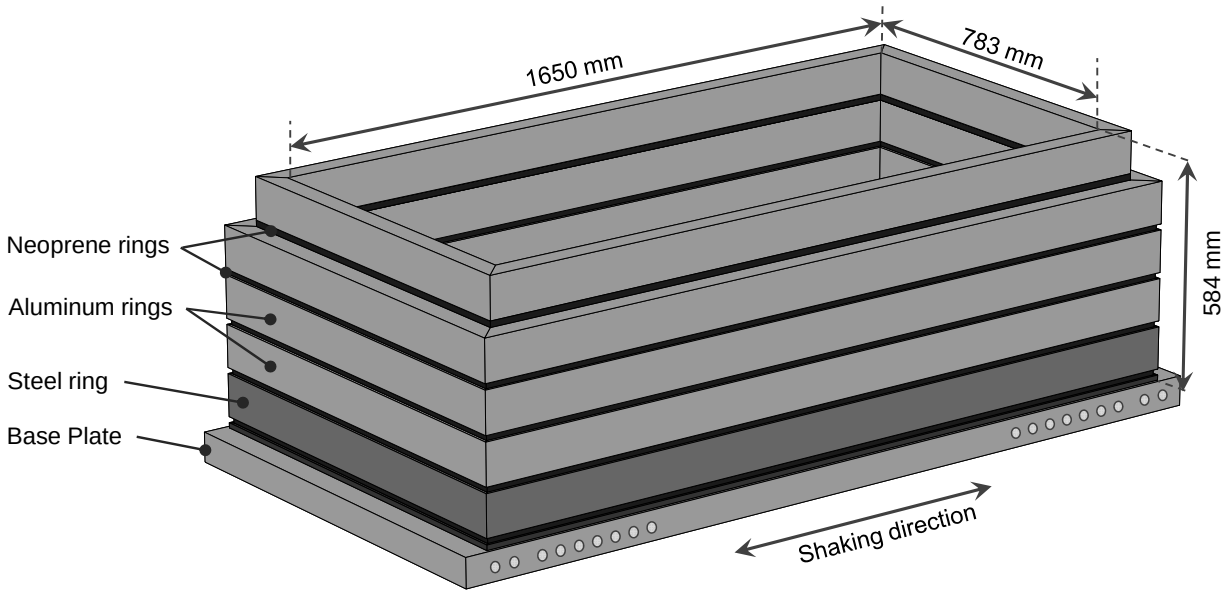

Figure 3.2 Schematic view of the container FSB2.1.

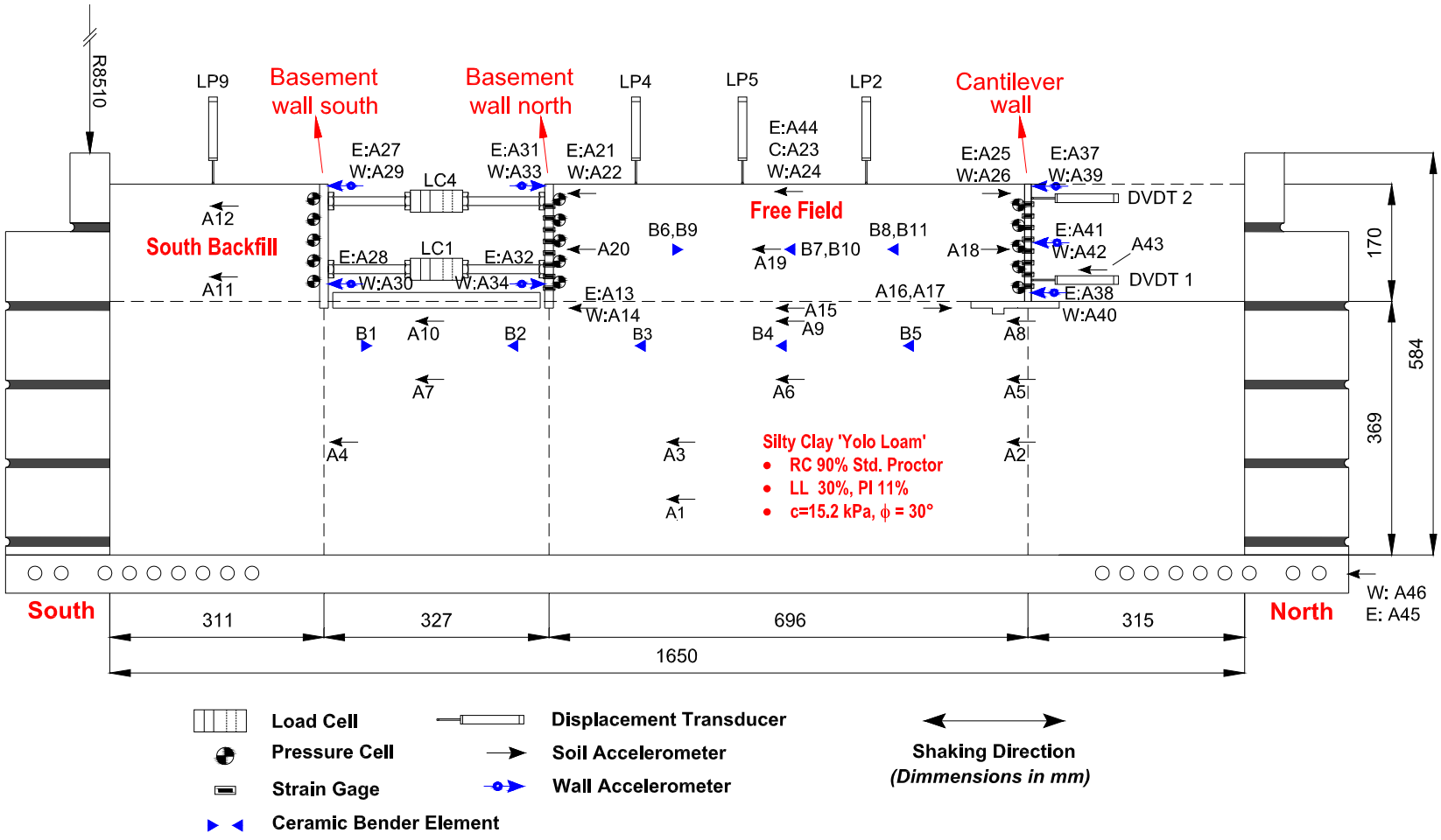

Figure 3.3 Profile of level ground model GC01

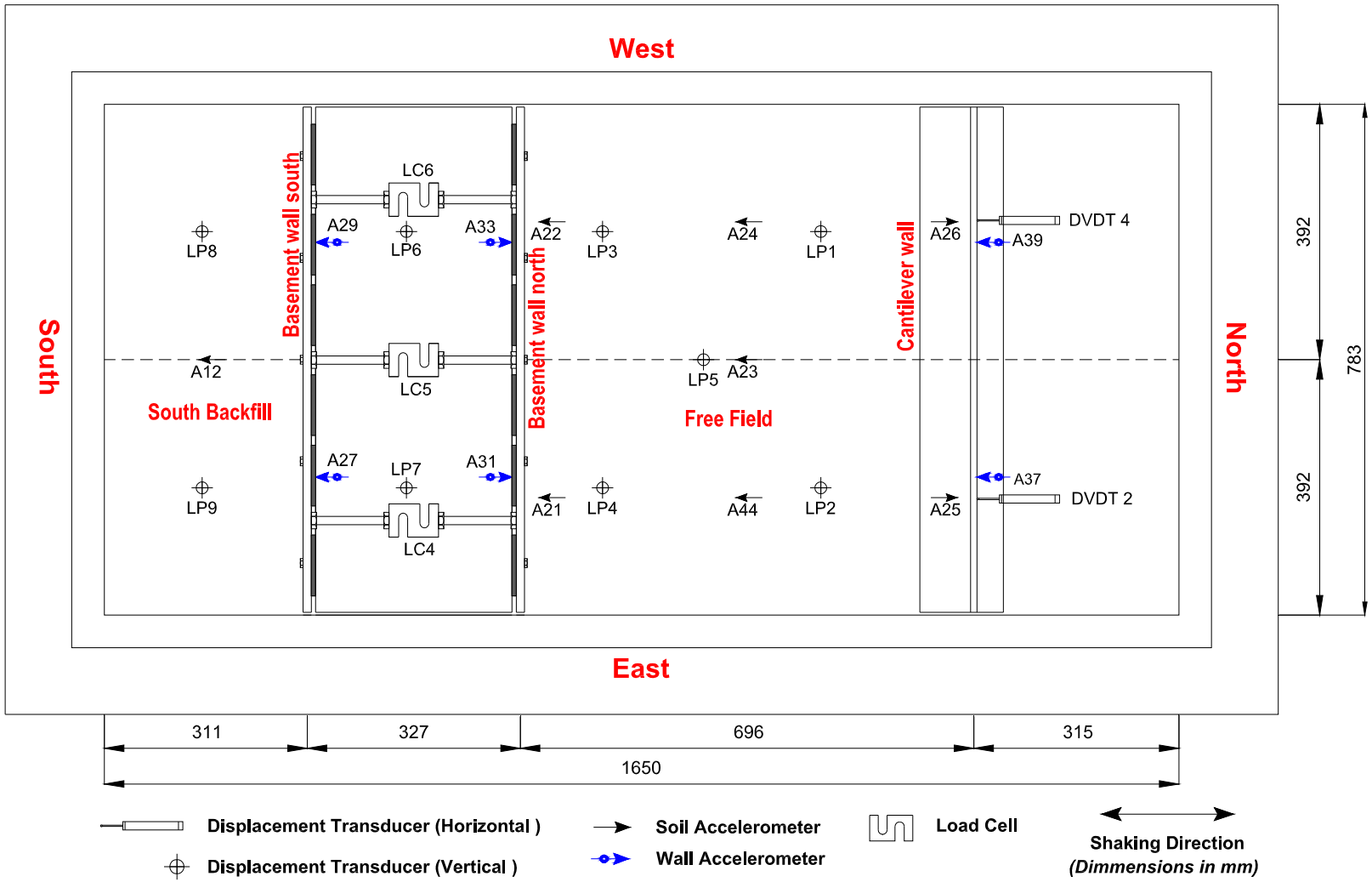

Figure 3.4 Plan view of level ground model GC01.

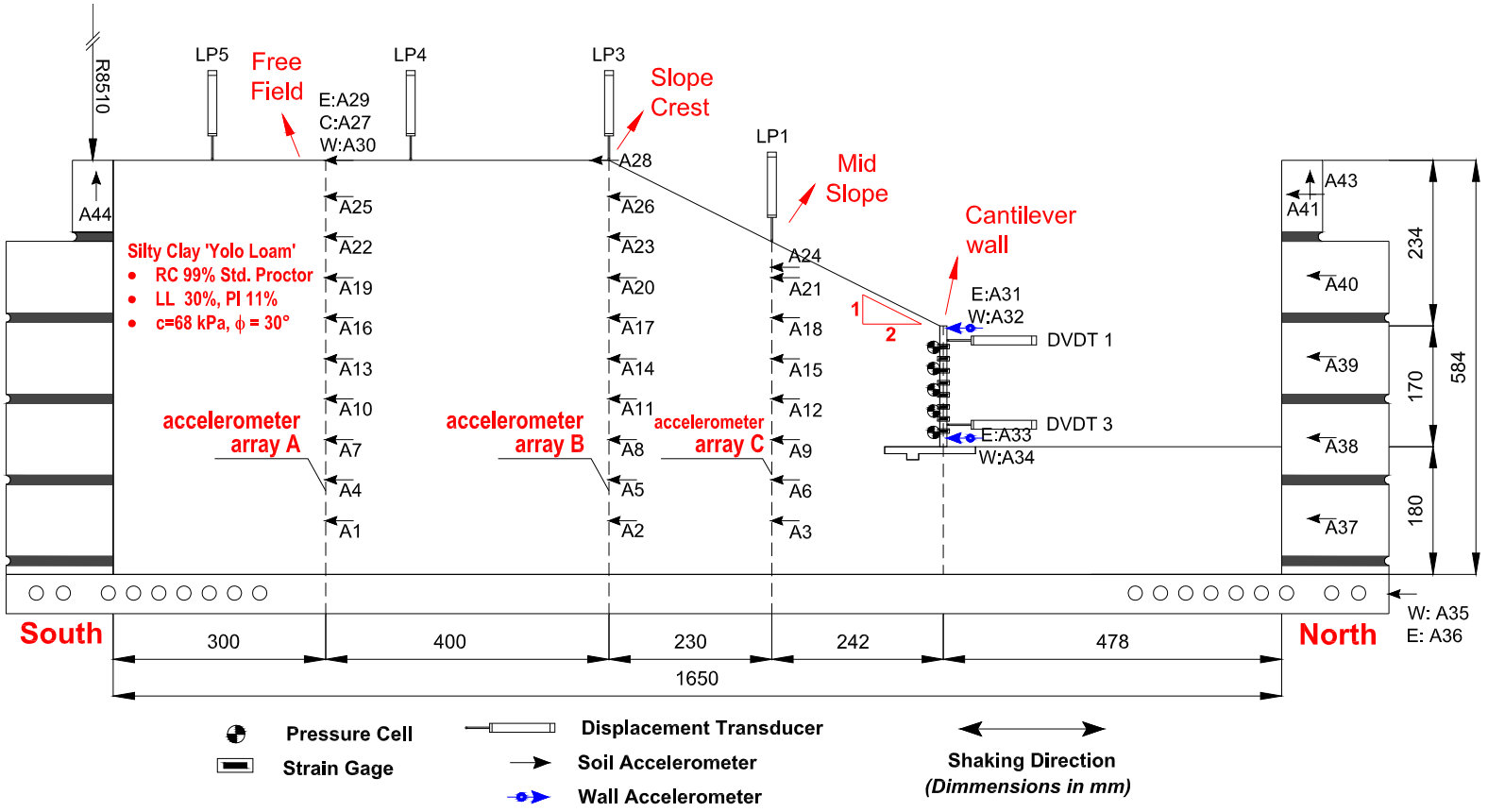

Figure 3.5 Profile of sloping ground model GC02.

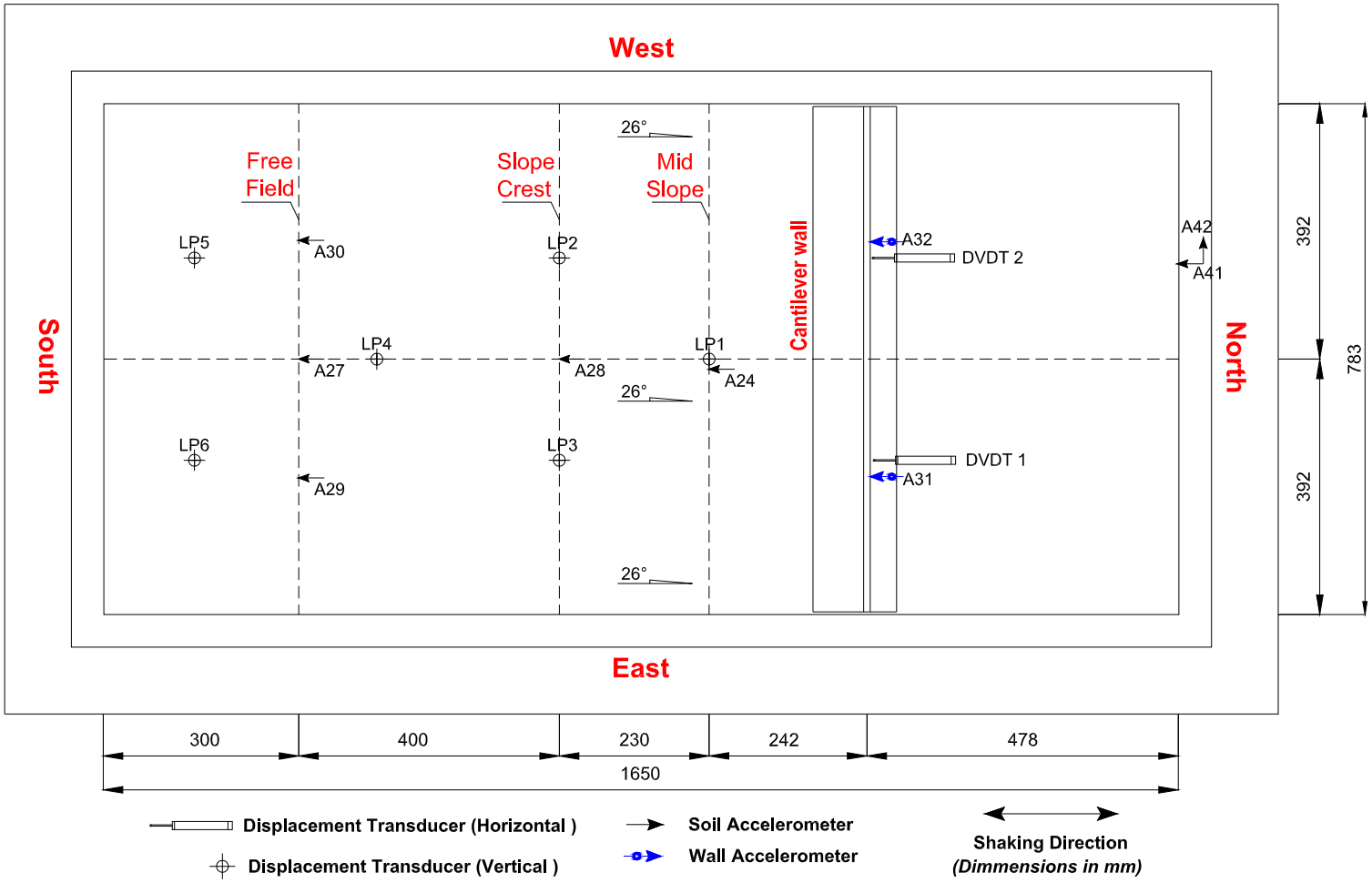

Figure 3.6 Plan view of sloping ground model GC02.

3.4. Soil Characterization

The soil used in the experiments is a low plasticity lean clay (CL), called Yolo Loam from a borrow pit at the centrifuge facility. A series of laboratory tests was performed for the purposes of classification and to determine mechanical properties of the soil as compacted. Atterberg limits (ASTM D4318) were found to be: LL = 29.5%, PL = 18.2%, giving a PI=11.3%. The maximum dry unit weight was 18.1 kN/m^3 and the optimum water content was 15%, based on the Standard Proctor compaction curves (ASTM D698, ASTM D1557), as shown in Figure 3.7. Strength parameters c and φ were determined from a series of unconfined-unconsolidated (UU) triaxial tests. The samples were retrieved from the model GC01 after the centrifuge experiment was over, and sheared until failure at confining stresses of 0.5, 1.0 and 2.0 atm.

Bender elements were used to measure shear wave velocities at different confining stresses (ASTM D4015) on samples retrieved from the centrifuge model GC01. The small shear strain modulus was expressed as $G_{max} = G_r(p/p_a)^{0.5}$, where G_r is the reference shear modulus at 1 atm. The measured shear strain versus shear modulus reduction curves agree with the published G/G_{max} relationships (Darandeli, 2001; Voucetic & Dobry, 1991; Sun & Seed, 1988), as seen in Figure 3.8. The most important soil parameters determined for experiments GC01 and GC02 are summarized in Table 3.2.

Table 3.2 Geotechnical parameters of compacted Yolo Loam

Parameter	Model GC01	Model GC02
γ (kN/m^3)	18.7	20.8
γ_d (kN/m^3)	16.0	18.1
ω (%)	17	15
c (kPa)	15.2	68.1
ϕ (deg)	30	30
c/γH	0.13	0.54

3.5. Model Dimensions and Geometry

The rigid basement wall used in GC01 was an adaptation of the stiff U-shaped walls used by Al Atik and Sitar (2010), consisting of 12.7 mm thick walls and a 22.9 mm thick base built in aluminum T6061. In order to stiffen the structure, the walls were connected by 6 steel struts instrumented with load cells, which allows measuring static and dynamic earth pressure in the basement. For this reason, the base of the structure was a free-floating slab separated from the walls a 6.4 mm (20+cm prototype) gap filled with soft foam. The self-weight of the walls was transferred to the base using 10 sliding pins distributed on either side of the base, as shown in Detail 'A' of Figure 3.9.

The cantilever wall used in GC01 and GC02 was a 1/36 scale model of a 6 m standard retaining wall used by Caltrans, consisting of a wall, a footing and a shear key, as already described. A detail of the wall-footing connection is shown in Figure 3.10. All the components were built in 3/8 in thick aluminum plates, and the dimensions were set to match the effective moment of inertia of the prototype sections. The total mass of the structure was matched by adding small lead blocks on the wall and base. The material properties of the walls and struts are presented in Table 3.3. The structural dimensions for each component of the rigid basement and cantilever wall are summarized in Table 3.4.

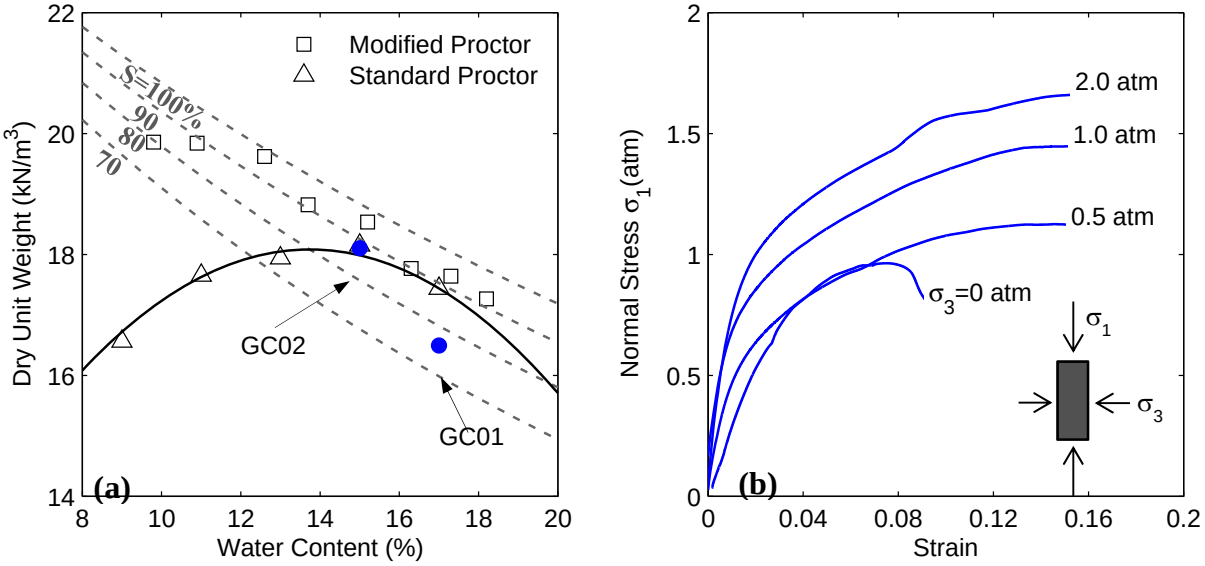

Figure 3.7 (a) Compaction curves and (b) stress-strain curves on the UU triaxial tests.

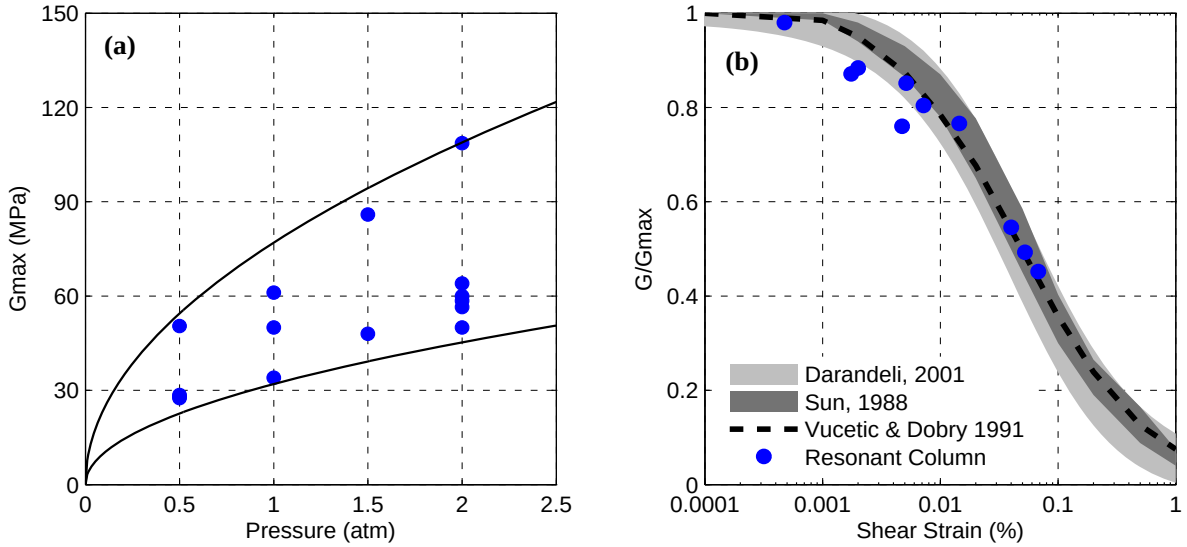

Figure 3.8 (a) G_{max} versus confining stress and (b) shear modulus reduction factor.

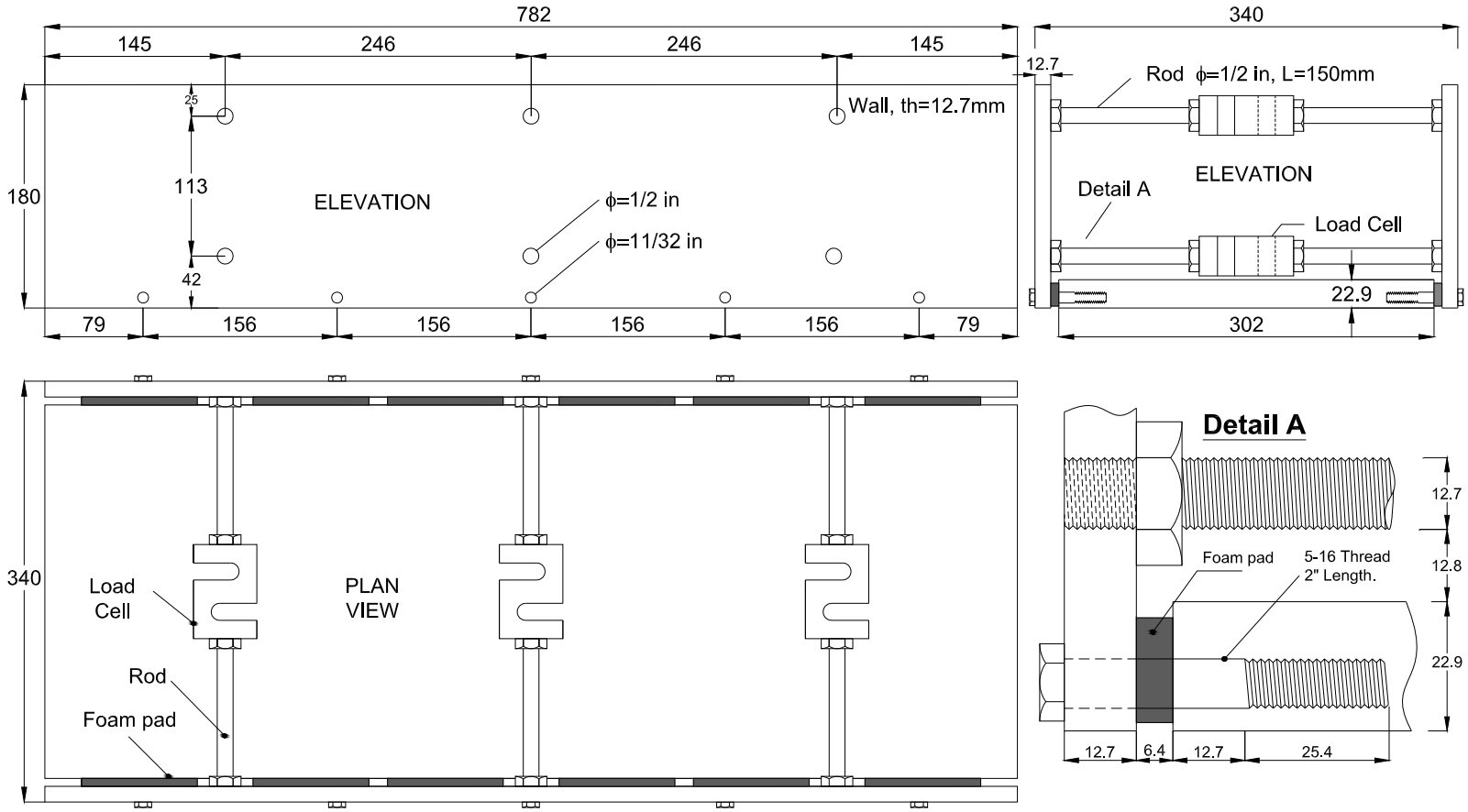

Figure 3.9 Rigid basement model (dimensions in mm).

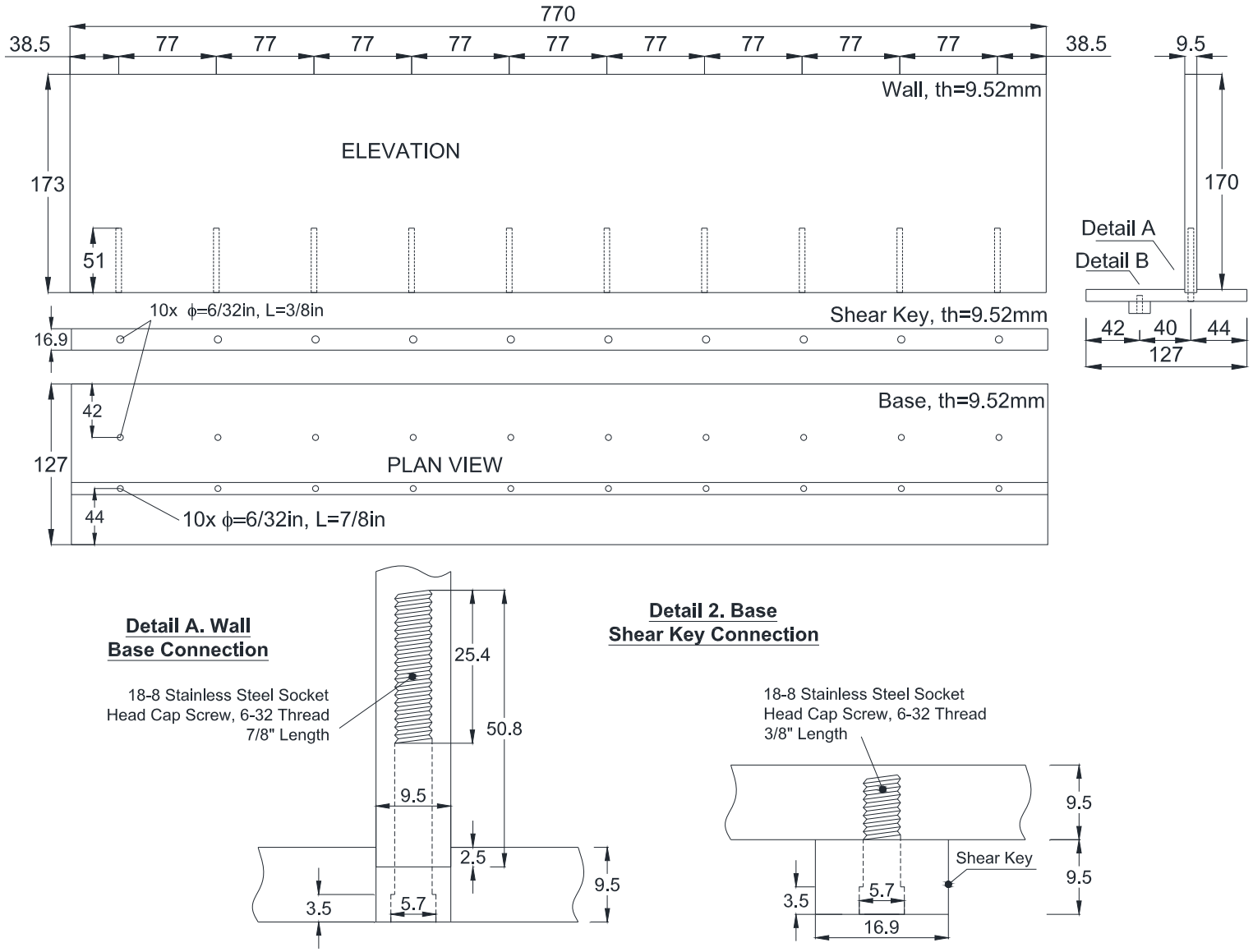

Figure 3.10 Cantilever wall model (dimensions in mm).

Table 3.3 Aluminum and Steel Properties

Material Properties		Alum		Steel	
Mass Density	ρ	2.700E+03	kg/m3	7.850E+03	kg/m3
Shear Modulus	G	2.612E+07	kPa	7.921E+07	kPa
Bulk Modulus	K	6.384E+07	kPa	1.716E+08	kPa

Table 3.4 Structural element dimensions of the model and the prototype based on a length scaling factor N=36

Rigid Basment properties		Model		Prototype		Prototype per unit width	
Plain Strain Width	d	7.82E-01	m	2.82E+01	m	1.00E+00	m
Aluminum Wall							
Unit Mass	ρ	4.10E+03	kg/m^3	4.10E+03	kg/m^3	4.10E+00	ton/m^3
Cross Section	A	9.93E-03	m^2	1.29E+01	m^2	4.57E-01	m^2/m
Moment of Inertia	I	1.33E-07	m^4	2.24E-01	m^4	7.96E-03	m^4/m
Cross Bracing							
Unit Mass Roof	ρ	2.13E+04	kg/m^3	2.13E+04	kg/m^3	2.13E+01	ton/m^3
Cross Section	A	2.19E-04	m^2	2.84E-01	m^2	1.01E-02	m^2/m
Moment of Inertia	I	1.14E-08	m^4	1.92E-02	m^4	6.83E-04	m^4/m

Cantilever wall properties		Model		Prototype		Prototype per unit width	
Plain Strain Width	d	7.70E-01	m	2.77E+01	m	1.00E+00	m
Aluminum Wall							
Unit Mass	ρ	3.19E+03	kg/m^3	3.19E+03	kg/m^3	3.19E+00	ton/m^3
Cross Section	A	7.33E-03	m^2	9.51E+00	m^2	3.43E-01	m^2/m
Moment of Inertia	I	5.545E-08	m^4	9.31E-02	m^4	3.36E-03	m^4/m
Aluminum Base							
Unit Mass	ρ	3.61E+03	kg/m^3	3.61E+03	kg/m^3	3.61E+00	ton/m^3
Cross Section	A	7.33E-03	m^2	9.51E+00	m^2	3.43E-01	m^2/m
Moment of Inertia	I	5.55E-08	m^4	9.31E-02	m^4	3.36E-03	m^4/m

3.6. Model Construction

The construction of experiment GC01 and GC02 was affected by a number of factors. Variables including the natural water content in the soil, compaction technique and previous experience considerably affected the time required to prepare the models, which varied from 3.5 weeks in the case of model GC01 to 2 weeks in the case of model GC02. The models construction consisted of several stages as described below and shown in Figures 3.11 and 3.12:

- **Soil excavation and sieving**: For each test, approximately 1 m^3 of Yolo Loam was retrieved from the centrifuge facility with a small excavator. Using a mechanical sieve, the soil was passed through a sieve #4 (4.76mm) and stored on barrels.
- **Soil mixing**: The target moisture content in GC01 was 17% and the natural moisture was about 7%. Thus, water was slowly sprinkled inside a drum mixer to homogenize the soil and prevent the formation of lumps. In experiment GC02 the target moisture was 15% which was very close to the natural moisture, significantly reducing the time required to prepare the soil.
- **Soil compaction**: In GC01, a 7 kg vibrating block with a corrugated base plate was used to compact the soil on 2.5cm lifts. After each lift a sheep-foot roller was passed to increase the interlayer bonding. This compaction device delivered low amounts of energy to the soil resulting in a dry density γ_d=16.5 kN/m^3, equivalent to 90% of the maximum dry unit weight achieved through the Standard Proctor test. A significantly higher compaction effort was used in GC02 by using a pneumatic hammer on 2.5 cm lifts, resulting in a dry density of γ_d=18.1 kN/m^3, approximately 100% of the maximum dry unit weight using the Standard Proctor test as a reference. The respective of water content versus dry density point values are plotted on the compaction plot in Figure 3.7.
- **Placement of instruments and structures**: Embedded accelerometers were added to the model between soil layers as shown in Figure 3.11(c). Each sensor was buried 2.5 cm under firm soil to prevent damage due to compaction. The structures were instrumented with load cells, strain gages and pressure cells, and then placed in the container. A special strut system was design to prevent lateral displacements in the cantilever walls and the 2:1 slope of experiment GC02. Vertical and horizontal displacement transducers were installed in the free surface and retaining wall using a special aluminum frame.
- **Configuration of the DAQ system and bucket balance**: Once the model is placed in the arm, all sensors are connected to the DAQ system and their response is checked with the arm at rest. In experiment GC02, the model asymmetry created an out balance moment of 1400 lbf·ft, which was corrected by removing counter weights from the south end of the bucket.
- **Spinning**: The arm was spun to 62 rpm, creating 36 g at a distance of 8.5 m from the centrifuge spindle. Special care was given to GC02, since a rapid increase of gravity could trigger a slope failure. Therefore, the arm was accelerated slowly in 6 g intervals allowing for the dissipation of any excess pore pressure.

Figure 3.11 Construction of level ground model GC01 (a) soil mixing, (b) compaction device, (c) placement of accelerometers, (d) basement wall on south end, (e) cantilever wall on north end, (f) model in the arm.

Figure 3.12 Construction of sloping backfill model GC02 a) placement of backfill, b) installation of accelerometers, c) pneumatic hammer compaction, d) wood struts used to prevent lateral displacements during compaction, e) finished slope, f) model in the arm.

3.7. Instruments Calibration

Different instrument types were used in the experiments to record the seismic response of the models. The main objective was to obtain a reliable measure of earth pressures and to characterize the ground motions. The instrumentation is described below and in Table 3.5.

Table 3.5 Instruments used and manufacturer's specifications

Instrument	Manufacturer / Model	Range	Frequency Limits	Natural Frequency
Accelerometers	PCB Piezotronics 352MC68	± 50 g	0.3 - 12000 Hz	≥ 35000 Hz
	PCB Piezotronics 352M54	± 100 g	0.3 - 13000 Hz	≥ 40000 Hz
Load Cells	Interface SSM-AJ-500	± 500 lbf	≤ 2000 Hz	2150 Hz
Strain Gages	Vishay Measurement Group J2A-13-S181H-350	± 3 %	≤ 2000 Hz	N/A
Displacement Transducers	BEI Duncan 603R3KL.25	0 - 3 in	N/A	N/A
	BEI Duncan 604R4KL.15	0 - 4 in	N/A	N/A
	Novotechnik TR 50 *(spring loaded)*	± 55 mm	0 - 14 Hz	N/A
Pressure Cells	Tactilus Free Form	0 - 15psi	0 - 100 Hz	N/A

- **Accelerometers**: used to measure accelerations in the soil, retaining structures and the container rings of model GC02. The sensitivity was provided by the manufacturer.
- **Load Cells**: used in GC01 to measure the axial load in the struts connecting the south and north walls of the basement. Jam nuts were used to fix the load cell to the struts. The load cell sensitivity was provided by the manufacturer.
- **Displacement Transducers**: soil settlement was measured at different points with Linear Potentiometers (LP) and the lateral wall displacements were recorded with 4 position transducers (DVDT) placed in a special frame attached to the centrifuge bucket. All transducers were calibrated using a standardized LVDT.
- **Pressure Cells**: Free Form Tactilus pressure sensors were installed in basement walls and cantilever walls as indicated in Figures B.2 to B.4. These sensors are 25.4 mm diameter and 0.4 mm thick, which minimizes the stress arching around the sensor. To calibrate the pressure cells, the vertical stress γH was measured at the footing of the cantilever walls during spin down at the end of the centrifuge experiment. Since Free Form Tactilus sensors are non-linear resistances, the relation between pressure and output voltage is also non-linear.

- **Strain Gages**: total bending moments were measured in the cantilever wall and the north basement wall with full bridge strain gages as indicated in Appendix Figures B.2 to B.4. The strain gages were calibrated off the arm by fixing the wall at the footing and applying a strip load at the top.
- **Bender Elements**: two arrays of ceramic bender elements were used in experiment GC01 to measure shear wave velocity. These instruments use a separate Data Acquisition System with a sampling rate of 90 KHz.

The high speed Data Acquisition System used in the centrifuge collects data at 4096 samples per second, on every channel. For experiments with a scaling factor of N=36, a typical ground motion input has frequencies between 10 – 300 Hz in model scale. Thus, based on Table 3.5, it is assumed that accelerometers and load cells capture all the frequencies of interest. The displacements transducers, on the other hand, should only be used to measure static displacements because their frequency response is limited. In the case of Tactilus pressure cells, the measured frequency content of the sensors is between 0 – 300 Hz, although the manufacturer indicates a maximum frequency response of 100 Hz.

3.8. Input Ground Motions

Nine and ten ground motions were used in models GC01 and GC02, respectively, to simulate real earthquakes. The selected ground motions were scaled to different amplitudes and predominant frequencies. The original recorded earthquakes are: 1989 Loma Prieta UCSC 090, 1989 Loma Prieta WCV 270, 1995 Kobe Takatori 090, 1999 Kocaeli Yarimca 060 and 1999 Kocaeli Yarimca 330. These earthquakes were previously scaled and filtered to fit the capabilities and limitations of the shaking table mounted on the centrifuge while preserving the main characteristics of the original ground motions (Al Atik & Sitar, 2010).

A comparison between the response spectrum from the original records and centrifuge input motions is presented in Figures 3.13 and 3.14. Seismic parameters of the input ground motions used in experiments GC01 and GC02 are presented in Tables 3.6 and 3.7, respectively. For each ground motion the parameters listed are the Peak Ground Acceleration (PGA), Peak Ground Velocity (PGV), Peak Ground Displacement (PGD), Arias Intensity (I_a), Significant Duration of the acceleration record ($D_{a5\text{-}95}$), the Mean Period (T_m), Predominant Period (T_p) and the center frequency of the input velocity (f_c). The Significant Duration of the acceleration record (Trifunac and Brady, 1975), defined as $D_{a5-95} = t(0.95I_a) - t(0.05I_a)$, is the time interval in which 90% of the seismic energy is dissipated. The Mean Period (Rathje et al., 1998) $T_m = \sum c_i^2 \, f_i^{-1} / \sum c_i^2$ and Predominant Period $T_p = T(S_a^{max})$, are used to characterize the frequency content of the acceleration history, where c_i is the Fourier amplitude of the acceleration series, f_i the discrete frequencies between 0.25-20 Hz and S_a is the 5% damped acceleration response spectrum. Finally, the center frequency of the input velocity $f_c = \sum s_i^2 \, f_i / \sum s_i^2$, where s_i is the Fourier amplitude of the velocity, is used to define the parameters for Rayleigh damping. The histories of input ground accelerations are presented in Figures 3.15 and 3.16, determined as the average base acceleration.

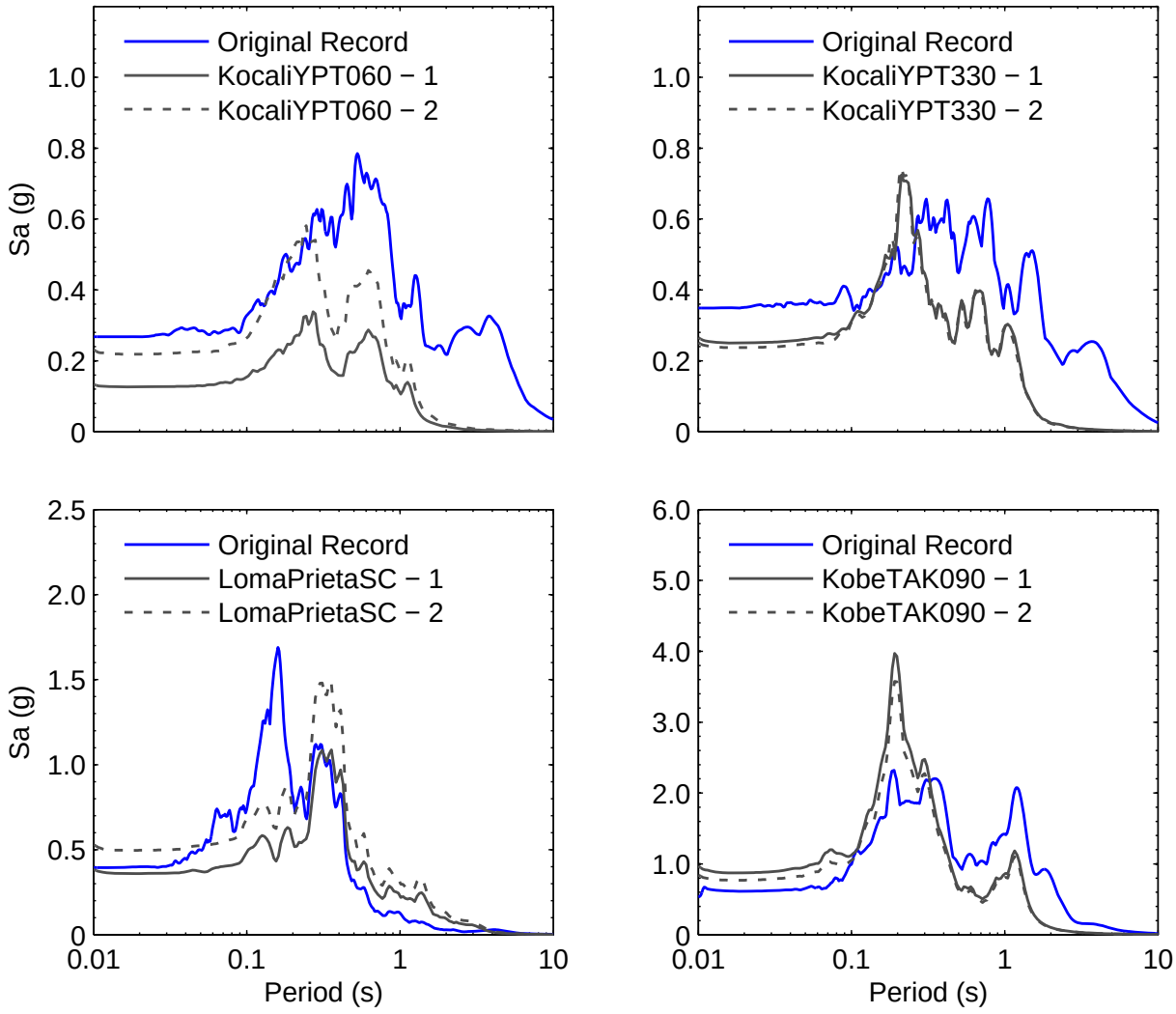

Figure 3.13 Response spectrum ξ=5% from originally recorded earthquakes and input base acceleration used in model GC01.

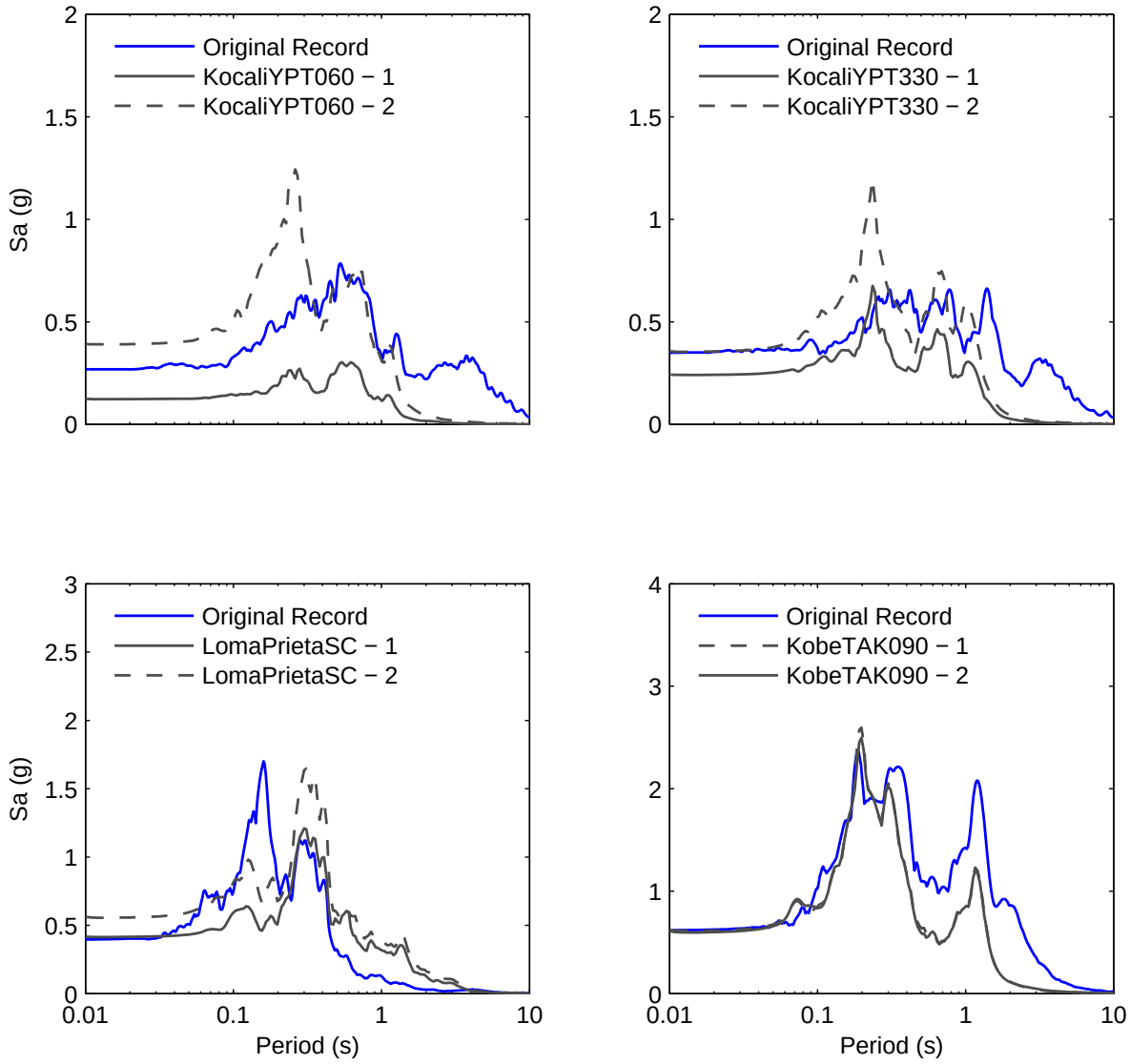

Figure 3.14 Response spectrum ξ=5% from originally recorded earthquakes and input base acceleration used in model GC02.

Table 3.6 Seismic parameters of input ground motions recorded in GC01

	Experiment: GC01	*PGA*	*PGV*	*PGD*	*Ia*	D_{a5-95}	T_m	T_p	f_c
	Input Ground Motion	**(g)**	**(cm/s)**	**(cm)**	**(cm/s)**	**(s)**	**(s)**	**(s)**	**(Hz)**
1)	Kocali YPT060 - 1	0.13	7.1	1.1	11.0	6.9	0.51	0.26	1.45
2)	Kocali YPT060 - 2	0.22	11.4	1.7	32.4	6.5	0.47	0.24	1.55
3)	Kocali YPT330 - 1	0.25	16.5	1.9	42.9	6.9	0.47	0.23	1.46
4)	Loma Prieta SC - 1	0.48	25.0	4.4	141	10.9	0.52	0.35	1.17
5)	Kobe TAK090 - 1	0.93	36.3	6.9	582	6.2	0.44	0.19	1.35
6)	Loma Prieta SC - 2	0.50	26.5	4.5	150	10.7	0.51	0.32	1.20
7)	Loma Prieta WVC270 - 1	0.25	15.9	1.9	30.5	5.0	0.49	0.23	1.33
8)	Kocali YPT330 - 2	0.24	15.8	1.8	42.8	6.8	0.46	0.22	1.50
9)	Kobe TAK090 - 2	0.82	32.7	6.5	488	6.3	0.45	0.19	1.33

Table 3.7 Seismic parameters of input ground motions recorded in GC02

	Experiment: GC02	*PGA*	*PGV*	*PGD*	*Ia*	D_{a5-95}	T_m	T_p	f_c
	Input Ground Motion	**(g)**	**(cm/s)**	**(cm)**	**(cm/s)**	**(s)**	**(s)**	**(s)**	**(Hz)**
1)	Kocali YPT060 - 1	0.12	8.1	1.1	9.2	6.8	0.57	0.58	1.4
2)	Loma Prieta SC - 1	0.41	25.1	4.3	105	11.0	0.59	0.30	1.1
3)	Kobe TAK090 - 1	0.72	41.2	6.9	426	6.3	0.55	0.19	1.2
4)	Kocali YPT330 - 1	0.24	14.8	1.9	38	6.9	0.53	0.24	1.4
5)	Kocali YPT060 - 2	0.40	18.6	3.1	121	6.6	0.46	0.26	1.6
6)	Loma Prieta WVC270-1	0.57	32.0	4.0	140	5.0	0.50	0.28	1.3
7)	Kobe TAK090 - 2	0.66	40.8	7.3	407	6.4	0.55	0.20	1.2
8)	Loma Prieta SC - 2	0.58	30.2	5.5	207	11.0	0.55	0.30	1.1
9)	Kobe TAK090 - 3	0.86	47.1	8.8	643	8.4	0.54	0.20	1.1
10)	Kocali YPT330 - 2	0.36	20.0	3.4	118	7.1	0.53	0.23	1.4

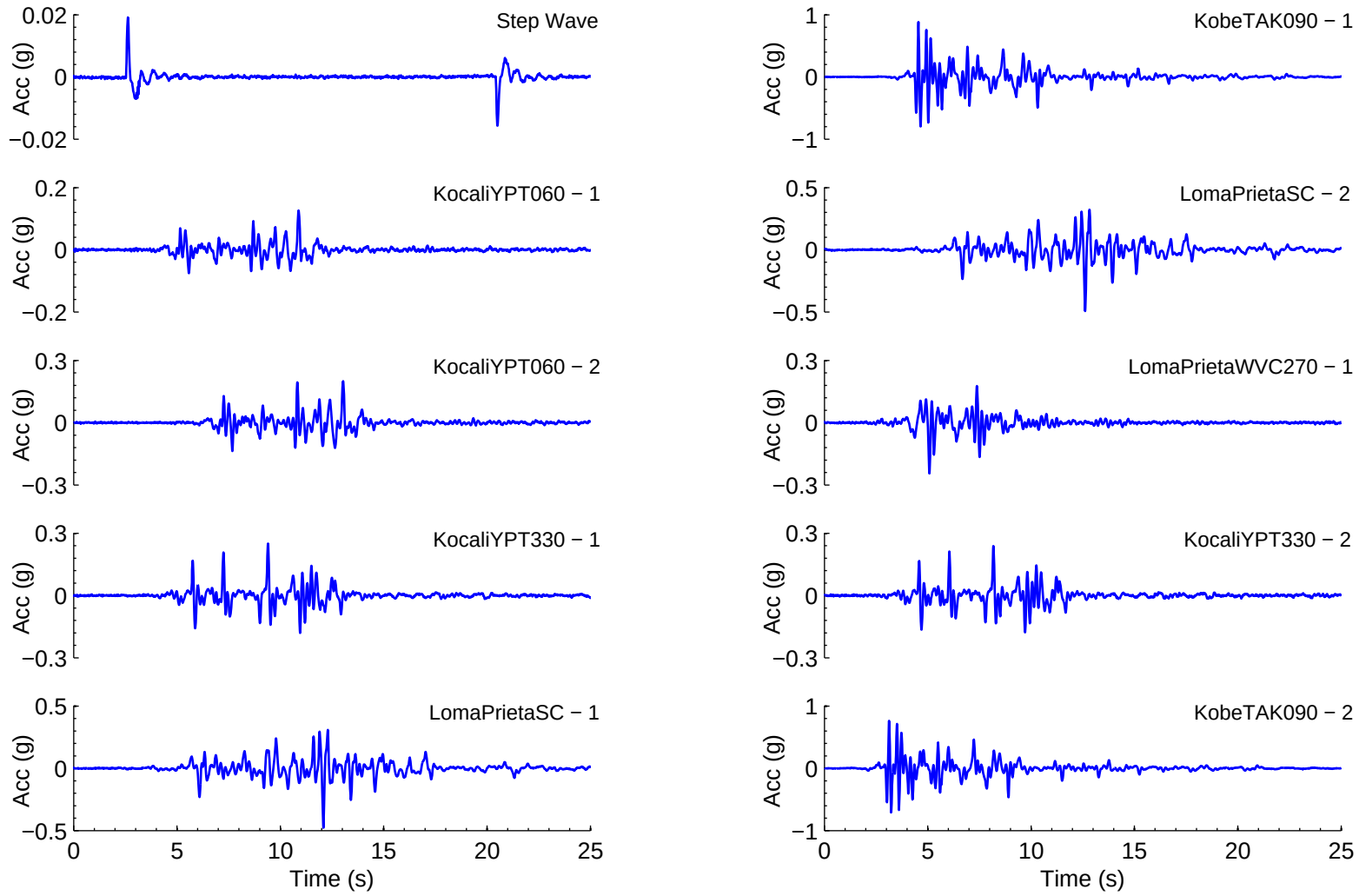

Figure 3.15 History of input acceleration in model GC01.

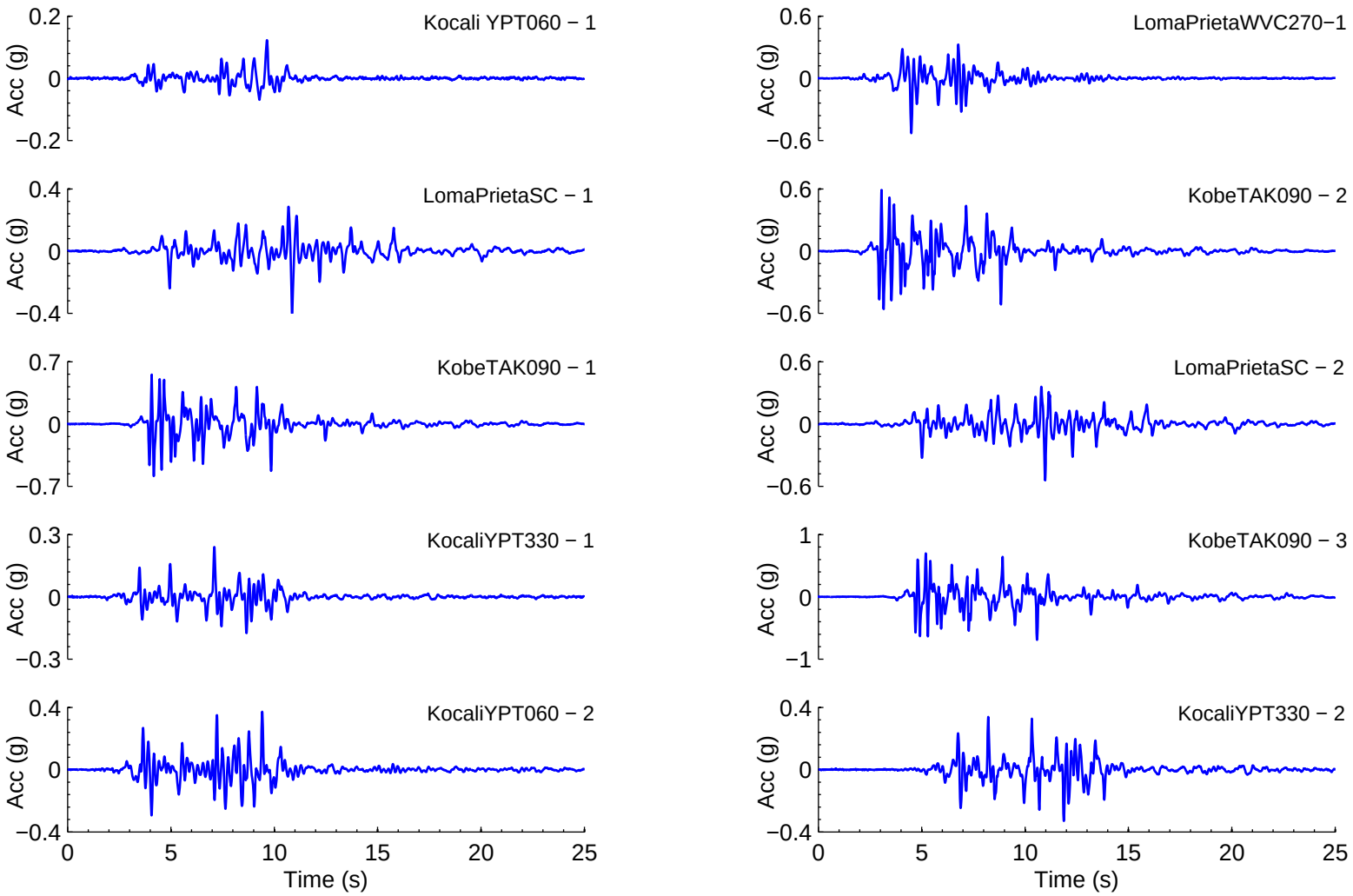

Figure 3.16 History of input acceleration in model GC02.

3.9. Data Processing Methods

The recorded data was processed systematically using MATLAB scripts in order to maintain uniformity. The data from each sensor was first converted to engineering units, scaled to prototype dimensions, and then filtered to remove high frequency noise and static drifts when applicable. The MATLAB codes and digital versions of the raw data and processed data are available at http://nees.org/warehouse/project/943. The methodology followed is outlined in this section.

- **Accelerations and displacements**: unless indicated otherwise, accelerations and displacements are defined as positive toward the north end of the container. Accelerations in the soil and in the structures were measured in both experiments at the locations indicated in Figures 3.3 to 3.6. A fifth order band pass Butterworth filter with cutoff frequencies f_{ch} = 0.25 Hz and f_{cl} = 15 Hz was applied to remove permanent offsets and high frequency noise. Based on the corrected acceleration records, elastic response spectra were evaluated using exact time integration. Displacement histories were evaluated using frequency domain integration, which is more accurate than using data from displacement transducers. Figure 3.17 compares the cantilever wall displacements integrated from the wall acceleration and measured directly with displacement transducers (DVDT). In this example both methods are in reasonable agreement, but in general the DVDT's underestimate the displacements due to vibration in the holding frame.
- **Inertial loads on retaining structures**: The inertia induced loads of the basement and cantilever walls were determined as $\Delta P_{in}(t) = -m\int_0^H \ddot{u}(t,z)dz$, where m is the mass of the wall per unit length, and $\ddot{u}(t,z)$ is the acceleration distribution. Using variable separations, $\ddot{u}(t,z)$ can be written as the product the shape functions $\mathbf{N} = [N_{bot} \quad N_{top}]$ and the wall accelerations vector $\ddot{\mathbf{u}} = [\ddot{u}_{bot} \quad \ddot{u}_{top}]^T$. The use of linear shape functions for the basement wall provides a simple approximation of the fundamental vibration mode shown in Figure 3.18; thus, the inertial forces can be expressed as

$$\Delta P_{in} \approx -m\int_0^H \left[1 - \frac{z}{H} \quad \frac{z}{H}\right] \ddot{\mathbf{u}}dz = -mH\frac{\ddot{u}_{bot} + \ddot{u}_{top}}{2} \tag{3.1}$$

where z is the position measured from the base. Analogously, quadratic shape functions can be used to approximate the fundamental vibration mode of the cantilever walls of experiments GC01 and GC02, leading to

$$\Delta P_{in} \approx -m\int_0^H \left[1 - \frac{z^2}{H^2} \quad \frac{z^2}{H^2}\right] \ddot{\mathbf{u}}dz = -mH\frac{2\ddot{u}_{bot} + \ddot{u}_{top}}{3} \tag{3.2}$$

The effects of different modal shapes on the inertial loads of the cantilever wall were found to be insignificant in this problem, since ΔP_{in} is largely controlled by rigid body displacements. A direct consequence of using these shape functions is the implied distribution of inertia induced stresses on the walls $\Delta q_{in}(t) = -m\mathrm{N}\ddot{\mathrm{u}}$, which is nonzero at the top. On the other hand, pressure cells indicate that the static and seismic stress distributions increase linearly with depth and, thus, the incremental stresses due to inertial

effects should have similar distribution. For this reason, Equations (3.1) and (3.2) are used only to estimate the magnitude of inertial loads.

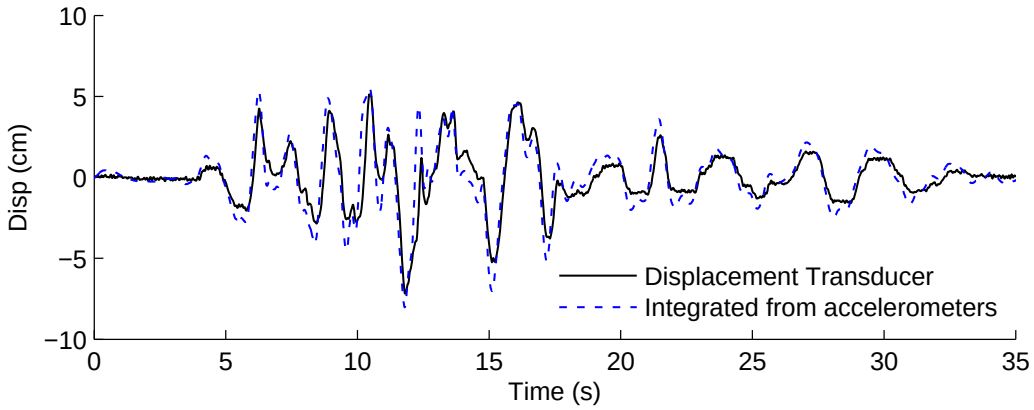

Figure 3.17 Cantilever wall displacements during Loma Prieta SC-1.

- **Seismic loads in basement walls of model GC01**: The net basement compression was determined by adding the load measured with the load cells at top and base as $P_{tot} = P_{LC}^{top} + P_{LC}^{base}$. The load histories were scaled to prototype dimensions and filtered to remove frequencies above 15 Hz. Using D'Alambert's principle and based on the free body diagram of Figure 3.18., the soil induced loads were determined by adding and subtracting the inertial load in the south and north walls at corresponding times, $P_{ae} = P_{tot} \mp \Delta P_{in}$. Applying a low frequency filter to remove the static component of the load cells, this expression can be written in incremental form as $\Delta P_{ae} = \Delta P_{tot} \mp \Delta P_{in}$. This equilibrium analysis shows that the basement compression P_{tot} is simply the average of the soil-induced loads on the walls and contains no information with respect to the inertial forces.

- **Seismic loads on cantilever walls**: Static and dynamic loads were back calculated using strain gages, pressure cells and accelerometers. A low pass Butterworth filter with corner frequency of 15 Hz was used to remove noise from the strain gage signals. Based on the elastic beam theory, the total bending moment on the wall is given by $M(t) = ES\varepsilon(z,t)$, where E is the aluminum's Young Modulus, $S = th^3b/6$ is the section modulus, and $\varepsilon(z,t)$ is the bending strain measured at a distance z from the footing. Then, using D'Alambert's principle the resultant of the soil induced earth pressure can be expressed at any given time as $P_{ae} = Q_b - \Delta P_{in}$, where $Q_b = dM(0,t)/dz$ is the shear at the base of the stem at time t, and ΔP_{in} is the inertial force at the corresponding time. These loads are shown schematically in the free body diagram of Figure 3.19. Removing the static component of Q_b, the incremental form of this equation is $\Delta P_{ae} = \Delta Q_b - \Delta P_{in}$. Since pressure cells data increases monotonically with depth and the strain distribution in the wall is well approximated by a cubic polynomial, the moment diagram and the shear at the base of the stem simplify to

$$M \approx ES\epsilon\,(0,t)\left(1-\frac{z}{H}\right)^3$$
$$Q_b \approx \frac{3ES}{H}\epsilon\,(0,t) \qquad (3.3)$$

- **Surface settlement**: Vertical soil deformations at the beginning and end of every earthquake were recorded with nine displacement transducers in GC01 and six transduces in GC02, respectively. This data was used to estimate volume changes in the soil or soil densification as a result of earthquakes.

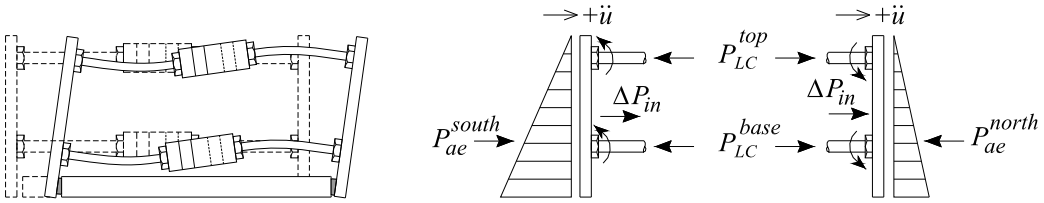

Figure 3.18 Vibration mode of basement wall and free body diagram; the sign convention for positive acceleration and loads is indicated by the arrows.

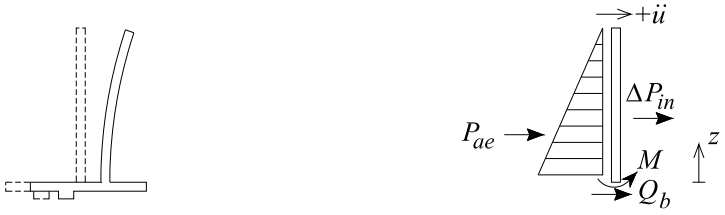

Figure 3.19 Vibration mode of cantilever wall and free body diagram; the sign convention for positive acceleration, loads and moments is indicated by the arrows.

- **Wall displacements and deflections**: Four spring loaded transducers were used to measure the rigid body displacements in the cantilever walls. Only the low frequency component of the displacement series was used, applying a low pass fifth order Butterworth filter with cutoff frequency of 0.25 Hz in prototype scale. Transient basement racking and cantilever wall deflections were estimated based on displacement histories integrated from accelerometers. Additionally, the tip deflection in the cantilever walls was computed using the solution of an elastic beam under a distributed triangular load as $\delta = Q_b H^3/15EI$.
- **Shear wave velocity**: Ceramic bender elements were place in two horizontal arrays in experiment GC01, as indicated in Figure 3.3. The travel time of a small shear wave between a "sender" and "receiver" elements was used to derive the shear wave velocity. In general, the data collected with this method was very noisy and had to be complemented with a series of resonant column experiments, as described in Section 3.4.

3.10. Errors and Problems Encountered in Level Ground Model GC01

The most significant problem in the model execution was the poor performance of pressure cells and the loss of strain gage connections during construction. The typical response of a Tactilus pressure sensor and a strain gage on the cantilever wall is shown in Figure 3.20. Although both instruments have good frequency response, the Tactilus sensors displayed a sharp drop in pressure at the beginning of the ground motion followed by a slow stress build-up towards the end of the excitation. Moreover, the output voltage from pressure cells kept increasing between

ground motions, leading to a spurious “zero” offset. This voltage drift was not observed in strain gages or load cells and. Therefore, pressure cell data was only used to interpret the earth pressure distribution, not its magnitude. A similar behavior was observed by Mikola and Sitar (2013), who used Tactilus sensors between aluminum walls and dry sand.

- Accelerometers A4 and A17 placed in the backfill failed during the experiment and accelerometer A43 located in the DVDT frame had noise in the 30-55 Hz range.
- Accelerometers A37 through A42 located in the cantilever wall reached their maximum output voltage during the second Kobe earthquake.
- Displacement transducer LP3 located at the southwest on the free surface had electrical noise; however, its static component is considered correct.
- The tip of the horizontal displacement transducers (DVDT’s) was fixed to the cantilever wall to prevent separation. A 2.5 cm settlement during spin-up made the transducers to dip ~10°, and after the earthquakes an additional 6°. The data was corrected accordingly.
- DVDT3 located near the base of the cantilever wall failed during the experiment.
- Due to an unexpected schedule delay, Tactilus pressure cells were significantly affected by moisture. Sensors PC9, PC10, failed during the model construction, and sensors PC1, PC16, PC17, PC18 and PC19 were lost during spin. Similarly, strain gages SG1, SG2, SG4 in the basement wall, and SG11, SG12, SG13, SG15 and SG16 in the cantilever wall were lost during the soil compaction. The layout of the functional and damaged sensors on the walls shown schematically in Figures 3.21 and 3.22.

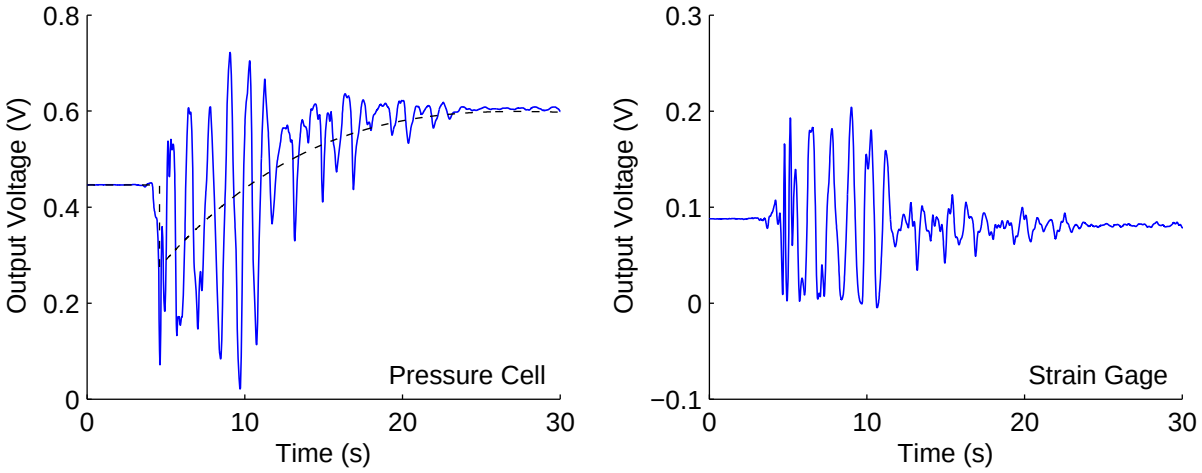

Figure 3.20 Behavior of pressure cell PC12 and strain gage SG9 during Kobe TAK-090.

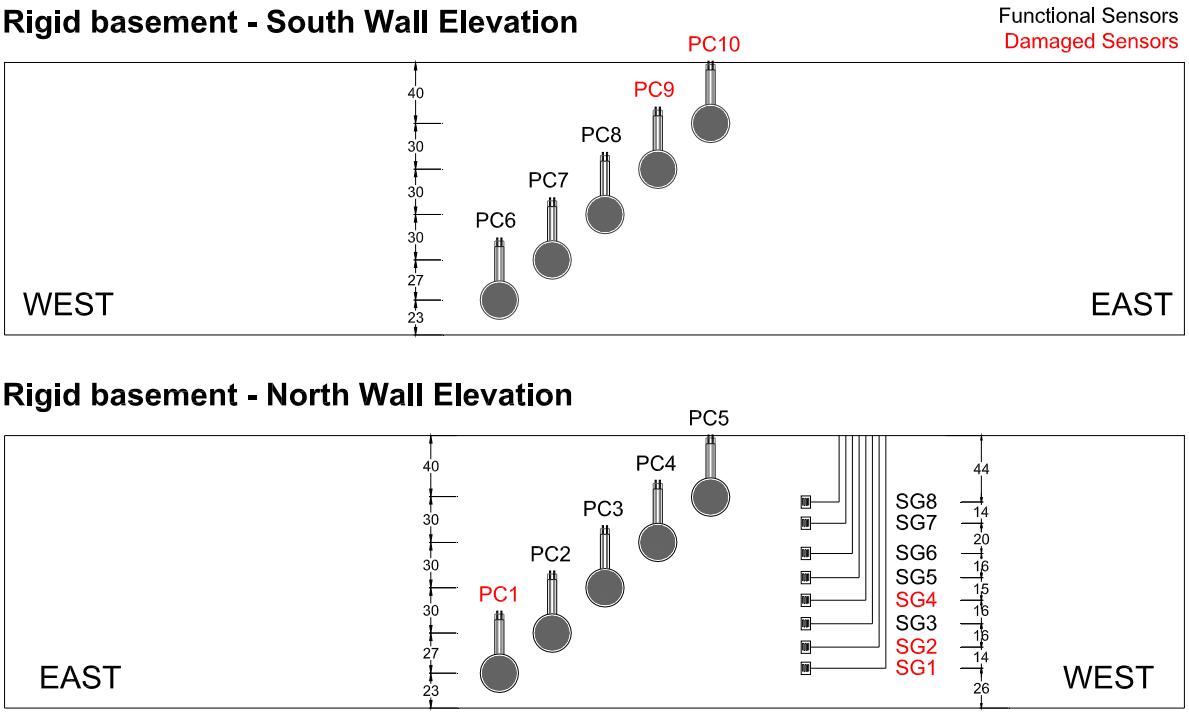

Figure 3.21 Strain gages and pressure cells of basement wall in level ground model GC01

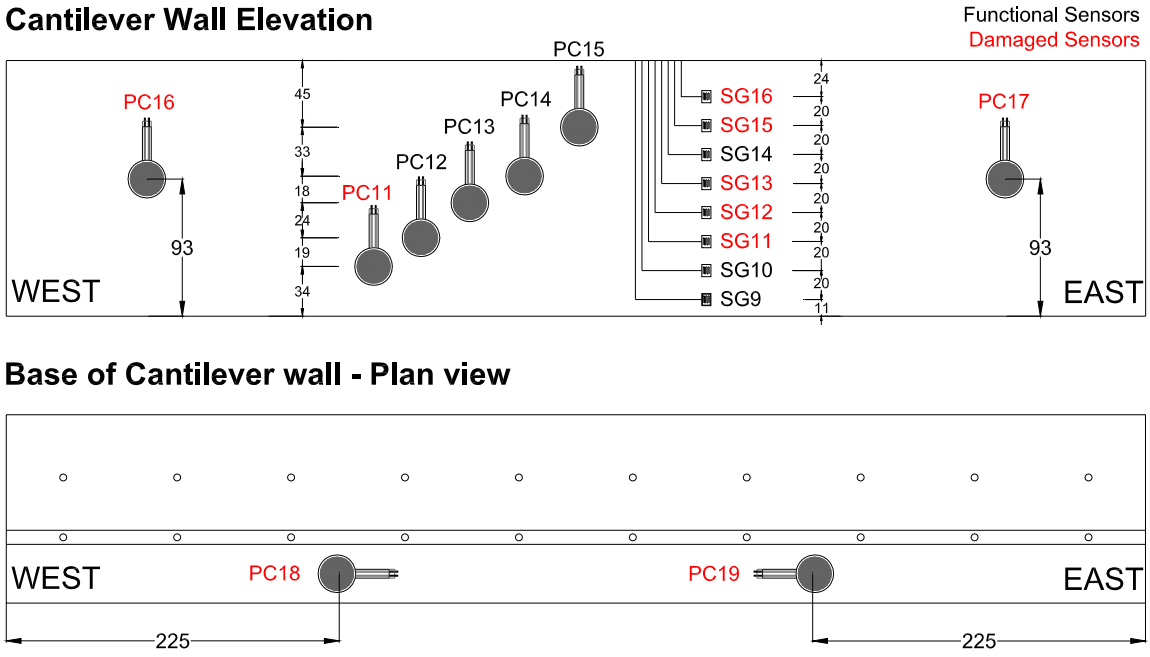

Figure 3.22 Strain gages and pressure cells of cantilever wall in level ground model GC01.

3.11. Errors and Problems Encountered in Sloping Backfill Model GC02

Similar to the level ground experiment GC01, Tactilus pressure sensors on the wall could only be used to identify the earth pressure distribution, but not its magnitude. Although the sensors showed an acceptable frequency response, the baseline of static pressures decreased sharply at the beginning of the earthquake and then kept increasing even if the model was at rest.

Another problem observed was the increased base rotations and vertical response because of mass asymmetry and the lack of complementary shear stresses on the north end of the container. The problem of base rotations is illustrated in Figure 3.23(a) in terms of the difference between the east and west input displacements. The observed base rotations of the 'asymmetric' model GC02 were twice as large as the 'symmetric' model GC01. The horizontal and vertical displacements of the top ring are shown in Figure 3.23 (b), showing significant coupling during the strong motion. Note that for a displacement towards the south, the south end of the container goes up and the north end goes downs, as in a sloshing mode.

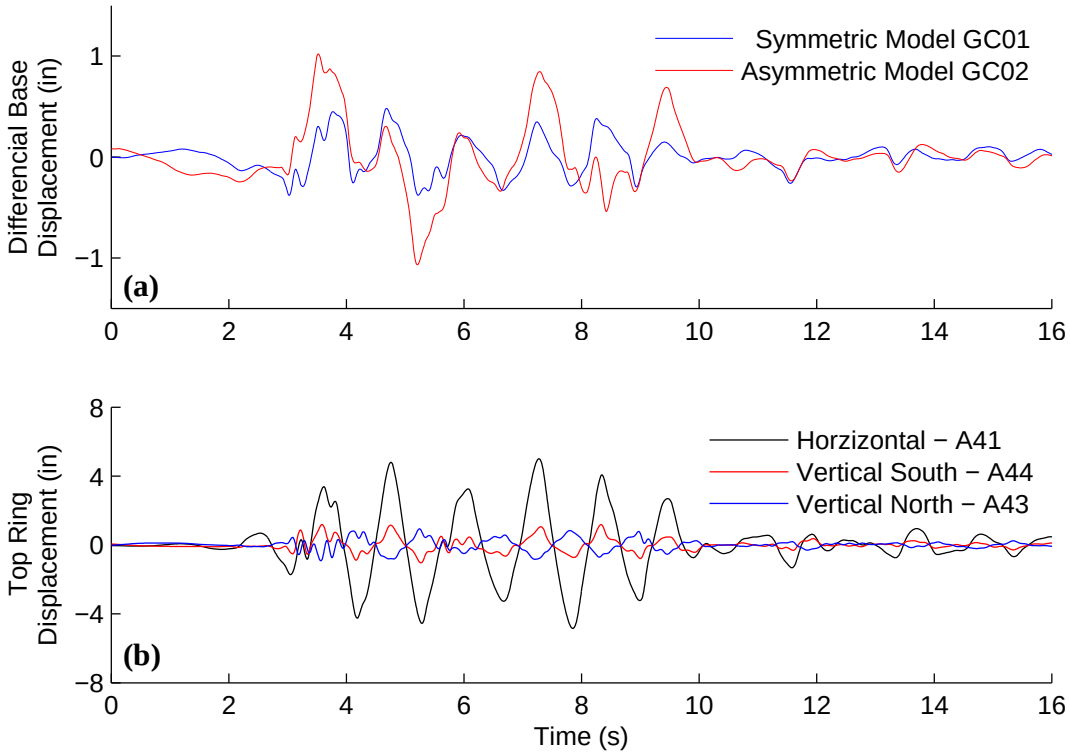

Figure 3.23 (a) Differential base displacements, and (b) top ring displacements measured during Kobe TAK090-2.

A summary of other issues encountered during the construction and execution of the experiment is listed next.

- Accelerometer A3, near the container base, and accelerometers A31, A32, A33, A34 placed in the cantilever wall failed during the experiment. Wall acceleration was interpreted from accelerometers A9 and A18 located in the backfill.
- Accelerometer A38 located in the second ring had noise in the 30-55 Hz range.
- Vertical transducer LP5 failed during the experiment.
- Due to an electrical failure, the DAQ system had to be reset after the third ground motion.
- Tactilus pressure cells PC3 and PC5 and strain Gages SG3, SG5, and SG6 failed during the experiment. The location of the damaged sensors is shown in Figure 3.24.

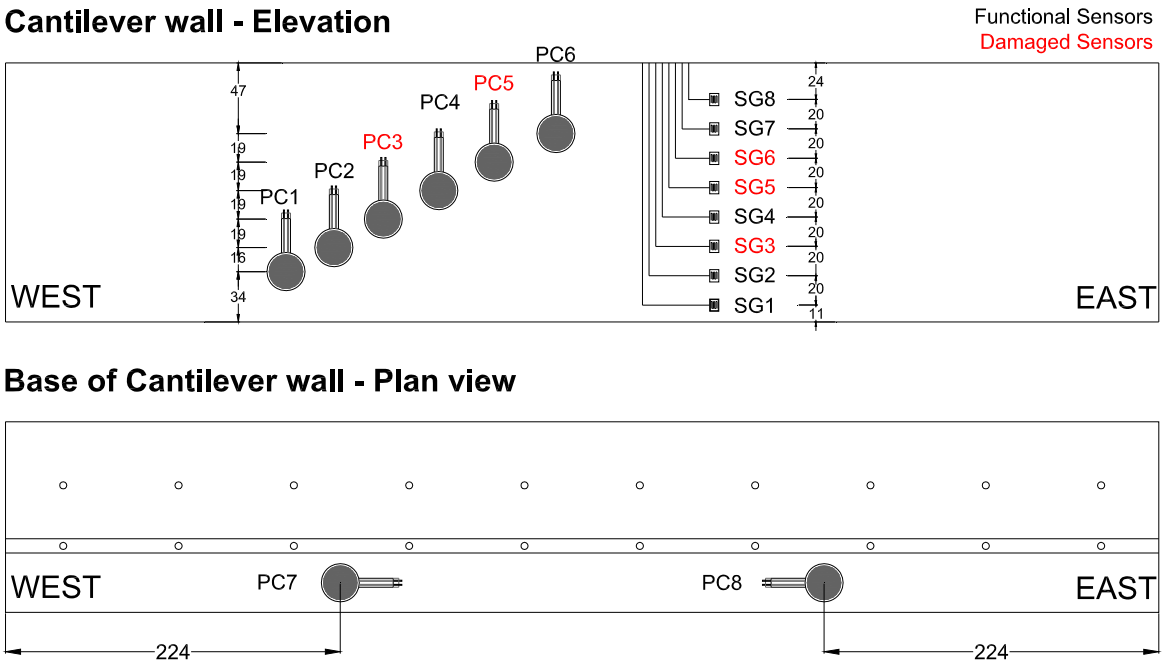

Figure 3.24 Strain gages and pressure cells of cantilever wall in sloping ground model GC02.

4. RESULTS OF EXPERIMENT GC01 - LEVEL GROUND

4.1. Acceleration in Soil and Structures

A complete set of plots of recorded acceleration time histories can be found on Appendix D. The amplification of the peak ground acceleration measured in the backfills and structures is presented in Figure 4.1. In all cases, the input acceleration was de-amplified at the foundation level as a result of energy dissipation and amplified at the top of the retaining structures. At the free surface, the ground motion was amplified for input PGA<0.3g and de-amplified at higher levels of shaking. Note that the peak acceleration at the base of the structures is consistent with that recorded at the foundation level in the soil. In the context of this study, the term 'free field PGA' (abbreviated as PGA_{ff}) denotes the peak ground acceleration on the model surface under 'free field' conditions.

Profiles of ground acceleration and ground displacement relative to the bottom of the container are presented in Figure 4.2 for different earthquakes, and correspond to snapshots at the time of PGA_{ff} and PGD_{ff}, respectively. These plots show that the ground acceleration and displacements increase towards the surface, primarily in the first and second vibration modes. The influence of higher modes was quantified using modal composition as proposed by Gazetas (1982); using three modal coordinates, the ground displacement can be written as:

$$u(z) \approx \psi_1 \bar{U}_1 + \psi_2 \bar{U}_2 + \psi_3 \bar{U}_3 \tag{4.1}$$

where $\bar{U}_n(z) = cos(\pi z(2n-1)/2H)$ are the natural modes of a uniform soil deposit, $f_n = (2n-1)V_s/4H$ are the corresponding natural frequencies and ψ_n are the mode participation factors. The coefficients ψ_n were determined with the method of least squares and are summarized in Appendix Table C.2 for all the ground motions. The analysis shows that in general, over 85% of the total displacement comes from the first mode ($f_1 = 2.1Hz$), 12% from the second mode ($f_2 = 6.2Hz$) and less than 3% from the third mode ($f_3 = 10.5Hz$). The coefficient of determination R^2 resulting from the least square analysis is also presented in Table C.1 if one, two or three modes are used. These results indicate that this approach captures nearly 99% of the total displacements. As expected, the influence of the third mode is insignificant since the ground motions delivered very small amounts of energy over 10 Hz.

Elastic response spectra with 5% damping at selected model locations are shown in Figure 4.3. The plots show that spectral accelerations at the free surface are amplified significantly for periods T>0.3 s, except for Kobe, which attenuates the response of systems with T<0.5 s.

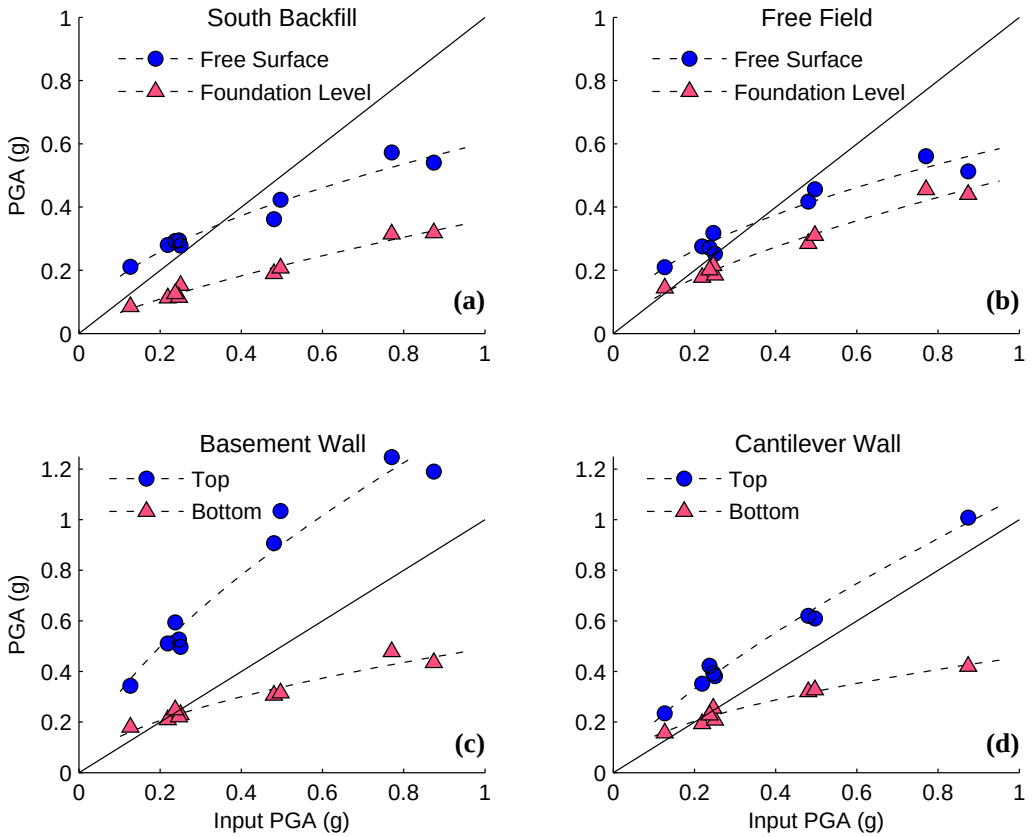

Figure 4.1 Ground motion amplification on the backfill (a,b) and structures (c,d).

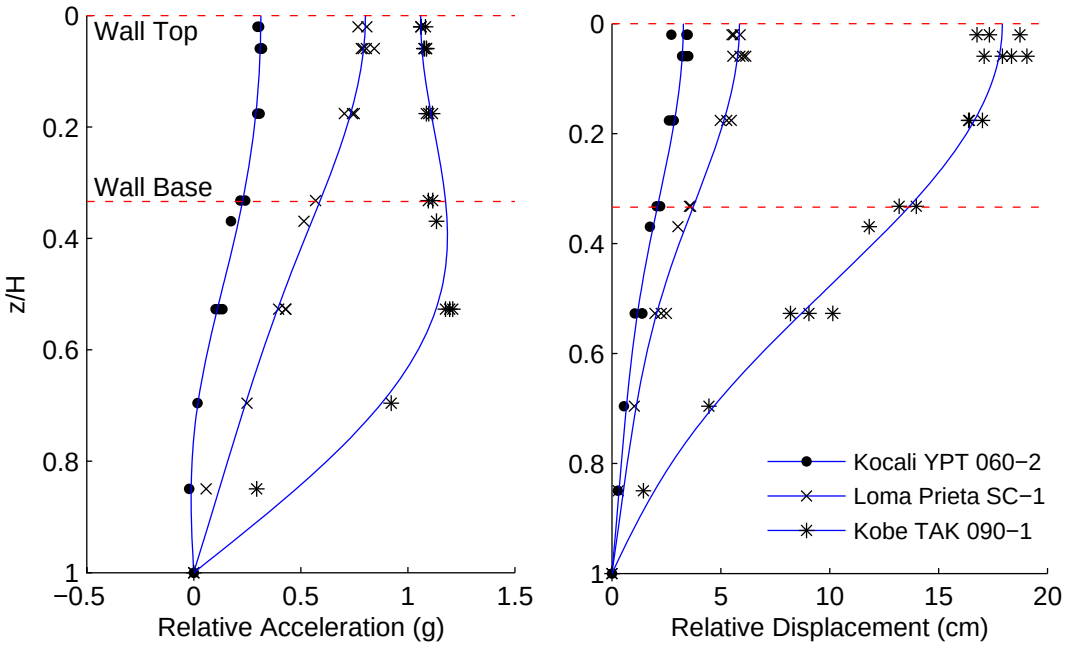

Figure 4.2 Free field ground acceleration and displacement relative to the model base at the time of PGA_{ff} and PGD_{ff}. Depth z normalized to model depth H=19.5 m.

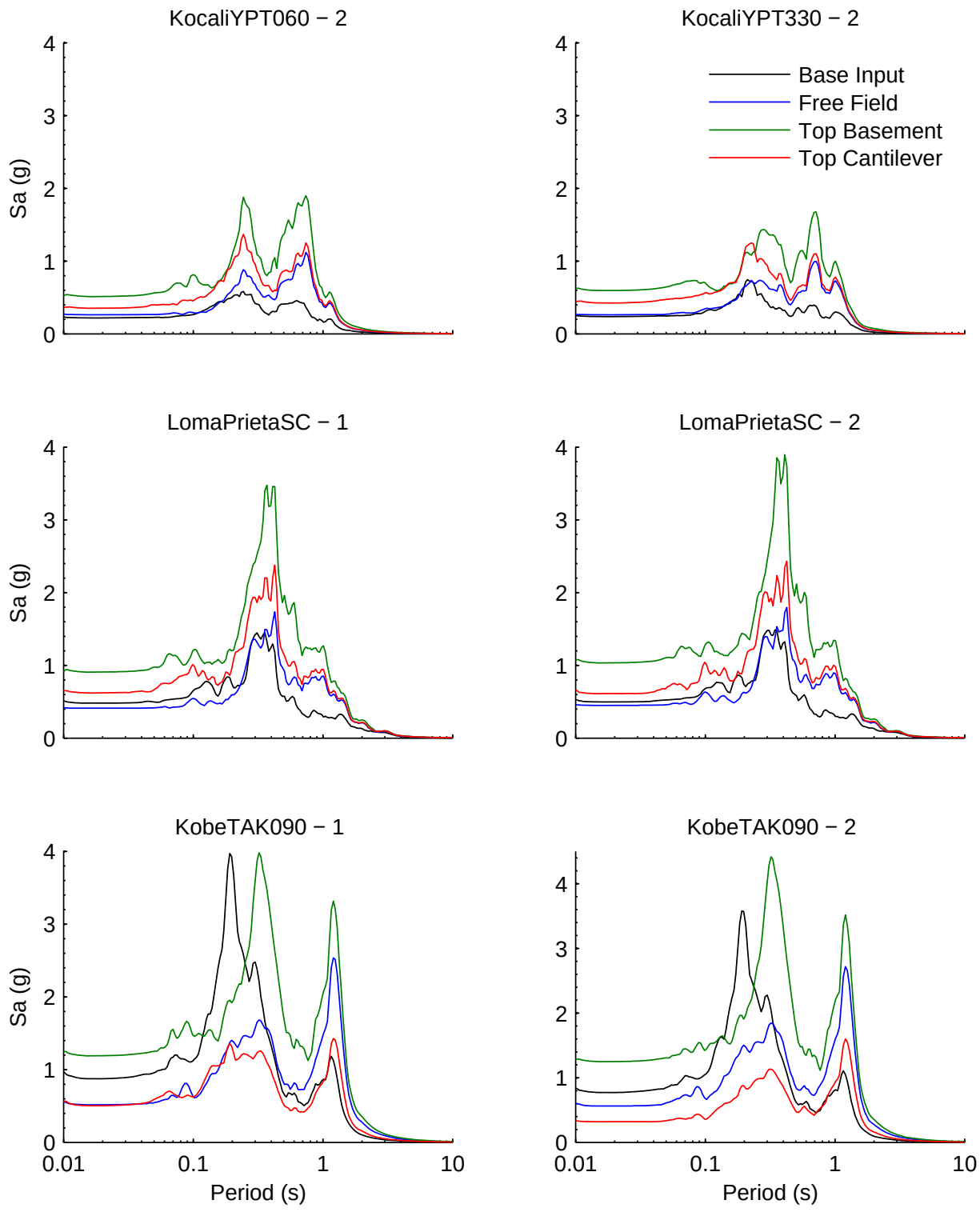

Figure 4.3 Acceleration Response Spectra (ξ=5%) recorded in the soil and structures.

Response spectra with 5% damping from accelerometers located at the top of the retaining structures are also included in Figure 4.3 and show that spectral accelerations on the basement wall are consistently higher than in the cantilever wall.

4.2. Seismic Earth Pressures

The magnitude of the total seismic earth pressures on the basement and cantilever walls was back-calculated from load cells and strain gages in addition to the inertial forces. Although problems were encountered in the direct measurement of earth pressures, as discussed in Section 3.10, the data shows that the static and seismic pressure distributions increase monotonically with depth.

Due to the construction process, the initial stresses induced by compaction cannot be compared directly with the static stresses predicted by traditional limit state methods which assume at rest or active stress conditions. As noted by Duncan and Seed (1986), despite the current advancements in the characterization of the compaction phenomenon, there are no readily amenable procedures to determine the compaction stresses accurately. Therefore, the results in this and the following sections are presented in terms of the seismic earth pressure increment (Δq_{ae}), determined using a baseline correction as discussed in Section 3.9.

For the basement and cantilever wall, Figure 4.4 presents the seismic pressure increments during the Loma Prieta and Kobe earthquakes, at the time of maximum total seismic load P_{ae}^{max}. The distribution predicted with the Okabe (1926) method, and the Seed and Whitman (1970) method is also included as a reference, in which k_h=PGA_{ff}/g. In these diagrams, it is apparent that the pressure cell readings increase with depth. Given the few sample points along the wall depth, a linear fit is a reasonable approximation and the point of application of the seismic load increment is considered to act at 0.33H from the base. Although this result is consistent with the experimental results in cohesionless soils (Al Atik & Sitar, 2010; Mikola & Sitar, 2013), the limit state theory proposed by Okabe suggest that the point of application should be nearer 0.4H.

As discussed earlier in Section 3.10, the pressure sensors exhibited good frequency response; however, the total earth pressure could not be determined accurately due to unpredictable changes in the pressure baseline. The interpreted total earth pressure at the base of the walls is shown in Figure 4.5 for the ground motion Kobe TAK090-1. Note that the static pressure before and after the ground motion remain the same as measured by load cells and strain gages, whereas the pressure interpreted from pressure sensors show a static offset.

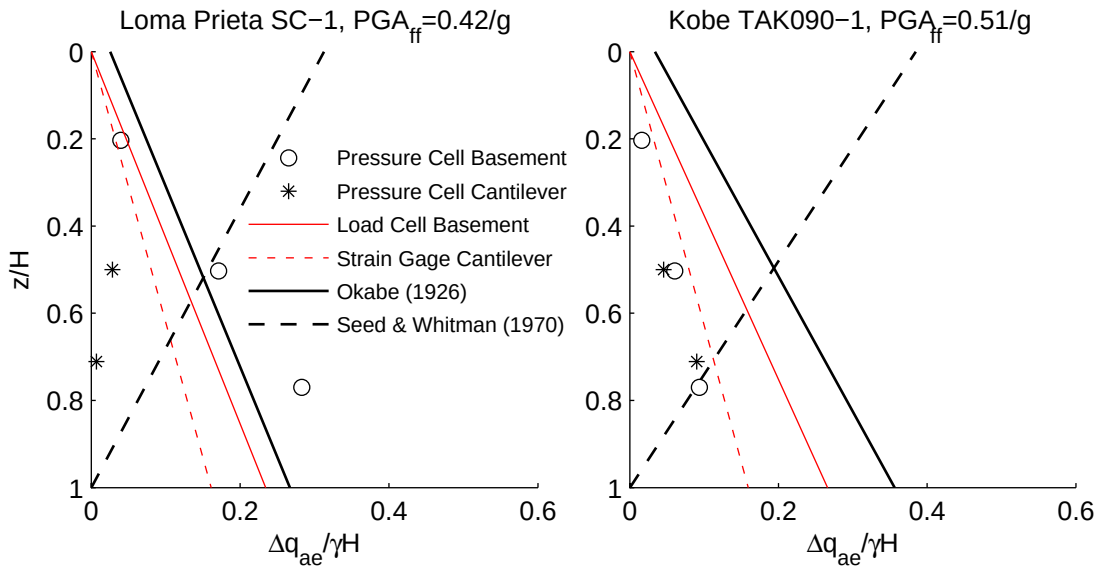

Figure 4.4 Maximum dynamic earth pressure in the basement and cantilever walls.

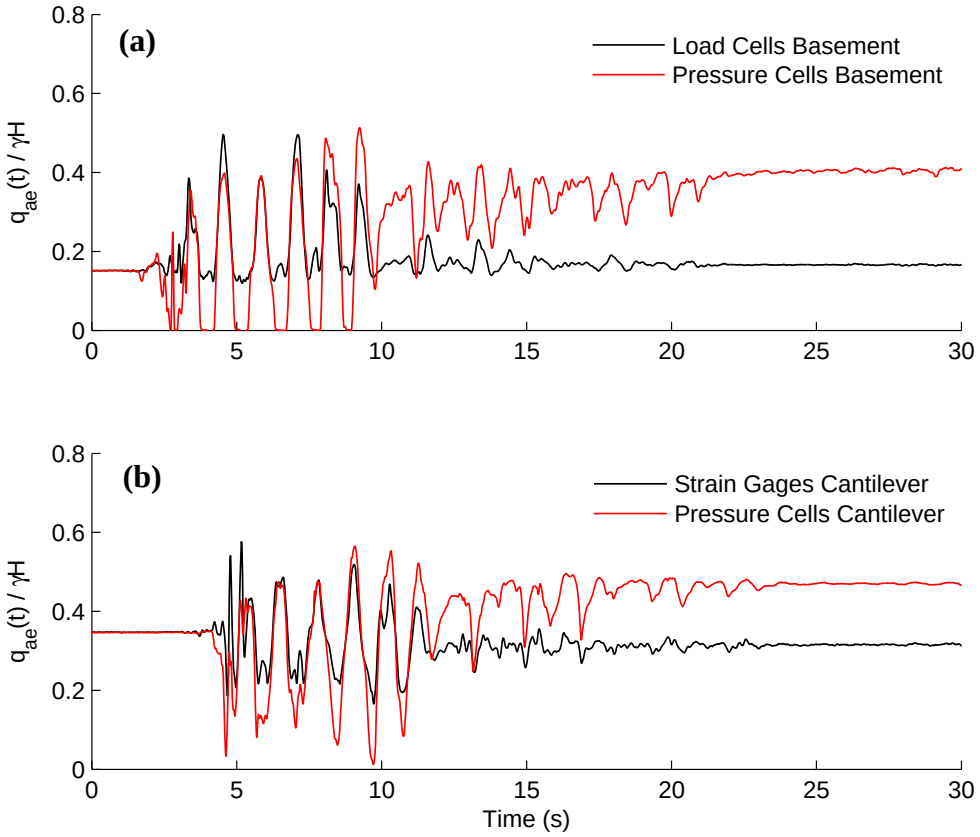

Figure 4.5 Total seismic pressure during Kobe TAK090-1 interpreted from load cells, strain gages and pressure cells. (a) Basement wall (b) Cantilever wall.

4.3. Response of Basement Wall

The seismic response of the basement wall and the backfill is a complex problem that involves kinematic and inertial interaction, caused by the strong coupling between the backfill and the wall system, which have different vibration modes and natural frequencies. Figure 4.6 shows the history of the dynamic load increments acting on the basement in response to the Loma Prieta earthquake input motion. As mentioned in Section 3.9, the net basement compression ΔP_{tot} corresponds to the average soil induced load on the north and south walls. It also must be noted that inertial loads act in the direction opposite to acceleration; a positive acceleration will induce active loads in the south wall and passive loads in the north wall. In this particular case, Figure 4.6(a) shows that peaks in basement compression are preceded by peaks in negative inertial loads, i.e. positive acceleration at the ground surface, causing an increase of active loads on the south basement wall. Similarly, the compression release in the basement is preceded by positive inertial loads, leading to increased active loads on the north wall. The phase difference between the basement compression and the inertial forces is 0.12 s, which is approximately the natural period of the backfill $T_{backfill}$=0.13 s. The soil induced load increments $\Delta P_{ae} = \Delta P_{tot} \mp P_{in}$ are shown in Figure 4.6(b), where the positive load represents active thrust. As expected, when the load on the south wall is near a maximum, the load on the north wall is near a minimum and vice versa. A similar behavior was observed during the Kobe TAK090-1 motion, as depicted in Figure 4.7. In this case, basement compression peaks also occurs 0.12 s after the inertial loads peaks.

A detailed analysis of the model response shows that the acceleration in the free field and the south backfill measured at the same elevation agree in magnitude and phase, however, the acceleration peaks in the basement are consistently delayed by $0.5T_o$ with respect the neighboring soil. This delay suggests that the input shear waves arrive first to the soil surface and then are transmitted to the basement, probably as a result of the low lateral stiffness of the basement.

Note that peak inertial loads are up to 60% of the total basement compression; however, these loads do not act simultaneously. Due to the container proximity, the seismic load increments in the south wall are 50% higher than in the north wall. Therefore, it is recommended for future experiments to place the structures at the center of the model to minimize the interaction with the container and other related boundary effects.

Plots of the recorded PGA_{ff} versus the basement loads measured in the north wall is presented in the Appendix Tables C.3, and include the load decomposition into its static and dynamic components. The results show that the seismic loads increase linearly with the free field PGA. Based on linear regression, the coefficient of dynamic earth pressure can be approximated as

$$\Delta K_{ae} = 0.67(PGA_{ff}/g - 0.10) \pm \epsilon \tag{4.2}$$

where $\epsilon = 0$ represents the mean and $\epsilon = 0.08$ represent the 95% confidence intervals. Note that the upper confidence bound can be approximated as $\Delta K_{ae} \approx 0.67 PGA_{ff}/g$, which is equivalent to the Seed and Whitman (1970) method with k_h taken as 90% of the design ground acceleration.

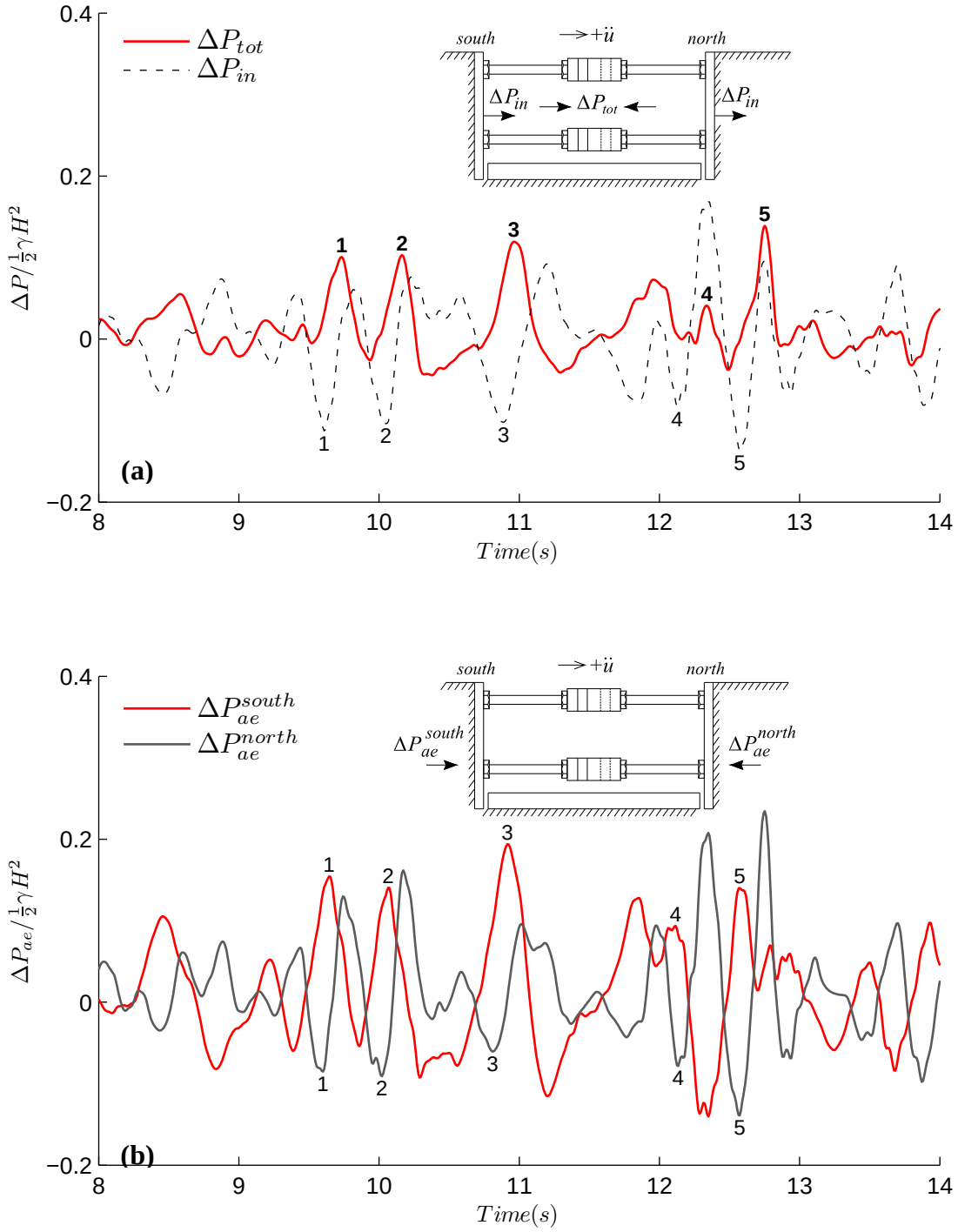

Figure 4.6 Seismic load increments on the basement wall during Loma Prieta SC-1 (a) basement compression and inertial loads, and (b) soil induced loads on the north and south walls ($0.5\gamma H^2$ = 386 kN/m).

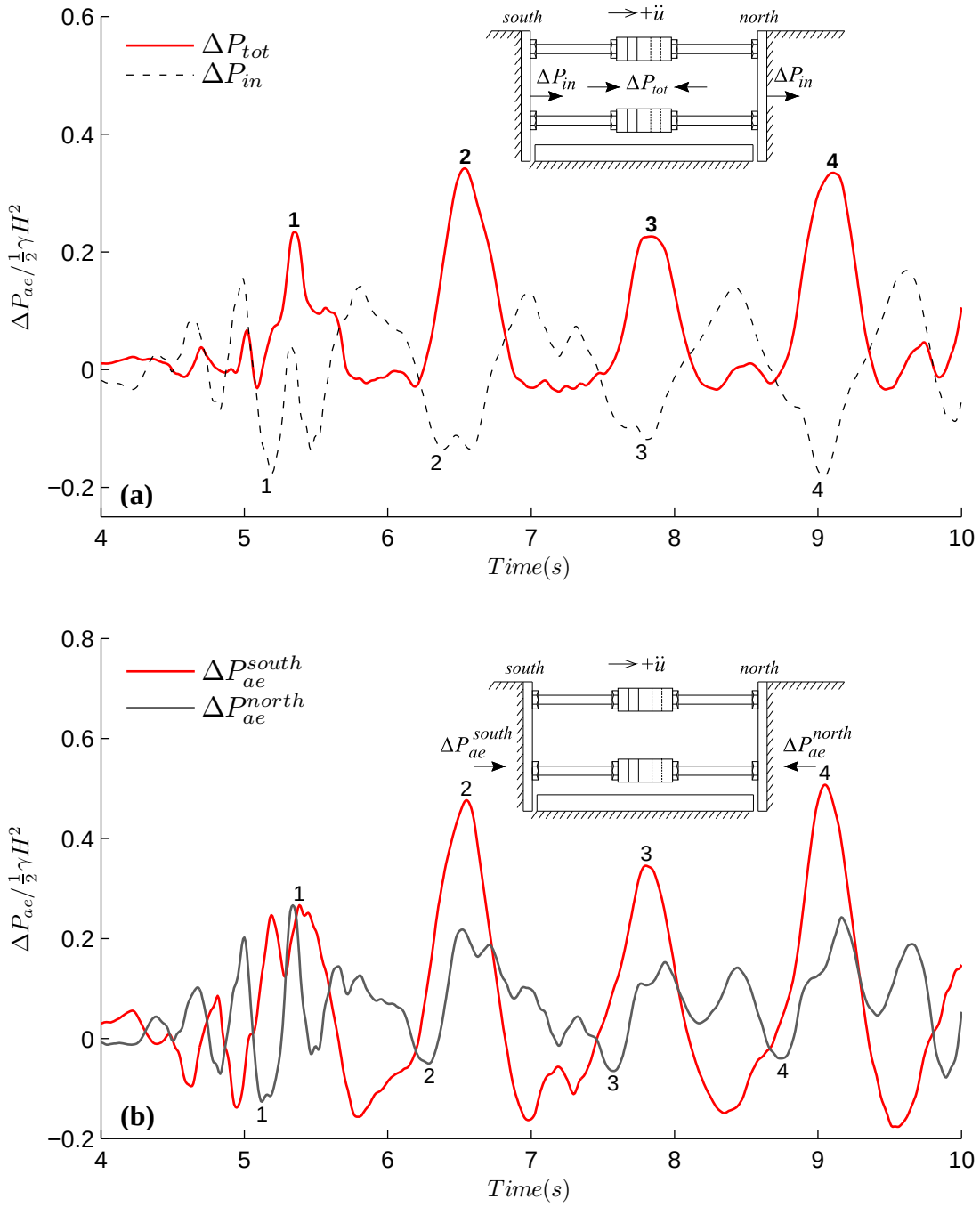

Figure 4.7 Seismic load increments on the basement wall during Kobe TAK090-1 (a) basement compression and inertial loads, and (b) soil induced loads on the north and south walls ($0.5\gamma H^2$ = 386 kN/m).

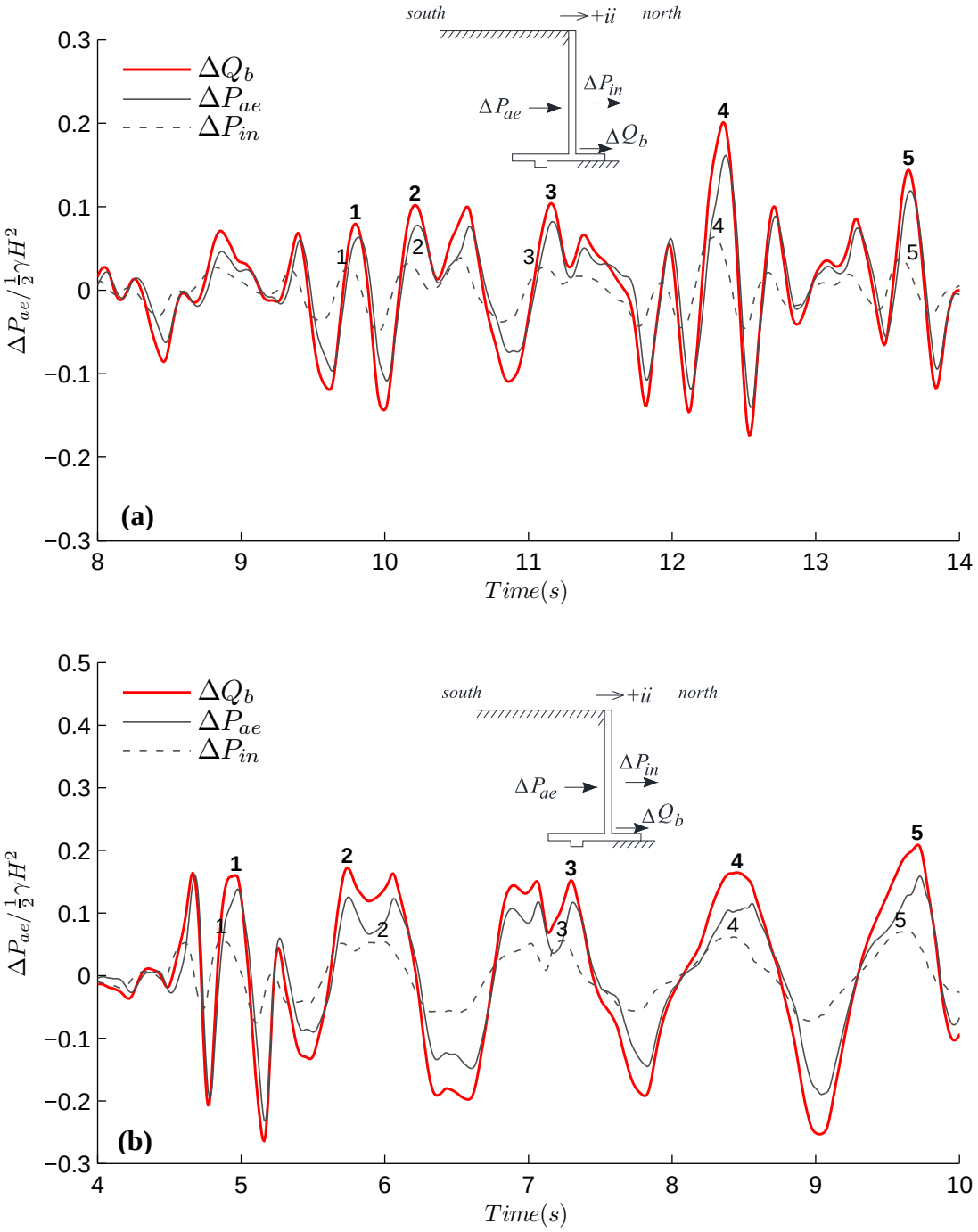

Figure 4.8 Shear at the base of the stem (Q_b), soil induced load (ΔP_{ae}) and wall inertial load (ΔP_{in}) during (a) Loma Prieta SC-1 and (b) Kobe TAK 090-1. Load values normalized by $0.5\gamma H^2$ = 386 kN/m.

4.4. Response of Cantilever Wall

Histories of ground acceleration in the free field, shear loads at the base of the stem (Q_b), inertial loads (ΔP_{in}), and total seismic loads (P_{ae}) on the cantilever wall are shown in the Appendix Figures C.1 to C.4. A time window of load histories during the Loma Prieta SC-1 and Kobe TAK 090-1 earthquakes is presented in Figure 4.8. As discussed earlier, the shear at the base of the stem on the cantilever wall is the sum of earth-induced loads and the wall inertial forces, $\Delta Q_b = \Delta P_{ae} + \Delta P_{in}$. In the range of ground motions used in the experiments, the inertial load at the time of maximum lateral load represent about 20% of ΔQ_b, and the phase difference between the inertial loads and the ΔQ_b is near $0.3T_{backfill}$. Since the natural period of the backfill and the cantilever wall are similar, the inertial interaction is not controlling in this case. In fact, the phase difference between the acceleration measured in the wall and the adjacent soil was negligible.

It should be noted that the cantilever wall response was affected by its interaction with the basement wall, even if the structures were 25 m apart. For instance, during spin-up the cantilever wall rotated outward by $\delta/H = 3\%$, which caused a horizontal stress decrease in the soil between the walls and a compression release in the basement. The interaction between adjacent structures is a source of errors in the measurements and could not be quantified with the available data.

A summary of seismic load increments versus free field PGA is shown in Figure 4.11 and detailed in the Appendix Table C.4. Based on linear regression, the coefficient of dynamic earth pressure ΔK_{ae} can be written as

$$\Delta K_{ae} = 0.42(PGA_{ff}/g - 0.10) \pm \epsilon \tag{4.3}$$

where $\epsilon = 0$ represents the mean and $\epsilon = 0.05$ the 95% confidence intervals. Since the cantilever wall can translate and rotate, the average dynamic earth pressure is 60% smaller than in the basement walls. Also note that the upper confidence bound can be expressed as $\Delta K_{ae} \approx 0.42 PGA_{ff}/g$, which is equivalent to the Seed and Whitman (1970) method with k_h taken as 55% of the design acceleration. If the wall inertial loads are included, Equation (4.3) becomes

$$\Delta K_{ae} = 0.52(PGA_{ff}/g - 0.10) \pm \epsilon \tag{4.4}$$

Similarly, if the upper confidence bound is used, the seismic coefficient including the inertial loads can be simplified to $\Delta K_{ae} \approx 0.52 PGA_{ff}/g$.

4.5. Surface Settlement

Linear potentiometers (LP) were distributed in the free surface as shown in Figures 3.3 and 3.4. The gravity-induced settlements were approximately 30 mm to 34 mm (1.2 m in prototype scale) at the free surface and approximately 21 mm (0.8 m in prototype scale) at the foundation level, as seen in the cross section of Figure 4.9. The cumulative seismic induced settlements at the free surface were approximately 9 mm (0.3 m in prototype scale) at the end of the experiment, with the largest increments triggered by the Kobe earthquakes. While the seismic settlement is a function of the soil density and the cyclic shear strains, the measured settlement was found to be

in excellent agreement with the Arias intensity of the input ground motion, which can be related as

$$log_{10}\delta = 0.002I_a \pm 0.10 \tag{4.5}$$

with I_a measured in cm/s the and δ in cm. A summary of the seismic settlements can be found in Appendix Table C.5

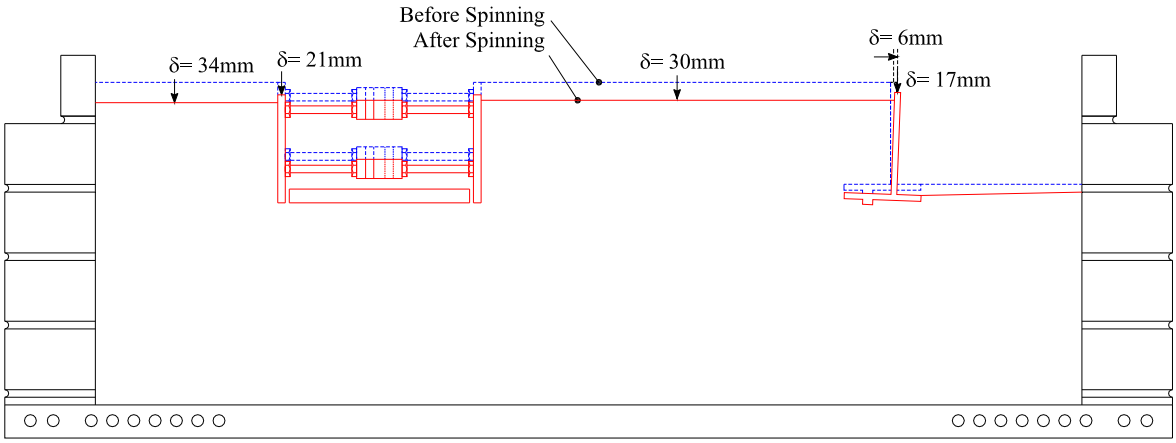

Figure 4.9 Gravity induced deformations after spin-up and before the ground motions.

4.6. Rigid Body Displacements and Wall Deflections

The basement rigid body displacements are on the average 30% higher than the maximum free field displacements, as seen in Figure 4.10(a). This difference is almost identical to the racking or distortion of the basement, which comprise approximately 25%-30% of the total dynamic motion of the soil-structure system. In this experiment, the Kobe earthquakes control the response at large accelerations and thus, the total dynamic displacements increase non-linearly with PGA_{ff}. However, the basement racking increased linearly with PGA_{ff} and is well approximated by $\delta/H \approx 0.019(PGA_{ff}/g - 0.10)$. Likewise, Figure 4.10(b) shows that the maximum dynamic displacements at the top of the cantilever wall are very close to the free field displacements. The cantilever wall deflection varies linearly with PGA_{ff} and can be approximated as $\delta/H \approx 0.015(PGA_{ff}/g - 0.16)$. The basement racking, which was principally due to the walls pivoting on the struts, was 25% higher than the cantilever wall deflection due to flexure. The observed magnitude of racking was probably due to the strong interaction with the container. This is contrary to the assumption that the model would behave as a nearly rigid structure and directly impacts the results and conclusions.

The residual rigid body translation in the basement wall was negligible and was not measured, whereas the cantilever wall exhibited small residual displacements on the order of $\delta/H = 0.05\%$ per earthquake.

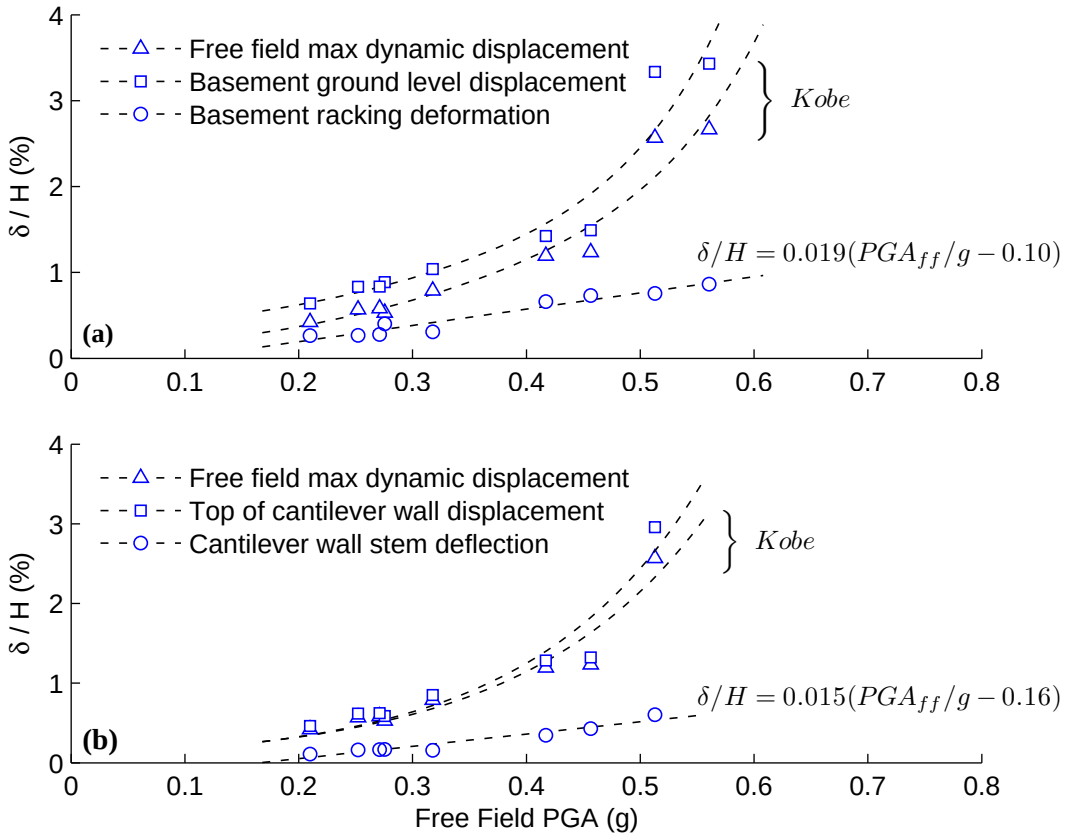

Figure 4.10 (a) Dynamic displacements of free field and basement wall (b) Dynamic displacements of free field and cantilever wall

4.7. Summary of Observations

Accelerations measured at various parts of the model show that large input ground motions are de-amplified toward the model surface as a result of energy dissipation in the soil. In contrast, the ground motions measured in the retaining structures show significant amplification, particularly in the basement wall due to its interaction with the container. The soil at free field responded in the first and second modes; using a modal composition of the displacement profiles, the contributions of the first and second modes were approximately 82% and 15%, respectively, for the all ground motions studied. Since the cantilever wall was free to rotate, the middle portion of the model backfill moved toward the north (toward the cantilever wall) during the spin-up. This experimental flaw resulted in a decrease in static earth pressure on the basement wall.

Overall, the data from pressure cells shows that static and dynamic stress distributions increase monotonically with depth, and consequently the resultant of the seismic loads acts at about 0.33H from the base. As already mentioned, while similar observations were made in retaining walls with cohesionless backfills (Al Atik & Sitar, 2010; Mikola & Sitar, 2013), the theory developed by Okabe (1926) suggests that for a soil with cohesion $c \approx 0.1\gamma H$ kPa the resultant of

earth pressures should act near 0.4H. The data presented here is not sufficiently robust to be able to identify the reason for this apparent difference.

Using D'Alambert's principle for dynamic equilibrium, the soil-induced loads on the retaining walls were determined from the total loads measured using load cells or strain gages and the wall inertial loads computed from accelerometers. While no significant phase offsets between inertial loads and soil-induced loads were identified in the cantilever walls, the analysis of the basement response shows that when the basement compression is at a maximum, the inertial loads are near zero or at a minimum. Similarly, maximum soil induced loads in the south wall are simultaneous with load reductions in the north wall and vice versa.

Because the soil was under-compacted, gravity induced settlements in the order of 6% of the model depth (110 cm in prototype) developed and the cantilever wall tilted by approximately 3%. Additional seismic induced settlements were approximately 2% of the model depth (36 cm in prototype) and their magnitude was in good agreement with the Arias Intensity of the input ground motion. The maximum dynamic displacements measured at the top of the structures are slightly higher than the maximum free field displacements. The basement racking and the cantilever wall deflection increase linearly with PGA_{ff} and are on the average 25% of the total dynamic displacement.

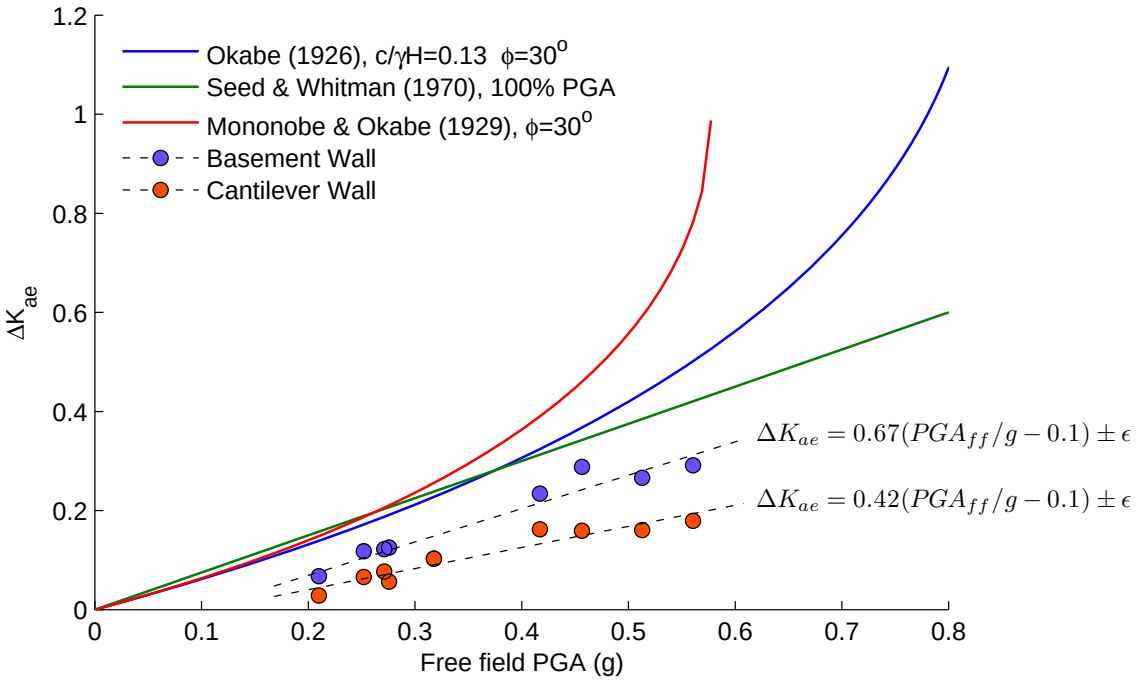

Figure 4.11 Coefficient of dynamic earth pressure versus free field PGA: summary of centrifuge data and limit state solutions.

The coefficients of earth pressure increment for the basement and cantilever walls are shown in Figure 4.11, together with the Okabe (1926) solution for cohesive soils on level ground, the semi-empirical Seed and Whitman (1970) equation and the Mononobe-Okabe (1929) solution for clean sands, in which the design acceleration has been defined as 100% PGA_{ff} This figure shows that the seismic load increments on the cantilever wall are consistently smaller than on the

basement wall, because of its ability to translate and rotate. Equations for the mean values and the 95% confidence intervals (CI) are shown in the plot as well, where $\epsilon = 0.08$ in the basement and $\epsilon = 0.05$ in the cantilever wall. Based on the wall accelerations and the use of quadratic shape functions, the inertial loads represent ~20% of the total shear at the base of the stem.

5. RESULTS OF EXPERIMENT GC02 – SLOPING BACKFILL

5.1. Acceleration in Soil and Structures

The model was instrumented with 3 accelerometer arrays as shown in Figure 3.5 in order to obtain distribution of accelerations vertically and horizontally within the soil profile. The acceleration amplification versus input PGA measured at two depths in the free field and the slope crest is presented in Figures 5.1(a) and 5.1(b). The data show that at the free surface the ground motion is amplified and at a depth of 15 m the acceleration is slightly de-amplified for strong ground motions. In comparison, the container shows strong amplification of the ground motion at the top ring, including significant vertical accelerations, as seen in Figures 5.1(c) and 5.1(d). The horizontal accelerations at the top ring were amplified by a factor of two, suggesting the possibility of separation with the neighboring soil. The peak vertical accelerations at the top ring measured on the north end were amplified by a factor of 1.5 to 2. The best interpretation is that the asymmetry of the model resulted in imbalance in complementary shear forces on opposite sides of the container which then introduced large eccentricity in ground motions. This in turn produced boundary loads that affected the performance of the model. Unfortunately, the accelerometers located in the cantilever wall reached the maximum capacity during the experiment and, therefore, the accelerations at the top of the wall are not reported, nor can they be used for more detailed analysis of the results.

Analogous to the level ground experiment GC01, profiles of relative ground acceleration and displacement were computed to illustrate the ground motion variations with depth and evaluate the contribution of different modes on the total model response. Figure 5.2 shows these profiles for the accelerometers located at free field (accelerometer array A in Figure 3.5). The plot shows that the relative displacements increase monotonically toward the free surface following the shape of the first mode, which has a participation factor over 95%. On the other hand, the acceleration profiles show a strong influence of the second mode, as high as 30% of the total acceleration in the case of Kobe. Also, displacement profiles on the free field were compared to the displacement measured below the slope crest (array B) and at the mid-slope (array C), as seen in Figure 5.3. These plots show a very similar response on the three profiles and no evidence of topographic amplification was apparent from the data.

Acceleration response spectra with 5% damping measured at selected locations are presented in Figure 5.4. The plots show that spectral accelerations are consistently amplified for periods between 0.1 s and 1 s. Due to the high strength of the soil, no significant difference is apparent between the ground motions recorded on the surface for periods over 0.3 s.

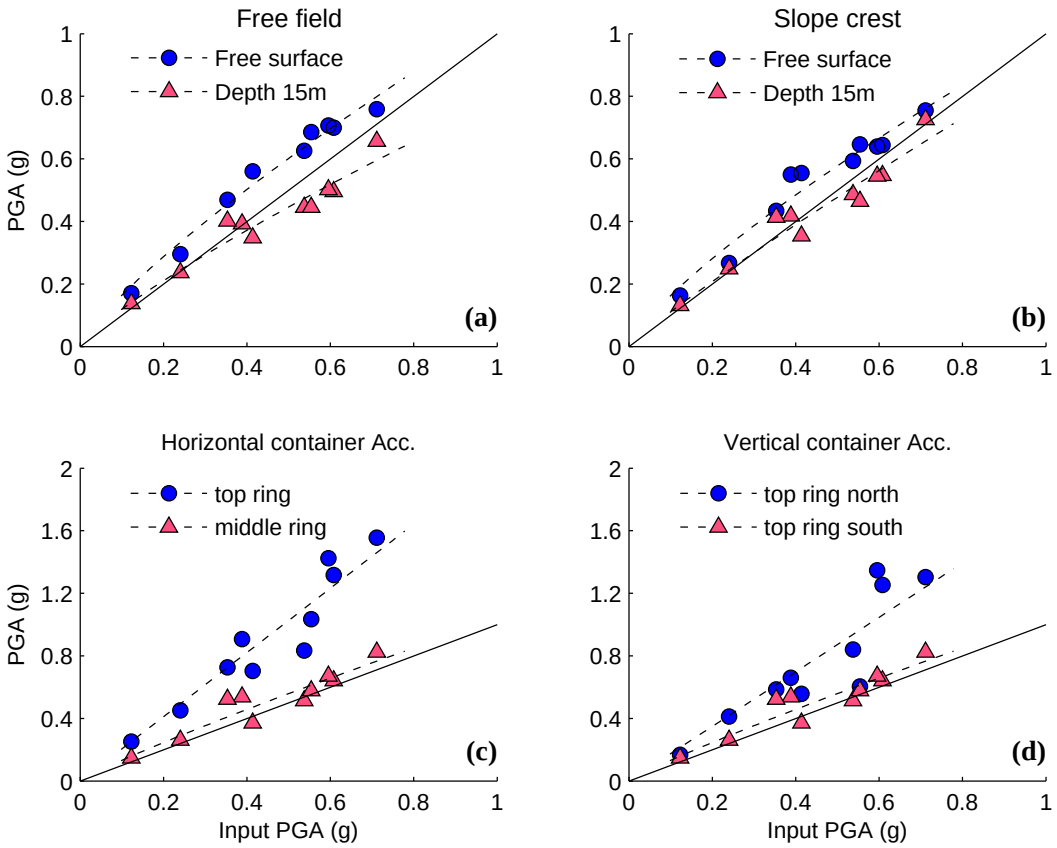

Figure 5.1 Ground motion amplification recorded (a) at free field, (b) below the slope crown, and (c,d) at the container rings.

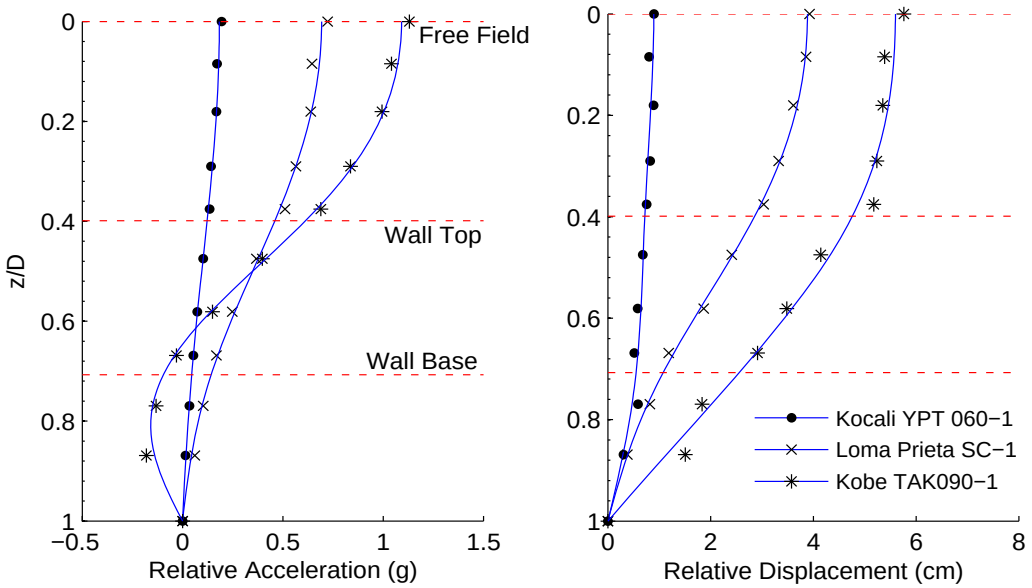

Figure 5.2 Relative ground acceleration and displacement of array 'A' at the time of PGA_{ff} and PGD_{ff}. Depth z normalized to model depth D=20 m.

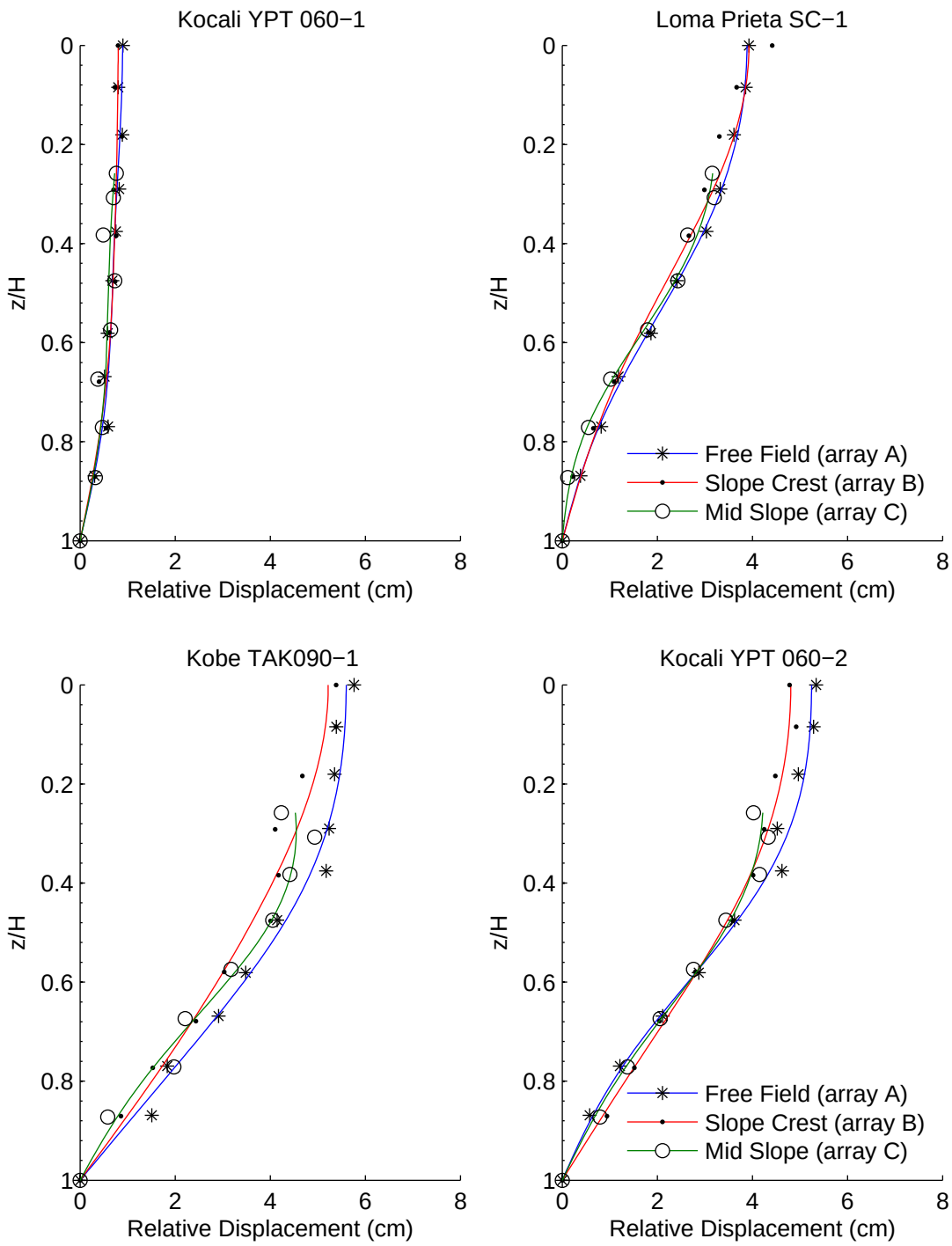

Figure 5.3 Relative displacement profiles of arrays A, B and C for different ground motions

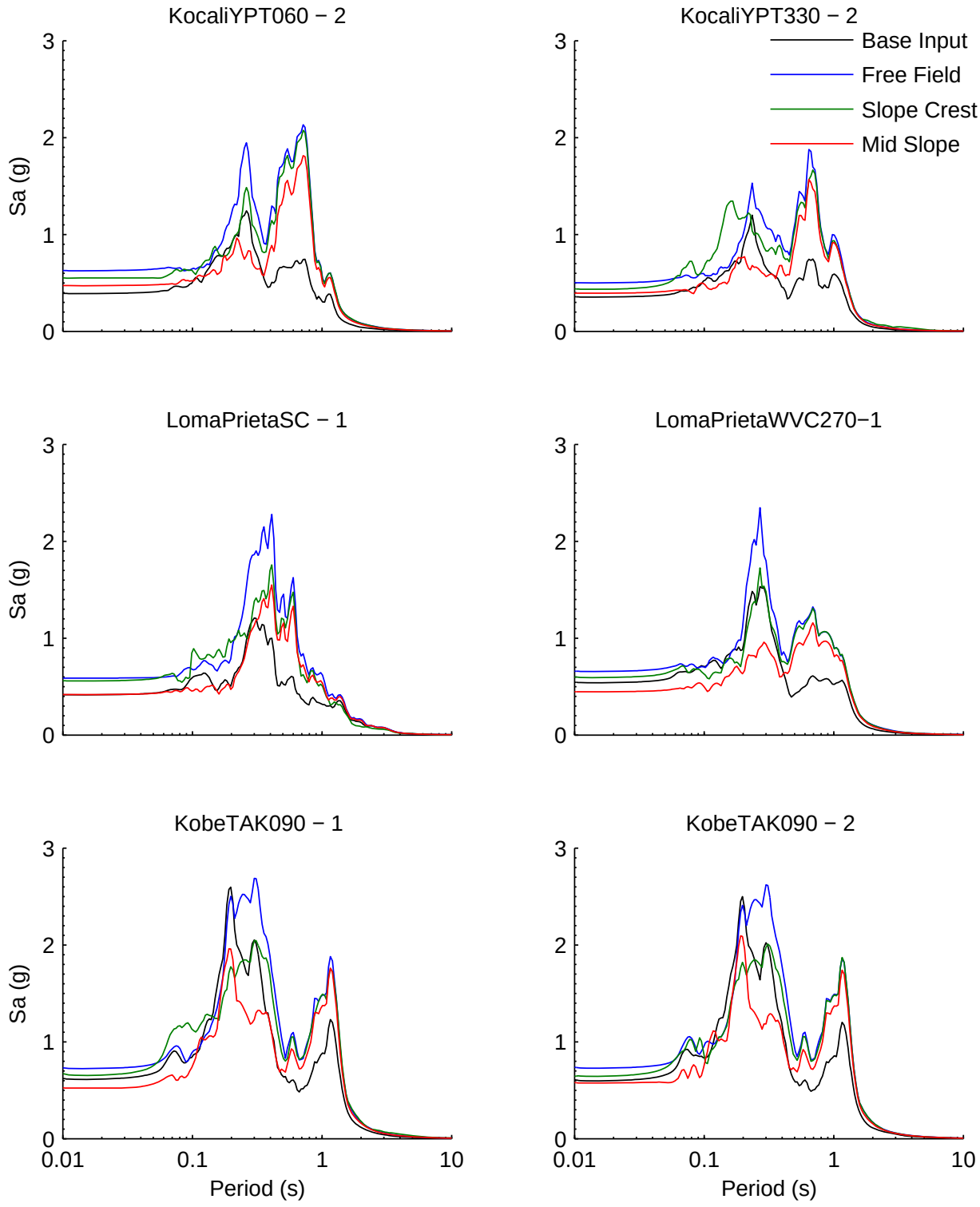

Figure 5.4 Acceleration Response Spectrum (ξ=5%) in the soil.

5.2. Response of Cantilever Wall

The compaction induced stresses on the wall remained constant throughout the test and can be approximated as $\sigma_a/\gamma H = 0.67$. The dynamic earth pressure distribution interpreted from Tactilus sensors increased with depth, and thus, the resultant is considered to act at 0.33H. However, this result is not consistent with Okabe's (1926) theory for walls with sloping backfill, which locates the resultant between 0.42H-0.48H. The magnitude of the soil induced loads were determined using the simplified equation $\Delta P_{ae} = \Delta Q_b - \Delta P_{in}$, as outlined in Section 3.9, where ΔQ_b is the dynamic shear at the base of the stem and ΔP_{in} is the inertial load at the corresponding time. Due to the high stiffness of the clay, no significant phase differences were observed between ΔP_{ae} and ΔQ_b. A summary of the seismic load increments versus PGA_{ff} is presented in Figure 5.5 and it is detailed in the Appendix Table D.2. Although ΔK_{ae} has large scatter at large ground accelerations, the upper confidence bound of the data can be well approximated using the Seed and Whitman (1970) method for level ground and the Okabe method for sloping ground (H:V=2:1), with k_h defined as 100% PGA_{ff}/g.

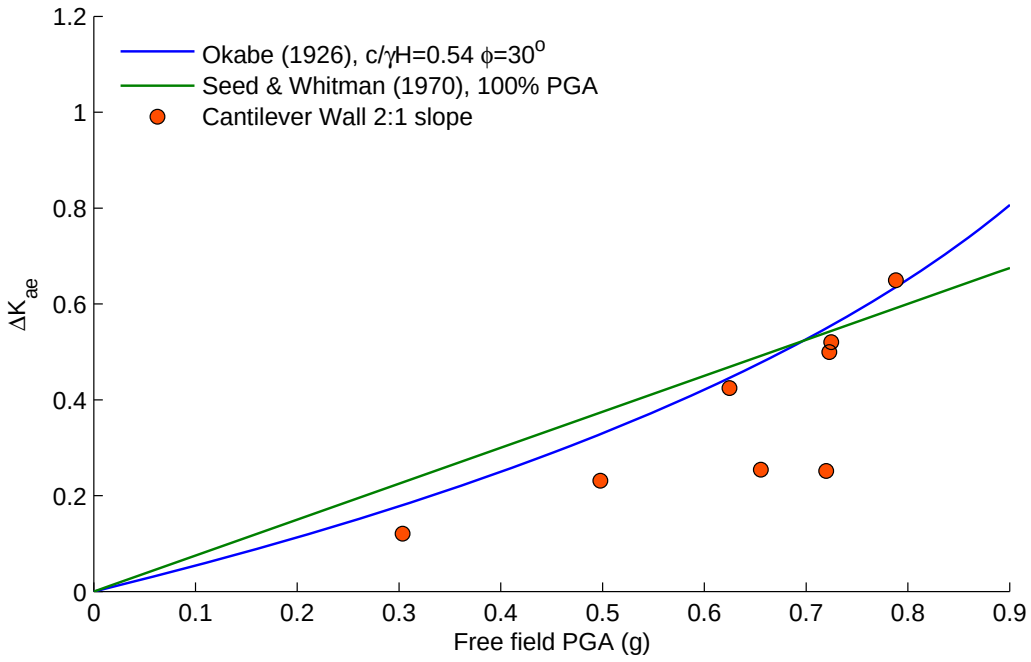

Figure 5.5 Coefficient of dynamic load increment on the cantilever wall.

5.3. Slope Displacement and Wall Deflections

The residual slope displacements after the series of input motions was approximately 25 mm prototype scale (less than 1 mm in model scale), as recorded with the displacement transducers located on the wall. The maximum dynamic free field displacements are very close to the slope crest and mid-slope displacements, and the cantilever wall deflections are on the average 30% of the total slope displacements, as shown in Figure 5.6. These wall deflections are consistent with

the fact that the slope did not fail and the soil had sufficient strength to remain stable with a static factor of safety of 2.2, as further discussed in Section 7.3.

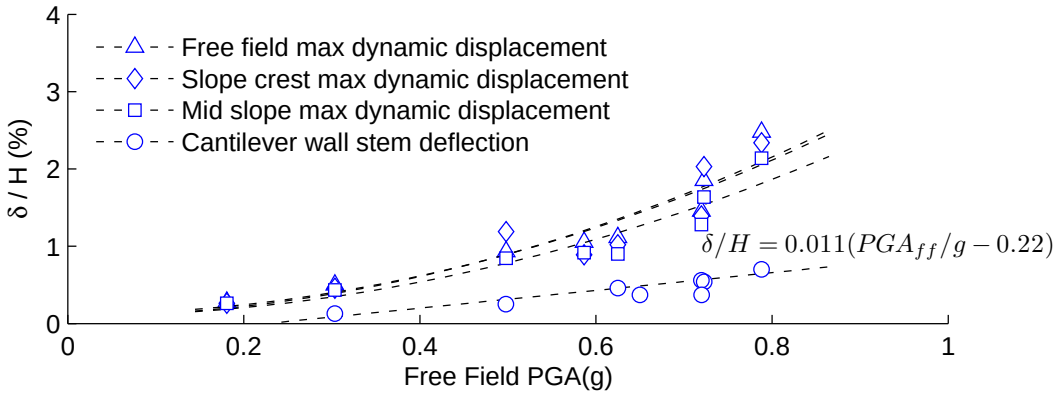

Figure 5.6 Maximum dynamic displacements in the soil surface, and transient wall deflection.

5.4. Summary of Observations

A centrifuge experiment was performed to study the seismic earth pressures of a cantilever wall retaining a compacted cohesive backfill on a 2:1 slope. The model wall represents a standard 6 m cantilever wall used by Caltrans.

In experiment GC02, only a slight de-amplification of the ground motion was measured in the soil due to the high compaction energy and strength of the clay. Accelerations in the retaining wall could not be measured since the sensors reached their maximum capacity. The unbalanced weight of the moving soil mass introduced large vertical accelerations in the model and differential horizontal displacements, on the average 50% larger than in typical symmetric models. These effects should be avoided in future centrifuge experiments by using counter weights embedded in the soil or attached to the container or, if possible, avoiding the use asymmetric models in dynamic experiments.

The residual horizontal slope displacement was approximately 25 mm (less than 1 mm in model scale) at the end of the experiment. The maximum dynamic free field displacements were very similar to the displacements measured on the slope crest and the mid-slope, and no signs of topographic amplification were evident. The dynamic wall deflections were approximately 30% of the total seismic displacements and increased linearly with PGA_{ff}. The dynamic earth pressure increments exhibited some scatter at large accelerations, however the Seed and Whitman (1970) method for level ground with the resultant applied at 0.33H represents a reasonable upper bound to the experimental data.

6. NUMERICAL MODELING OF EXPERIMENT GC01 – LEVEL GROUND

The level ground experiment GC01 was modeled in FLAC$^{2\text{-}D}$ using a nonlinear hysteretic relation for the soil and interface elements. The objective of the modeling effort was to evaluate the ability of the numerical model to reproduce the experimental results and to be able to investigate the details of the complexities of soil-structure interaction under different conditions. Special attention was given to the influence of the boundary elements and their interaction with the soil.

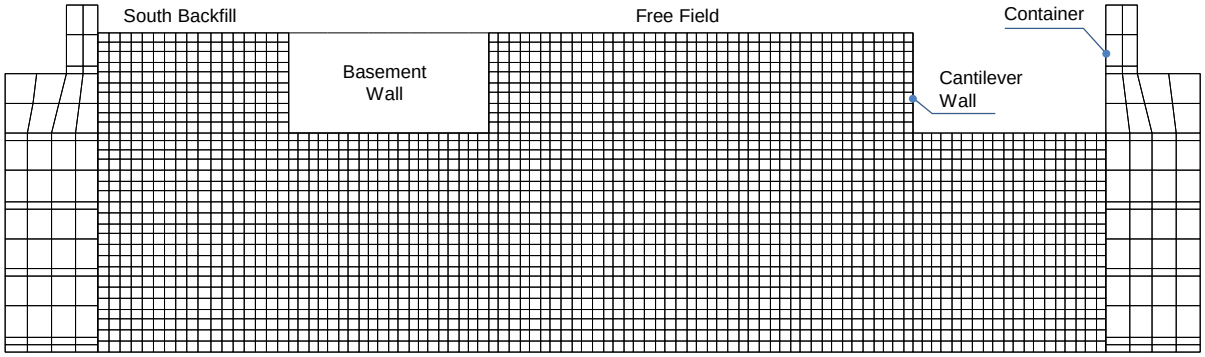

Figure 6.1 Grid discretization of retaining walls with level ground.

6.1. Overview of FLAC$^{2\text{-}D}$

The FLAC$^{2\text{-}D}$ (*Fast Lagrangian Analysis of Continua*) computer code was used for the numerical analyses performed in this study. The code converts the governing differential equations at discrete points into a set of algebraic equations, and uses an explicit time-marching scheme to ensure that plastic collapse and flow are modeled accurately. The main advantage of this scheme is that the plasticity equations are solved in one step, thus, no iterations are necessary when computing stresses from a constitutive relationship. Secondly, since mass and stiffness matrices are not assembled, memory requirements are always at a minimum and no additional computational effort is needed to work in the large-deformations mode. The most important disadvantage is that small time steps are required to ensure stability and convergence of the solution. Several built-in constitutive relations are available in FLAC$^{2\text{-}D}$ to model the behavior of soils. User-defined constitutive relations may also be added using the embedded programming language FISH or in the form of C++ codes compiled as DLL (Dynamic Link Libraries). Beam elements and interface elements are included in FLAC$^{2\text{-}D}$ to model the response of structural elements and the interaction forces between the different parts of the model.

6.2. Numerical Model Definition

A plain strain finite difference model of centrifuge experiment GC01 was developed, consisting of 3300 quadrilateral elements, 72 structural elements and 6 interface elements as shown in Figure 6.1. The soil was modeled with a single region using the constitutive relation UBCHYST (Naesgaard, 2011).

The retaining structures were modeled using linear elastic beam elements, with the exception of the cantilever base, which was modeled with embedded quad elements. For simplicity, the shear key in the cantilever wall was not included, and a simplified model of the flexible shear beam container was added to represent more accurately the boundary conditions existing in the experiment. The acceleration histories recorded at the base of the centrifuge model were used as input acceleration in the numerical model; additional simulations of Kocaeli and Loma Prieta included amplification factors, as listed in Table 6.1.

Table 6.1 Ground motions used in the numerical simulations

FLAC Ground Motion	Centrifuge Equivalent*	Amplification Factor
Kocali YPT 060	(1) , (2)	100%, 125%, 150%, 175%, 200%
Kocali YPT 330	(3) , (8)	100%
Kobe TAK 090	(5) , (9)	100%
Loma Prieta SC	(4) , (6)	50%, 100%, 130%, 150%

** Centrifuge ground motion as listed in Table 3.6*

The compaction sequence and buildup of gravity stresses on the centrifuge model could not be simulated accurately with the numerical model, and thus, the initial stresses in the soil and interface elements were an important source of uncertainty. Nevertheless, reasonable estimates of seismic earth pressures were obtained by first subjecting the model to the Kocaeli ground motion.

The FLAC User's guide (Itasca, 2011) recommends limiting the elements size to one tenth of the wavelength associated with the highest frequency component of the input, i.e., $\Delta l \leq \frac{1}{10} v_s / f_{max}$. Considering that the average shear wave velocity of the backfill is 125 m/s, and that the maximum frequency of centrifuge ground motions is about 10 Hz (prototype), the element size should be less than 1.25 m in prototype. Accordingly, the soil grid was defined using elements of maximum length 0.6m, allowing for an accurate representation of shear waves with frequencies up to 20 Hz. In addition, a 10 Hz low-pass filter was applied to the input ground accelerations to reduce the propagation of spurious noise. As seen in the power density spectra of Figure 6.2, more than 99% of the earthquake power concentrates at low frequencies; thus, filtering frequencies greater than 10 Hz does not affect the input ground motions.

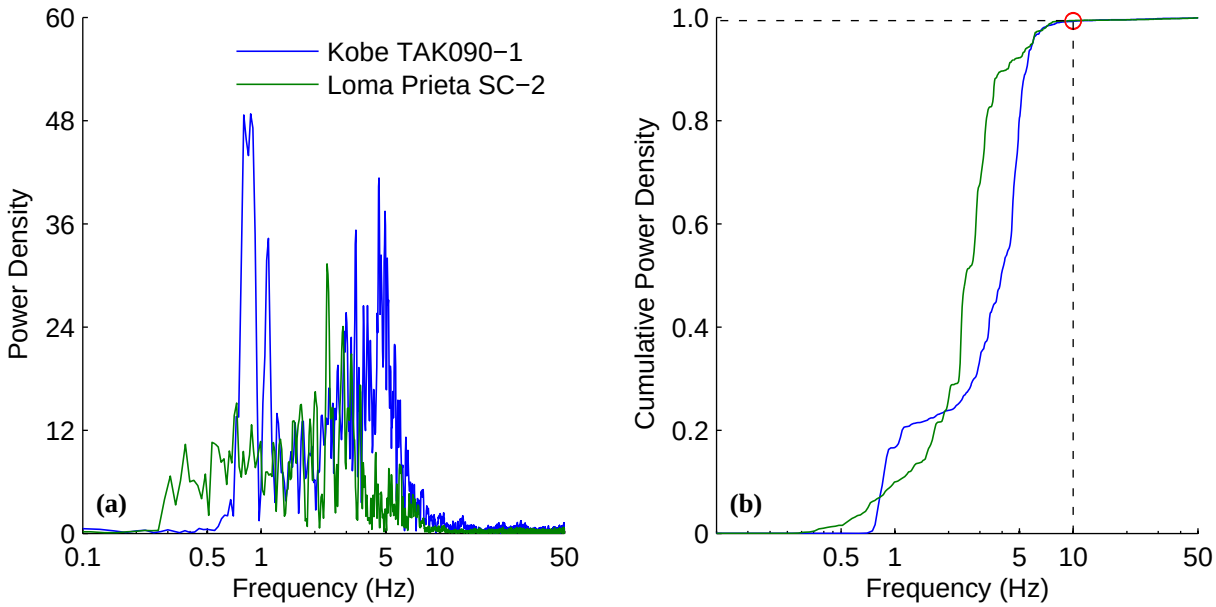

Figure 6.2 (a) Power spectral density and (b) cumulative power density of unfiltered input ground acceleration for Kobe and Loma Prieta.

6.2.1. Constitutive Model and Calibration of Soil Parameters

The compacted clay used in the centrifuge experiments was modeled with UBCHYST, a two-dimensional nonlinear hysteretic model developed at University of British Columbia (Naesgaard, 2011). Originally implemented in FLAC$^{2\text{-D}}$ using a FISH function, the model was later converted to DLL (Mikola & Sitar, 2013), significantly improving the efficiency of the code. UBCHYST is a simple total stress model for the dynamic analysis of silty non-liquefiable soils subjected to cyclic shearing of horizontal planes. The Mohr Coulomb failure criterion is used together with a stress dependent shear modulus reduction, which generates non-linear hysteretic cycles and helps to reduce the amount of Rayleigh damping required.

The expression for the tangent shear modulus has ten input parameters, the reference shear modulus G_r, the shear modulus exponent m, the Mohr Coulomb parameters c and ϕ, and six parameters that control the size and shape of the hysteresis loops. The functional form of the tangent shear modulus is given by (Naesgaard, 2011)

$$G_t = G_r \left(\frac{p}{p_a}\right)^m \left(1 - \frac{\eta - \eta_{max}}{\eta_f - \eta_{max}} R_f\right)^n mod_1 \cdot mod_2 \tag{6.1}$$

where $\eta = \tau_{xy}/\sigma'_v$ is the current the stress ratio, $\eta_f = \sin\phi + c \cdot \cos\phi \,/\sigma'_v$ is the stress ratio at failure, η_{max} is the maximum stress ratio at last reversal, and R_f and n are calibration parameters with recommended values of 1 and 2, respectively (Naesgaard, 2011). The correction factor mod_1, typically between 0.6-0.8, accounts for modulus reduction on the initial loading cycle and $mod_2 = 1 - \eta^{rm} \cdot dfac > 0.2$ is an optional factor for permanent modulus reduction at large strains. In this study *dfac*=0 resulted in large hysteretic damping at large strains in the

one-element tests; however, it improved the ground motion comparison between centrifuge and the numerical models.

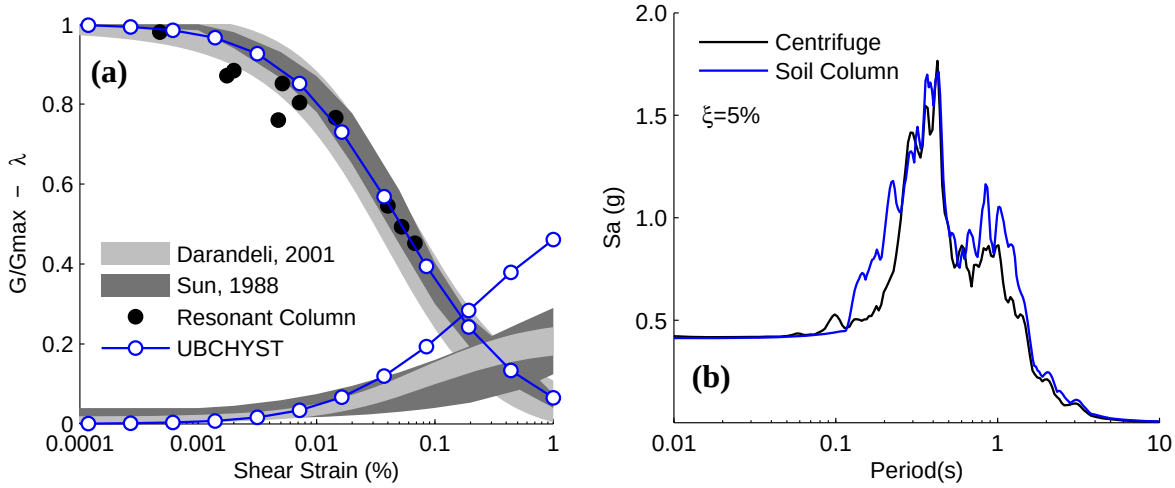

Figure 6.3 (a) Shear modulus reduction and damping curves on single element tests, (b) Free field acceleration response spectra with 5% damping for Loma Prieta SC-1.

The calibrated soil parameters for experiment GC01 are presented in Table 6.2, and were determined based on the laboratory experiments described in Section 3.4. Addition numerical simulations of a single element under cyclic shear loads and the free field response of a one-dimensional soil column were used to define the hysteresis loop parameters. As seen in Figure 6.3(a), the shear modulus reduction modeled with UBCHYST is in good agreement with the values measured in resonant column tests and published data. Figure 6.3(b) compares the free field response spectra with 5% damping measured during Loma Prieta SC-1 and computed from a 1-D soil column. Note that PGA_{ff} is matched correctly and the spectral amplifications are in good agreement for a wide range of natural periods.

Table 6.2 Soil parameters of constitutive model UBCHYST for experiment GC01

Unit weight	γ	= 20.0	kN/m^3	Dilatancy angle	*dil*	= 0.00	
Cohesion	c	= 15.2	kPa	Stress rate factor	R_f	= 1.00	
Peak friction angle	ϕ	= 30	deg	Stress rate exponent	*n*	= 2.00	
Reference shear modulus	G_r	= 38	MPa	First cycle factor	mod_1	= 0.75	
Reference bulk modulus	K_r	= 76	MPa	Large strains exponent	*rm*	= 0.50	
Shear modulus exponent	*m*	= 0.50		Large strains factor	*dfac*	= 0.00	

As discussed later, these model parameters allowed capturing the most important aspects of the model response as measured in the centrifuge, namely energy dissipation, soil acceleration and soil induced load. Nevertheless, local responses at the element or material levels were not necessarily accurate. This level of accuracy would require a comprehensive constitutive relation and more experimental data.

6.2.2. Structural Elements

Linear elastic beam elements were used to model the basement walls, the cross bracing and the freestanding cantilever wall. The equivalent plain strain mass and stiffness of the structural elements are summarized in Table 6.3 for a unit width in prototype scale. The basement and the cantilever walls were discretized into elements of maximum length 0.6 m, thus conforming to the grid density used in the soil. The stiffness of the cross bracing accounts for the load cells stiffness used in the experiment to measure the net basement compression. Although this configuration did not significantly affect the dynamic load increments, it reduced the lateral stiffness of the basement and led to increased racking. Using a basic frame model, it can be shown that the lateral stiffness of a culvert with height H and width B can be written as

$$k_{lat} = \frac{24EI_{wall}}{H^3}\frac{\alpha}{\alpha + B/H} \tag{6.2}$$

where $\boldsymbol{\alpha = I_{slab}/I_{wall}}$ is the ratio between the moment of inertia of the slabs and the walls. Using Equation 5.2 and the values of Table 6.3, the lateral stiffness of the basement modeled in the centrifuge is approximately 2300 kN/m/m ($\boldsymbol{\alpha} \approx 0.1$), whereas a prototype basement built with concrete slabs and stiff moment connections has a lateral stiffness 8 to 10 times larger ($\boldsymbol{\alpha} \approx 1$).

Table 6.3 Structural element properties per unit width

Property per unit width	Units	Basement Wall	Basement Struts	Basement Foundation	Cantilever Wall	Cantilever Base
Young Modulus (E*)	kPa	7.68E+07	7.68E+07	7.68E+07	7.68E+07	7.68E+07
Unit Mass (ρ)	ton/m^3	4.10E+00	2.13E+01	2.13E+04	3.19E+00	3.61E+00
Cross Section (A)	m^2/m	4.57E-01	1.01E-02	1.01E-05	3.43E-01	3.43E-01
Moment of Inertia (I)	m^4/m	7.96E-03	6.83E-04	7.96E-03	3.36E-03	3.36E-03

(*) *Equivalent plain strain Young modulus for aluminum* $E^* = E/(1-\nu^2)$

6.2.3. Interface Elements

Interface elements were used to model the contact between soil, the structures, and the container. Interface elements in FLAC$^{2\text{-}D}$ consist of shear and normal springs coupled with a slider element, allowing for tensile separation and Coulomb shear forces (Itasca, 2011). The normal and shear stiffness parameters have a great influence on the computed dynamic earth pressures. Typical k_n and k_s values based on the equivalent normal stiffness of the soil elements resulted in earth pressures significantly larger than those measured in experiment GC01. Consequently, k_n and k_s were set equal to 100 MPa to match the seismic earth pressures during the ground motions and to limit the penetration distance of contact nodes ($\delta = \sigma_n/k_n$) to less than 1% of the minimum zone height. The shear friction angle and cohesion along the interface was set to $\phi = 10°$ and $c = 0$, respectively.

The total load on the soil-wall interface P_{ae} was determined assuming a linear variation of the normal stress in between contact nodes, and the dynamic increment was computed as the difference between the total load and the static component. For a wall of composed of N segments, the loads on the interface can be computed as

$$P_{ae} = \int_0^H \sigma_n dz \approx \frac{H}{N-1} \sum_{i=1}^{N-1} \frac{\sigma_n^i + \sigma_n^{i+1}}{2} \tag{6.3}$$

6.2.4. Boundary Conditions

Since the north and south ends of the centrifuge model GC01 had different elevations, the inclusion of the container box was necessary to obtain reasonable boundary conditions on the south backfill. The geometry and mechanical properties used to model the flexible shear beam container are summarized in Table A.1. These properties were derived from static load tests on an empty container (Ilankatharan, 2008) and the values converted to an equivalent plain strain model. The effects of the container on the earthquake response of a uniform soil deposit were evaluated numerically and compared to the case with no container, in which the boundary nodes at the same elevation were attached. The analyses showed that the ground motions at the free surface are identical at a distance greater than 9 m (25 cm in model scale) from the boundaries.

6.2.5. System Damping

One of the advantages of modeling the soil with the constitutive relation UBCHYST is that most of the input energy is dissipated in the stress-strain cycles. However, additional Rayleigh damping is required to provide numerical stability at small strains and remove spurious noise introduced by the interface elements and the explicit integration scheme. For a multiple degree of freedom system, the damping ratio of the *i-th* angular frequency can be written as $2\xi_i = \alpha/\omega_i + \beta\omega_i$, where the mass and stiffness factors α and β are determined by specifying the damping ratio at two prescribed angular frequencies, or alternatively, by specifying the minimum damping ratio ξ_{min} at the angular frequency ω_{min} . Rayleigh damping in FLAC is defined using the latter form and the coefficient α and β can be determined in as

$$\begin{bmatrix} 1/\omega_{min} & \omega_{min} \\ -1/\omega_{min}^2 & 1 \end{bmatrix} \begin{bmatrix} \alpha \\ \beta \end{bmatrix} = \begin{bmatrix} 2\xi_{min} \\ 0 \end{bmatrix} \tag{6.4}$$

For the Loma Prieta and Kocaeli ground motions, a damping ratio $\xi_{min} = 1\%$ centered at the predominant frequency of the input velocity $f_{min} = \omega_{min}/2\pi = 1.4\,Hz$ provided a good agreement between the measured and computed surface response. The corresponding damping ratios at the first three natural periods of the soil deposit are 1.1%, 2.3% and 3.8%. As mentioned earlier, due to the frequency dependence of the input, a single set of Rayleigh damping coefficients may not be adequate to predict the model response under general loading conditions; for example, in the Kobe ground motions, a damping ratio of $\xi_{min} = 2\%$ centered at $f_{min} = 4.0\,Hz$ allowed to match the recorded seismic loads more accurately. The input velocity and the frequency dependent damping ratio are shown in Figure 6.4 for two ground motions.

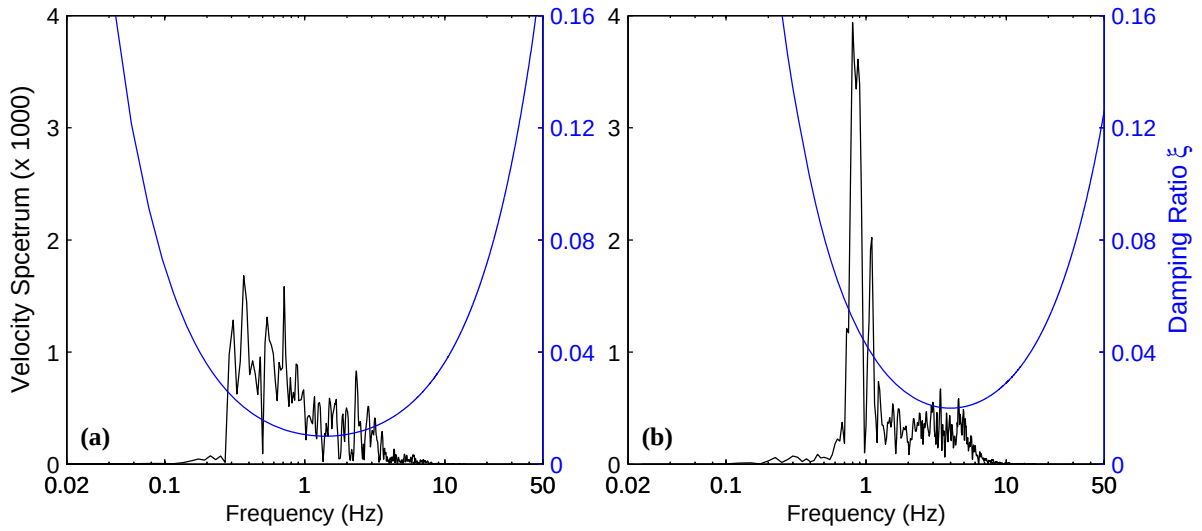

Figure 6.4 Fourier transform of the input velocity and damping ratio versus frequency for (a) Loma Prieta SC-2 and (b) Kobe TAK 090-1.

6.3. Acceleration in Soil and Structures

The computed acceleration histories were integrated in the frequency domain and filtered to remove spurious noise introduced by the explicit integration scheme. The profiles of relative ground acceleration and displacement in the free field are shown in Figure 6.5. Note that the acceleration distribution with depth is in excellent agreement with the recorded values; however, the computed relative displacements are 30% smaller during Kobe.

An example of acceleration, velocity, and displacement time histories computed in the free field are presented in Figure 6.6 and compared to the ground motion integrated from accelerometers; the complete set of figures is shown in Appendix C. These plots show that the numerical model captures the most important characteristics of free field response and is able to reproduce accurately the experimental data.

Comparisons of computed and recorded acceleration at selected points of the model are presented in Figures 6.7 and 6.8 for the Loma Prieta earthquake. For the complete set of figures, refer to Appendix C. The points considered in this analysis are located in the south backfill and the middle backfill (free field) at different depths. These plots show that the free field response of the numerical model is in excellent agreement with the centrifuge data in terms of phase, amplitude, and spectral amplifications. However, near the base of the model the response spectra at short periods (0.1s - 0.25s) are slightly different for the strong motions in the simulated Kobe and Loma Prieta events. Since the energy dissipated by the container was not accounted for in the numerical model, some of the kinetic energy of the container was transferred to the soil. Consequently, the computed accelerations in the south backfill overestimate the recorded values. To avoid this problem in future simulations, the structures should be located far from the boundaries and the energy dissipation characteristics of container should be accounted for.

Acceleration response spectra computed on the structures are presented in Figure 6.9. Over the range of ground motions used in the experiment, the computed acceleration at the basement top underestimates the recorded response. On the other hand, measured and computed accelerations at the top of the cantilever wall are in good agreement, except for the Kobe motion, for which larger accelerations are predicted in the numerical model.

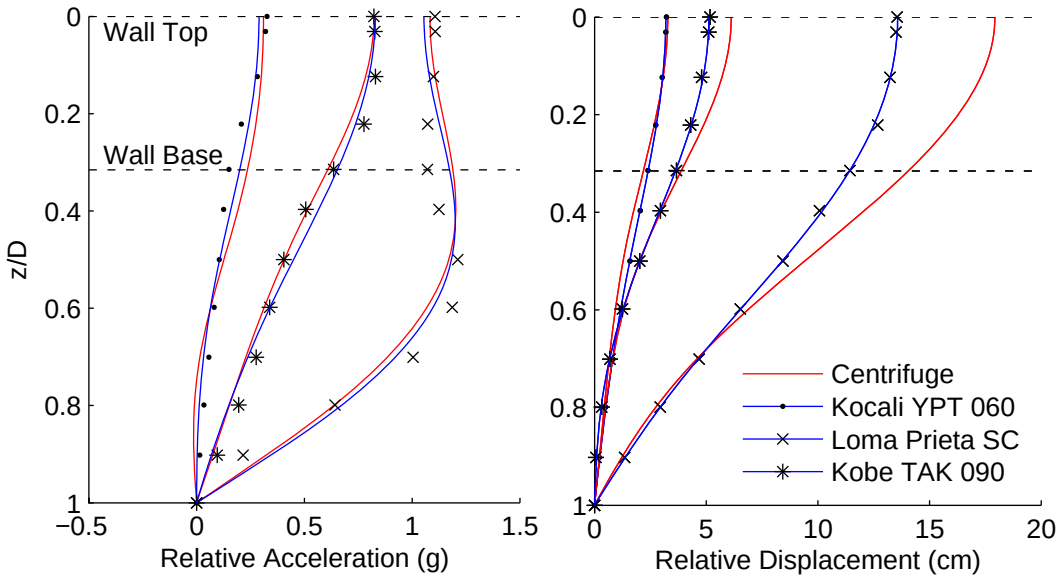

Figure 6.5 Comparison relative ground acceleration and displacement at the time of PGA_{ff} and PGD_{ff}. Depth z normalized to model depth D=20 m.

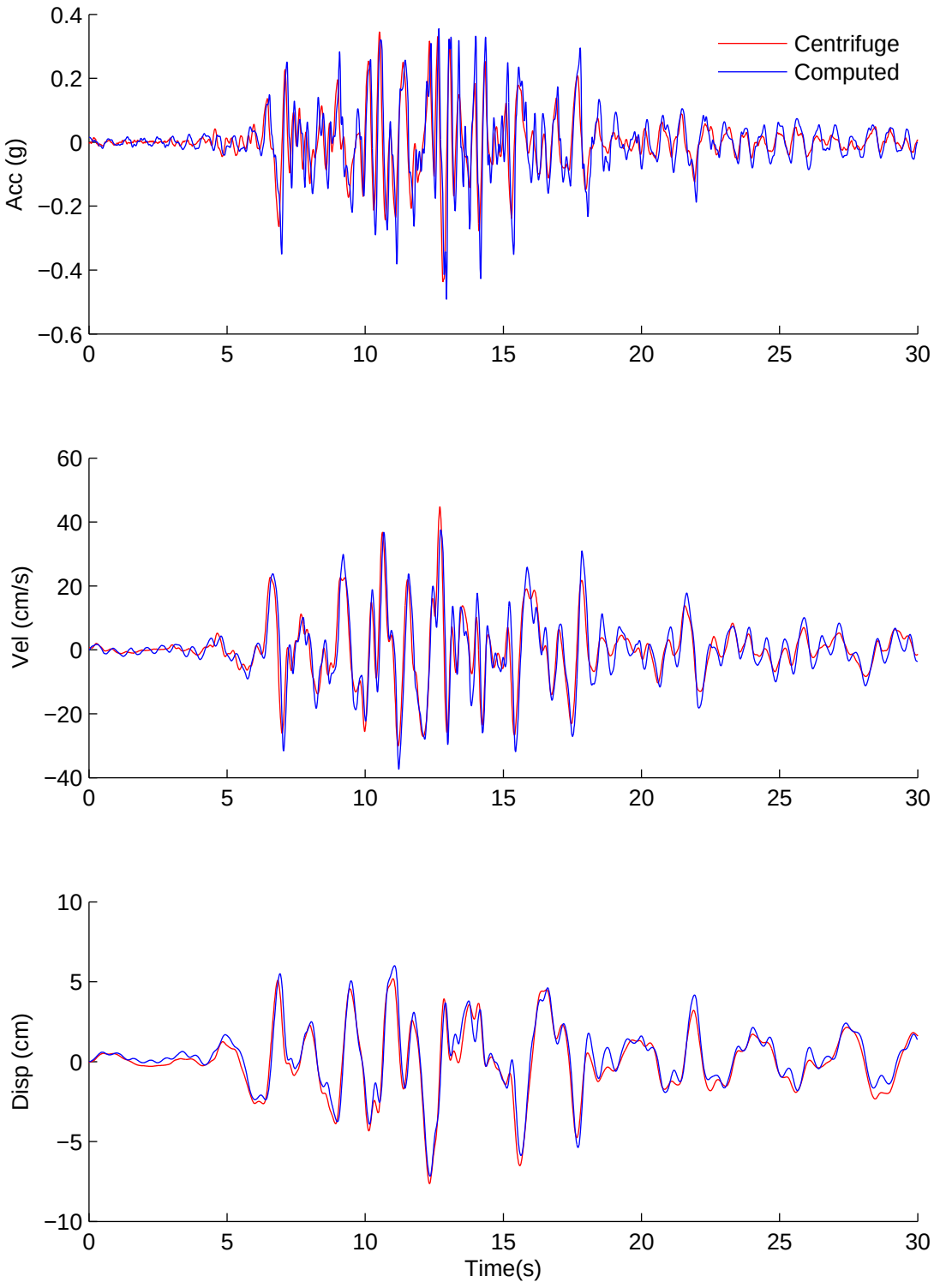

Figure 6.6 Comparison of free field acceleration, velocity, and displacements during Loma Prieta SC-2.

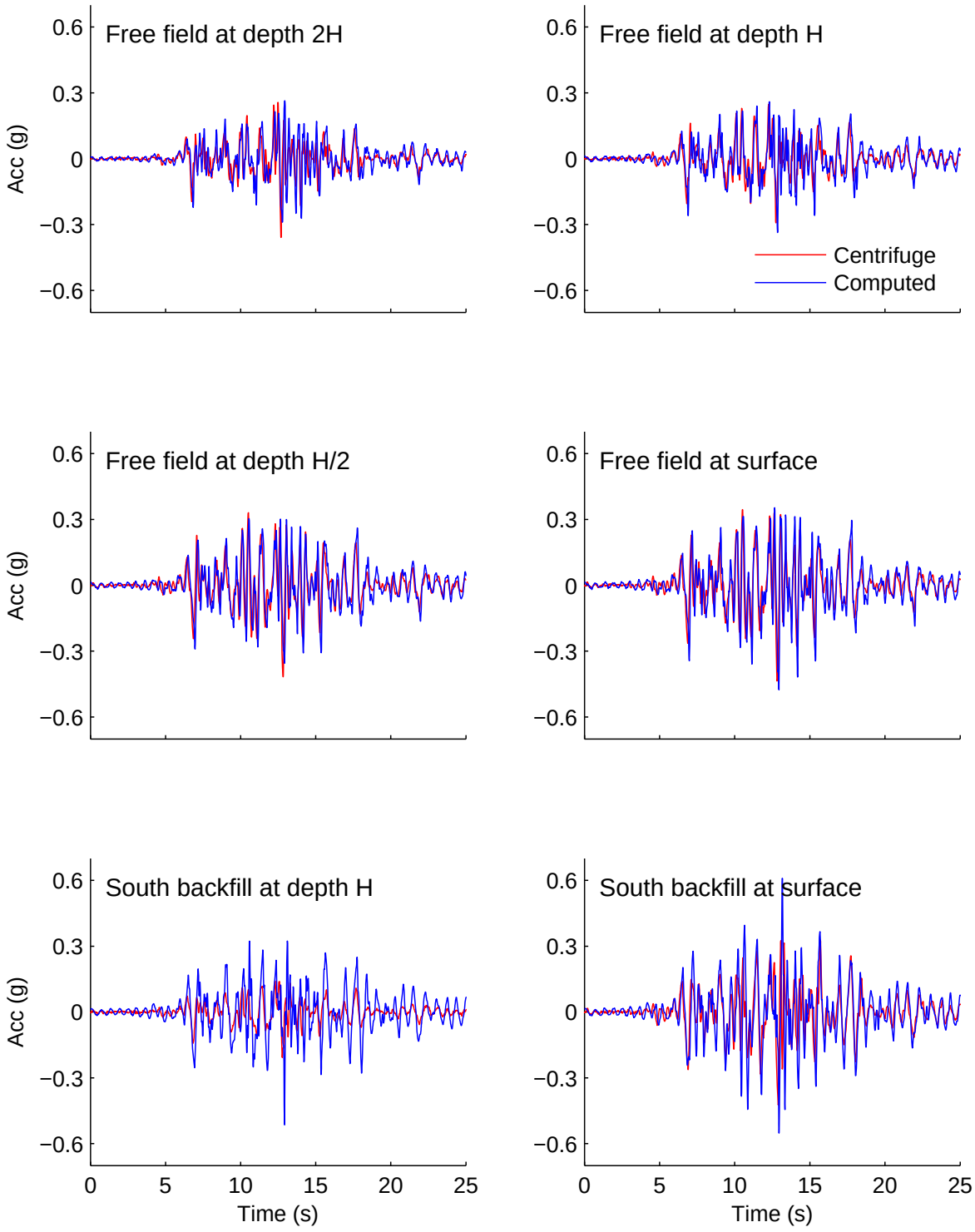

Figure 6.7 Comparison of measured and computed acceleration in the soil during Loma Prieta SC – 2.

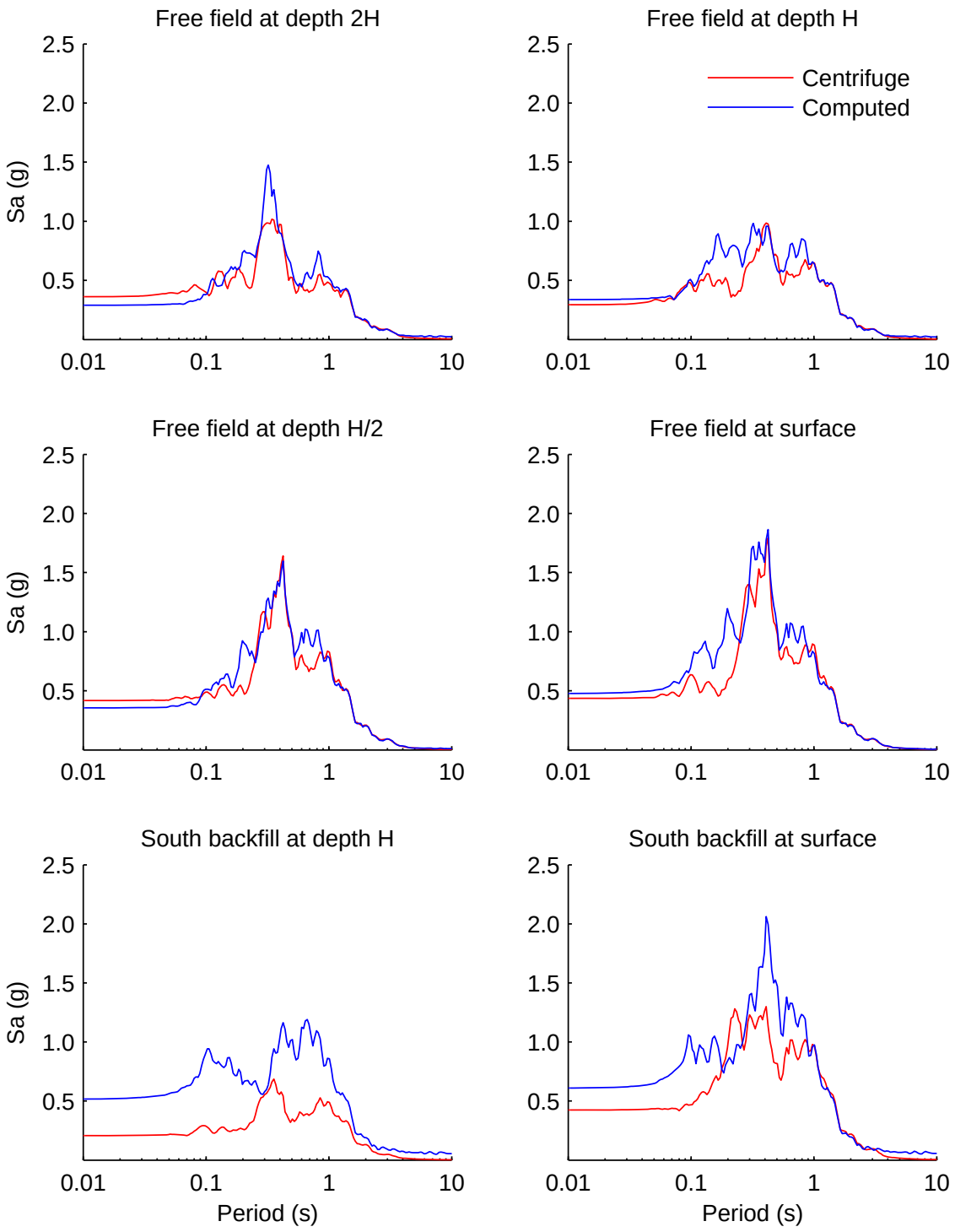

Figure 6.8 Comparison of measured and computed acceleration response spectra at 5% damping for Loma Prieta SC – 2.

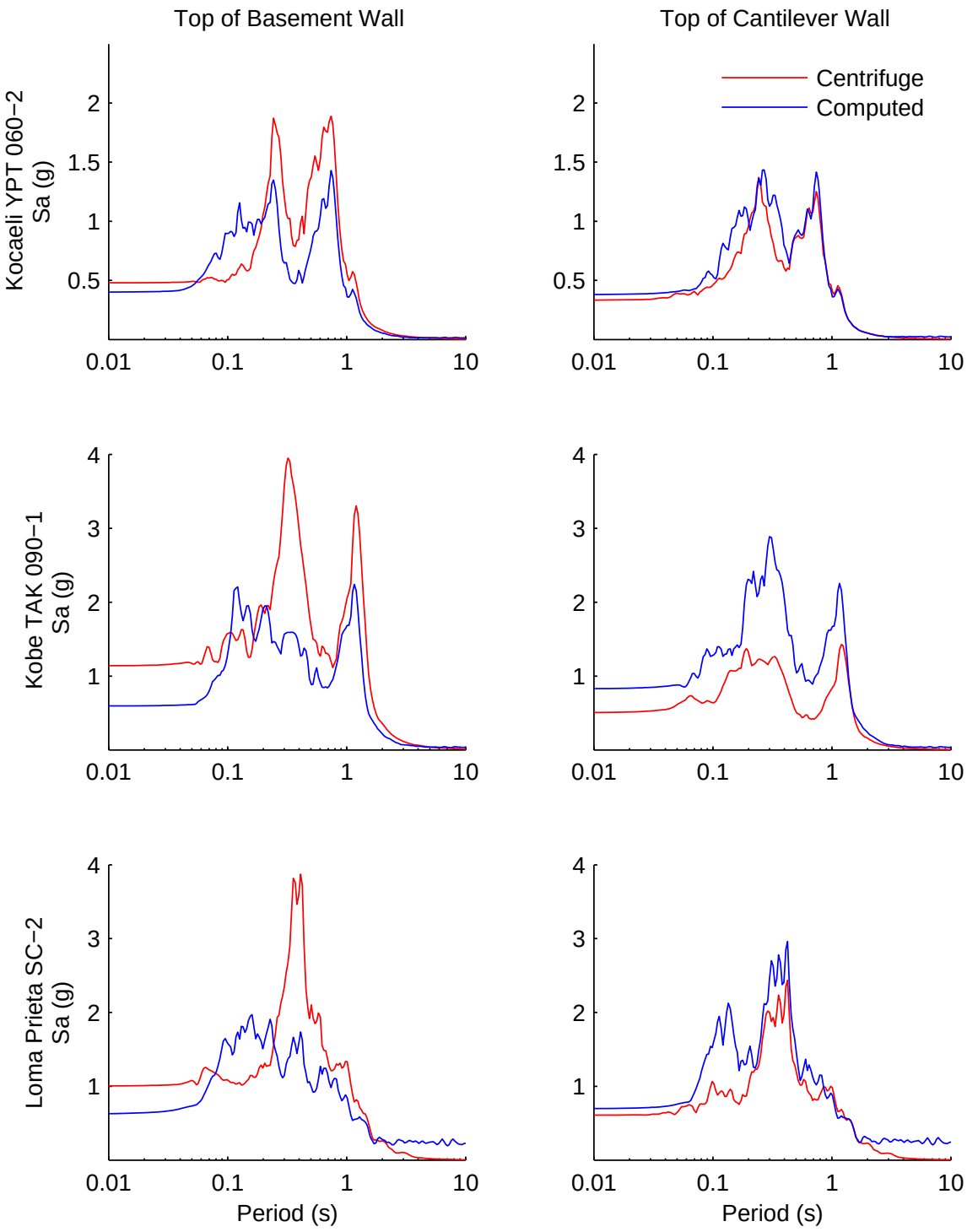

Figure 6.9 Comparison of measured and computed acceleration response spectra at 5% damping at the top of basement and cantilever walls.

6.4. Basement Wall Response

A comparison of the computed and measured basement response during the Kobe and Loma Prieta earthquakes is shown in Figure 6.10 in terms of histories of total basement compression P_{tot}, inertial load ΔP_{in}, and the dynamic load increment on the north wall ΔP_{ae}^{north}. This plot shows that the basement response and its interaction with the container were not captured accurately in the numerical model. Since the residual stresses due to compaction and the buildup of gravity stresses in the experiment were not accounted for, the initial static loads (static basement compression) were over estimated by a factor of 2 to 2.5. The computed inertial loads on the wall were integrated over the wall depth and produced a good agreement with the measured response; however, the peak inertial loads were generally underestimated. The dynamic load increments ΔP_{ae} on the basement were integrated from interface elements; although the peak ΔP_{ae} values are similar to the experimental results, their time histories are not consistent with each other. In addition to the compaction-induced stresses, the model basement was a rather complex experiment setup that led to fundamental differences between the measured and computed response. A comparison of the loads acting on the north basement wall is also presented in Table 6.4.

Table 6.4 Summary of loads on the north basement wall; values normalized by $0.5\gamma H^2$

Ground Motion	Centriuge Model				FLAC Model			
	$P_a^{initial}$	P_a^{final}	P_{ae}^{max}	ΔP_{ae}^{max}	$P_a^{initial}$	P_a^{final}	P_{ae}^{max}	ΔP_{ae}^{max}
Kocali YPT 060	0.14	0.15	0.27	0.13	0.37	0.45	0.49	0.15
Kocali YPT 330	0.14	0.15	0.26	0.12	0.37	0.40	0.48	0.13
Kobe TAK 090	0.15	0.17	0.42	0.27	0.29	0.51	0.73	0.29
Loma Prieta SC	0.16	0.16	0.45	0.29	0.36	0.55	0.64	0.28

The distribution of horizontal stresses on the north basement wall and its variation with time are presented in Figure 6.11 for the Kobe and Loma Prieta earthquakes. Note that the stresses increase approximately linearly with depth before the earthquake begins. However, during the earthquake, the stress distribution is non-linear and changes as a function of the wall deflection. At the time of maximum horizontal load, the earth pressure distribution can be approximated as linear with the resultant applied between 0.35-0.45H. This is consistent with Okabe's (1926) theory of earth pressure that places the resultant near 0.40H. The time variation in the location of the resultant is presented in Figure C.19. This plot shows that for active loading cycles, i.e. for seismic earth pressure increment toward the wall, the resultant moves up as high as 0.45H. During the unloading cycles, however, the resultant drops below 0.33H. The magnitude of the resultant varies linearly with PGA_{ff} and can be approximated as $\Delta K_{ae} = 0.68(PGA_{ff}/g - 0.10) \pm 0.08$. To gain more insight into the seismic behavior of basement walls, the numerical model was used to validate the simplified equation $\Delta P_{ae} = \Delta P_{tot} \mp \Delta P_{in}$. This equation was introduced in Section 3.9 to estimate the soil induced loads from the basement compression in lieu of accurate measurements of earth pressures. As seen in Appendix Figure C.21, the load increments computed from the basement compression and inertial loads are very similar, if not identical, to the load increments integrated from interface elements.

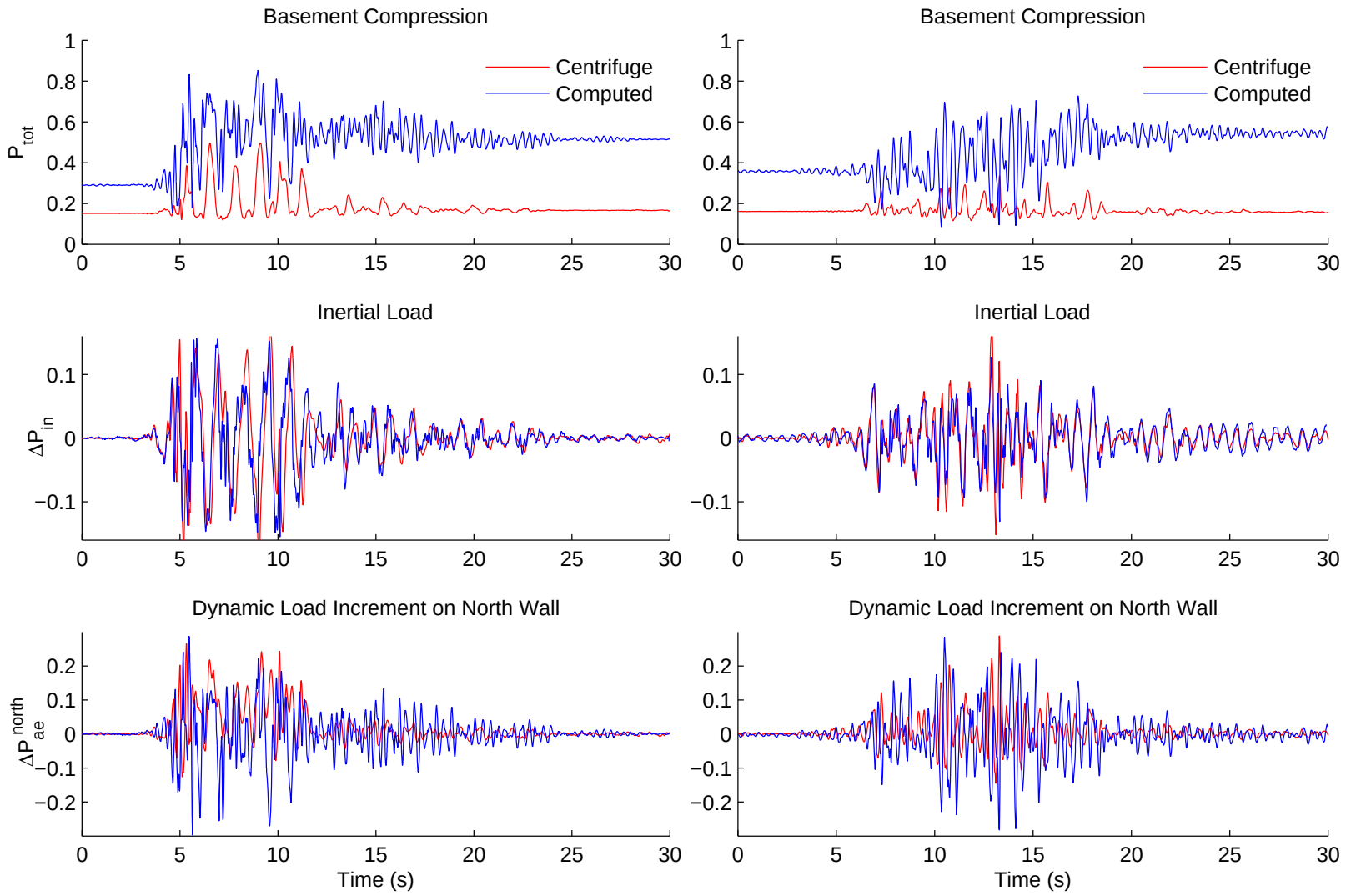

Figure 6.10 Comparison of measured and computed loads on the basement wall during Kobe TAK 090 (left) and Loma Prieta SC-1 (right). Loads normalized by $0.5\gamma H^2$.

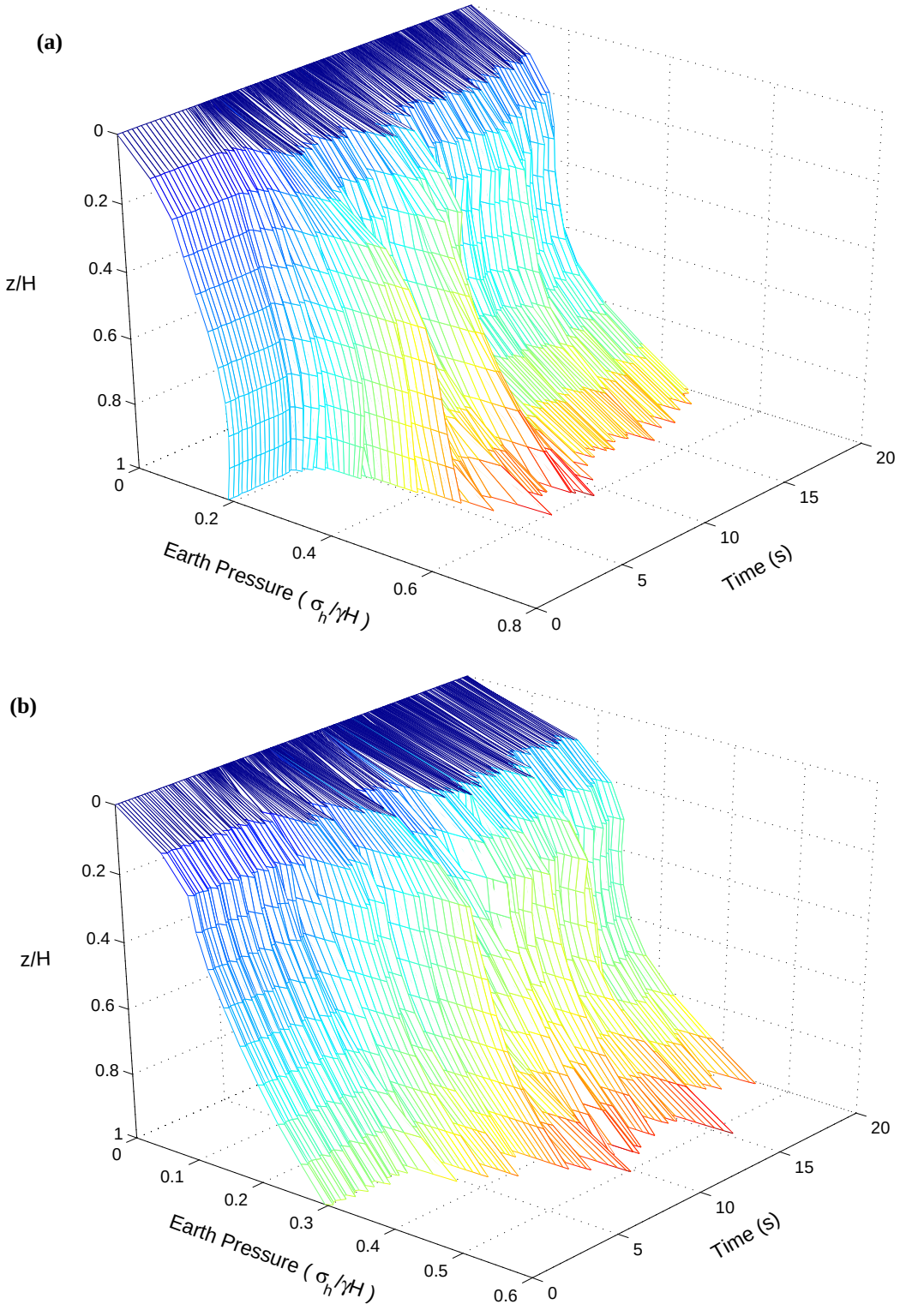

Figure 6.11 Evolution of computed seismic earth pressure distribution on the north basement wall during (a) Kobe TAK 090-1 and (b) Loma Prieta SC-2.

6.5. Cantilever Wall Response

The time histories of total base shear, inertial loads, and dynamic load increments are shown in Figure 6.12, for the ground motions Kobe and Loma Prieta. As seen in these plots, the cantilever wall response was adequately captured by the numerical model and is consistent with the measured response. The static loads, the base shear and the seismic loads are also in good agreement with the measured values as seen in Table 6.5, despite the initial conditions in the numerical model do not explicitly account for compaction.

Table 6.5 Summary of active loads on the cantilever wall; values normalized by $0.5\gamma H^2$.

Ground Motion	Centriuge Model				FLAC Model			
	$P_a^{initial}$	P_a^{final}	Q_b^{max}	ΔP_{ae}^{max}	$P_a^{initial}$	P_a^{final}	Q_b^{max}	ΔP_{ae}^{max}
Kocali YPT 060	0.35	0.38	0.45	0.06	0.34	0.32	0.49	0.09
Kocali YPT 330	0.34	0.35	0.43	0.07	0.34	0.39	0.50	0.10
Kobe TAK 090	0.35	0.37	0.58	0.16	0.26	0.40	0.69	0.26
Loma Prieta SC	0.34	0.34	0.54	0.16	0.34	0.38	0.62	0.22

The computed horizontal stresses on the cantilever wall increase linearly with depth, as shown in the time history plots of Figure 6.13. Likewise, at the time of maximum moment, the computed earth pressure increases linearly with depth as shown in Figure 6.14. The resultant of the static earth pressures acts between 0.33H-0.35H above the wall base, and for seismic conditions acts between 0.35-0.40H. This result is also in good agreement with Okabe's (1926) theory, as opposed to placing the total load at 0.5H as typically assumed in current practice (Seed and Whitman, 1970). A close examination of the earth pressure distribution showed that during loading cycles, i.e. for earth pressure increments towards the wall, the resultant remained between 0.33H-0.40H, however during unloading cycles, the resultant location varied between 0.2-0.5H, as shown in Figure C.20. The magnitude of the seismic load can be approximated as $\Delta K_{ae} = 0.47(PGA_{ff}/g - 0.10) \pm 0.06$, and the upper confidence bound $\Delta K_{ae} \approx 0.47 PGA_{ff}/g$ is equivalent to the Seed and Whitman solution with a design acceleration of 60% PGA_{ff}.

As discussed in Section 3.9, pressure cells could not be used to measure the magnitude of the seismic earth pressures. Instead, the use of strain gages and accelerometers allowed estimating the seismic load based on the simplified equilibrium equation $\Delta P_{ae} = \Delta Q_b - \Delta P_{in}$, where ΔQ_b is the wall base shear and ΔP_{in} the wall inertial load. This equation was verified empirically in the numerical model and allowed calculating ΔP_{ae} accurately from beam elements, as shown in Figure C.22. The computed inertial loads ΔP_{in} are in excellent agreement with the centrifuge data and are about 20% of the base shear. Thus, a simple expression that relates dynamic load increments and the total shear forces on the base of the cantilever wall can be written as

$$\Delta P_{ae} \approx 0.8 \Delta Qb \tag{6.5}$$

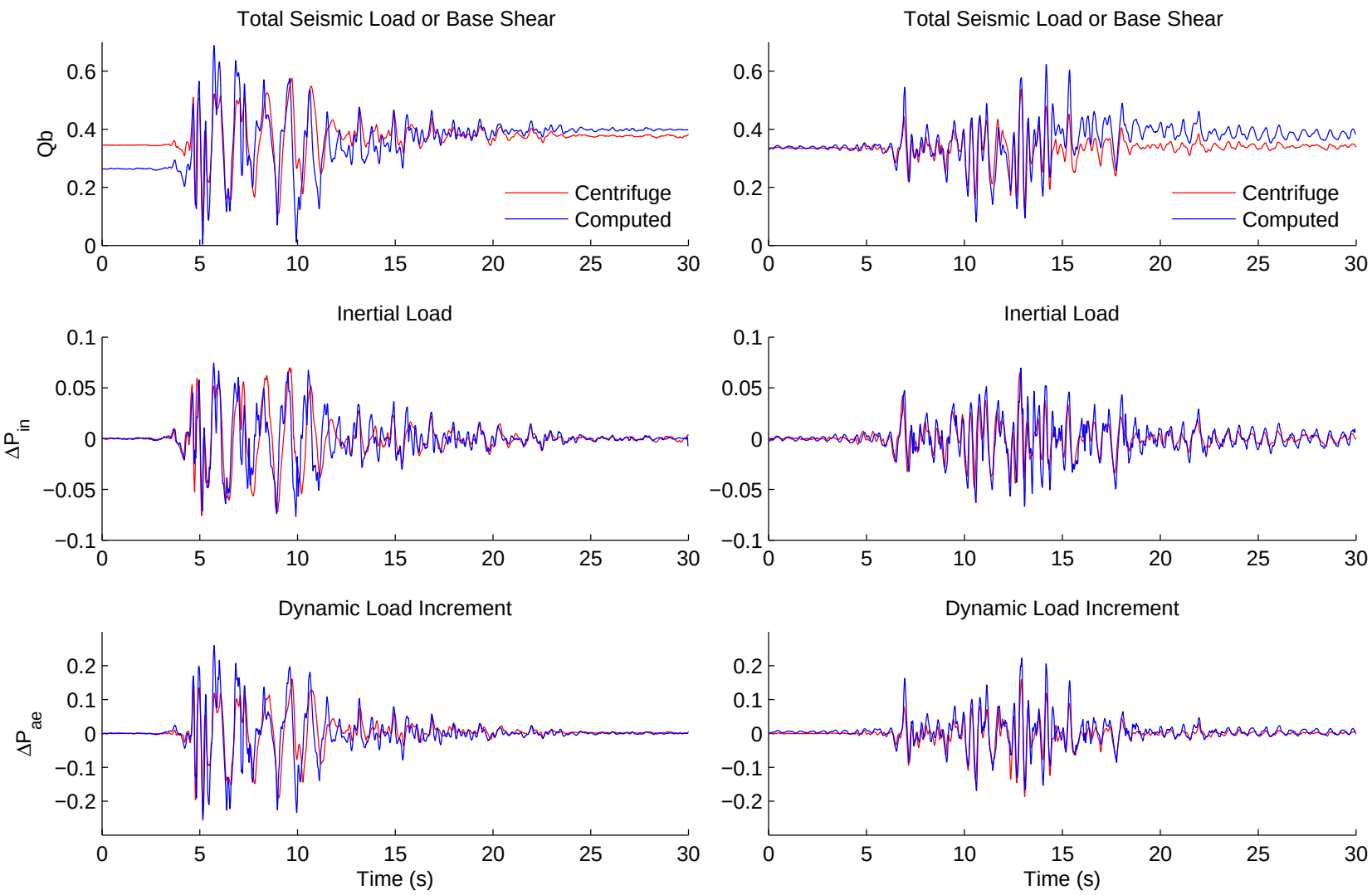

Figure 6.12 Comparison of measured and computed loads on the cantilever wall during Kobe TAK 090 (left) and Loma Prieta SC-1 (right). Loads normalized by $0.5\gamma H^2$.

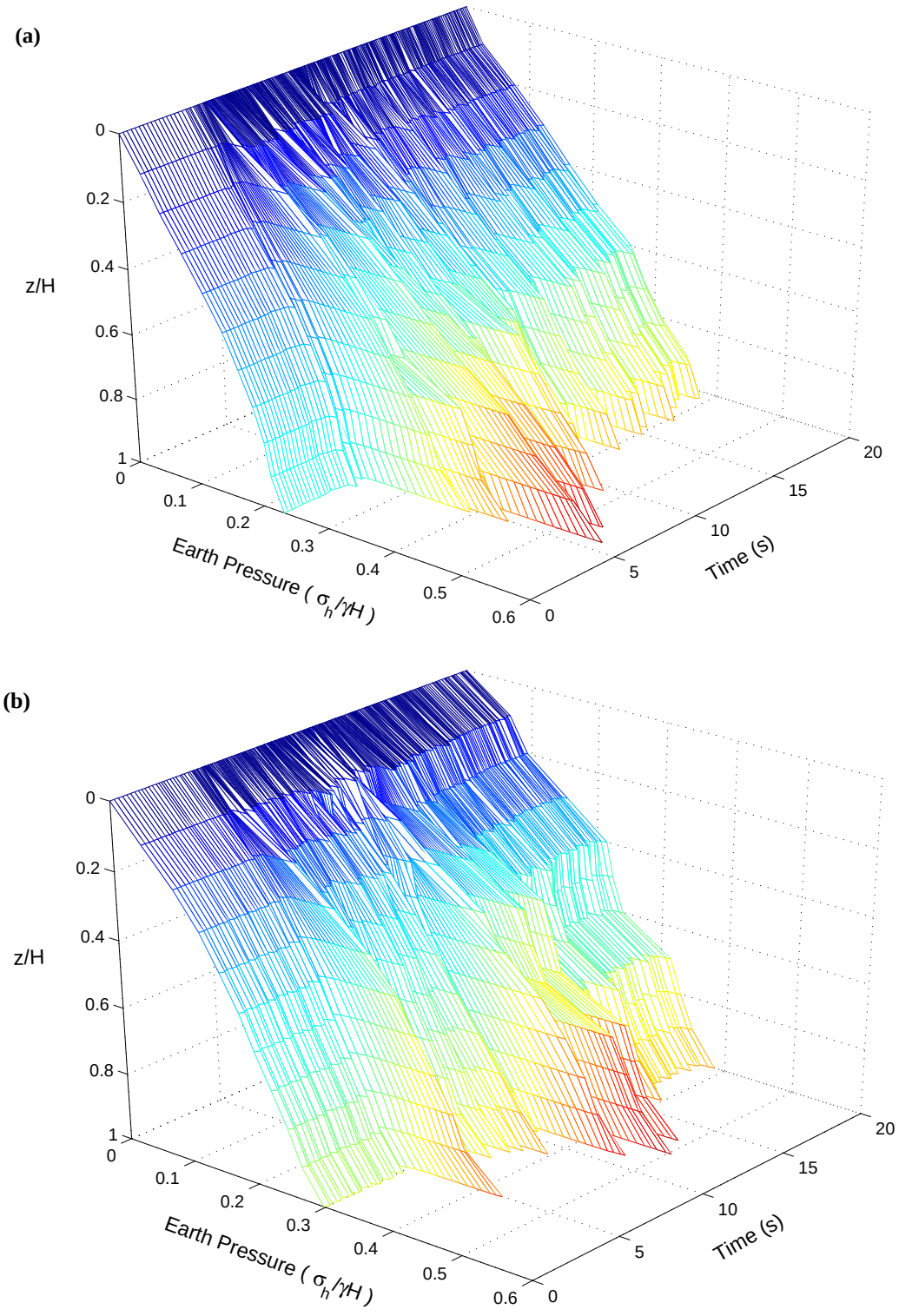

Figure 6.13 Evolution of computed seismic earth pressure distribution on the cantilever wall during (a) Kobe TAK 090-1 and (b) Loma Prieta SC-2.

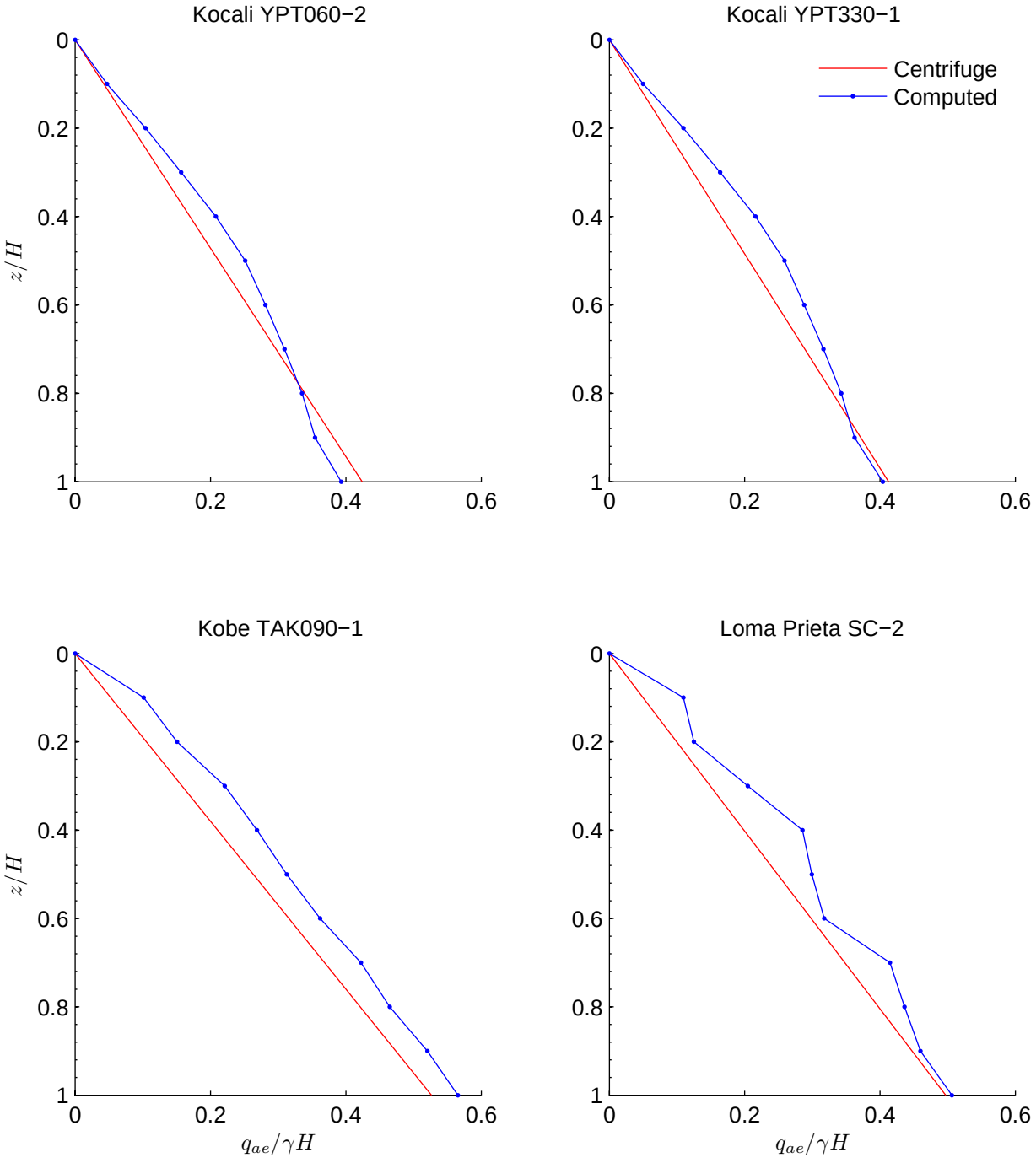

Figure 6.14 Comparison between the measured and computed total earth pressures on the cantilever wall at the time of maximum overturning moment.

6.6. Displacements and Deflections

Figure 6.15 presents a comparison between the measured and computed maximum wall deflections versus free field PGA. The computed deflections scale linearly with the free field acceleration and are in reasonable good agreement with the centrifuge data. The effect of the basement lateral stiffness, represented by the racking parameter $\alpha = I_{slab}/I_{wall}$, was evaluated numerically with the simplified model described in Section 6.7. As shown in Figure 6.15(a), if the basement is modeled with flexible cross bracing elements, the basement racking is five times higher than if the basement is modeled with more rigid cross bracing. Henceforth, the effects of stiffness reduction must be considered in future experiments to model the behavior of rigid culverts more accurately.

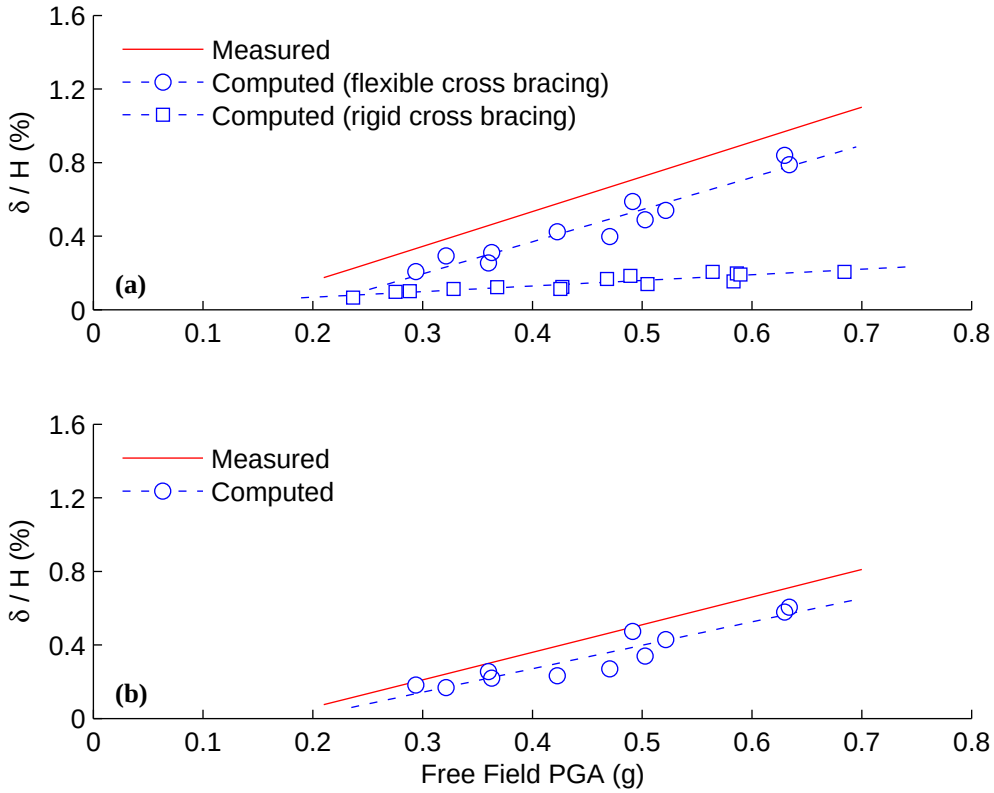

Figure 6.15 Measured and computed deflections in the (a) basement and (b) cantilever walls.

6.7. Simplified Basement Model

Based on the soil parameters and the basement dimensions described in Section 6.2, a simplified numerical model of the basement wall was developed to remove the boundary effects associated with the flexible shear beam container. The model discretization is perfectly symmetric, with periodic boundaries placed 30 m away from the basement, as shown in Figure 6.16. The basement was modeled using a stiffness parameter $\alpha = 1.0$, i.e., the moment of inertia of the

cross bracing and walls are the same. The input ground motion used in the analyses is the centrifuge record Loma Prieta SC-2 scaled at 40%, 70%, 100%, 130%, and 160% of the centrifuge motion.

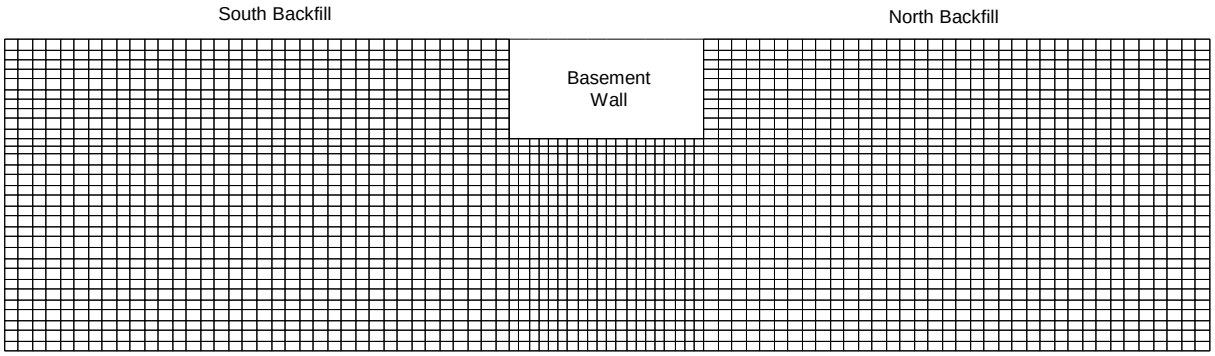

Figure 6.16 Cross section of simplified basement wall model.

As shown in Figure 6.17(a), the free field response spectra computed on either side of the basement are in excellent agreement with that recorded in the middle backfill of centrifuge model. This confirms that the response of the south backfill in the centrifuge was strongly influenced by the proximity of the container, as shown earlier in Figure 6.8. It also proves that centrifuge models can reproduce free field conditions quite accurately in a soil mass that is sufficiently far from the boundaries.

A sensitivity analysis was performed to study the effects of cohesion on the ground motion amplification and the results are presented in Figure 6.17(b) in terms of PGA_{ff} ratios versus input PGA. Note that with increasing cohesion, the soil dissipates less energy and yields to higher ground motion amplification at the free surface. This observation was confirmed after studying the hysteresis cycles of soil elements at different depths on a 1-D soil column. As seen in the stress-strain loops of Appendix Figure C.23, the soil with lower cohesion ($c/\gamma H=0.10$) has wider hysteresis cycles and larger residual strains, which helps to attenuate the ground motion at the free surface.

The sensitivity analysis was also used to study the effects of cohesion on the seismic earth pressure coefficient, ΔK_{ae}. The results are presented in Figure **6.**18 along with the centrifuge data and classic earth pressure theories. This plot shows that the soil cohesion has a minor effect on the seismic load increments. Moreover, combining the data from all numerical simulations, the coefficient ΔK_{ae} can be written as a function of PGA_{ff} as

$$\Delta K_{ae} = 0.66(PGA_{ff}/g - 0.10) \pm 0.07 \tag{6.6}$$

where ±0.07 represent the 95% confidence bounds. This equation is identical to the expression derived for the experimental data, therefore, the simplified basement model validates the results presented in the previous sections. Note that the upper confidence bound can simply be expressed as $\Delta K_{ae} \approx 0.66 PGA_{ff}/g$, which is equivalent to using Seed and Whitman's (1970) method with a design acceleration of 90% PGA_{ff}.

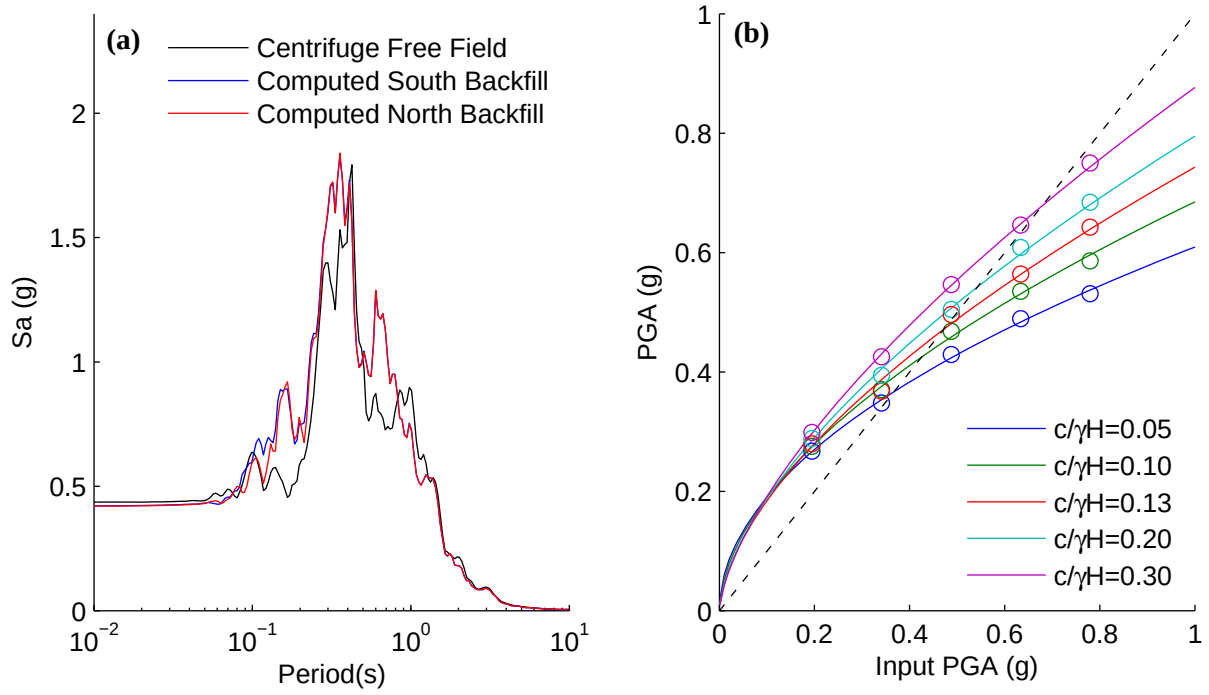

Figure 6.17 (a) Acceleration spectra at the free surface (ξ=5%) for c/γH=0.13, (b) Ground motion amplification as a function of input PGA and cohesion.

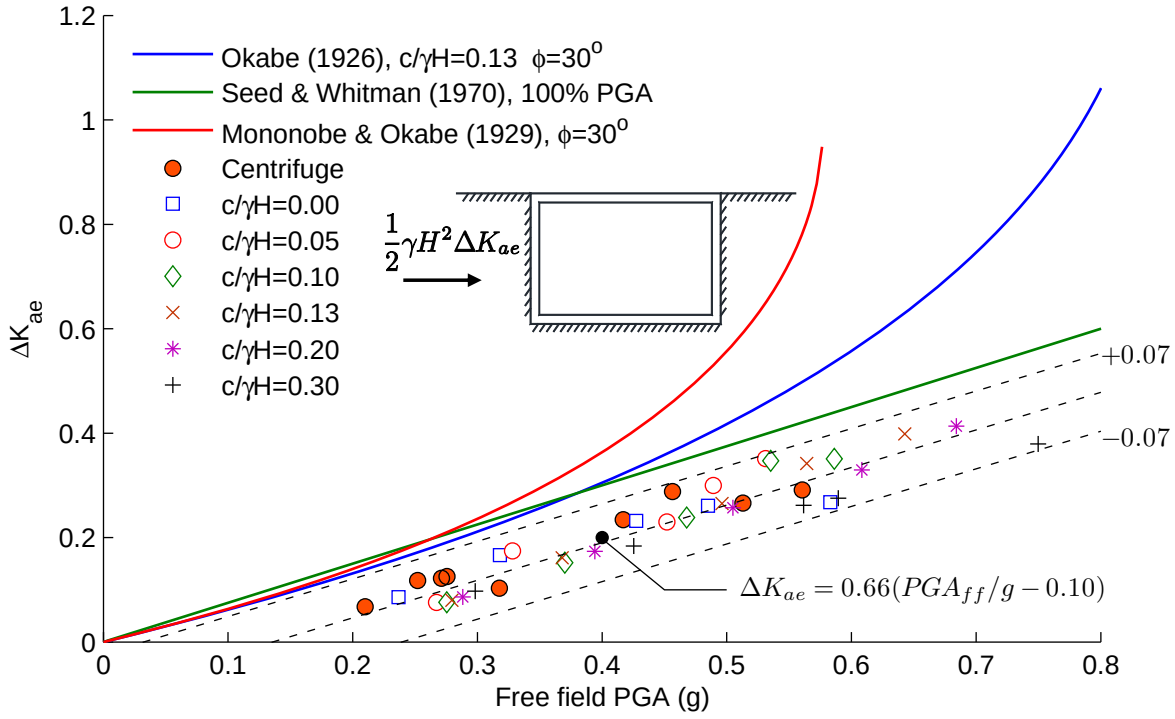

Figure 6.18 Dynamic load increments computed on the simplified basement model. Mean values and 95% confidence bounds shown as dashed lines.

6.8. Summary

Plain strain numerical simulations of the level ground centrifuge experiment GC01 were performed in FLAC$^{2\text{-}D}$ (Itasca, 2011). The model consisted of a 20 m deep deposit of compacted clay supported on stiff bedrock, a 6m basement wall and a 6m cantilever wall spaced apart 25 m from each other. The flexible container was added to simulate the boundary conditions existing in the experiment. The non-linear hysteretic relation UBCHYST was used to model the seismic response of the clay and its parameters were calibrated with laboratory experiments, the simulation of elements under cyclic shearing, and 1-D free field shear columns.

The numerical model captured the most important characteristics of the ground motion, namely acceleration histories, acceleration response spectra, frequency response, and special variability. In general, the computed soil response in the free field and the cantilever wall response were in good agreement with the measured behavior. However, the dynamic interaction between the model and the flexible boundary was not predicted accurately due to experimental difficulties and modeling uncertainties; for instance, the compaction induced stresses and the dynamic properties of the container were not fully characterized. The initial static loads on the basement wall could not be modeled accurately; nevertheless the dynamic load increments were similar in magnitude and comparable to centrifuge measurements. The effects of cohesion on the basement response were studied with a simplified model; as expected, soil deposits with higher cohesion yield larger ground motion amplification and a reduction on the static earth pressures, but the seismic load increments remain unaffected.

The computed static and seismic earth pressures increase monotonically with depth. For design purposes, the maximum horizontal stresses on the walls can be approximated by a linear distribution with the resultant applied between 0.35H-0.45H in the basement walls, and between 0.35H-0.40H in the cantilever walls. In contrast, current design methods like Seed and Whitman (1970) or Wood (1973) place the dynamic load increments near 0.6H and lead to significantly higher overturning moments.

Transient deflections in the basement and cantilever walls were found to be in good agreement with the centrifuge measurements. The numerical simulations verified that the basement configuration consisting on walls and struts significantly reduced its lateral stiffness and led to large basement distortions.

A summary of the dynamic earth pressure coefficients is shown in Figures 6.19 and 6.20 along with classic earth pressure theories. Combining the experimental and numerical results, the upper 95% confidence bound of ΔK_{ae} can be written as $\Delta K_{ae} \approx 0.68 PGA_{ff}/g$ in the basement wall, which is equivalent to using the Seed and Whitman (1970) method with a design acceleration of 90% of PGA_{ff} and the resultant applied at 0.35H-0.45H. Analogously, the upper confidence bound of ΔK_{ae} in the cantilever wall is $\Delta K_{ae} \approx 0.47 PGA_{ff}/g$, equivalent to using the Seed and Whitman solution with a design acceleration of 60% PGA_{ff} and the resultant applied at 0.35H-0.40H. Overall, the numerical simulations in FLAC$^{2\text{-}D}$ showed results consistent with experimental observations and allowed to study the backfill-walls interaction in great detail. In particular, the numerical models validated the empirical equations used in the experiment to deduct the wall inertial forces from load cells and strain gage data. These simulations can be improved if the soil is modeled with a constitutive relation that handles compaction, and if the

constitutive relation that handles compaction, and if the dynamic properties of the container, e.g. secant stiffness and hysteretic behavior of the rubber bearings, are accounted for.

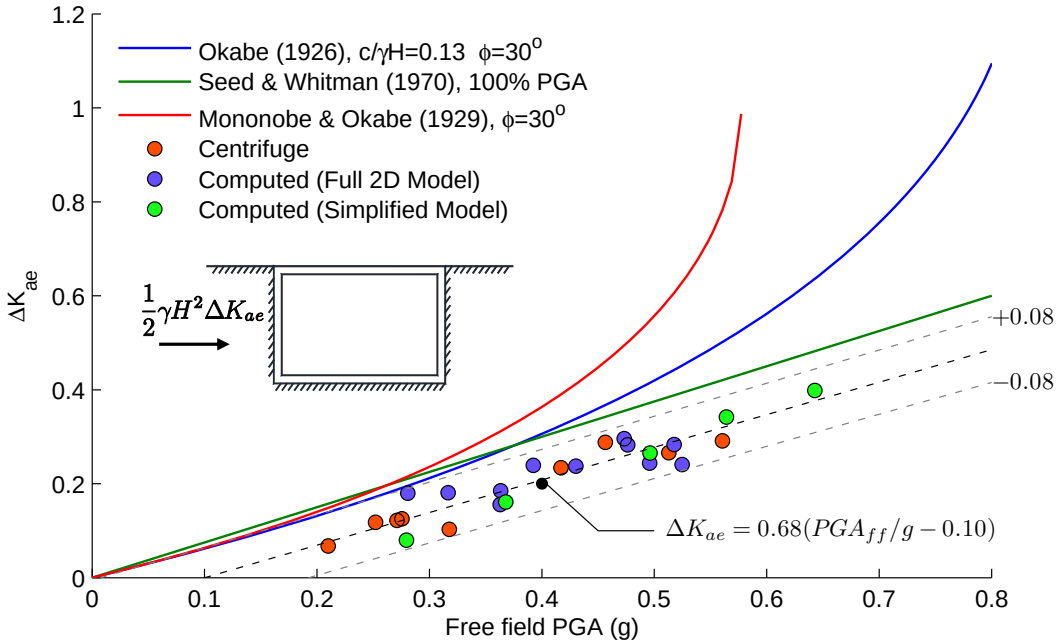

Figure 6.19 Dynamic load increments in the basement wall. Mean values and 95% confidence bounds shown as dashed lines.

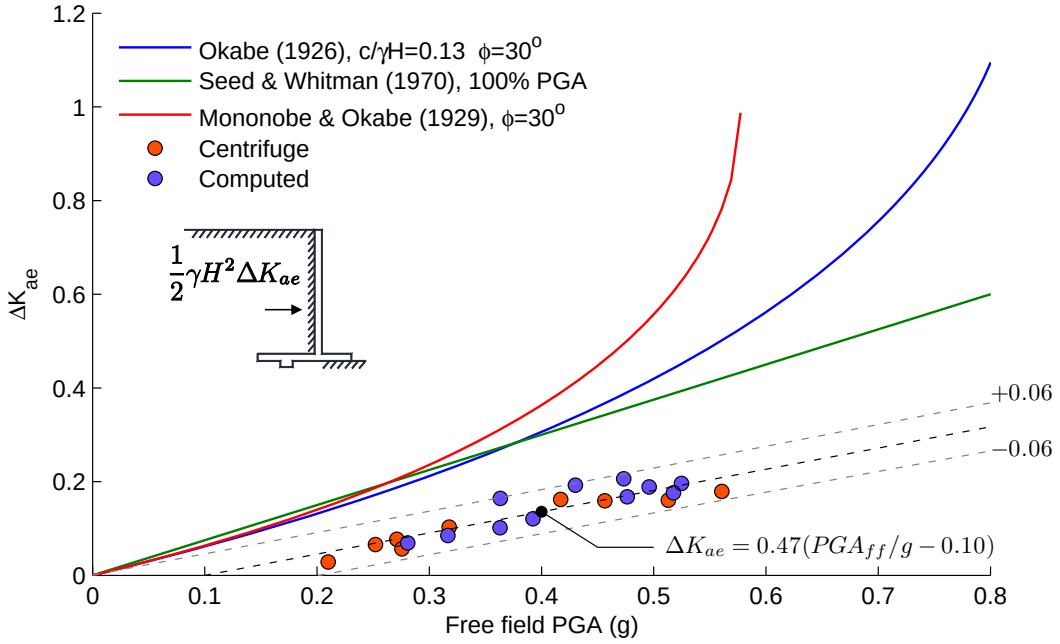

Figure 6.20 Dynamic load increments in the cantilever wall with horizontal backfill. Mean values and 95% confidence bounds shown as dashed lines.

7. ANALYSIS OF EXPERIMENT GC02 – SLOPING GROUND

Experiment GC02 was representative of a rather common situation with a slope rising beyond the retaining wall and as such offered an opportunity to compare non-linear numerical analyses with limit equilibrium based methods of slope stability analysis.

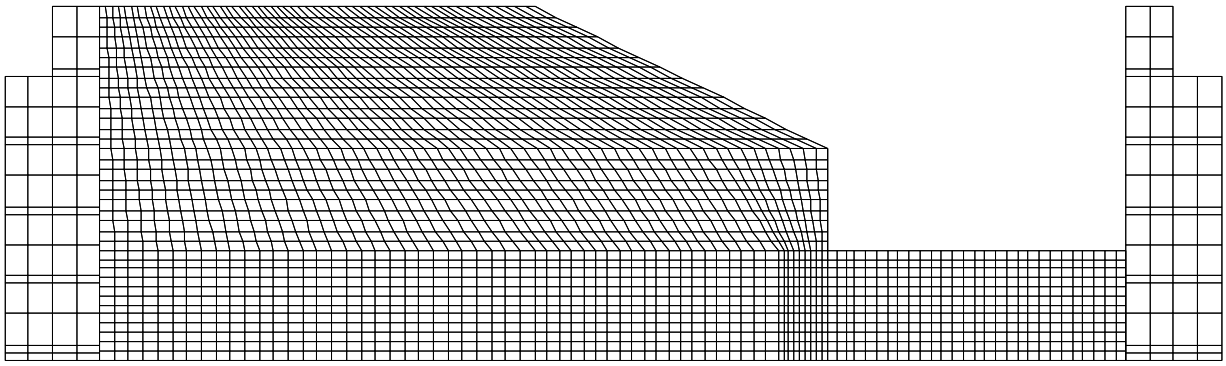

Figure 7.1 Grid discretization of retaining wall with sloping backfill.

7.1. Numerical Model Definition

Experiment GC02 was simulated in FLAC$^{2\text{-}D}$ using approximately 3500 zones for the soil, 12 beam elements to model the retaining wall, interface elements and a simplified plain strain model of the container, as seen in Figure 7.1. The guidelines used to defined the soil grid, the cantilever retaining wall, interface elements and boundary conditions of the current model are similar to those followed on the level ground model GC01 (Section 6.2). Total stress analysis was performed and the compacted unsaturated soil was modeled using the Mohr-Coulomb failure criterion with parameters $c = 45\ kPa$, ϕ=30^o, and no tensile strength. The small strain shear modulus was defined using Hardin's (1978) relationship

$$G_{max} = 625\frac{1}{0.3+0.7e^2}OCR^k\left(\frac{\sigma_m}{p_a}\right)^n p_a \tag{7.1}$$

with OCR=2, $e_0 \approx 0.5$, k=0.09 and n=0.5, and the Poisson ratio was defined using Seed and Duncan's (1983) empirical relation for compacted soils given by

$$\nu = \frac{1}{2}\left(\nu_o + \frac{1}{2}\right) = \frac{4 - 3\sin\phi}{8 - 4\sin\phi} \tag{7.2}$$

where $\nu_0 = K_0/(1 + K_0)$ and $K_0 = 1 - \sin\phi$. These elastic parameters yield a volumetric modulus in the order of 5 to 6 times G_{max}. The initial K_0-conditions in the model were determined by applying gravity on a level ground, then by excavating the soil and finally adding the retaining wall.

The shear modulus reduction at large strains was defined using Hardin and Drnevich's (1972) hyperbolic model and was calibrated to match with Darandeli's (2001) shear modulus reduction factors. The resulting damping ratio at large strains, however, was higher than published values as seen in Figure 7.2(a).

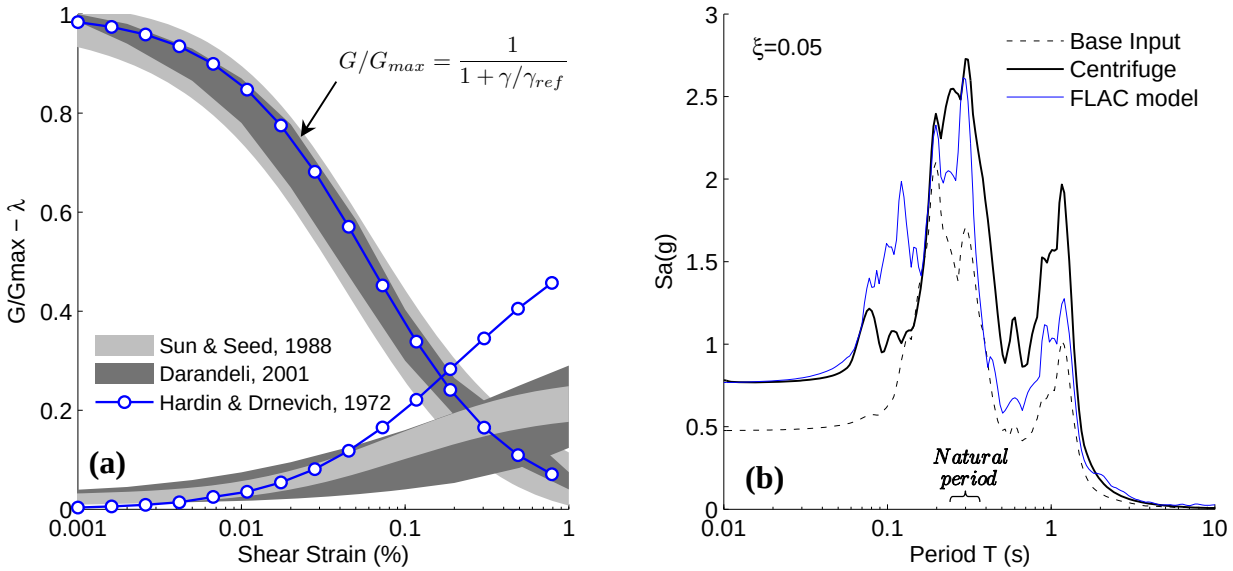

Figure 7.2 (a) Shear modulus reduction factor and damping ratio of a single element in simple shear (b) Measured and computed free surface response spectra for Kobe TAK090.

Two types of analyses were performed in this study to characterize the earthquake response of the slope and retaining wall: a pseudo-static slope stability analysis and a non-linear time history analysis. Four acceleration histories recorded at the base of the centrifuge model were used as input ground motions for the non-linear time history analysis: Kocaeli YPT330-1 (PGA=0.24g), Kocaeli YPT060-2 (0.40g), Loma Prieta WVC270-1 (0.57g), and Kobe TAK090-2 (0.66g).

7.2. Model Capabilities and Limitations

Overall, the non-linear time history analysis was able to reproduce the most important aspects of the centrifuge experiments, i.e. the seismic pressure increments, the ground acceleration, and the cantilever wall response. For example, a comparison between the recorded and computed acceleration spectra during Kobe is shown in Figure 7.2(b), with the corresponding ground motion time histories shown in Figure 7.3. These plots show that the numerical model captures

the essential characteristics of the ground motion like the free field acceleration, and spectral acceleration at different periods, especially near the natural period of the slope, estimated at ~0.3s. For a complete set of comparison figures with different ground motions, see Appendix D.

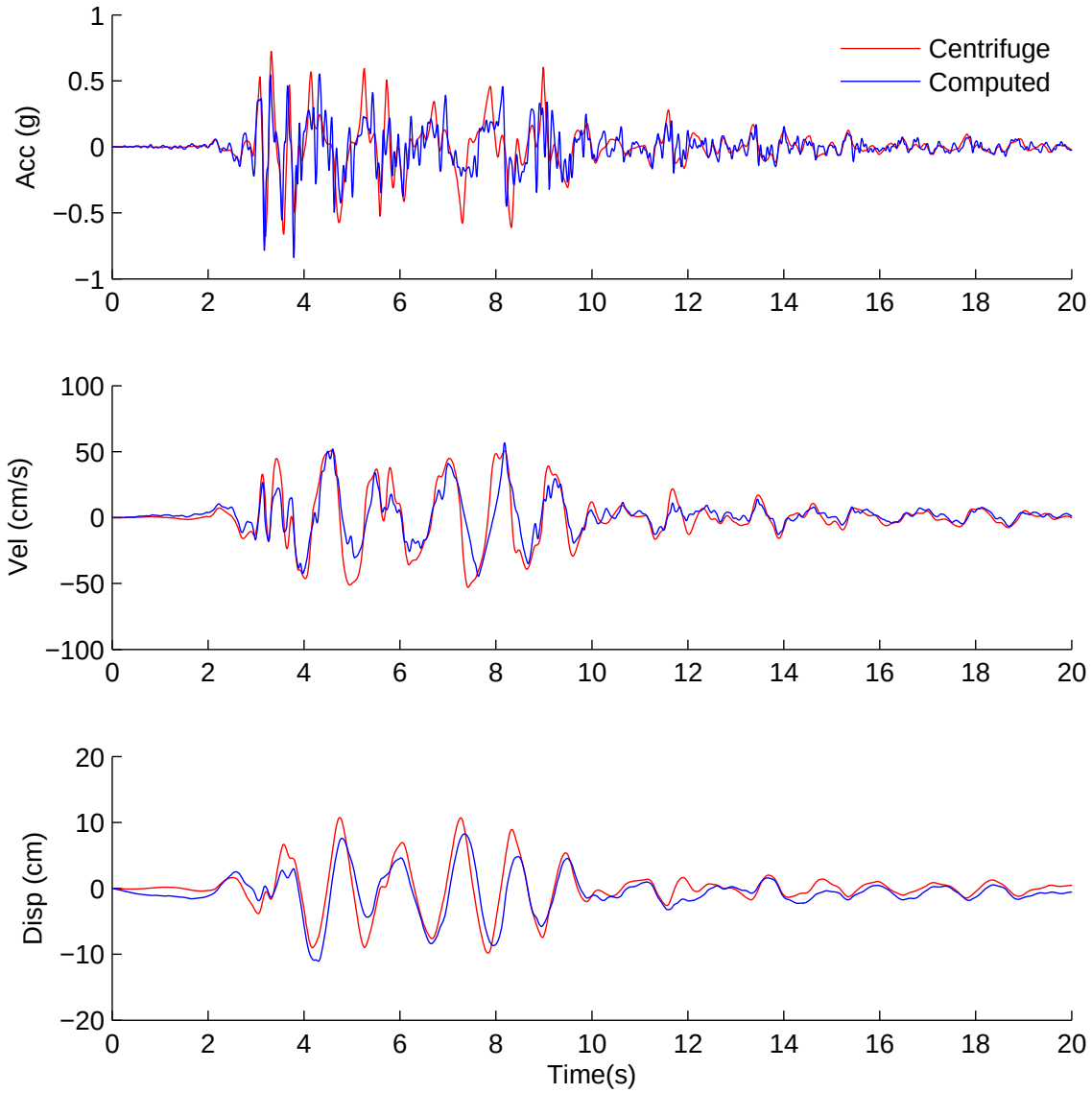

Figure 7.3 Comparison of free field acceleration, velocity, and displacements during Kobe TAK 090 in sloping backfill model GC02.

The earth pressure computed from the interface elements is initially zero due to the very small slope displacements induced by gravity. However, during the dynamic earthquake loading, the slope displaces and results in large residual stresses. The horizontal stress distribution varies with time, but it can be approximated as linear increasing with depth and the resultant applied at ~0.40H, as shown in Figures 7.4 and 7.5. Although the experimental results suggest that the point of application of seismic loads is 0.33H, the numerical results are consistent with Okabe's (1926) theory of earth pressures for sloping backfills, which predicts that the resultant should be applied approximately at 0.4H.

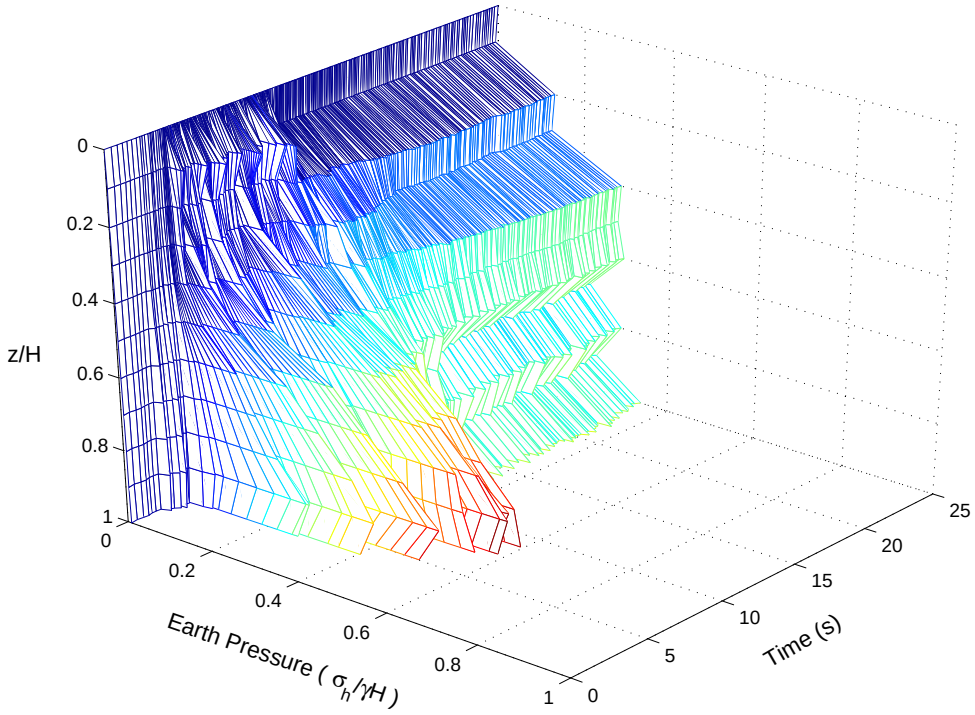

Figure 7.4 Evolution of computed seismic earth pressure distribution on the cantilever wall during Kocaeli YPT330-1

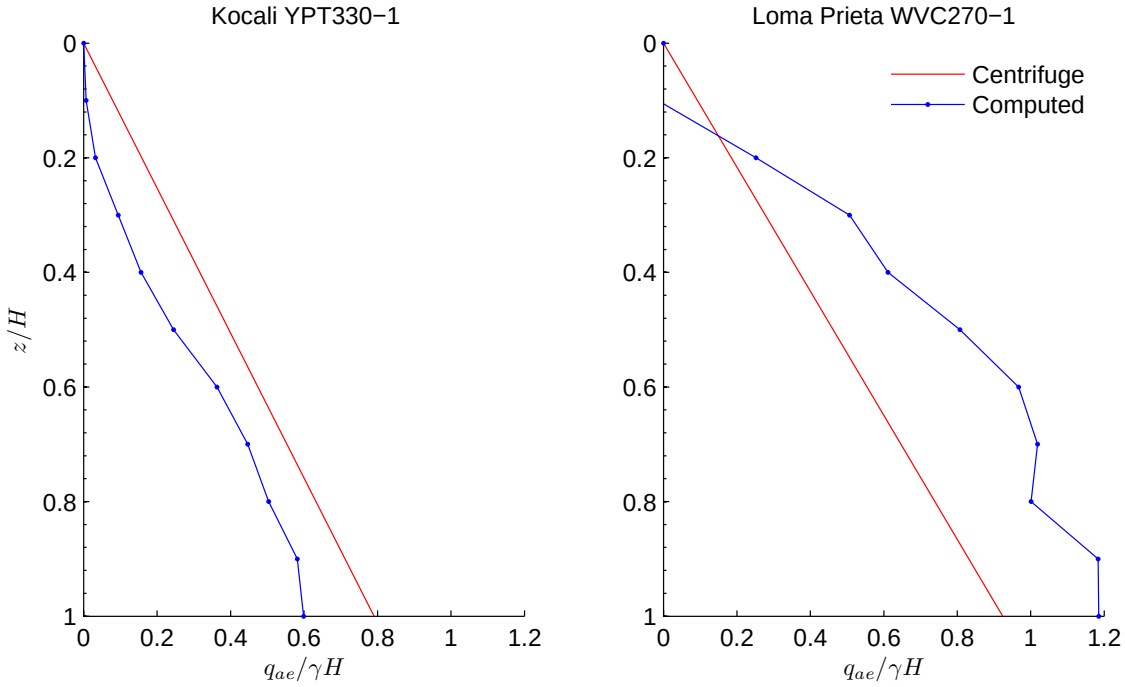

Figure 7.5 Comparison between the measured and computed total earth pressures on the cantilever wall at the time of maximum overturning moment.

The non-linear time history analysis also captured the trend of seismic load increments reasonably well, as shown in Figure 7.6. The plot shows that the computed ΔK_{ae} increases linearly with PGA_{ff} and is consistent with Okabe's (1926) Coulomb wedge analysis and Seed and Whitman's (1970) solution with a design acceleration of 100% PGA. Nevertheless, the residual slope displacements computed with this simplified numerical model were not consistent with the observed centrifuge performance. Due to the model asymmetry and the relative flexibility of the boundary elements, the slope developed plastic deformation towards both ends of the container. This issue is further discussed in Section 7.3, which presents the results of slope stability analyzes and the simplified procedure for computing the seismically induced slope displacements developed by Bray and Travasarou (2007).

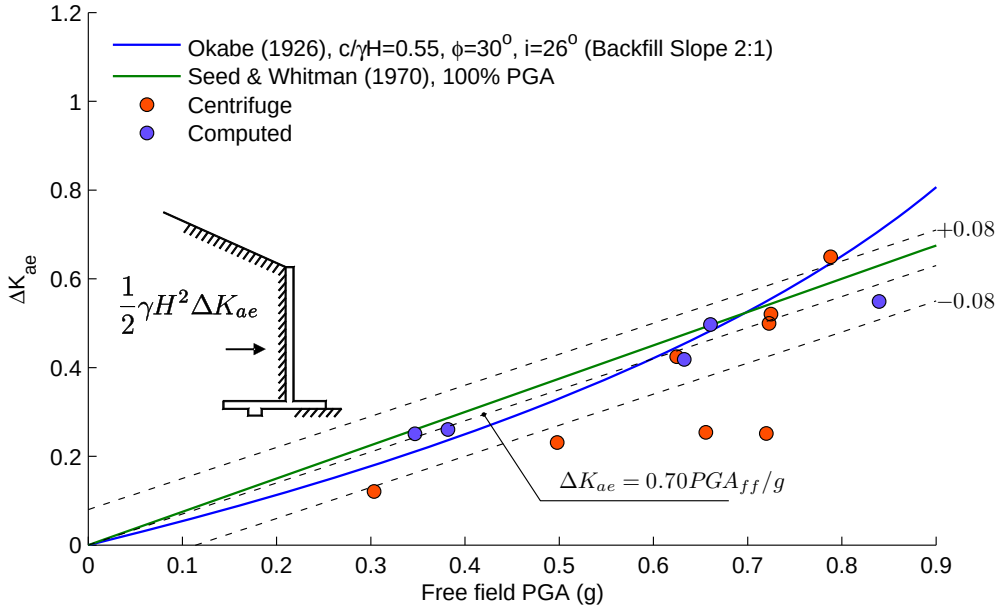

Figure 7.6 Dynamic load increments in the cantilever wall with a 2:1 backfill slope.

7.3. Slope Stability Analysis

A series slope stability analyzes were performed and the factors of safety were determined based on the 'strength reduction technique' (Dawson et. al, 1999). The clay in the sloping ground experiment GC02 was compacted near optimum so it would remain stable under gravity loads, even without the presence of the retaining wall. In these conditions, the predominant failure mode is a planar wedge passing through the toe with a factor of safety (FS) of 1.42. If the retaining wall is included, the FS increases significantly to 2.17 and the failure mode is a deep circle that passes under the wall foundation.

A pseudo-static analysis of the slope including the retaining wall shows that the yield acceleration is a_y=0.45g (i.e. horizontal ground acceleration that yields FS=1), with a failure surface that extends approximately 12 m behind the slope crest. The failure surface of the pseudo-static analyzes are shown in Figure 7.7. Further simulations using fixed boundary nodes showed that flexible container has no significant influence on the static response of the model.

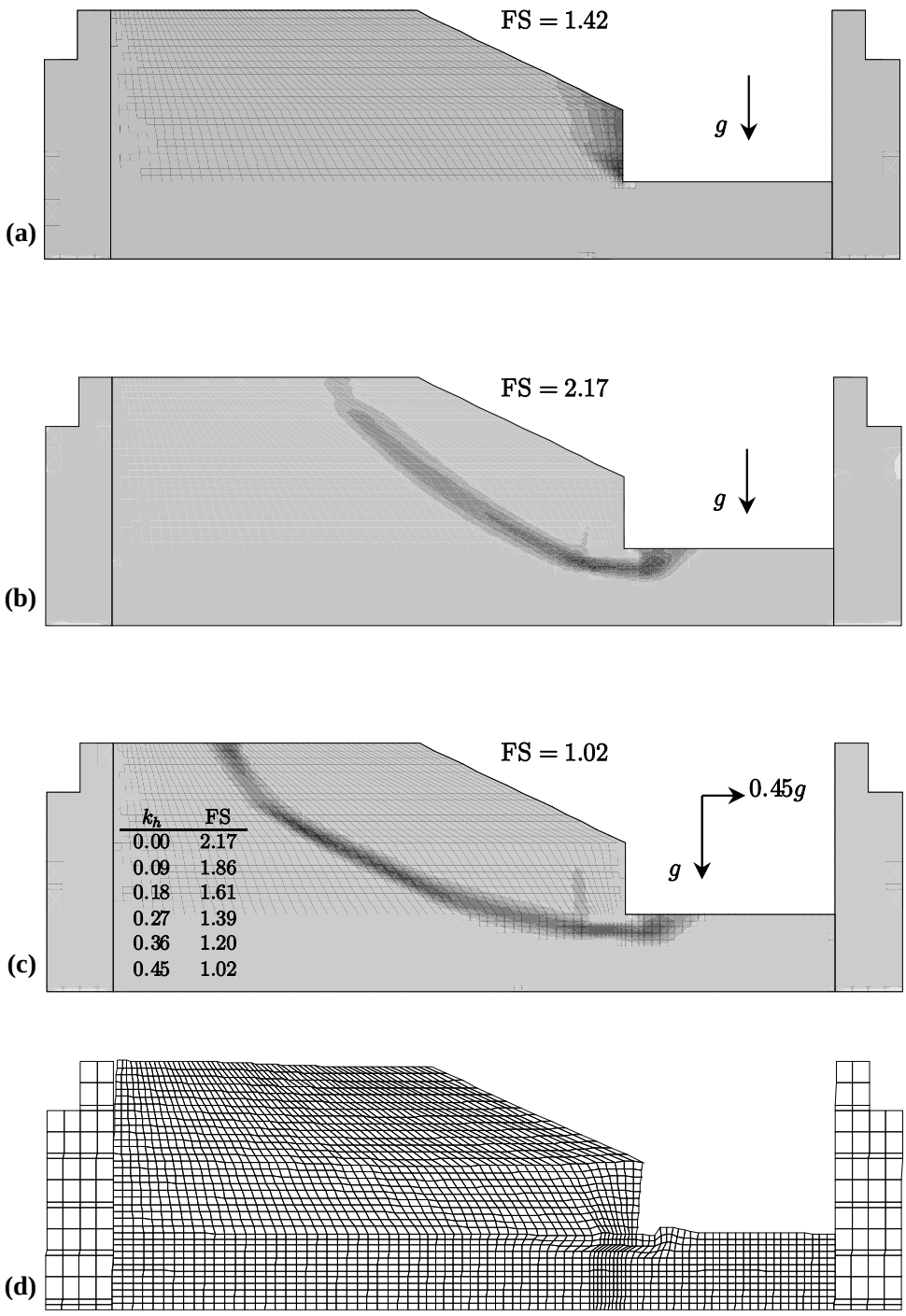

Figure 7.7 Factors of safety and failure surface under static conditions for (a) slope without retaining wall, (b) slope with retaining wall, and (c) slope with retaining wall and horizontal ground acceleration of a_y=0.45g. (d) Deformed model grid due to gravity loads and yield acceleration in a pseudo-static analysis. Displacements magnified 20 times.

7.4. Seismic Slope Displacements

The permanent slope displacements measured at the top of the cantilever wall were approximately 25 mm (prototype scale) after ten earthquakes were applied in the centrifuge. Although the dynamic simulations predicted accelerations in good agreement with centrifuge data, an accurate prediction of the residual displacements was not possible due to the large uncertainty on the model parameters, particularly regarding the behavior of the flexible container, and because the slope accumulated large plastic deformations in the direction of the container, as shown schematically in Figure 7.8. An independent assessment of the residual slope displacements was performed using the Bray and Travasarou's (2007) simplified semi empirical procedure. This method uses a fully coupled nonlinear frictional block model to simulate the seismic response earth dams, natural slops or landfills, and was been validated against several case-histories. Bray and Travasarou's (2007) displacement model is a function of the system's yield acceleration k_y, the natural period of the slope T_s and the pseudo acceleration at the degraded natural period $S_a(1.5T_s)$, and is given by

$$\begin{aligned}\ln(D) = &-1.10 - 2.83\ln(k_y) - 0.333(\ln(k_y))^2 \\ &+ 0.566\ln(k_y)\ln(S_a(1.5T_s)) + 3.04\ln(S_a(1.5T_s)) \\ &- 0.244(\ln(S_a(1.5T_s)))^2 + 1.50T_s + 0.278(M-7) \pm \epsilon\end{aligned} \tag{7.3}$$

where ϵ is normally distributed with zero mean and standard deviation σ=0.66. The yield acceleration was estimated in k_y=0.45, as discussed in Section 7.3, and the natural period was determined by applying an initial grid velocity of 0.01m/s and letting the model oscillate. As shown in the displacement transfer function of Figure D.6, the maximum amplification occurs at $T_s \approx 1/3.3$ Hz$\approx$ 0.3 s.

Equation 7.3 was evaluated for the 10 centrifuge ground motions and, in general, there is a good agreement with to the residual displacements measured using linear potentiometers. The results summarized in Table 7.1 show that the centrifuge data is within the 84th and 16th percentile displacement estimates. Overall, the measured and computed displacements can be considered as 'small' to 'very small'.

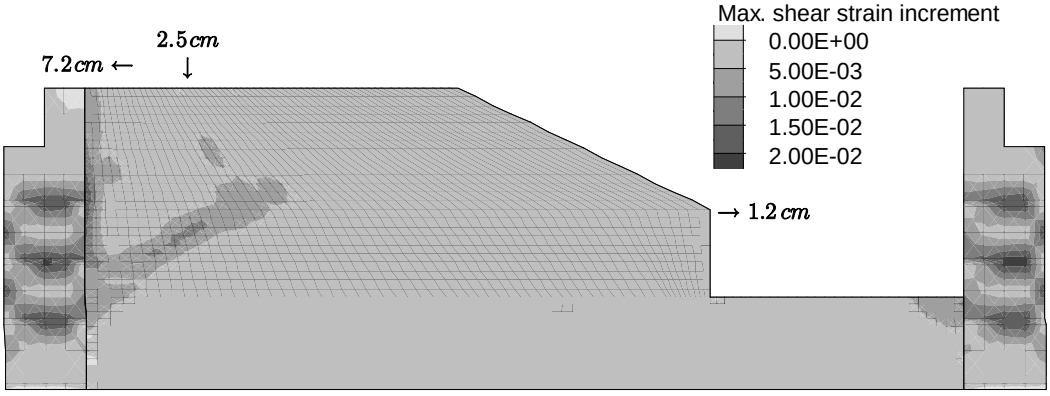

Figure 7.8 Contours of maximum shear strain after the ground motion Kocaeli YPT 330-1. Residual slope displacements (prototype scale) are indicated with arrows.

Table 7.1 Permanent slope displacements based on Bray and Travasarou's (2007) simplified procedure for k_y=0.45, T_s=0.3s and M=7

	Ground Motion		Slope Displacements			
Experiment: GC02 Ground Motion	PGA (g)	Sa(1.5T_s) (g)	Measured (cm)	P(D="0") -	D_{84} (cm)	D_{16} (cm)
1) Kocali YPT060 - 1	0.12	0.24	0.18	1.00	0.00	0.00
2) Loma Prieta SC - 1	0.41	0.55	0.06	0.88	0.05	0.05
3) Kobe TAK090 - 1	0.72	0.78	0.90	0.49	0.12	2.71
4) Kocali YPT330 - 1	0.24	0.26	0.31	1.00	0.01	0.01
5) Kocali YPT060 - 2	0.40	0.59	0.23	0.83	0.06	0.43
6) Loma Prieta WVC270-1	0.57	0.45	0.11	0.97	0.03	0.03
7) Kobe TAK090 - 2	0.66	0.77	0.18	0.50	0.11	2.62
8) Loma Prieta SC - 2	0.58	0.76	0.18	0.52	0.11	2.53
9) Kobe TAK090 - 3	0.86	1.10	0.42	0.10	1.79	9.00
10) Kocali YPT330 - 2	0.36	0.34	0.18	1.00	0.01	0.01

7.5. Summary

Non-linear static and dynamic analyzes of the sloping backfill experiment GC02 were performed in FLAC$^{2\text{-}D}$ (Itasca, 2011), with the soil modeled as Mohr-Coulomb material and the hysteretic behavior modeled with Hardin and Drnevich's (1972) hyperbolic model. A series of slope stability analyzes were performed to characterize the slope under static conditions. The results show that without the wall the slope is stable and has a factor of safety is 1.42. If the wall is included, the factor of safety is 2.17 and the failure surface is a deep circle encompassing the structure.

The non-linear dynamic analysis captured important aspects of the ground motion, namely acceleration histories, acceleration response spectra, and the seismic induced loads on the retaining wall. However, the seismically induced residual displacements were inconsistent with centrifuge measurements, due to the influence of the boundary elements. Alternatively, the slope displacements evaluated using the simplified procedure proposed by Bray and Travasarou (2007) were found to be in good agreement with the centrifuge data.

The computed earth pressures distribution on the cantilever wall increases monotonically with depth and the resultant acts near 0.40H, as predicted by the limit state theory proposed by Okabe (1926). The seismic coefficient ΔK_{ae} increases linearly with PGA_{ff} and can be approximated as $\Delta K_{ae} = 0.70 PGA_{ff}/g$, which is consistent with the load increments predicted by Okabe's (1926) model and the semi-empirical equation proposed by Seed and Whitman (1970).

8. CONCLUSSIONS AND DESIGN RECOMMENDATIONS

This study was aimed at the evaluation of the seismic response of retaining walls with cohesive backfills. To this end, two scaled centrifuge experiments were conducted at the Center for Geotechnical Modeling of UC Davis. The first model (GC01) consisted of a 6 m high basement wall and a 6 m high freestanding cantilever wall on level ground and founded on 13 m of soil. The second model (GC02) was a freestanding cantilever wall with a sloping backfill founded on 6.5 m of soil. The soil used in both experiments was a low plasticity clay with 15% water content, compacted to a dry unit weight that is, respectively, 90% and 99% of the maximum dry unit weight achieved with the Standard Proctor test (ASTM D698). The models were built in a flexible shear beam container, which allows a better simulation of free field conditions, and were subjected to several ground motions of varying intensity.
The centrifuge experiments GC01 and GC02 were then analyzed with the FLAC$^{2\text{-}D}$ finite difference code. The models were calibrated using the physical parameters determined through laboratory testing of samples. The experimental and numerical results presented herein provide an insight into the dynamic interaction between retaining structures and cohesive soil backfills, and provide data essential to guide the designers in the selection of dynamic pressure increments on retaining structures. The findings presented in this report are applicable to retaining walls with a height of 6.0 m ±0.5m, with a relatively stiff backfill.

8.1. Experimental Model GC01 – Level Ground

8.1.1. Acceleration and Displacements

The results show that the input motion is de-amplified in the soil beneath the structures and then is amplified in the backfill towards the free surface. Likewise, the ground motion measured at the top of the structures shows a consistent amplification of accelerations and a marked effect of the boundary conditions on the basement wall. A modal decomposition of the free field displacement on a vertical soil column indicates that the first and second modes contribute approximately 85% and 12%, respectively, of the total measured displacements.
The maximum rigid body displacements of the structures are very close to the horizontal backfill displacements and increase non-linearly with the free field PGA at the surface, referred herein as PGA_{ff}. In contrast, the basement racking and the cantilever wall deflections increase linearly with PGA_{ff} and represent approximately 30% of the total seismic displacement. Maximum seismic deflections can be approximated by $\delta/H=0.019(PGA_{ff}/g-0.10)$ for the cross-braced basement structures and $\delta/H=0.015(PGA_{ff}/g-0.16)$ for the cantilever wall. Based on the limiting displacements commonly assumed for compacted clay, as shown in Table 8.1, it is very likely

that the basement and cantilever walls developed minimum active earth pressures, however, there were no signs of any soil wedge development in the backfill.

Table 8.1 Approximate magnitude of movements required to reach minimum active and maximum passive earth pressure conditions (Source: Clough & Duncan, 1991)

Type of Backfill	Values of δ/H	
	Active	Passive
Dense sand	0.001	0.01
Medium-dense sand	0.002	0.02
Loose sand	0.004	0.04
Compacted silt	0.002	0.02
Compacted lean clay	0.01	0.05
Compacted fat clay	0.01	0.05

8.1.2. Earth Pressure Distribution

The use of load cells and strain gages in addition to pressure sensors was indispensable in the evaluation of the soil induced earth pressures on the basement and cantilever walls. Despite the difficulties encountered with the use of pressure sensors and their dynamic performance, the data from the experiments suggests that static and seismic earth pressures increase essentially linearly with depth, and thus, the point of application of the total seismic load is considered to be at 0.33H from the base of the walls. In comparison, the numerical model results suggest that the point of application of the dynamic earth pressure increment should be between 0.33 and 0.45 H, which is consistent with Okabe's (1926) conclusions. This result differs from the recommendations made by Seed & Whitman (1970), who suggested applying the dynamic load at 0.6H. A direct implication for engineering practice is that the moment demand at the base of the walls is reduced by as much as a factor of two. Similar results have been reported for retaining walls with cohesionless backfills in past centrifuge experiments (Ortiz, 1983; Al Atik & Sitar, 2010; Mikola & Sitar, 2013).

8.1.3. Basement and Cantilever Wall Responses

Measuring the interaction forces between the basement wall and the backfills continues to be a challenge. Since the magnitude of earth pressures could not be reliably determined with pressure sensors, the walls were connected with a system of struts and load cells that allowed measuring the net basement compression. Based on the force equilibrium in the horizontal direction, the resultant of earth pressures at the south and north walls were computed by subtracting and adding the inertial forces from the load cells. This idealized behavior was later validated with the numerical model and proved adequate to characterize the dynamic forces on the basement. Further analysis showed that when the seismic earth pressure on one side of the basement was at a local maximum, the pressure on the opposite side was at a local minimum. In addition, the measured phase difference between the basement compression and the inertial forces was approximately equal to the natural period of the backfill.

Analogous to the basement wall, a direct measurement of earth pressures in the cantilever wall based solely on pressure sensors was not possible. Instead, the earth pressures were interpreted from bending moments and inertial loads (see Section 3.9). The analysis showed that the wall inertial loads represent approximately 20% of the shear at the base of the stem. Since the natural period of the wall and backfill were similar, no significant phase differences were evident in the corresponding acceleration histories.

8.1.4. Dynamic Earth Pressure Increments

A summary of the dynamic earth pressure increments in the basement and cantilever walls is presented in Figures 8.1 and 8.2, respectively. Analytical solutions and the data from recent centrifuge experiments by Mikola and Sitar (2013) on dry Nevada Sand and are also included for comparison and completeness. As shown in these plots, the experimental ΔK_{ae} values increase linearly with PGA_{ff} and no significant differences were observed between cohesive and cohesionless backfills.

For basement walls, the dynamic earth pressure coefficient for both types of soils can be approximated by

$$\Delta K_{ae} = 0.68(PGA_{ff}/g - 0.10) \pm \epsilon \tag{8.1}$$

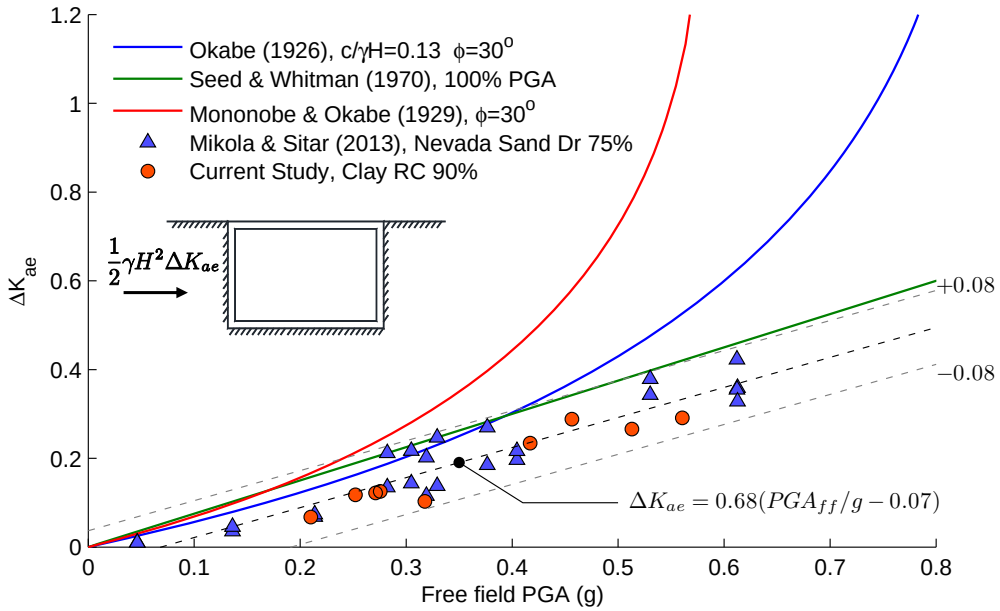

Figure 8.1 Comparison of the seismic coefficient on basement walls with experimental data on cohesionless backfills (from Mikola and Sitar, 2013).

where $\epsilon = 0$ represents the mean and $\epsilon = 0.08$ represents 95% confidence bounds. Note that the mean values are approximately one third of those given by Wood's (1973) solution as recommended in NEHERP for non-yielding walls. Likewise, the upper confidence bound can be approximated by $\Delta K_{ae} = 0.68 PGA_{ff}/g$ and is equivalent to using the Seed and Whitman's (1970) solution with 90% of the design acceleration with the resultant applied at 0.33H.

Similarly, the measured load increment for clay and sand (Mikola & Sitar, 2013) on the freestanding cantilever wall can be approximated by

$$\Delta K_{ae} = 0.42(PGA_{ff}/g - 0.15) \pm \epsilon \tag{8.2}$$

where $\epsilon = 0.07$ represents the 95% confidence bounds. The upper confidence bound can be expressed simply as $\Delta K_{ae} = 0.42 PGA_{ff}/g$, equivalent to using the Seed and Whitman's (1970) solution with 55% of the design acceleration. To account for the wall inertial loads, the dynamic coefficient can be increased by 20%. These load increments are significantly smaller compared to the M-O (1929) or Okabe (1926) with a design acceleration of 100% PGA.

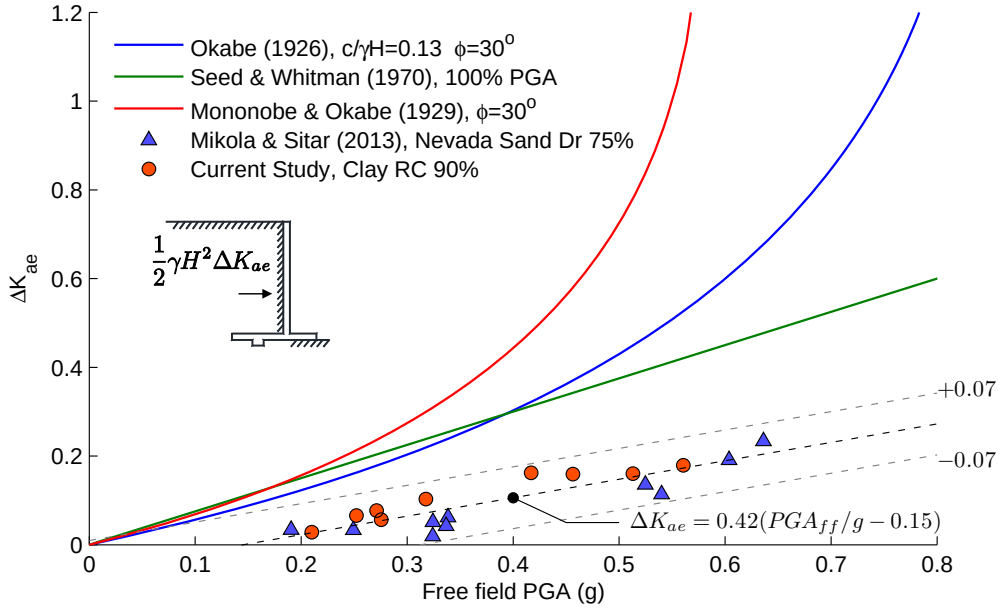

Figure 8.2 Comparison of the seismic coefficient on cantilever walls with experimental data on cohesionless backfills (from Mikola and Sitar, 2013).

8.2. Sloping Ground

8.2.1. Acceleration and Displacements

The model slope of the retaining wall had a static factor of safety of 2.2 and was quite stable under dynamic loading with free field accelerations up to 0.75g. The accelerations recorded at the free surface show that the input motion is amplified approximately by 50% in low intensity ground motions and 5% in strong ground motions. A similar trend was observed at different depths. The modal decomposition of the displacements shows that the soil responded primarily in the first mode, with a participation factor of 95%.

Large horizontal and vertical accelerations were recorded on the flexible container rings due to the mass asymmetry of the model and the lack of complementary shear stresses. Additionally, a 50% increase in base rotation was noted with respect to the 'symmetric' model GC01.

The settlements of the free surface were negligible and the profiles of maximum dynamic displacements recorded on the slope were similar to the profiles of free field displacements. No evidence of topographic amplification was detected in the acceleration response of the slope crest. Transient wall deflections interpreted from strain gages show that maximum displacements increase linearly with PGA_{ff} as $\delta/H = 0.011(PGA_{ff}/g - 0.22)$. Permanent slope displacements were approximately 25 mm in prototype scale after a series of ten earthquakes, with the maximum displacements triggered by the Kobe TAK090-1 earthquake.

8.2.2. Dynamic Earth Pressures Increments on a Cantilever wall with Sloping Backfill.

The dynamic earth pressures were interpreted from the strain gages and inertial loads based on the dynamic equilibrium of horizontal forces. The dynamic earth pressures versus PGA_{ff} shows some scatter for strong ground motions as seen in Figure 8.3, however, the upper bound of the data increases linearly with PGA_{ff} and is reasonably well approximated by Okabe's (1926) method or Seed and Whitman's (1970) method with $\Delta K_{ae} = 0.70 PGA_{ff}/g$ and the resultant applied at 0.33H.

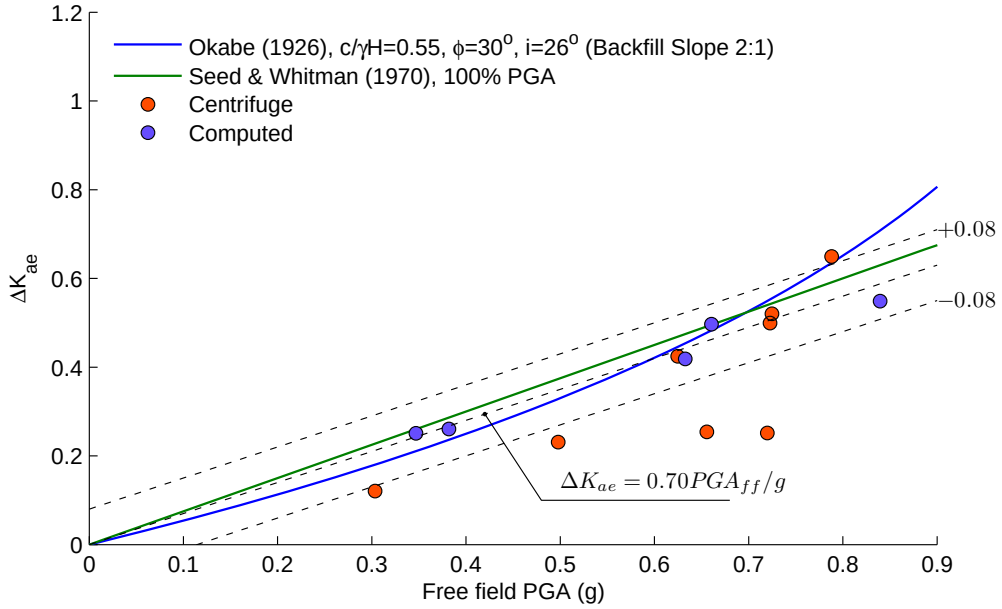

Figure 8.3 Dynamic load increments in the cantilever wall with a 2:1 backfill slope.

8.3. Numerical Modeling

Plain strain numerical models of centrifuge experiments GC01 and GC02 were performed using FLAC$^{2\text{-}D}$ (Itasca, 2011). The numerical models were able to accurately reproduce fundamental responses of the experiments including, but not limited to, the ground motion propagation through the soil and structures, acceleration time histories, free field displacement and acceleration profiles, and the dynamic response of the retaining walls. However, the 'K_0-conditions' and residual slope deformations were not fully captured in FLAC$^{2\text{-}D}$ due to uncertainties in key aspects of the model (e.g. heterogeneity of soil properties, interfaces element

parameters, behavior of boundary elements, basement configuration, etc.) and the simplified procedure used to account for compaction of the soil. In spite of these limitations, the seismic load increments on the retaining structures are in good agreement with the experimental data.
Due to modeling uncertainties of the basement wall, a sensitivity analysis was performed to study the effects of boundary conditions, varying soil properties and basement configuration. The analysis shows that the basement racking is reduced with increasing lateral stiffness, but its effects on the dynamic earth pressures are not significant. Similarly, dynamic earth pressures showed only a slight variation with soil cohesion.
The sloping backfill experiment GC02 was modeled in FLAC$^{2\text{-}D}$ using Mohr-Coulomb failure criterion and hysteretic damping to account for energy dissipation in the soil. A series of slope stability analyses showed that the slope without the wall is stable under gravity loads and has a Factor of Safety (FS) of 1.4 against sliding of a shallow wedge on the vertical cut. If the retaining wall is included in the analysis, the FS increases to 2.2, and the critical failure mode is a deep circle that passes below the foundation and extends past the slope crest. The permanent slope displacements predicted by the numerical model were generally higher than experimental observations and showed significant scatter. A comparison with the simplified Bray and Travasarou (2007) method showed that the 50th and the 16th percentile displacement estimates are reasonable bounds to the displacements measured in the experiments.

8.4. Influence of Cohesion

The effects of cohesion were part of Okabe's General Theory of Earth Pressure (Okabe, 1926) and have been further studied by several authors (Prakash & Saran, 1966; Chen & Liu, 1990; Richards & Shi, 1994). Yet, a major issue is the lack of well-documented case histories and experimental results that validate their basic assumptions. Moreover, due to uncertainties in the magnitude of cohesion, a common practice by geotechnical engineers is to neglect the effects of cohesion and use design methods developed, in principle, for cohesionless soils. A recent NCHRP report (Anderson et al., 2008) provides guidelines to account for cohesion in practical design problems, and suggests the use of seismic coefficient charts as in Figure 8.4(a). The seismic coefficient K_{ae} can be further split into its inertial component $N_{a\gamma}$ and cohesion component N_{ac}, as shown in Figure 8.4(b). These plots were developed using Okabe's trial wedge approach and show that the seismic loads are reduced by 50% to 75% for typical design conditions (e.g. $c/\gamma H \approx 0.1$). However, this solution has limitations in practical cases involving compacted backfills or displacing structures. For instance, on highly cohesive soils the mobilized shear strength could be greater than the inertial forces, leading to 'zero' dynamic earth pressures and potentially unsafe designs. In such cases, it is convenient to separate the total seismic loads into static and dynamic components and compute them independently, as suggested by Seed and Whitman (1970).
The experimental and numerical results presented herein show that the dynamic component of the seismic load is relatively independent of cohesion and increases linearly with PGA_{ff}. However, it still remains necessary to obtain a reliable assessment of the static or K_0-conditions, which take into account the initial wall displacements, over-consolidation, and compaction induced stresses (see e.g. Duncan and Seed (1986), Duncan et.al (1991), and Clough and Duncan (1991)). For design purposes, a seismic load that increases linearly with PGA_{ff} is equivalent to fixing the geometry of the seismic wedge; this is contrary to the assumptions of most limit state

methods, in which the wedge geometry is a function of the ground acceleration. The centrifuge experiments suggest that the point of application of the total seismic load acts at 0.33H, which is consistent with the observations made by Al Atik and Sitar (2010), and Mikola and Sitar (2013) in cohesionless soils, while Okabe's (1926) theory and the numerical simulations show the point of application should be closer to 0.4H.

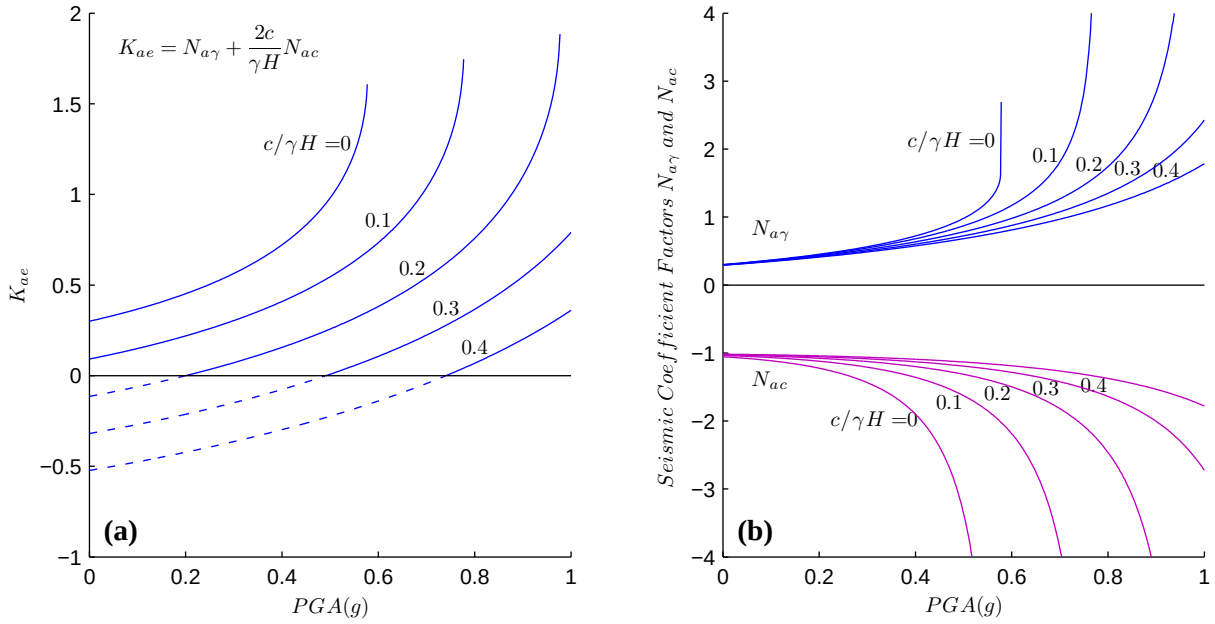

Figure 8.4 (a) Seismic coefficient for cohesive soils with ϕ=30° and level backfill, (b) Seismic coefficient separated into the inertial component $N_{a\gamma}$ and cohesion component N_{ac}.

8.5. Design Recommendations for the Cases Analyzed

The observations from the centrifuge experiments and numerical simulations presented herein provide essential information to guide the designers in the selection of seismic loads on earth retaining structures with cohesive backfills. The results consistently show that the dynamic load increases linearly with the free field PGA, and that the earth pressure distribution varies linearly with depth. Following the same notation as Seed and Whitman (1970), the total seismic load is the sum of a static and dynamic load increment as follows

$$P_{ae} = P_{static} + \Delta P_{ae} \tag{8.3}$$

A key parameter in this equation is the static load, which must take into account not only the backfill strength properties but also the wall displacements, previous stress history and compaction induced stresses. For instance, in free standing cantilever walls with level ground and naturally deposited backfills, P_{static} typically has a value between active and at-rest conditions. For basement walls or braced excavations, P_{static} can be determined using Mayne and Kulhawy's (1982) equation for the at-rest coefficient $K_{0u} = K_{0nc} OCR^{sin\phi'}$. Similarly, the compaction induced stresses can be determined using the simplified charts developed by Clough

and Duncan (1991), which take into account the different compaction equipment. An example of the post-compaction earth pressures is shown in Figure 8.5. In the case of retaining walls with sloping backfill the static loads should be derived from a slope stability analysis, since traditional limit state methods provide no information with respect the local or global stability of the system. The factors of safety and the critical failure paths should be identified for two conditions: slope without a wall and slope with a wall under gravity loads.

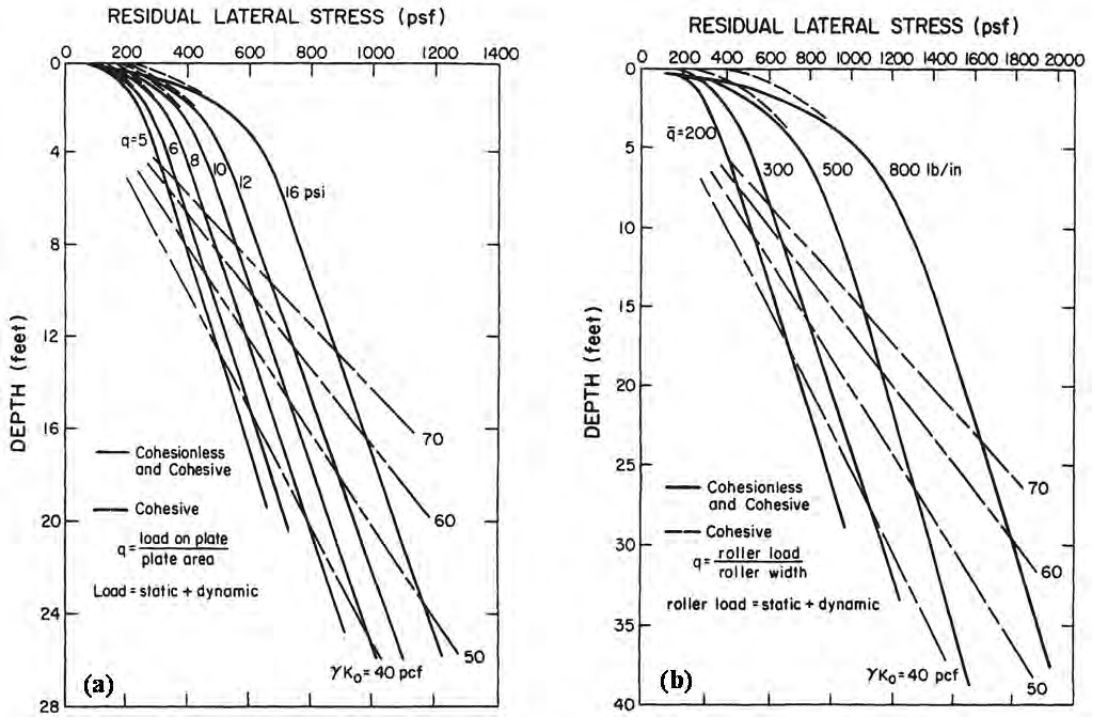

Figure 8.5 Residual stresses in cohesive and cohesionless soils after compaction (a) by vibratory plates, and (b) by rollers (Source: Clough & Duncan 1991).

The term ΔP_{ae} on Equation (8.3) is a function of the structure's ability to accommodate permanent displacements and is a linear function of the peak ground acceleration. For the different configurations studied, the dynamic load increment can be computed as

$$\begin{aligned} &Basement\ wall\ on\ level\ ground && \rightarrow \Delta P_{ae} = \tfrac{1}{2}\gamma H^2(0.68\, PGA_{ff}/g) \\ &Cantilever\ wall\ on\ level\ ground && \rightarrow \Delta P_{ae} = \tfrac{1}{2}\gamma H^2(0.42\, PGA_{ff}/g) \\ &Cantilever\ wall\ with\ sloping\ backfill && \rightarrow \Delta P_{ae} = \tfrac{1}{2}\gamma H^2(0.70\, PGA_{ff}/g) \end{aligned} \tag{8.4}$$

Additionally, for retaining walls with sloping backfill the seismic slope displacements should be evaluated using simplified methods, such as Bray and Travasarou (2007), and compared to the acceptable performance.

Although the experimental data was not sufficient to accurately determine the point of application of the seismic loads (h_c), the current numerical models and Okabe's (1926) theory suggest that with increasing cohesion the resultant acts at a point higher than 0.33H. An exact analytical expression was proposed by Okabe (1926), however, this equation is not practical for

design purposes, since it requires the evaluation of the critical wedge angle. Alternatively, a simplified equation is proposed herein for computing the location of the seismic load on vertical walls in level ground and with sloping backfill (see derivation in Appendix E):

$$\frac{h_c}{H} = \frac{1}{3} + \frac{\tilde{c}}{6\tilde{c} + 2k_h + 1.5(1-\sin\phi)/\cos(\phi)} \tag{8.5}$$

where $\tilde{c} = c/\gamma H$ and $k_h = PGA/g$ are dimensionless coefficients. Note that for cohesionless soils this equation yields $h_c = 1/3H$, and for typical cohesion values, e.g. $\tilde{c} \approx 0.1$, h_c varies between 0.37H-0.40H. Combining Equations (8.3) and (8.5), the total moment on the base of the retaining structures can be computed as

$$M_{ae} = P_{ae}\, h_c \tag{8.6}$$

While the resultant acts at a point higher than H/3 on cohesive soils, the total moment is reduced due to the significant reduction in the total load P_{ae}, particularly for large ground accelerations. As noted by Clough and Fragaszy (1977), conventional factors of safety used in static analysis provide the structures with substantial strength reserve to resist strong earthquakes, which suggests that additional seismic loads are unnecessary in some cases. Based on a simplified analysis, Seed and Whitman (1970) determined the strength reserve of a retaining wall as a function of the static coefficient K_a and the static and dynamic factors of safety as $\Delta K \approx K_a \cdot (FS_s/FS_d - 1)$.

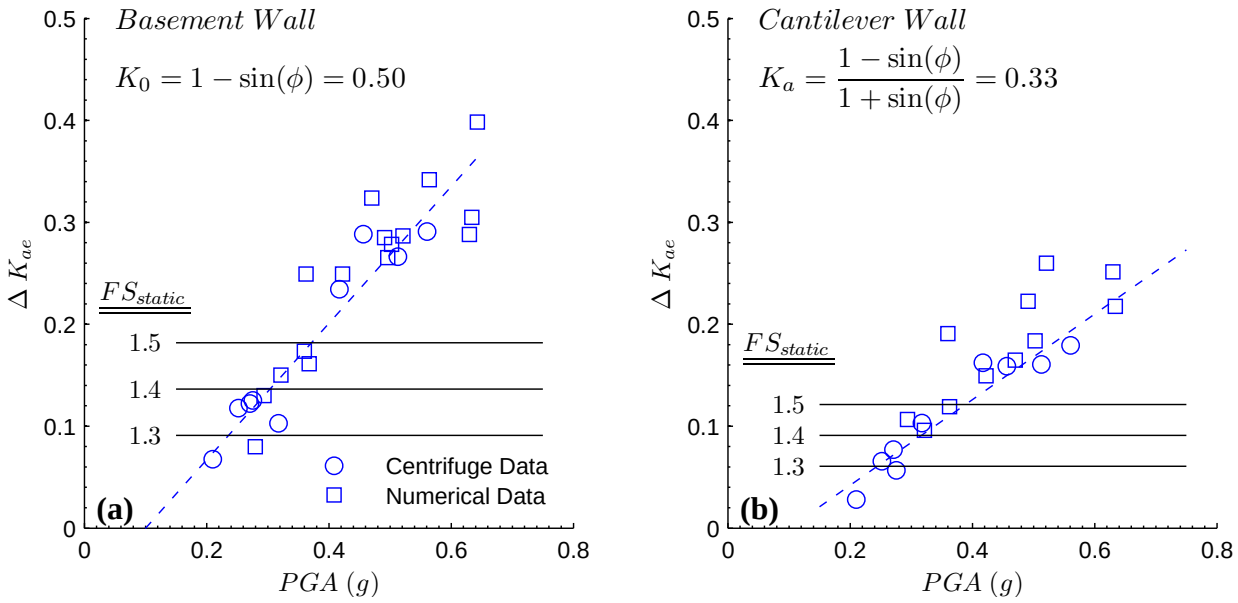

Figure 8.6 Seismic load increments in the basement and cantilever walls. Load increments below the FS_{static} lines need not be included in the wall design.

For the current experimental and numerical data, this basic analysis shows that if the walls are designed with a static factor of safety 1.5, the seismic load increments can be omitted in the design for accelerations up to 0.4g, as shown in Figure 8.6. Similar recommendations were made by Al Atik and Sitar (2010) and Geraili and Sitar (2013) based on centrifuge experiments with cohesionless soils, and are consistent with the recommendations made by Seed and Whitman (1970) and with the observed performance of retaining structures in recent strong earthquakes in Chile (2010) and Japan (2011).

8.6. Limitations and Suggestions for Future Research

The experimental program provided invaluable insights into the seismic behavior of retaining walls with cohesive backfills. To understand the applicability of these results and to assist in future research, the limitations and issues encountered during the execution of the experiments are discussed herein.

- **Pressure sensors:** One of the goals of the experimental phase was to measure earth pressures on the walls directly using pressure sensors. Despite their small size, the sensors were extremely sensitive to the effective contact area (unknown) and consequently, the baseline of static pressure was not well defined. Thus, pressure sensors should be calibrated in flight with the model in its final construction stage if at all possible.
- **Model Layout**: In the level ground experiment, the location of the basement near a free standing cantilever wall and adjacent to the flexible container introduced errors in the measurements, particularly on the south basement wall. The permanent displacement of the free field towards the north caused a reduction of the static stresses on the basement. In addition, the dynamic response of the container induced larger load increments on the south. Thus, it is recommended in future experiments to work with symmetric models, placing the structures far from the boundaries.
- **Model symmetry:** Experiment GC02 had the center of mass shifted from the geometric center. Additionally, the complementary shear stresses were not balanced, which induced spurious vertical accelerations and base rotations. It is recommended for future tests that the any mass asymmetry be properly compensated, so that the geometric and mass centers are aligned. For instance, in experiment GC03 (retaining wall on piles with level ground, Figure 8.7) the weight of the excavated soil in front of the wall was replaced with steel blocks located inside the container.
- **Model configuration:** More experimental data is required to study the seismic earth pressures of soils with different cohesion and different model geometries. This research focused on 20 ft basement and cantilever walls with a silty-clayey backfill founded on 13 m of soil, and a cantilever wall with a 2:1 slope and a backfill founded on 6 m of soil.

Figure 8.7 Construction of asymmetric model GC03 with counter weights placed inside the container.

- **At-rest conditions:** The construction sequence of the centrifuge model and the instrumentation should be properly designed for a better control over the initial at-rest stresses. In the present experiments, the initial stresses acting on the walls were an experiment outcome. Future experiments of retaining walls should consider filling the container with soil, run the model through medium intensity ground motions to densify the soil and then excavate the openings.

References

1. Al Atik, L., & Sitar, N. (2010). Seismic earth pressures on cantilever retaining structures. Journal of Geotechnical and Geoenvironmental engineering, 136(10), 1324-1333.
2. Anastasopoulos, I., Gazetas, G., & Psarropoulos, P. N. (2004). On the seismic response of flexible retaining structures. In Proc. 11th Int. Conf. On Soil Dynamics and Earthquake Engineering–Proc. 3rd Int. Conf. On Earthquake Geotechnical Engineering (Vol. 1, pp. 96-103).
3. Anderson, D. G., Martin, G. R., Lam, I., & Wang, J. N. (2008). Seismic analysis and design of retaining walls, slopes and embankments, and buried structures. NCHRP Rep, 611.
4. Azuma, H., & Ishii, Y. (1956). Aseismic Design of Quay Walls in Japan By Riokichi Amano. In Proceedings of the world conference on earthquake engineering, Berkeley, California, June 1956.
5. Benuska, L. (1990). Loma Prieta earthquake reconnaissance report (p. 488). Earthquake Engineering Research Institute.
6. Bolton M. D., and Steedman, R. S. (1982). Centrifugal testing of micro-concrete retaining walls subject to base shaking. Proceedings of Conference on Soil dynamics and Earthquake Engineering, Southampton, 1, 311-329, Balkema.
7. Bolton M. D., and Steedman, R. S. (1984). The behavior of fixed cantilever walls subject to lateral shaking, Proceedings of Symposium on the Application of Centrifuge Modeling to Geotechnical Design, University of Manchester, 302-314, Balkema.
8. Bolton M. D., and Steedman, R. S. (1985). The behavior of fixed cantilever walls subject to lateral loading. Application of Centrifuge Modeling to Geotechnical Design, Craig (ed.), Balkema, Rotterdam.
9. Bray, J. D., & Travasarou, T. (2007). Simplified procedure for estimating earthquake-induced deviatoric slope displacements. Journal of Geotechnical and Geoenvironmental Engineering, 133(4), 381-392.
10. Bray, J. D., Travasarou, T., & Zupan, J. (2010). Seismic displacement design of earth retaining structures. In Proceedings, Earth Retention Conference (Vol. 3, pp. 1-4).
11. Bray, J., Rollins, K., Hutchinson, T., Verdugo, R., Ledezma, C., Mylonakis, G., Assimaki, D., Montalva, G., Arduino, P., Olson, S.M., Kayen, R., Hashash, Y., & Candia, G. (2012). Effects of ground failure on buildings, ports, and industrial facilities. Earthquake Spectra, 28(S1), S97-S118.
12. Candia, G. & Sitar, N. (2013). "Seismic earth pressures on retaining wall on pile in sand with clay layer underneath (GC03)", Network for Earthquake Engineering Simulation (distributor), Dataset, DOI:10.4231/D3319S29K
13. Candia, G., Mikola, R.G., & Sitar, N. (2013). "Seismic earth pressures on braced wall and displacing retaining wall in clay (GC01)", Network for Earthquake Engineering Simulation (database), Dataset, DOI:10.4231/D37W67572
14. Candia, G., Mikola, R.G., & Sitar, N. (2013). "Seismic earth pressures on displacing retaining wall in clay soil with sloping ground (GC02)", Network for Earthquake Engineering Simulation (database), Dataset, DOI:10.4231/D34746R4K

15. Chen, W. F. and X. L. Liu (1990). Limit Analysis in Soil Mechanics. Elsevier.
16. Clough, G. W., & Fragaszy, R. F. (1977). A study of earth loadings on floodway retaining structures in the 1971 San Fernando Valley earthquake. In Proceedings of the Sixth World Conference on Earthquake Engineering (Vol. 3).
17. Clough, G.W., & Duncan, J.M. (1971). Finite element analyses of retaining wall behavior. ASCE Journal of Soil Mechanics 97(12): 1657-1673.
18. Clough, G.W., & Duncan, J.M. (1991). Earth pressures. In Foundation engineering handbook (pp. 223-235). Springer US.
19. Coulomb, C. A. (1776). Essai sur une application des règles de maximis & minimis à quelques problèmes de statique, relatifs à l'architecture. De l'Imprimerie Royale.
20. Darandeli, M. (2001). Development of a new family of normalized moduli reduction and material damping curves [Ph. D. Thesis] (Doctoral dissertation, Austin: University of Texas at Austin).
21. Das, B. M., & Puri, V. K. (1996). Static and dynamic active earth pressure. Geotechnical & Geological Engineering, 14(4), 353-366.
22. Dawson, E. M., Roth, W. H., & Drescher, A. (1999). Slope stability analysis by strength reduction. Geotechnique, 49(6), 835-840.
23. Dewoolkar, M. M., Ko, H. Y., & Pak, R. Y. (2001). Seismic behavior of cantilever retaining walls with liquefiable backfills. Journal of Geotechnical and Geoenvironmental engineering, 127(5), 424-435.
24. Dobry, R., and Liu, L. 1994. Centrifuge modeling of soil liquefaction. Proceedings of the Tenth World Conference on earthquake Engineering, Balkema, Rotterdam, 6801-6809.
25. Duke, C. M., & Leeds, D. J. (1963). Response of soils, foundations, and earth structures to the Chilean earthquakes of 1960. Bulletin of the Seismological Society of America, 53(2), 309-357
26. Duncan, J. M., & Seed, R. B. (1986). Compaction-induced earth pressures under K0-conditions. Journal of Geotechnical Engineering, 112(1), 1-22.
27. Duncan, J. M., Williams, G. W., Sehn, A. L., & Seed, R. B. (1991). Estimation earth pressures due to compaction. Journal of geotechnical engineering, 117(12), 1833-1847.
28. Elgamal, A. W., & Alampalli, S. (1992, July). Earthquake response of retaining walls: full-scale testing and computational analysis. In Proceedings of 10th world conference on earthquake engineering, Madrid, Spain. AA Rotterdam: Balkema (Vol. 3, pp. 1671-6).
29. Gazetas, G. (1982). Vibrational characteristics of soil deposits with variable wave velocity. International journal for numerical and analytical methods in Geomechanics, 6(1), 1-20.
30. Gazetas, G., Psarropoulos, P. N., Anastasopoulos, I., & Gerolymos, N. (2004). Seismic behavior of flexible retaining systems subjected to short-duration moderately strong excitation. Soil Dynamics and Earthquake Engineering, 24(7), 537-550.
31. Ghosh, S., & Sengupta, (2012) S. Formulation of Seismic Active Earth Pressure of Inclined Retaining Wall Supporting c-Φ Backfill.
32. Hall, J.F. (1995). “Northridge Earthquake of January 17, 1994 Reconnaissance Report – Volume 1.” Earthquake Spectra, Supplement C to Vol. 11.
33. Hardin, B. O. (1978). The nature of stress-strain behavior for soils. In From Volume I of Earthquake Engineering and Soil Dynamics - Proceedings of the ASCE Geotechnical Engineering Division Specialty Conference, June 19-21, 1978, Pasadena, California.

34. Hardin, B. O., & Drnevich, V. P. (1972). Shear modulus and damping in soils. Journal of the Soil Mechanics and Foundations Division, 98(7), 667-692.
35. Hayashi, S., Kubo, K., & Nakase, A. (1966). Damage to harbor structures by the Niigata earthquake. Soil and foundation, 6(1), 89-112.
36. Holmes, W.T., and Somers, P. (1996). "Northridge Earthquake of January 17, 1994 Reconnaissance Report – Volume 2." Earthquake Spectra, Supplement C to Vol. 11.
37. Iida, H., Hiroto, T., Yoshida, N., & Iwafuji, M. (1996). Damage to Daikai subway station. Soils and foundations, 283-300.
38. Ilankatharan, M., and Kutter, B. L. 2008. Numerical simulation of soil model-model container-centrifuge shaking table system. Proceedings of Geotechnical Earthquake Engineering and Soil Dynamics-IV, Sacramento, California.
39. Inagaki, H., Iai, S., Sugano, T., Yamazaki, H., & Inatomi, T. (1996). Performance of caisson type quay walls at Kobe port. Soils and foundations, 119-136.
40. Ishibashi, I., and Fang, Y. S. 1987. Dynamic earth pressures with different wall movement modes, soils and foundations. Japanese Soc. of Soil Mechanics and Foundation Engineering, 27(4), 11–22.
41. Ishii, Y., Arai, H., Tsuchida, H. 1960. Lateral earth pressure in an earthquake. Proceedings of the second World Conference on Earthquake Engineering: Tokyo and Kyoto, Japan, July 11-18, 1960. pp. 211-230
42. Itasca, FLAC (20011). Fast Lagrangian Analysis of Continua, Version 7.0 User's Guide. Itasca Consulting Group, Inc., Thrasher Square East, 708.
43. Jacobson, L.S. (1939); Described in Appendix D of "The Kentucky Project" Technical Report No. 13 TVA, 1951.
44. Jacobson, P. N. 1980. Translational behavior of gravity retaining walls during earthquakes. Research Report 80-9. University of Canterbury, New Zealand.
45. Kloukinas, P., Langousis, M., & Mylonakis, G. (2012). Simple Wave Solution for Seismic Earth Pressures on Nonyielding Walls. Journal of Geotechnical and Geoenvironmental Engineering, 138(12), 1514-1519.
46. Kutter, B. L, Idriss, I. M., Kohnke, T., Lakeland, J., Li, X.S., Sluis, W., Zeng, X., Tauscher, R.C., Goto, Y., and Kubodera, I. 1994. Design of a large earthquake simulator at UC Davis. Centrifuge 94, Leung, Lee, and Tan(eds.), Balkema, 169-175.
47. Kutter, B. L. (1995, April). Recent advances in centrifuge modeling of seismic shaking. In Proc., 3rd Int. Conf. on Recent Advances in Geotechnical Earthquake Engineering and Soil Dynamics (Vol. 2, pp. 927-942). Rolla, MO: Univ. of Missouri.
48. Lew, M., Sitar, N., & Al Atik, L. (2010, August). Seismic earth pressures: fact or fiction. In Invited Keynote Paper, Earth Retention Conference, ER.
49. Matsuo, H. 1941. Experimental study on the distribution of earth pressures acting on a vertical wall during earthquakes. Journal of the Japanese Society of Civil Engineers 27(2).
50. Matsuo, H., & O'Hara, S. (1965). Dynamic pore water pressure acting on quay walls during earthquakes. In Proceedings of the Third World Conference on Earthquake Engineering (Vol. 1, pp. 130-140).
51. Matsuo, H., and O'Hara, S. 1960. Lateral earth pressure and stability of quay walls during earthquakes. Proceedings, Earthquake Engineering, Second World Conference, Tokyo, Japan, 1.
52. Matsuzawa, H., Ishibashi, I., & Kawamura, M. (1985). Dynamic soil and water pressures

of submerged soils. Journal of Geotechnical Engineering, 111(10), 1161-1176.

53. Mayne, P. W., & Kulhawy, F. H. (1982). K0-OCR Relationships in Soil. Journal of the Geotechnical Engineering Division, 108(6), 851-872
54. Mikola, R. G., & Sitar, N. (2013). Seismic Earth Pressures on Retaining Structures in Cohesionless Soils.
55. Mikola, R. G., Candia, G. & Sitar, N. (2013). "Seismic earth pressures on braced wall in sand (Rooz01)", Network for Earthquake Engineering Simulation (database), Dataset, DOI:10.4231/D3HD7NS4P
56. Mikola, R. G., Candia, G. & Sitar, N. (2013). "Seismic earth pressures on non-displacing and displacing retaining wall in sand (Rooz02)", Network for Earthquake Engineering Simulation (database), Dataset, DOI:10.4231/D3CN6Z00Z
57. Mononobe, N., and Matsuo M. 1929. On the determination of earth pressures during earthquakes. Proceedings, World Engineering Congress 9: 179-187.
58. Mylonakis, G., Kloukinas, P. and Papatonopoulos, C. (2007). “An Alternative to the Mononobe-Okabe Equation for Seismic Earth Pressures”, Soil Dyn. And Earthquake Eng., (27) 10, 957-969.
59. Nadim, F., Whitman, R. 1982. A numerical model for evaluation of seismic behavior of gravity retaining walls. R82-33. Massachusetts Institute of Technology, Report 1982, 232p (480 S43 no.2 1982)
60. Naesgaard, E. (2011). A hybrid effective stress–total stress procedure for analyzing soil embankments subjected to potential liquefaction and flow.
61. Nakamura, S. (2006). Reexamination of Mononobe-Okabe theory of gravity retaining walls using centrifuge model tests. Soils and foundations, 46(2), 135-146.
62. Okabe S. 1926. General theory of earth pressure,” Journal of the Japanese Society of Civil Engineers, Tokyo, Japan 12(1).
63. Ortiz, L. A., Scott, R. F., and Lee, J. 1983. Dynamic centrifuge testing of a cantilever retaining wall. Earthquake Engineering and Structural Dynamics 11: 251–268.
64. Prakash, S. and Basavanna, B. M. 1969. Earth pressure distribution behind retaining wall during earthquakes. Proceedings of the Fourth World Conference on Earthquake Engineering, Santiago, Chile.
65. Prakash, S. and Saran, S. (1966) Static and dynamic earth pressures behind retaining walls. Proceedings of the Third Symposium on Earthquake Engineering, University of Roorkee, Roorkee, India, Vol. 1, pp. 277-88.
66. Psarropoulos, P. N., Klonaris, G., & Gazetas, G. (2005). Seismic earth pressures on rigid and flexible retaining walls. Soil Dynamics and Earthquake Engineering, 25(7), 795-809.
67. Rankine, W. M. (1857). On the stability of loose earth. Philosophical Transactions of the Royal Society of London, 9-27.
68. Rathje, E. M., Abrahamson, N. A., & Bray, J. D. (1998). Simplified frequency content estimates of earthquake ground motions. Journal of Geotechnical and Geoenvironmental Engineering, 124(2), 150-159.
69. Richards R. and X. Shi (1994). “Seismic Lateral Pressures in Soils with Cohesion.” Journal of Geotechnical Engineering, ASCE, Vol. 120,No. 7, pp 1230–1251.
70. Richards, R., and Elms, D. G. 1979. Seismic behavior of gravity retaining walls. Journal of the Geotechnical Engineering Division, ASCE 105(GT4): 449–64.
71. Richards, R., and Elms, D. G. 1980. Seismic behavior of gravity retaining wallsg1 closure. Journal of the Geotechnical Engineering Division, ASCE 106(GT6): 737-738.

72. Richards, R., Jr., Elms, D., and Budhu, M. (1990). ”Dynamic Fluidization of Soils.” J. Geotech. Engrg., 116(5), 740–759.
73. Schmertmann, G.R.; Chew, S.; Mitchell, J. Finite element modeling of reinforced soil wall behavior. UCB/GT-89-01, University of California, Berkeley, Geotechnical Engineering, 1989-09, PDF (6 MB)
74. Schnabel, P. B., J. Lysmer, and H. B. Seed (1972). “SHAKE: A Computer Program for Earthquake Response Analysis of Horizontally Layered Sites.” University of California—Berkeley, Earthquake Engineering Research Center, Report No. EERC 72-12, December.
75. Scott, R. F. 1973. Earthquake-induced earth pressures on retaining walls. Proceedings, Earthquake Engineering, Fifth World Conference, Rome, Italy, 2.
76. Seed, H. B., and Idriss, I. M. 1970. Soil moduli and damping factors for dynamic response analyses. Earthquake Research Center, Report EERC 70-10, University of California, Berkeley, California.
77. Seed, H. B., and Whitman, R. V. 1970. Design of earth retaining structures for dynamic loads. ASCE Specialty Conference, Lateral Stresses in the Ground and Design of Earth Retaining Structures, Cornell Univ., Ithaca, New York, 103–147.
78. Seed, R. B., & Duncan, J. M. (1986). FE analyses: compaction-induced stresses and deformations. Journal of Geotechnical Engineering, 112(1), 23-43.
79. Shamsabadi, A., Xu, S. Y., & Taciroglu, E. (2013). A generalized log-spiral-Rankine limit equilibrium model for seismic earth pressure analysis. Soil Dynamics and Earthquake Engineering, 49, 197-209.
80. Sherif, M. A., Fang, Y. S., 1984. Dynamic earth pressures on walls rotating about the top. Soils and Foundations 24(4): 109-117.
81. Sherif, M. A., Ishibashi, I., and Lee, C. D. 1982. Earth pressure against stiff retaining walls. Journal of Geotechnical Engineering, ASCE 108: 679-695.
82. Shukla, S. K., Gupta, S. K., & Sivakugan, N. (2009). Active earth pressure on retaining wall for c-ϕ soil backfill under seismic loading condition. Journal of Geotechnical and Geoenvironmental engineering, 135(5), 690-696.
83. Siddharthan, R., and Maragakis, E. M. 1989. Performance of flexible retaining walls supporting dry cohesionless soils under cyclic loads. International Journal for Numerical and Analytical Methods in Geomechanics 13: 309-326.
84. Sitar, N., Mikola, R. G., & Candia, G. (2012). Seismically induced lateral earth pressures on retaining structures and basement walls. In Geotechnical Engineering State of the Art and Practice@ Keynote Lectures from GeoCongress 2012 (pp. 335-358). ASCE.
85. Steedman, R. S., and Zeng, X. 1990. The seismic response of waterfront retaining walls. Design and Performance of Earth Retaining Structures, Conference Proceedings, Cornell University, Ithaca, New York, June 18-21, ASCE Geotechnical Special Publication No. 25.
86. Steedman, R. S., and Zeng, X. 1991. Centrifuge modeling of the effects of earthquakes on free cantilever walls. Centrifuge’91, Ko (ed.), Balkema, Rotterdam.
87. Stewart, J.P., Bray, J.D., Seed, R.B., and Sitar, N., eds. (1994). Preliminary Report on the Principal Geotechnical Aspects of the January 17, 1994, Northridge Earthquake. Earthquake Engineering Research Center Report No. UCB/EERC 94/08. University of California, Berkeley.
88. Sun, J. I., Golesorkhi, R., & Seed, H. B. (1988). Dynamic moduli and damping ratios for

cohesive soils. Earthquake Engineering Research Center, University of California.

89. Terzaghi, K. 1934. Large retaining wall tests—I. Pressure in dry sand. Engineering News Record, February, pp. 136–140.
90. Trifunac, M. D., & Brady, A. G. (1975). A study on the duration of strong earthquake ground motion. Bulletin of the Seismological Society of America,65(3), 581-626.
91. Veletsos A. S. and Younan A. H. (1994a). "Dynamic Soil Pressures on Rigid Vertical Walls". Earthquake Engrg. and Struct. Dyn., 23(3), 275-301.
92. Veletsos, A. S., and Younan, A. H. 1997. Dynamic response of cantilever retaining walls. Journal of Geotechnical and Geoenvironmental Engineering 123(2): 161-172.
93. Whitman, R.V. (1991). "Seismic Design of Earth Retaining Structures." Proceedings, Second International Conference on Recent Advances in Geotechnical Earthquake Engineering and Soil Dynamics, St. Louis, MO. 1767-1778.
94. Wilson, D. W. (1998). Soil-pile-superstructure interaction in liquefying sand and soft clay (Doctoral dissertation, University of California, Davis).
95. Wilson, D. W., Boulanger, R. W., Kutter, B. L., and Abghari, A. 1997. Aspects of dynamic centrifuge testing of soil-pile-superstructure interaction. Observation and Modeling in Numerical Analysis and Model Tests in Dynamic Soil-Structure Interaction Problems, Geotechnical Special Publication, ASCE (64): 47-63.
96. Wood, J. H. 1973. Earthquake induced soil pressures on structures. PhD Thesis, California Institute of Technology, Pasadena, CA.
97. Yoshida, N. (2009) Damage to subway station during the 1995 Hyogoken-Nambu (Kobe) earthquake. Earthquake geotechnical case histories for performance-based design – Kokusho (ed) © 2009 Taylor & Francis Group, London, ISBN 978-0-415-80484-4

Appendix

Appendix A: solution of the 1-d shear wave equation applied to the computation of seismic earth pressures

Seismically induced earth pressures on a yielding wall with a visco-elastic backfill

This section shows the solution of the dynamic wave Equation on a visco-elastic material applied to the computation of earth pressures on a retaining wall. This solution is an extension to the method proposed by Steedman and Zeng (1990), and includes the effect of the rebounding shear wave at the surface and viscous damping.

The shear stress on a visco-elastic material, or Kelvin-Voight solid, has a linear elastic component proportional to the shear strain and a dissipative component proportional to the strain rate, and can be written as

$$\tau = G\gamma + \eta\dot{\gamma} \tag{A.1}$$

where G is the shear modulus and η is the damping factor. Then, the dynamic equilibrium of an infinitesimal point subject to shear forces can be written as

$$\rho\ddot{u} = \tau_z = G\gamma_z + \eta\dot{\gamma}_z \tag{A.2}$$

where ρ is the unit weight of the soil. Expressing the shear strain in terms of displacement derivatives, Equation (A.2) becomes

$$\rho\ddot{u} = Gu_{zz} + \eta\dot{u}_{zz} \tag{A.3}$$

To determine the damping parameter η, viscous damping is assumed. Thus, if a shear strain cycle of the form $\gamma = \gamma_0 \sin(\omega t)$ is applied, the equivalent damping ratio is given by

$$\xi = \frac{1}{4\pi}\frac{\Delta W}{W} = \frac{1}{4\pi}\frac{\int_0^{2\pi/\omega} \tau\dot{\gamma}dt}{\frac{1}{2}G\gamma_0^2} = \frac{\eta\omega}{2G} \tag{A.4}$$

from where

$$\eta = \frac{2G\xi}{\omega} \tag{A.5}$$

Using variable separation, a trial solution of Equation (A.3) has the form

$$u(z,t) = U(x,\omega)e^{i\omega t} \tag{A.6}$$

Substituting (A.6) into (A.3), a ordinary differential equation on *U* is obtained

$$U_{zz} + \frac{\rho\omega^2}{G + i\omega\eta}U = 0 \tag{A.7}$$

with general solution

$$U = E_1 e^{ikz} + E_2 e^{-ikz} \tag{A.8}$$

where ***k*** is the complex frequency $k^2 = \frac{\rho\omega^2}{G+i\omega\eta} = \frac{\rho\omega^2}{G(1+2i\xi)}$. Thus, the complete solution is

$$u(z,t) = \left(E_1 e^{ikz} + E_2 e^{-ikz}\right) e^{i\omega t} \tag{A.9}$$

To finds constants E_1 and E_2, the boundary condition of zero shear stress at the surface is imposed, i.e. $G^* u_z(0,t) = 0$, leading to

$$G^* u_z(0,t) = G^* ike^{i\omega t}(E_1 - E_2) = 0 \quad \rightarrow \; E_1 = E_2 = C \tag{A.10}$$

Therefore, the solution is reduced to one constant C

$$u(z,t) = C(e^{ikz} + e^{-ikz})e^{i\omega t} = 2C\cos(kz)e^{i\omega t} \tag{A.11}$$

Using the principle of superposition, the base acceleration can be written as the sum harmonic waves with frequency $+\omega$ and $-\omega$ as

$$\ddot{u}(H_{soil}, t) = k_h g \sin(\omega t) = k_h g\left(\frac{e^{i\omega t} - e^{-i\omega t}}{2i}\right) \tag{A.12}$$

leading to two '*C*' constants, say C_1 and C_2. Setting the second time derivative of Equation (A.11) equal to (A.12) the constants C_1 and C_2 are

$$C_1 = \frac{ik_h g}{4\omega^2\cos(kH_{soil})} \quad , \quad C_2 = \bar{C}_1 = \frac{-ik_h g}{4\omega^2\cos(\bar{k}H_{soil})} \tag{A.13}$$

where $\bar{k} = \text{conj}(k)$. Finally, the displacement profile on the backfill is

$$\begin{aligned} u(z,t) &= 2C_1\cos(kz)e^{i\omega t} + 2\bar{C}_1\cos(\bar{k}z)e^{-i\omega t} \\ &= -\frac{k_h g}{\omega^2}\text{Im}\left(\frac{\cos(kz)}{\cos(kH_{soil})}e^{i\omega t}\right) \end{aligned} \tag{A.14}$$

and the acceleration profile is

$$\ddot{u}(z,t) = k_h g\text{Im}\left(\frac{\cos(kz)}{\cos(kH_{soil})}e^{i\omega t}\right) \tag{A.15}$$

It can be readily verified that the natural boundary conditions of this problem are satisfied, i.e., zero shear stress at the surface and harmonic base acceleration:

$$
\begin{aligned}
&(i)\quad G^*\tfrac{du}{dz}\big|_{z=0} &&= -\tfrac{k_h g G^*}{\omega^2}\tfrac{d}{dz}\left(\mathrm{Im}\left(\tfrac{\cos(kz)}{\cos(kH_{soil})}e^{i\omega t}\right)\right)_{z=0} = \tfrac{k_h g G^*}{\omega^2}\mathrm{Im}\left(\tfrac{\sin(kz)}{\cos(kH_{soil})}e^{i\omega t}\right)_{z=0} = 0\\
&(ii)\quad \ddot{u}(H_{soil},t) &&= k_h g\,\mathrm{Im}(e^{i\omega t}) = k_h g\sin(\omega t)
\end{aligned}
\tag{A.16}
$$

The computation of the total seismic load on the wall assumes the existence of a Mononobe-Okabe sliding wedge determined by the angle α, as shown in Figure A.1. The inertial loads on the soil wedge OAB are determined by integrating Equation (A.15) on the wall depth as

$$
Q_h(H_{wall},t) = \frac{k_h\gamma H_{wall}^2}{\tan\alpha}\mathrm{Im}\left(\frac{1-\cos(kH_{wall})}{k^2H_{wall}^2\cos(kH_{soil})}e^{i\omega t}\right) \tag{A.17}
$$

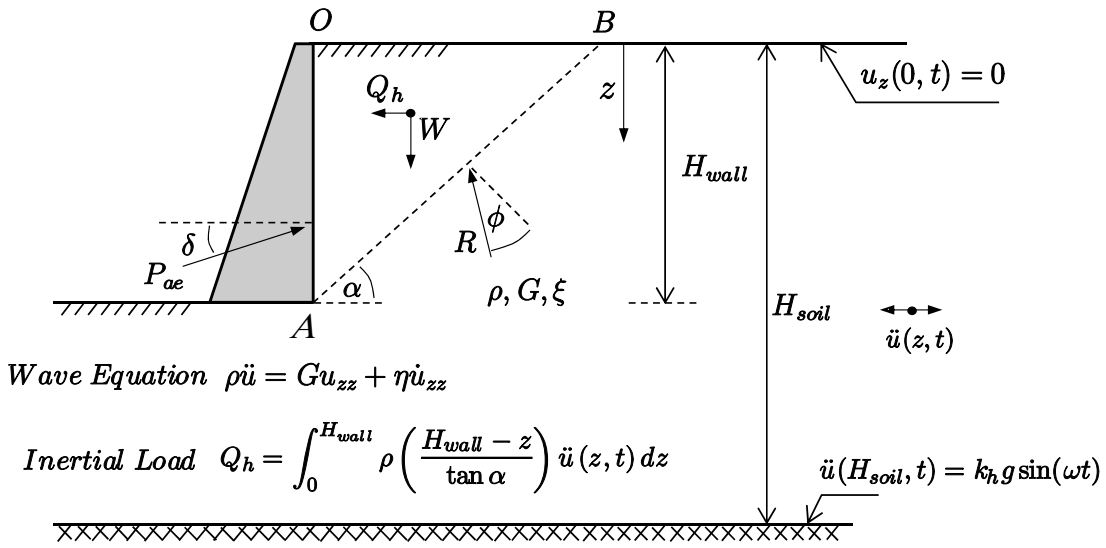

Figure A.1 Force diagram of the wall-backfill system.

The horizontal and vertical equilibrium of forces P_{ae}, R,W and Q_h, requires that

$$
\begin{aligned}
P_{ae}\cos(\delta) &= Q_h + R\sin(\alpha-\phi)\\
P_{ae}\sin(\delta) &= W - R\cos(\alpha-\phi)
\end{aligned}
\tag{A.18}
$$

From where the total seismic load on the wall is given by

$$
P_{ae} = \frac{Q_h\cos(\alpha-\phi) + W\sin(\alpha-\phi)}{\cos(\delta-\alpha+\phi)} \tag{A.19}
$$

Finally, the coefficient of total seismic earth pressures can be defined as

$$
K_{ae} = \frac{2P_{ae}}{\gamma H^2} \tag{A.20}
$$

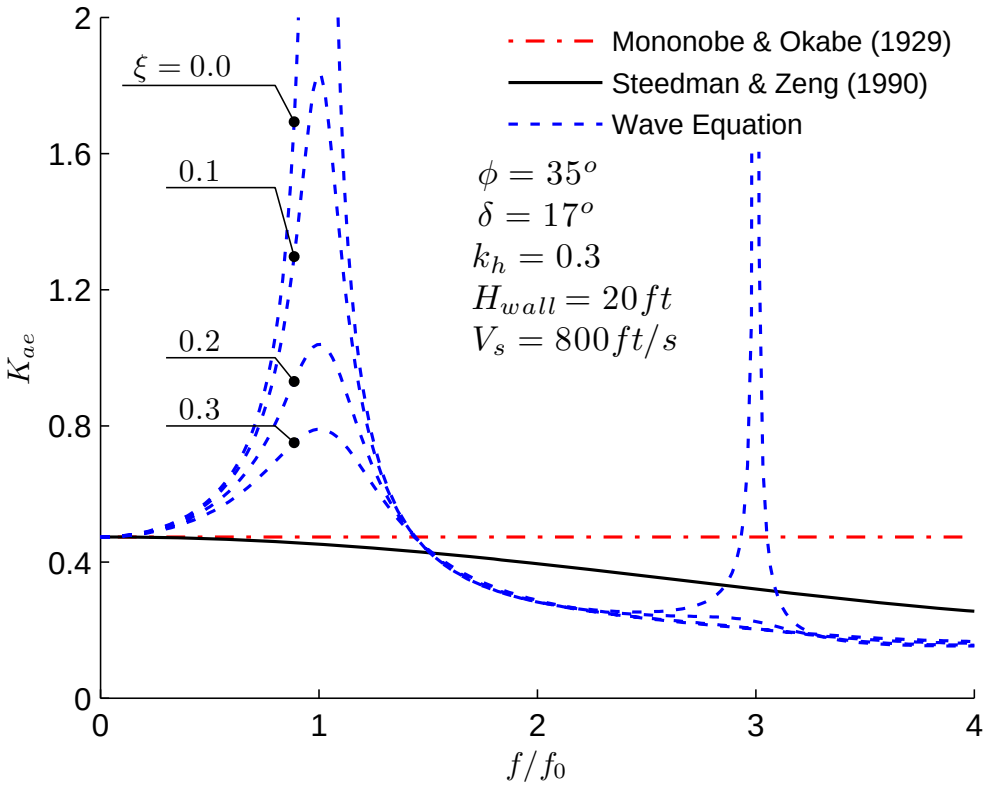

Figure A.2 Influence of input frequency and soil damping on the earth pressure coefficient for a gravity wall founded on rock.

Appendix B: Prototype wall and centrifuge container properties

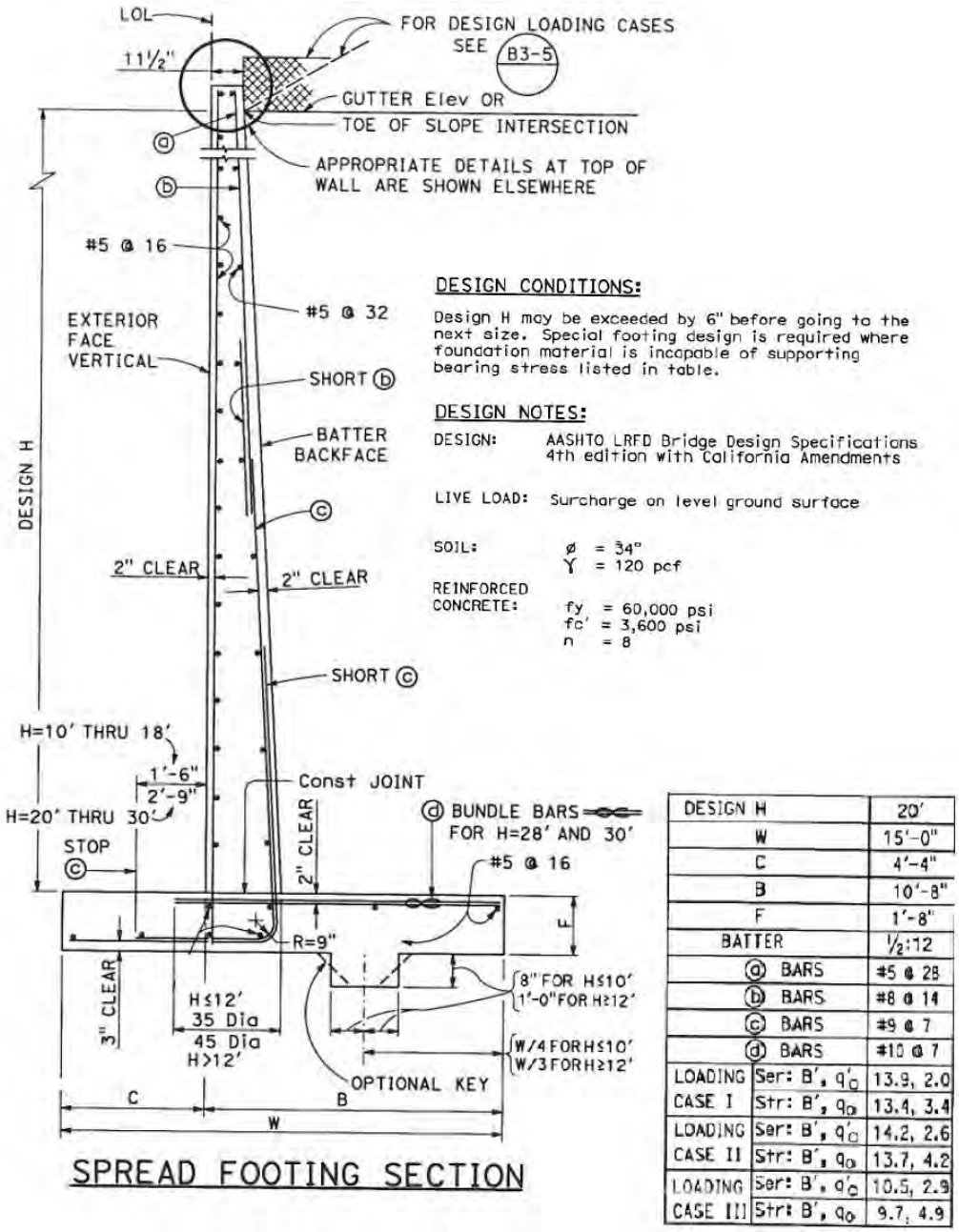

DESIGN H		20'
W		15'-0"
C		4'-4"
B		10'-8"
F		1'-8"
BATTER		½:12
ⓐ BARS		#5 @ 28
ⓑ BARS		#8 @ 14
ⓒ BARS		#9 @ 7
ⓓ BARS		#10 @ 7
LOADING CASE I	Ser: B', q'_a	13.9, 2.0
	Str: B', q_a	13.4, 3.4
LOADING CASE II	Ser: B', q'_a	14.2, 2.6
	Str: B', q_a	13.7, 4.2
LOADING CASE III	Ser: B', q'_a	10.5, 2.9
	Str: B', q_a	9.7, 4.9

Figure B.1 Prototype ASSTHO-LRFD cantilever wall used by Caltrans.

Table B.1 Dimensions and material parameters of the 2D container model

FSB2 Element	Thickness	Width	Mass	Young Modulus	Poisson Ratio
	mm	mm	ton/m^3	kPa	-
Container Base	76.2	1650.6	3.86	6.89E+07	0.32
Floor Plate	12.7	152.4	9.51	6.89E+07	0.32
Rubber 1	12.7	152.4	3.16	1.86E+03	0.49
Ring 1 (Bottom)	101.6	152.4	4.91	2.00E+08	0.32
Rubber 2	12.7	152.4	3.16	1.86E+03	0.49
Ring 2	101.6	152.4	3.61	6.89E+07	0.32
Rubber 3	12.7	152.4	2.73	1.86E+03	0.49
Ring 3	101.6	152.4	1.92	6.89E+07	0.32
Rubber 4	12.7	152.4	2.73	1.86E+03	0.49
Ring 4	101.6	152.4	1.92	6.89E+07	0.32
Rubber 5	12.7	57.7	3.47	1.86E+03	0.49
Ring 5 (Top)	101.6	57.7	1.47	6.89E+07	0.32

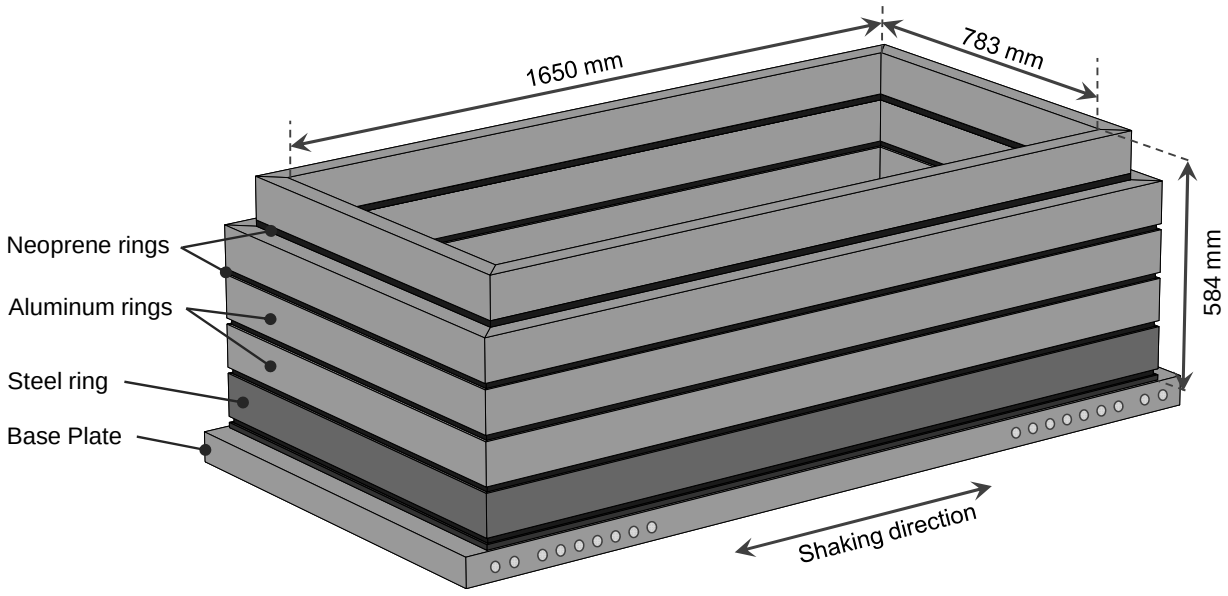

Figure B.2 Flexible Shear Beam Container

Appendix C: Additional tables and figures of level ground experiment and numerical model GC01

Table C.1 Peak ground acceleration (g) at selected model locations

Experiment: GC01 Ground Motion	Base Input	South backfill	Free Field (North backfill)	Basement wall top	Cantileverwall top
1) Kocali YPT060 - 1	0.13	0.21	0.19	0.34	0.25
2) Kocali YPT060 - 2	0.22	0.28	0.24	0.52	0.33
3) Kocali YPT330 - 1	0.25	0.28	0.23	0.51	0.37
4) Loma Prieta SC - 1	0.48	0.36	0.42	0.92	0.57
5) Kobe TAK090 - 1	0.97	0.54	0.57	1.21	1.02
6) Loma Prieta SC - 2	0.50	0.42	0.45	1.05	0.55
7) Loma Prieta WVC270 - 1	0.25	0.30	0.30	0.53	0.37
8) Kocali YPT330 - 2	0.24	0.29	0.25	0.61	0.45
9) Kobe TAK090 - 2	0.84	0.57	0.61	1.27	-

Table C.2 Modal participation factors of free field response in level ground model GC01

	Modal participation			Coef. R^2		
Ground Motion	ψ_1 (cm)	ψ_2 (cm)	ψ_3 (cm)	1 mode	2 modes	3 modes
1) Kocali YPT 060-1	1.85	0.41	0.06	0.83	0.97	0.98
2) Kocali YPT 060-2	2.55	0.60	0.13	0.81	0.97	0.97
3) Kocali YPT 330-1	3.14	0.36	0.04	0.93	0.98	0.98
4) Loma Prieta SC-1	4.52	1.12	0.22	0.81	0.98	0.99
5) Kobe TAK 090-1	15.62	2.44	0.12	0.91	0.99	0.99
6) Loma Prieta SC-2	4.49	1.40	0.24	0.77	0.98	0.99
7) Loma Prieta WVC 270-1	2.82	0.47	0.19	0.85	0.97	0.98
8) Kocali YPT 330-2	3.01	0.37	0.08	0.91	0.98	0.98
9) Kobe TAK 090-2	15.28	2.32	0.13	0.90	0.98	0.98

Table C.3 Free field acceleration coefficients and basement loads measured in the level ground model GC01. Loads normalized by $0.5\gamma H^2$ = 386 kN/m

Ground Motion	PGA_{ff}	P_{tot}	P_a	ΔP_{ae}	ΔP_{in}	$P_{ae}=P_{tot}+\Delta P_{in}$
1) Kocali YPT 060-1	0.21	0.21	0.15	0.07	0.006	0.21
2) Kocali YPT 060-2	0.28	0.28	0.15	0.13	-0.010	0.27
3) Kocali YPT 330-1	0.25	0.17	0.14	0.12	0.088	0.26
4) Loma Prieta SC-1	0.42	0.29	0.15	0.23	0.095	0.39
5) Kobe TAK 090-1	0.51	0.38	0.15	0.27	0.034	0.42
6) Loma Prieta SC-2	0.46	0.33	0.16	0.29	0.113	0.45
7) Loma Prieta WVC 270-1	0.32	0.19	0.16	0.10	0.070	0.26
8) Kocali YPT 330-2	0.27	0.17	0.15	0.12	0.102	0.28
9) Kobe TAK 090-2	0.56	0.45	0.17	0.29	0.006	0.46

Table C.4 Free field acceleration coefficients and cantilever wall loads measured in the level ground model GC01. Loads normalized by $0.5\gamma H^2$ = 386 kN/m

Ground Motion	PGA_{ff}	Q_b	P_a	ΔP_{ae}	ΔP_{in}	$P_{ae}=Q_b-\Delta P_{in}$
1) Kocali YPT 060-1	0.21	0.40	0.35	0.03	0.014	0.38
2) Kocali YPT 060-2	0.28	0.45	0.37	0.06	0.022	0.43
3) Kocali YPT 330-1	0.28	0.43	0.35	0.07	0.009	0.42
4) Loma Prieta SC-1	0.36	0.57	0.37	0.16	0.033	0.53
5) Kobe TAK 090-1	0.54	0.58	0.37	0.16	0.047	0.53
6) Loma Prieta SC-2	0.42	0.54	0.34	0.16	0.040	0.50
7) Loma Prieta WVC 270-1	0.29	0.46	0.33	0.10	0.029	0.44
8) Kocali YPT 330-2	0.29	0.44	0.34	0.08	0.021	0.41
9) Kobe TAK 090-2	0.57	0.55	0.34	0.18	0.030	0.52

Table C.5 Seismically induced surface settlements in level ground model GC01

Ground Motion	Arias Intensity (cm/s)	Settlement	
		Incremental (cm)	Cumulative (cm)
1) Kocali YPT 060-1	11	0.5	0.5
2) Kocali YPT 060-2	32	1.2	1.6
3) Kocali YPT 330-1	43	1.2	2.8
4) Loma Prieta SC-1	141	2.8	5.6
5) Kobe TAK 090-1	582	16.5	22.1
6) Loma Prieta SC-2	150	1.8	23.9
7) Loma Prieta WVC 270-1	31	0.4	24.3
8) Kocali YPT 330-2	43	0.5	24.8
9) Kobe TAK 090-2	488	8.9	33.7

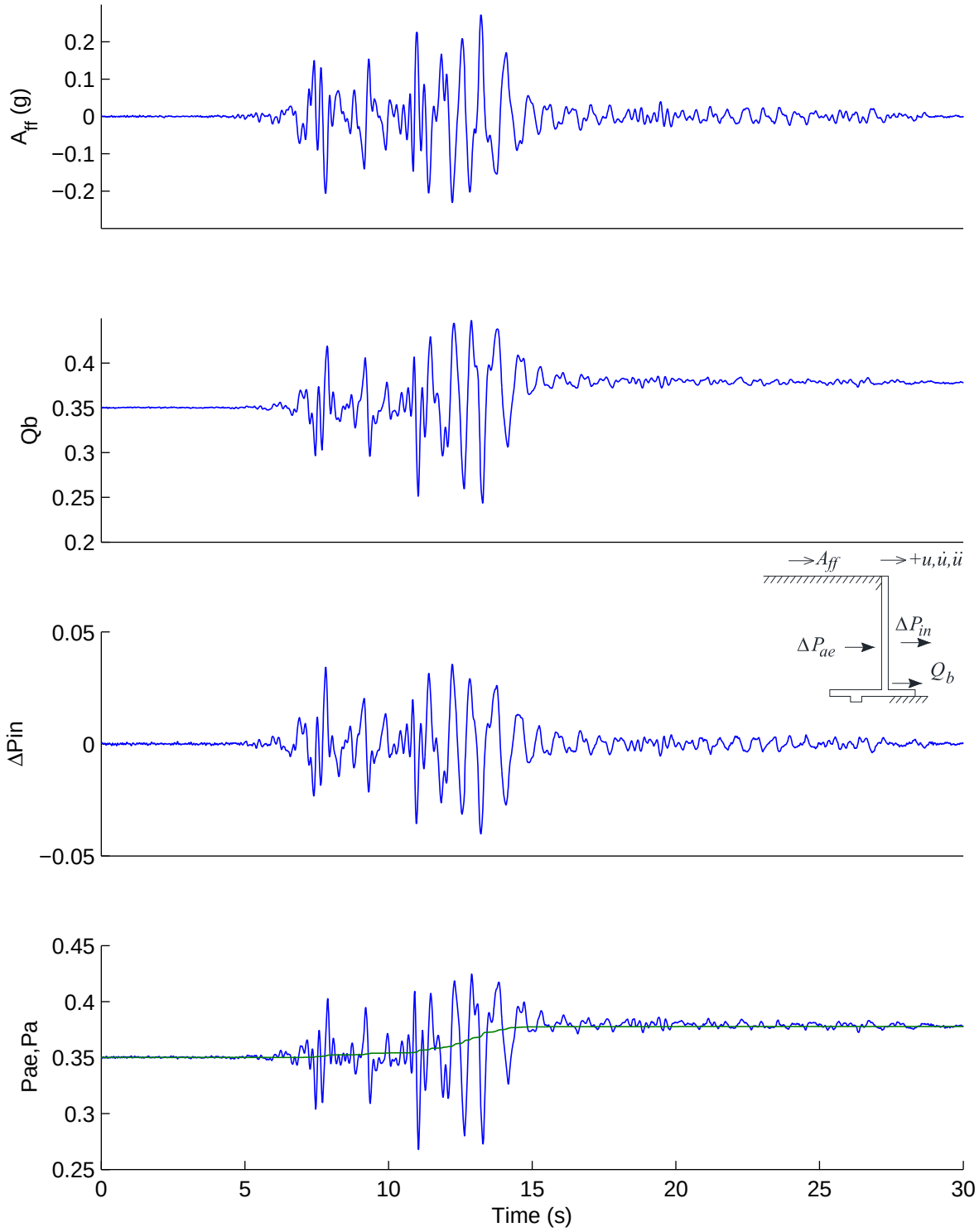

Figure C.1 Measured free field acceleration and cantilever wall load during Kocaeli YPT 060-2. Loads normalized by $0.5\gamma H^2$.

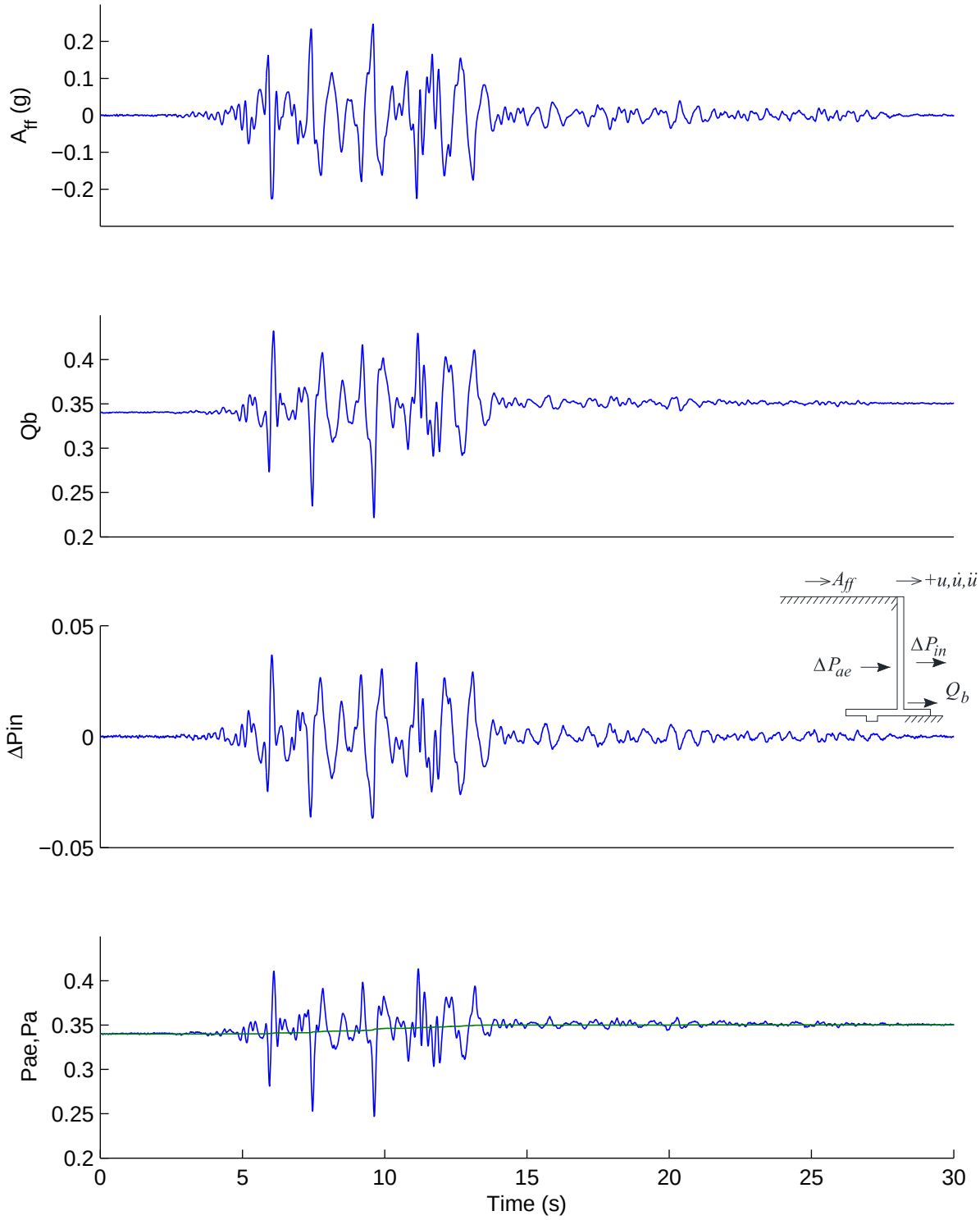

Figure C.2 Measured free field acceleration and cantilever wall load during Kocaeli YPT 330-1. Loads normalized by $0.5\gamma H^2$.

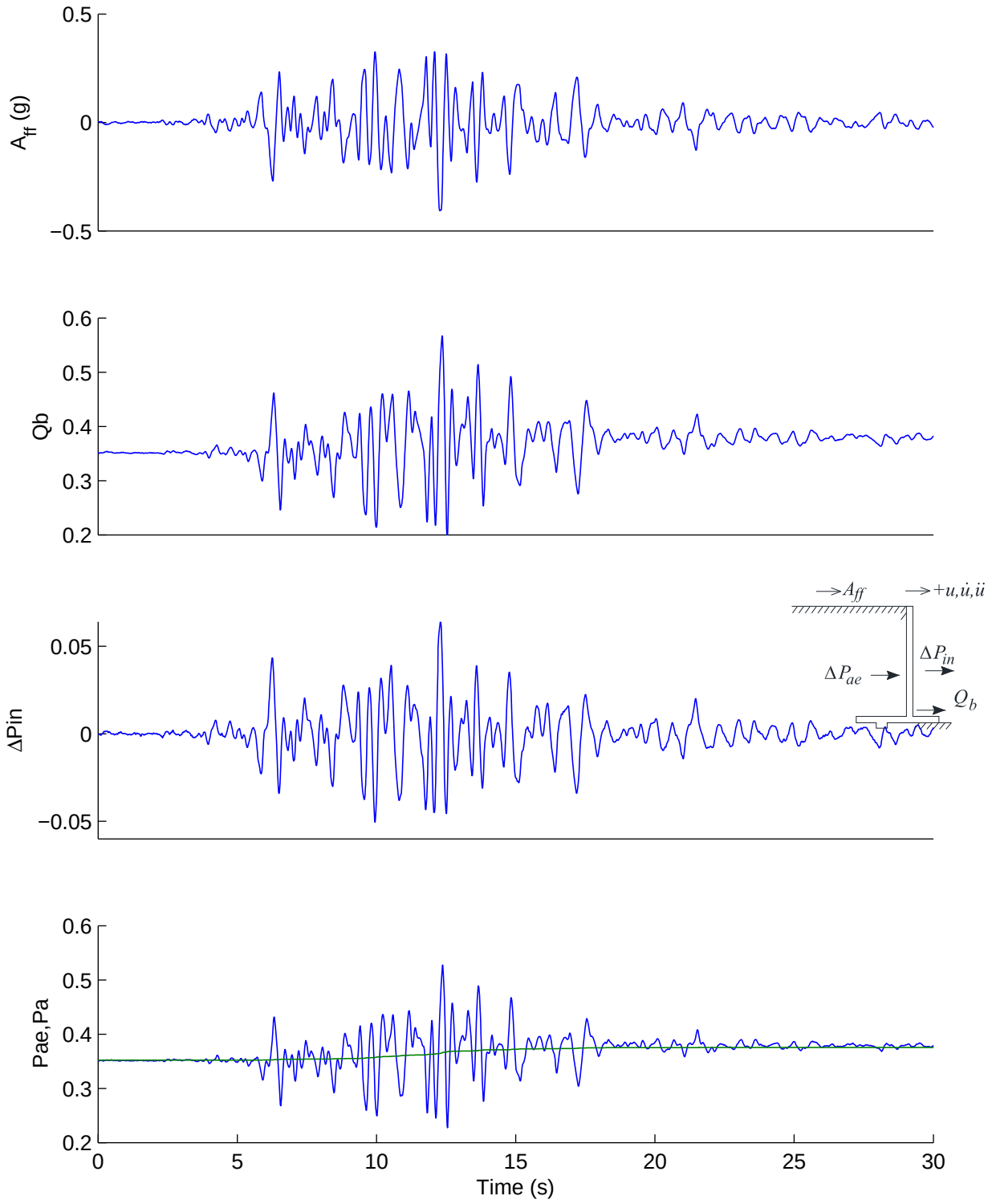

Figure C.3 Measured free field acceleration and cantilever wall load during Loma Prieta SC-1. Loads normalized by $0.5\gamma H^{2.}$

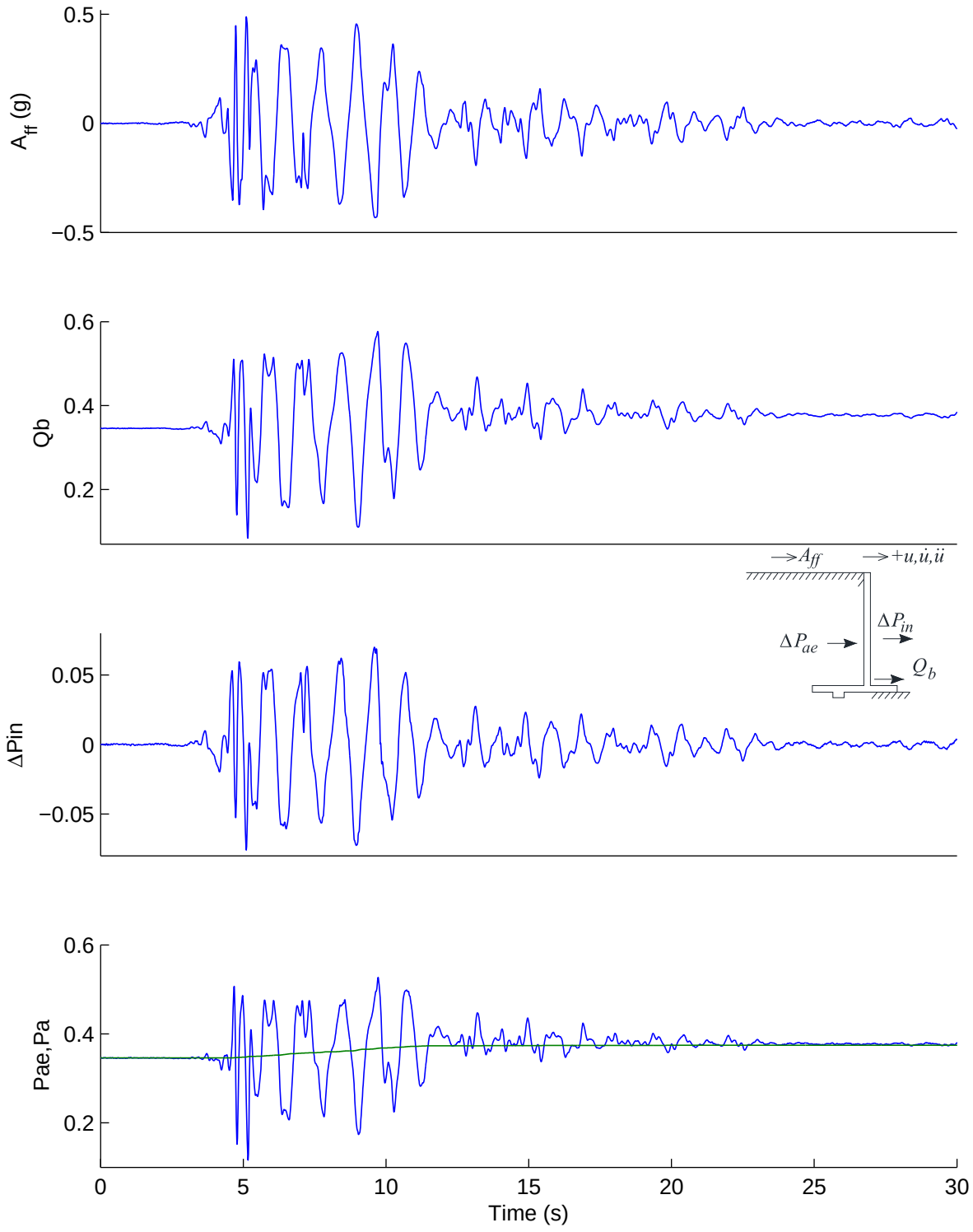

Figure C.4 Measured free field acceleration and cantilever wall load during Kobe TAK 090-1. Loads normalized by $0.5\gamma H^2$.

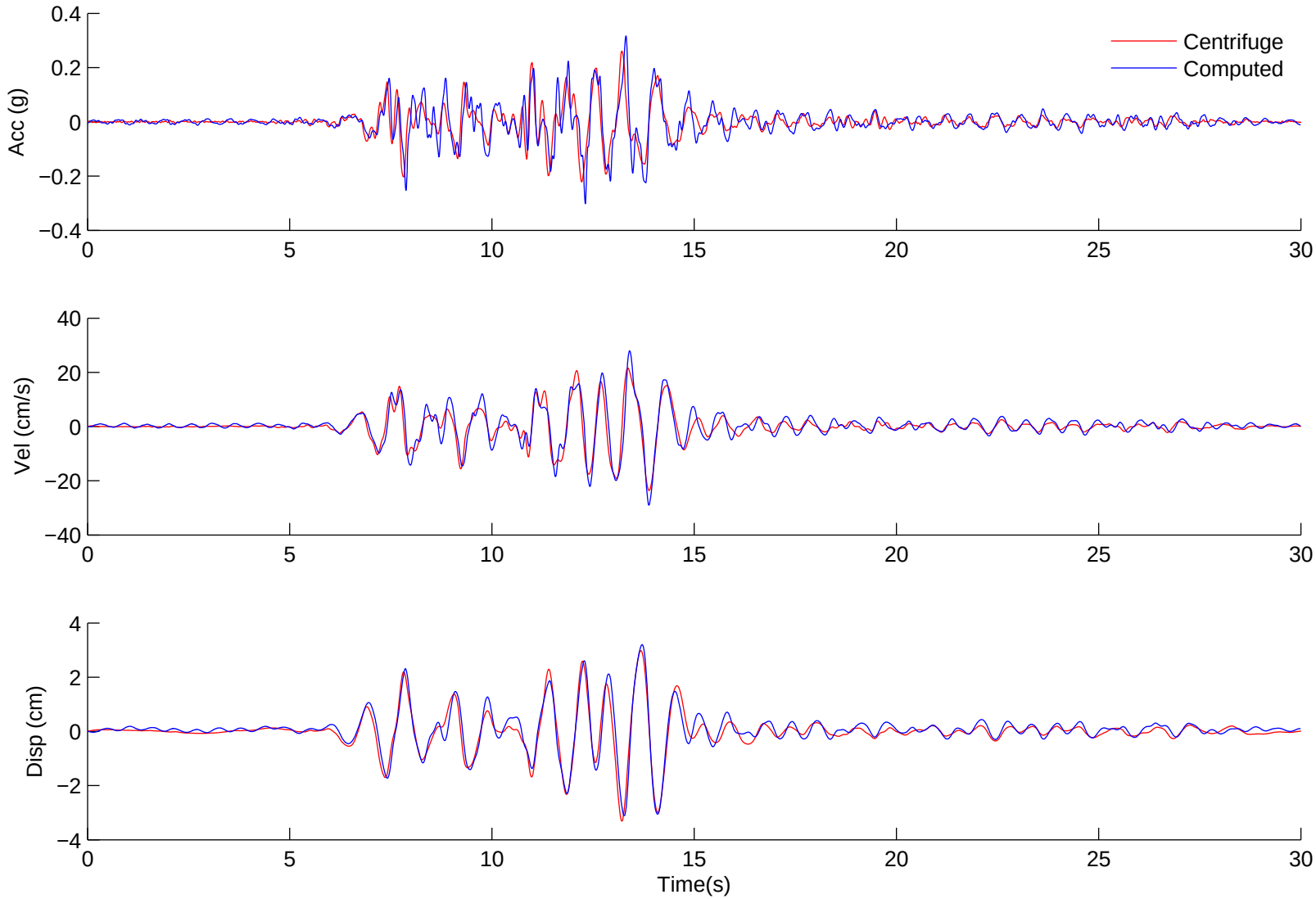

Figure C.5 Comparison of free field acceleration, velocity, and displacements during Kocaeli YPT 060-1.

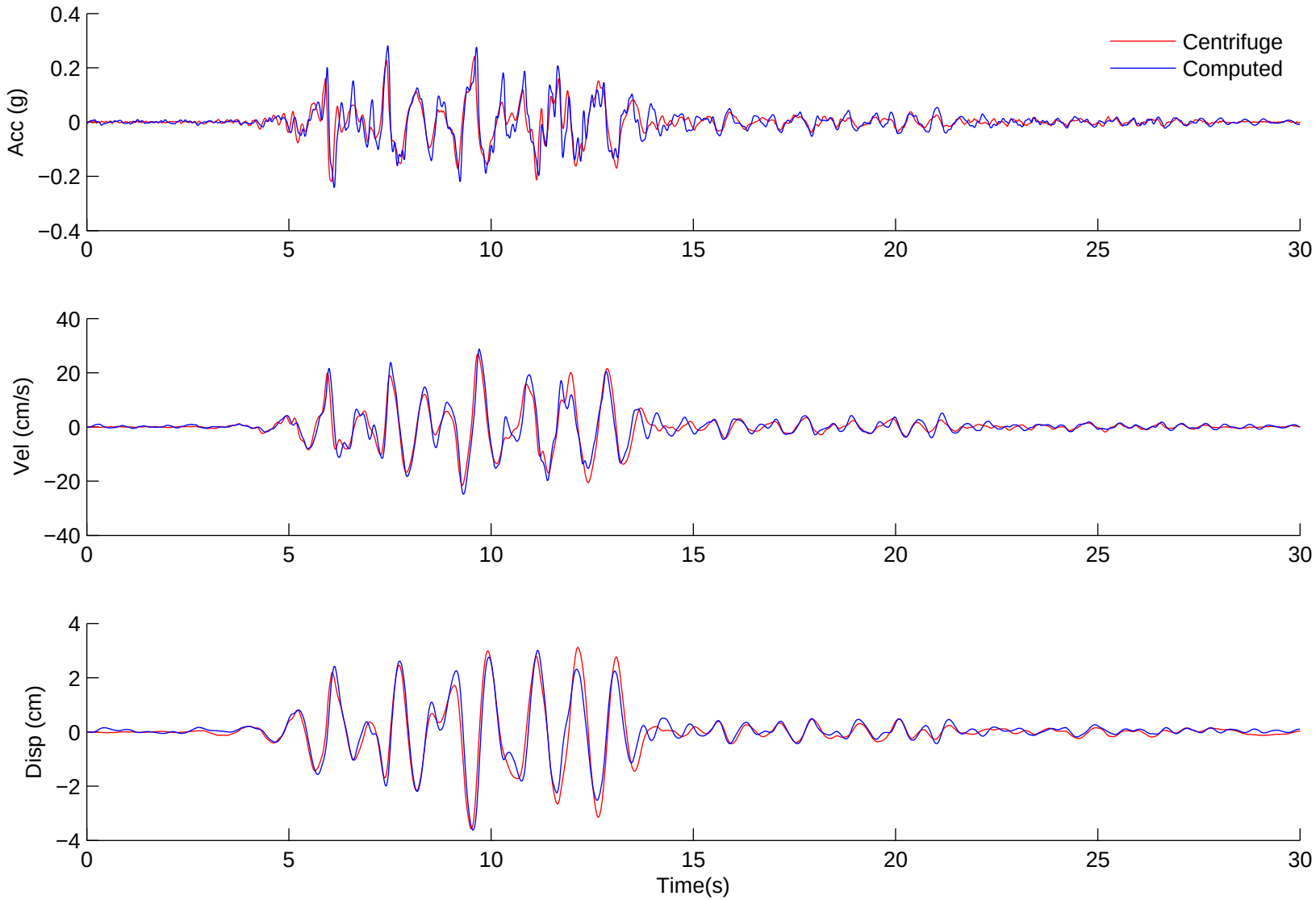

Figure C.6 Comparison of free field acceleration, velocity, and displacements during Kocaeli YPT 330-1.

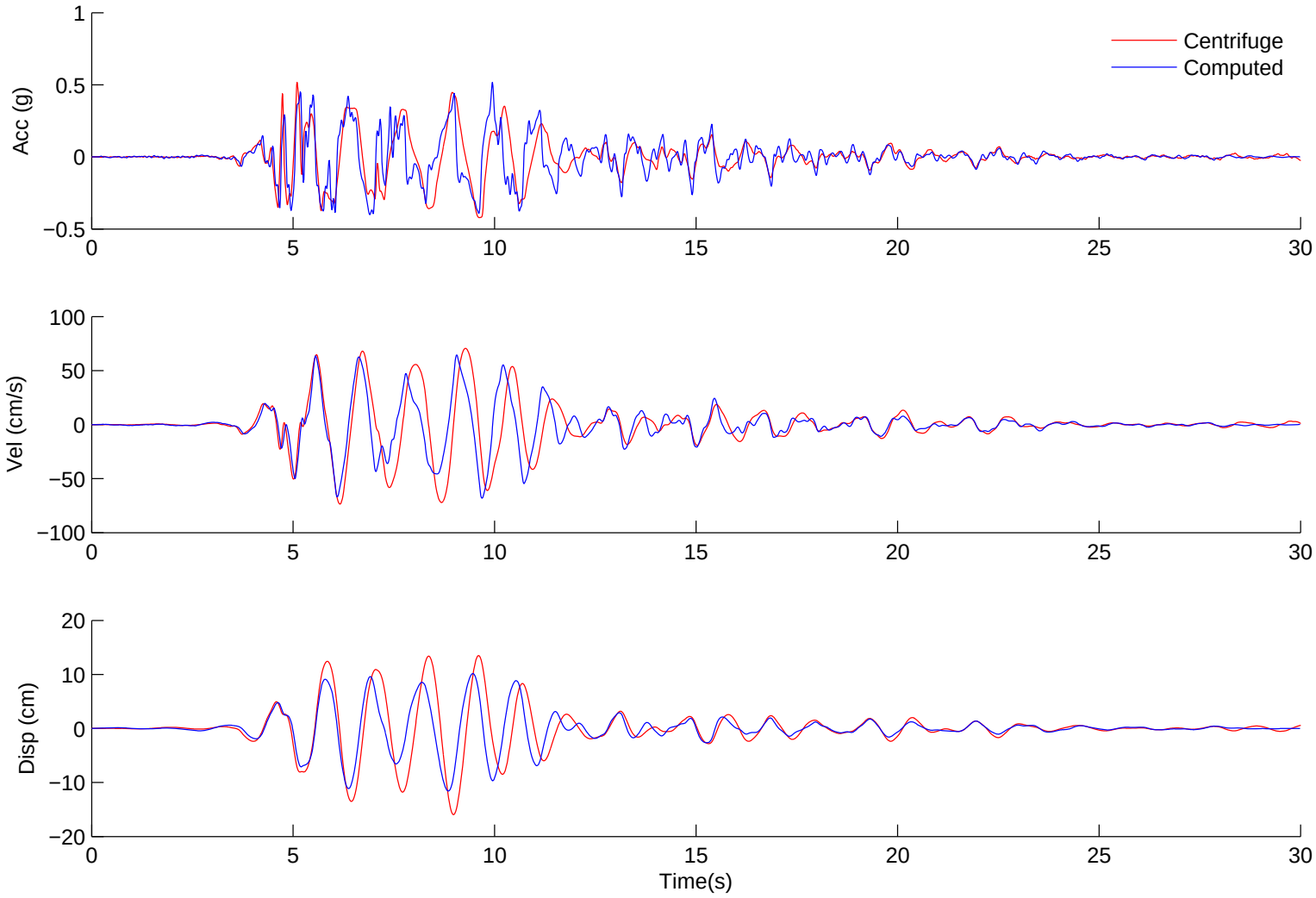

Figure C.7 Comparison of free field acceleration, velocity, and displacements during Kobe TAK 090-1.

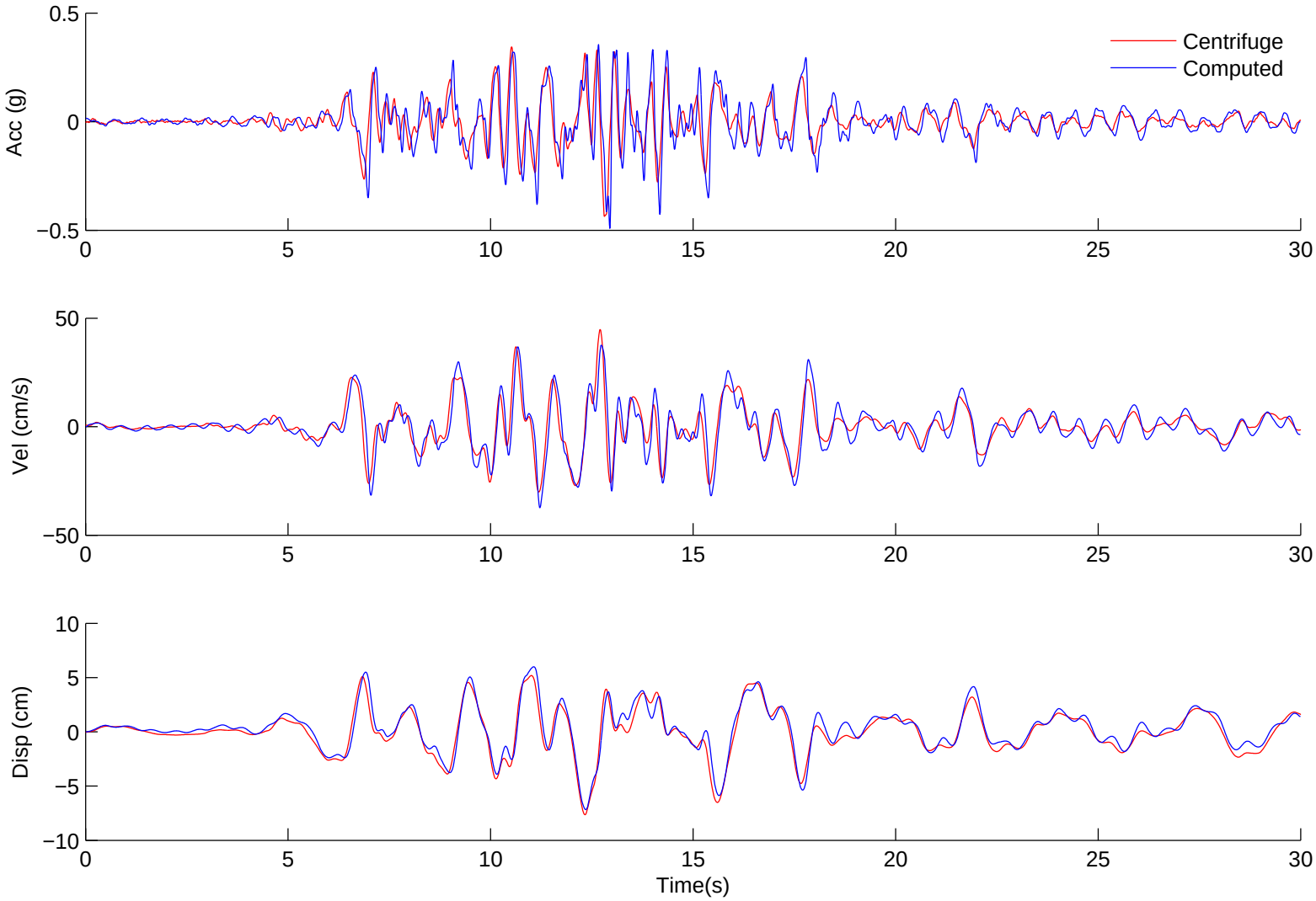

Figure C.8 Comparison of free field acceleration, velocity and displacements during Loma Prieta SC-2.

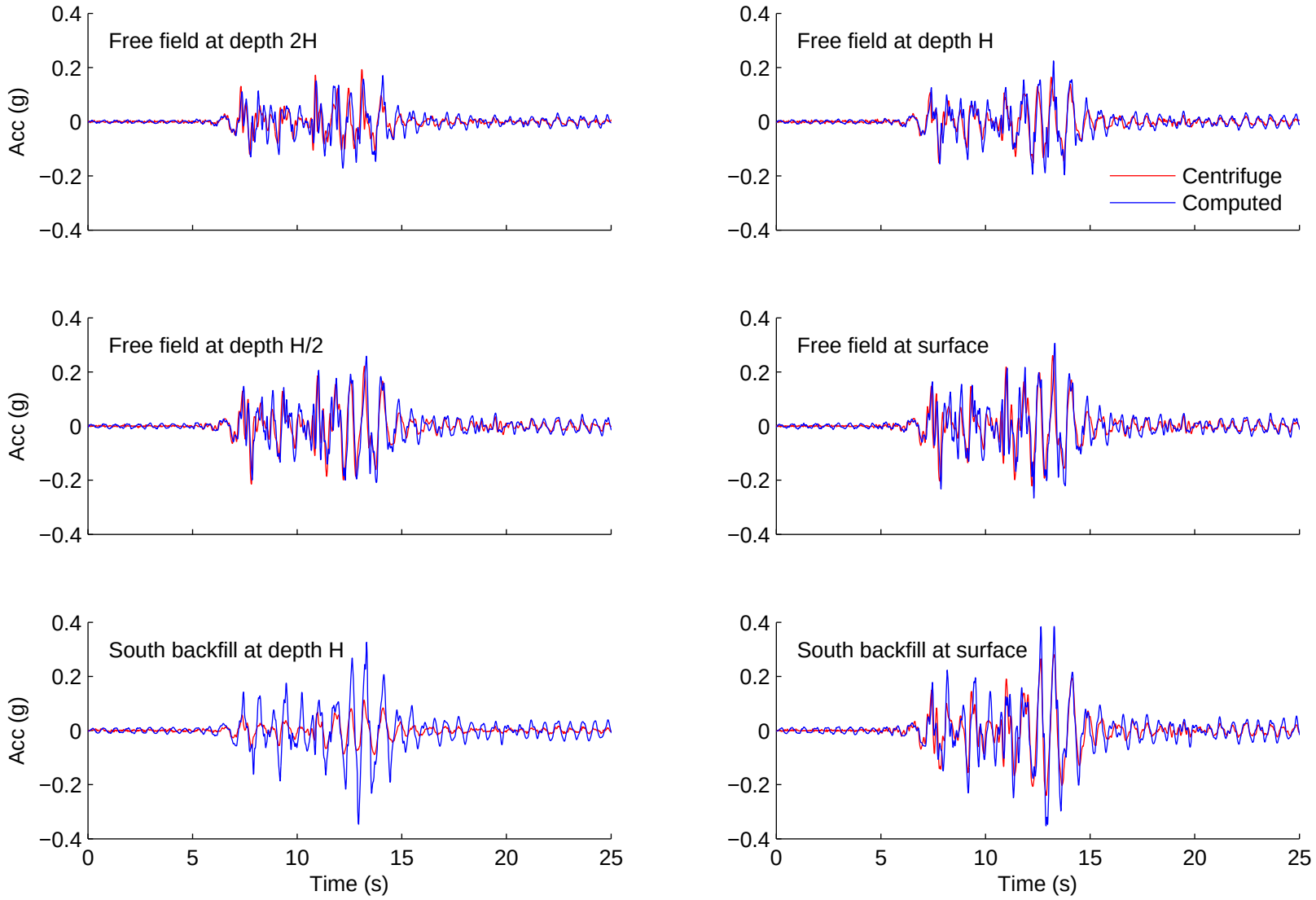

Figure C.9 Comparison of measured and computed acceleration in the soil during Kocaeli YPT 060 – 2.

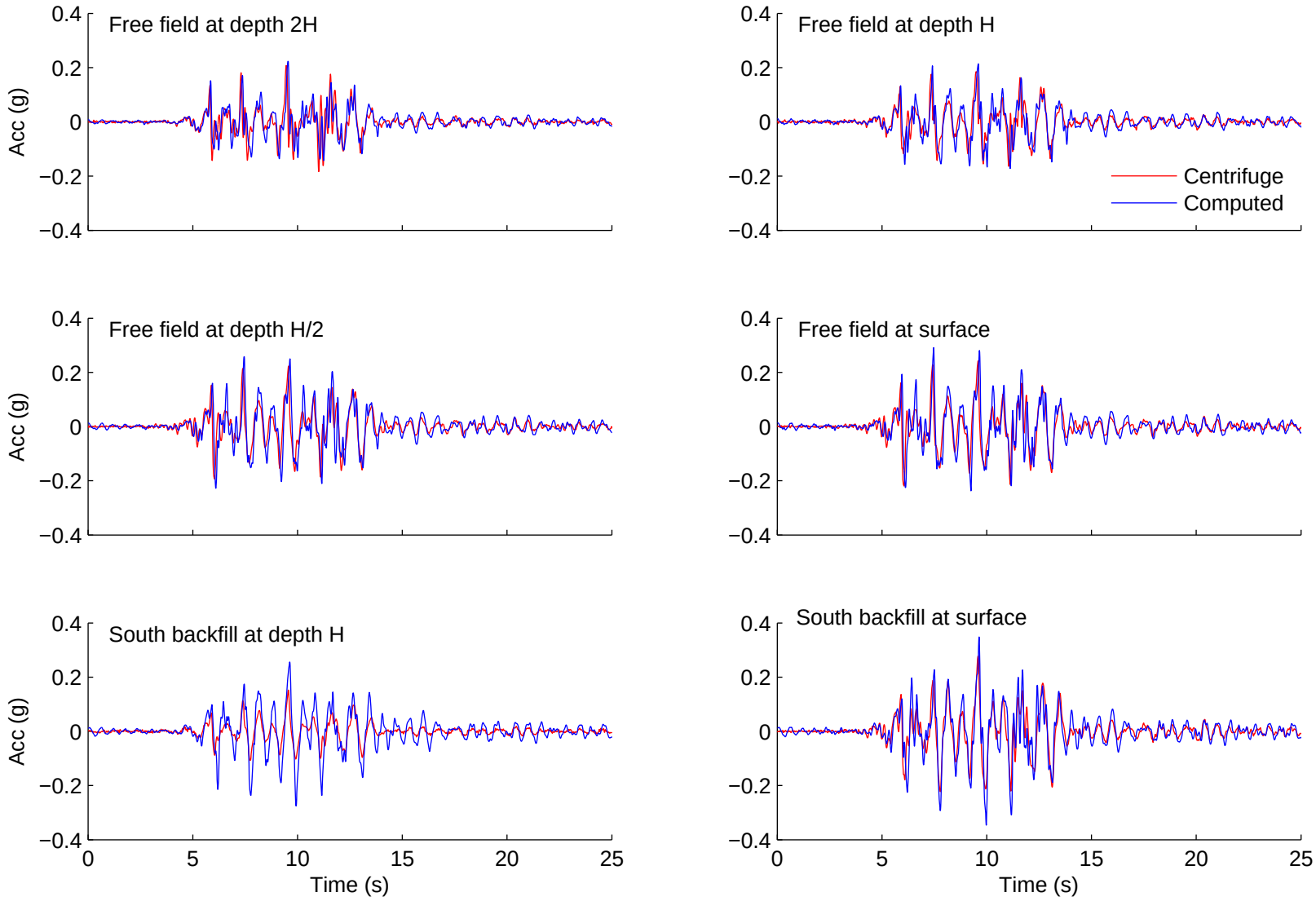

Figure C.10 Comparison of measured and computed acceleration in the soil during Kocaeli YPT 330 – 1.

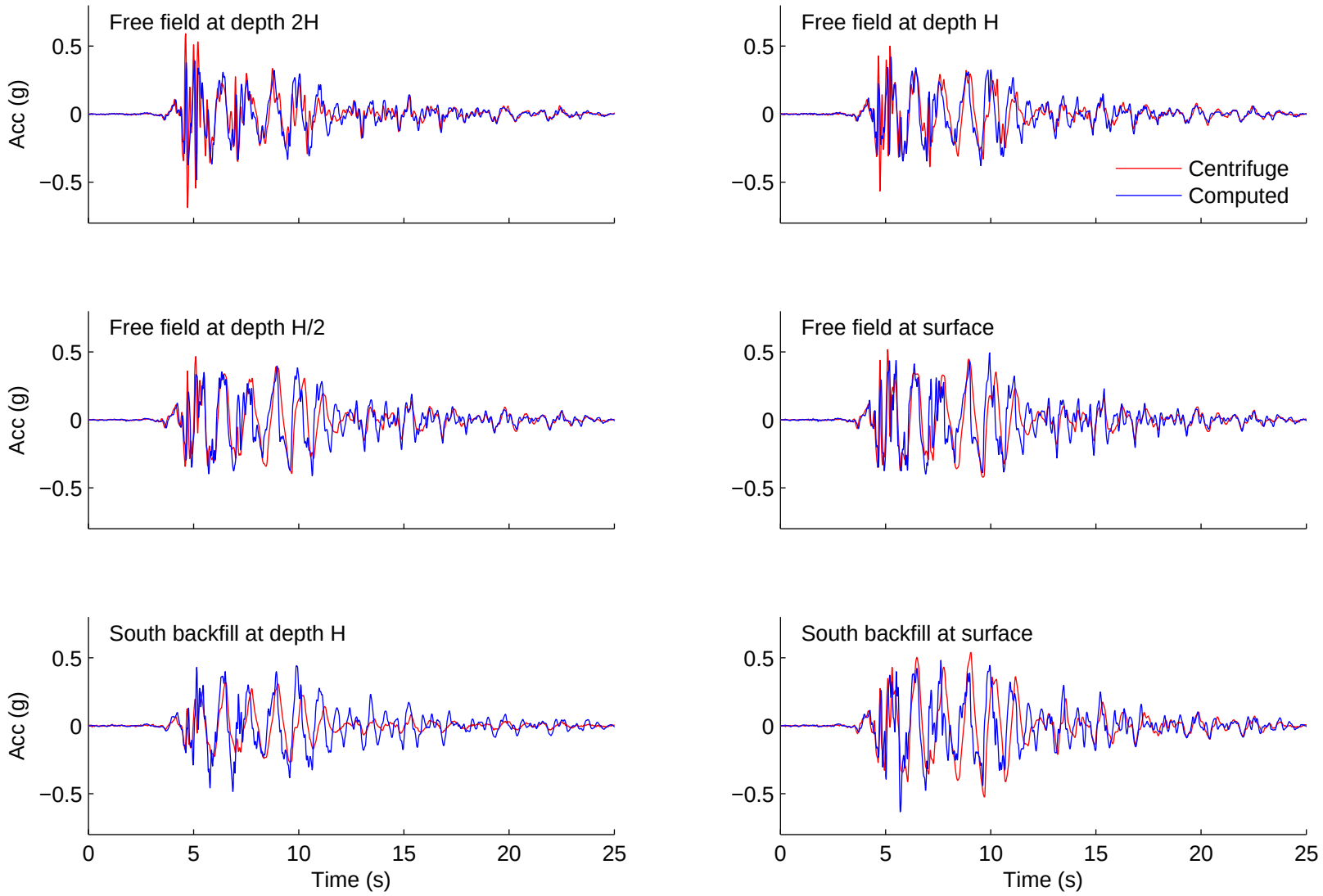

Figure C.11 Comparison of measured and computed acceleration in the soil during Kobe TAK 090 – 1.

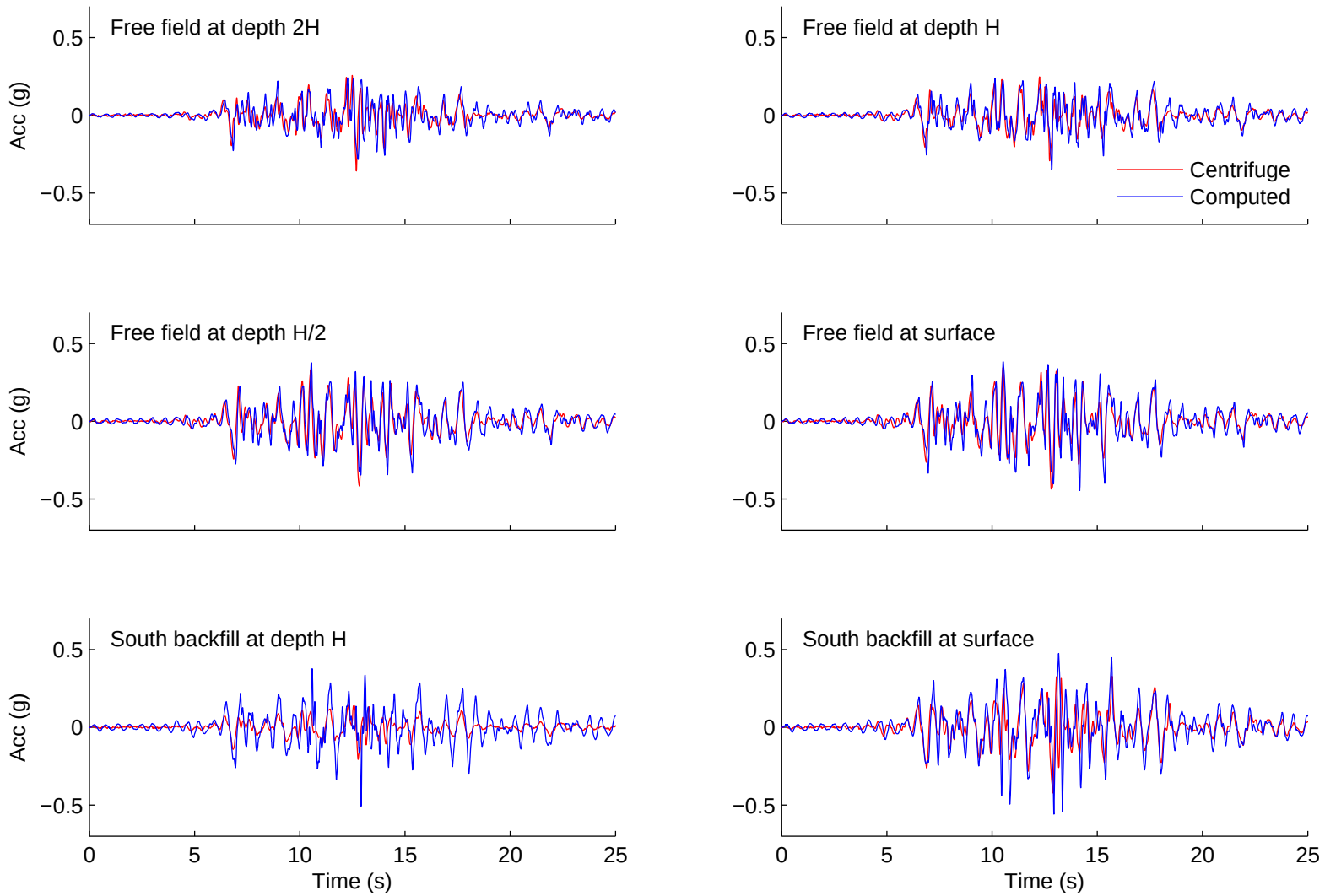

Figure C.12 Comparison of measured and computed acceleration in the soil during Loma Prieta SC – 2.

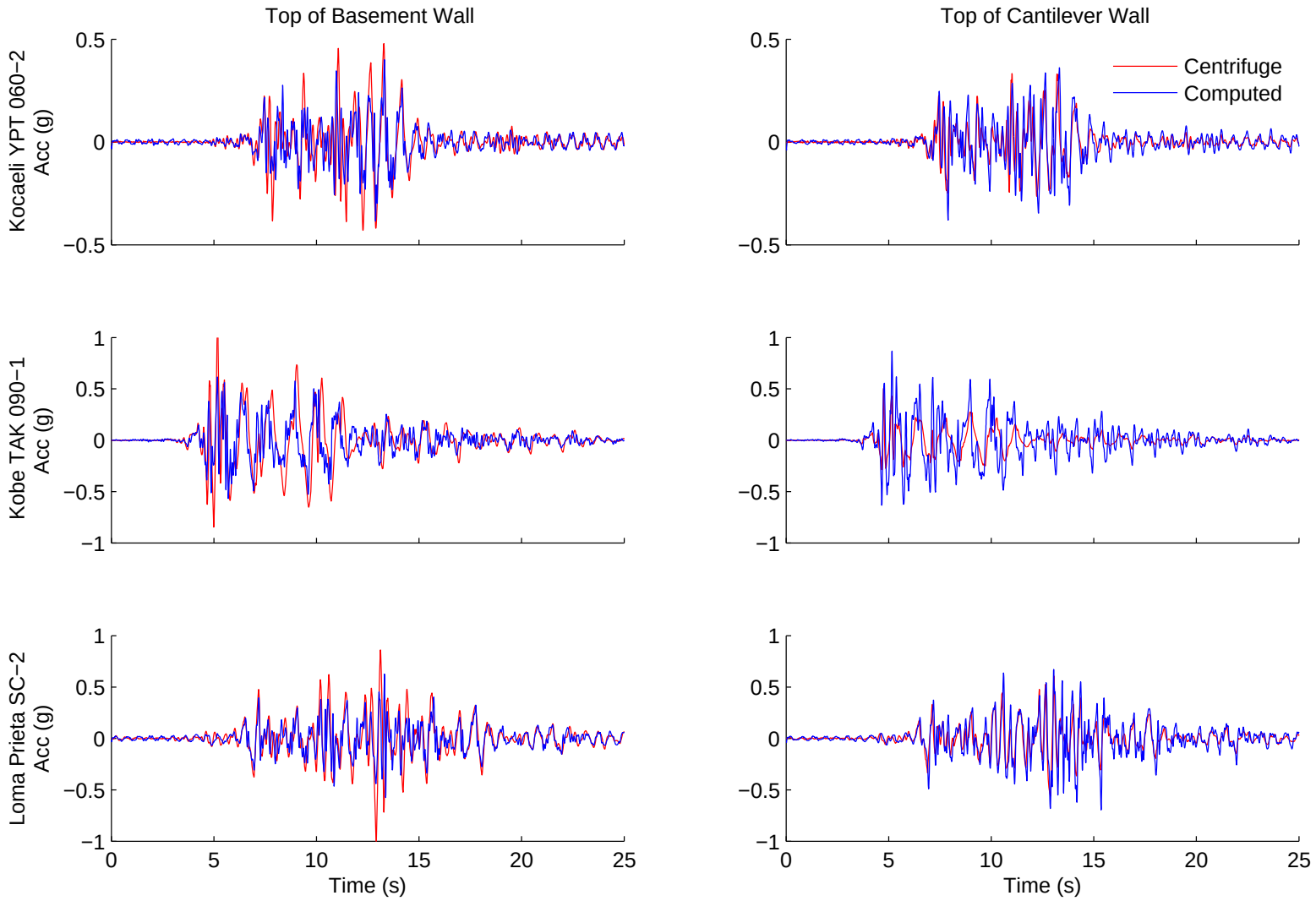

Figure C.13 Comparison of measured and computed acceleration in the structures.

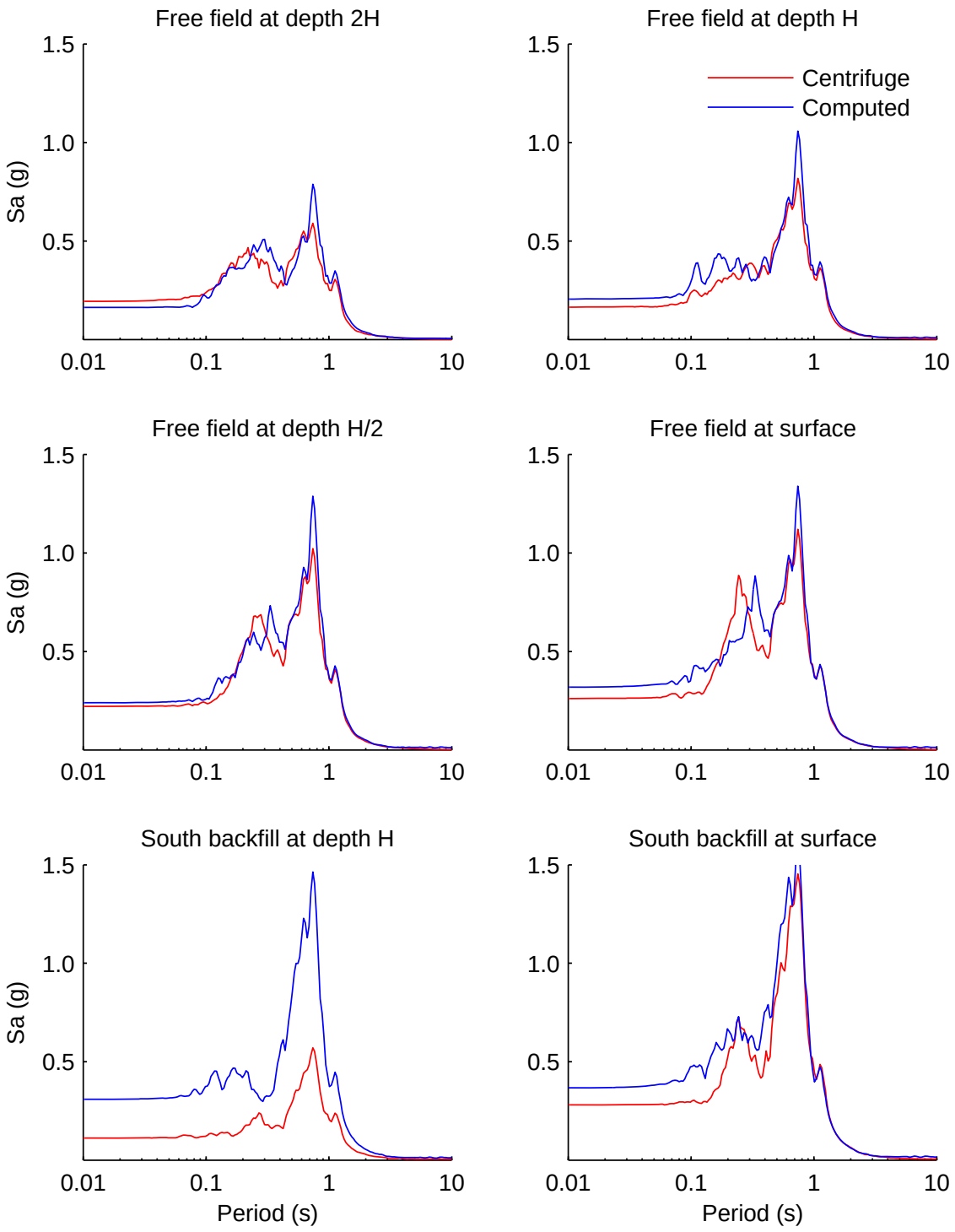

Figure C.14 Comparison of measured and computed acceleration response spectra at 5% damping for Kocaeli YPT 060 – 2.

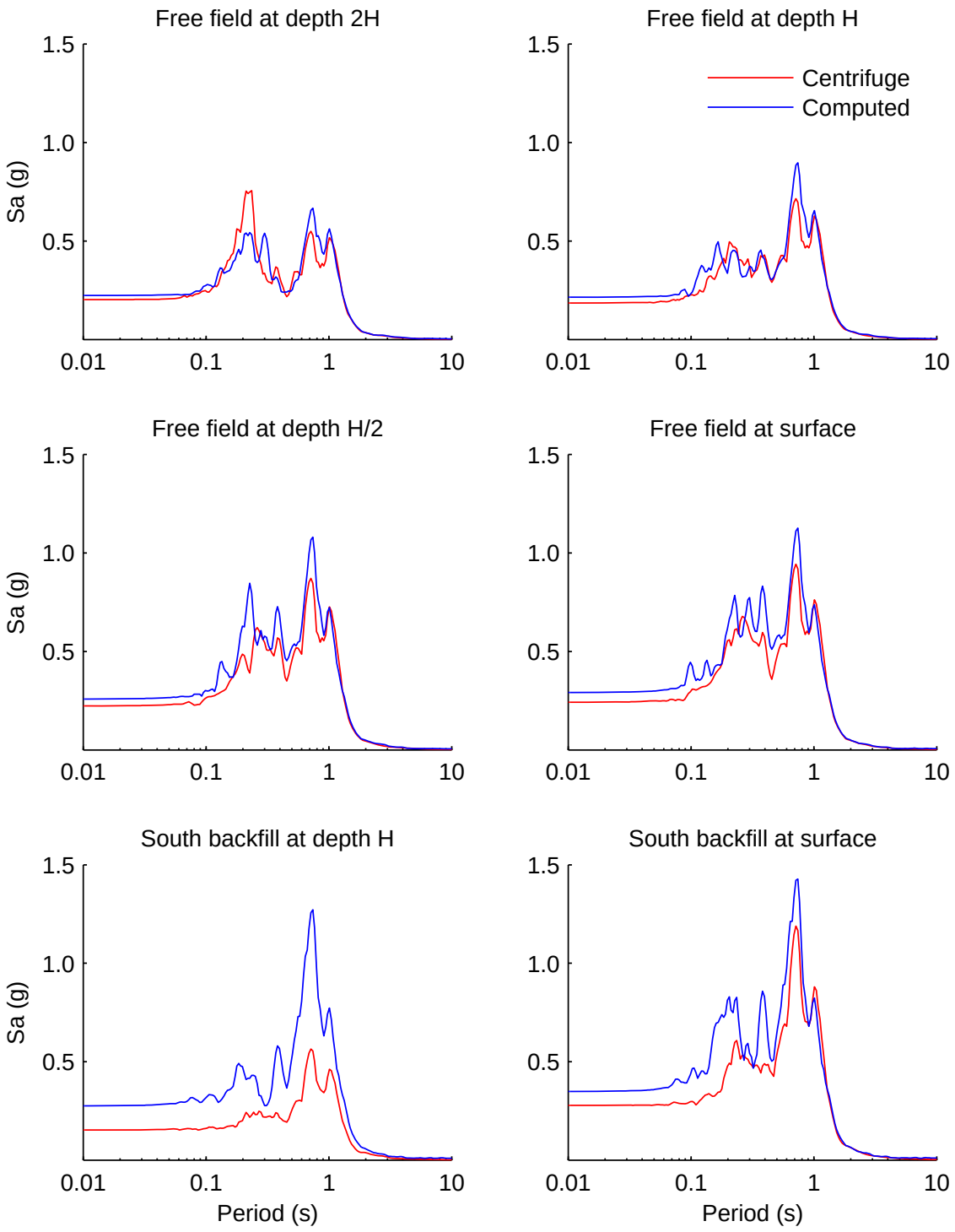

Figure C.15 Comparison of measured and computed acceleration response spectra at 5% damping for Kocaeli YPT 330 – 2.

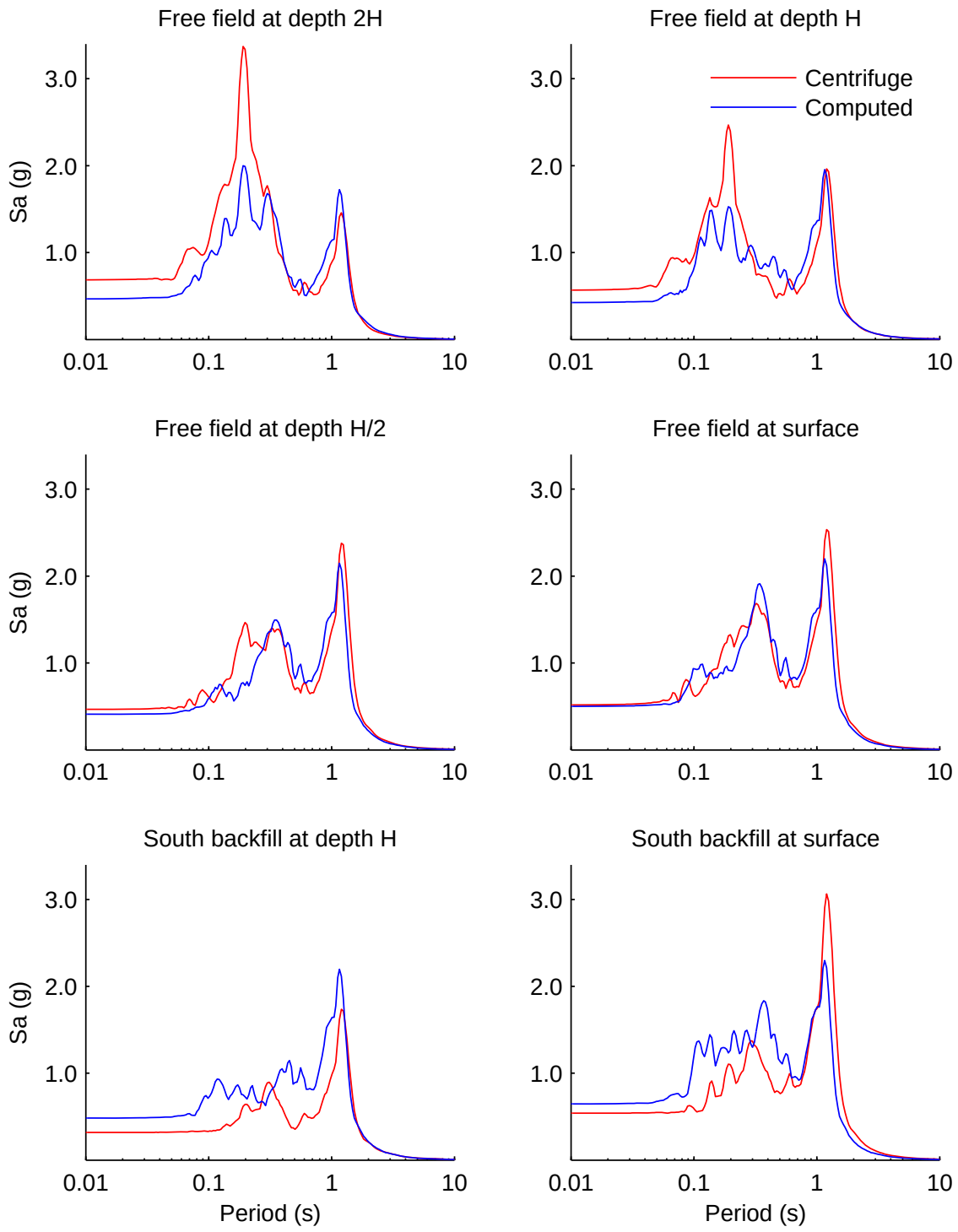

Figure C.16 Comparison of measured and computed acceleration response spectra at 5% damping for Kobe TAK 090 – 1.

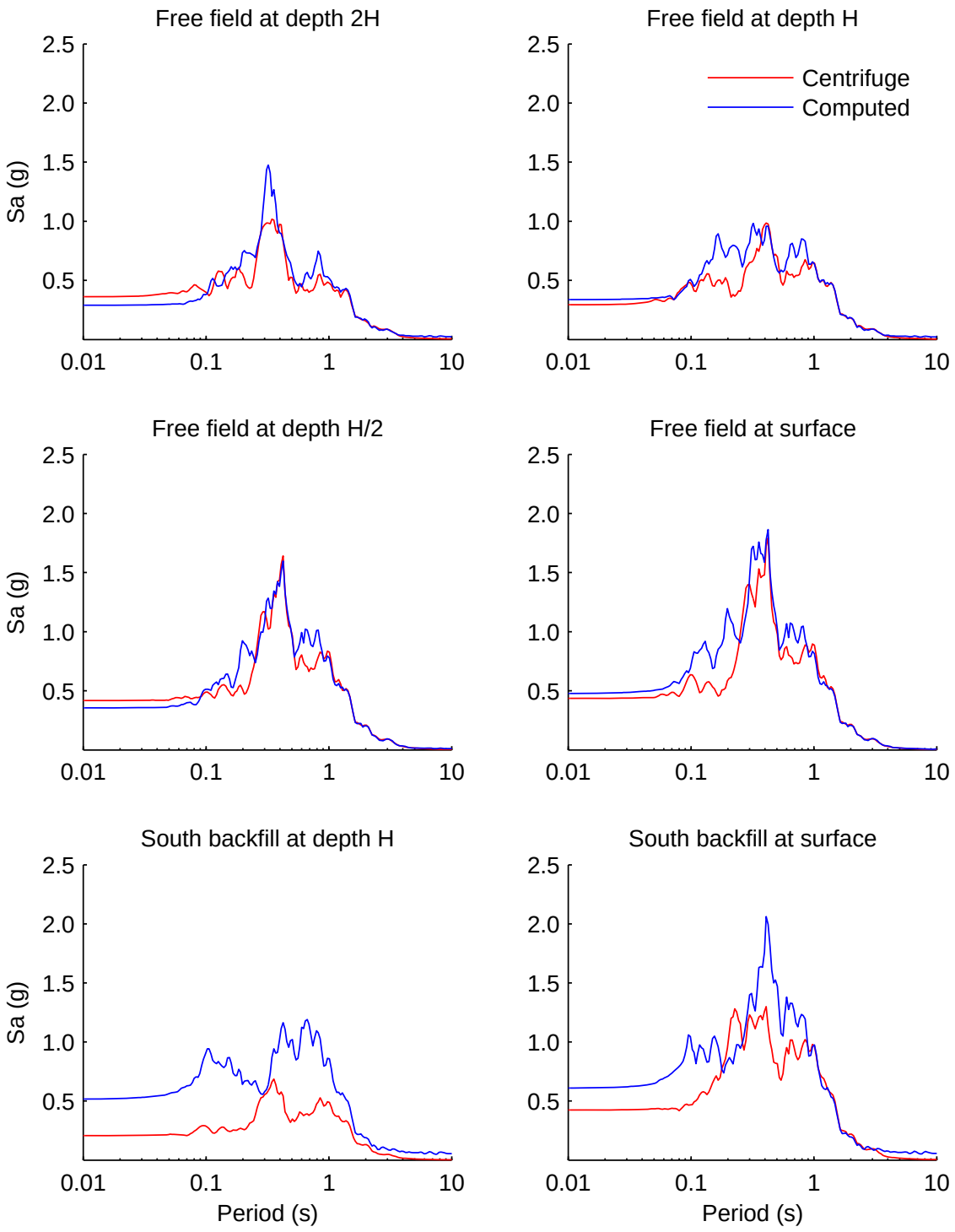

Figure C.17 Comparison of measured and computed acceleration response spectra at 5% damping for Loma Prieta SC – 2.

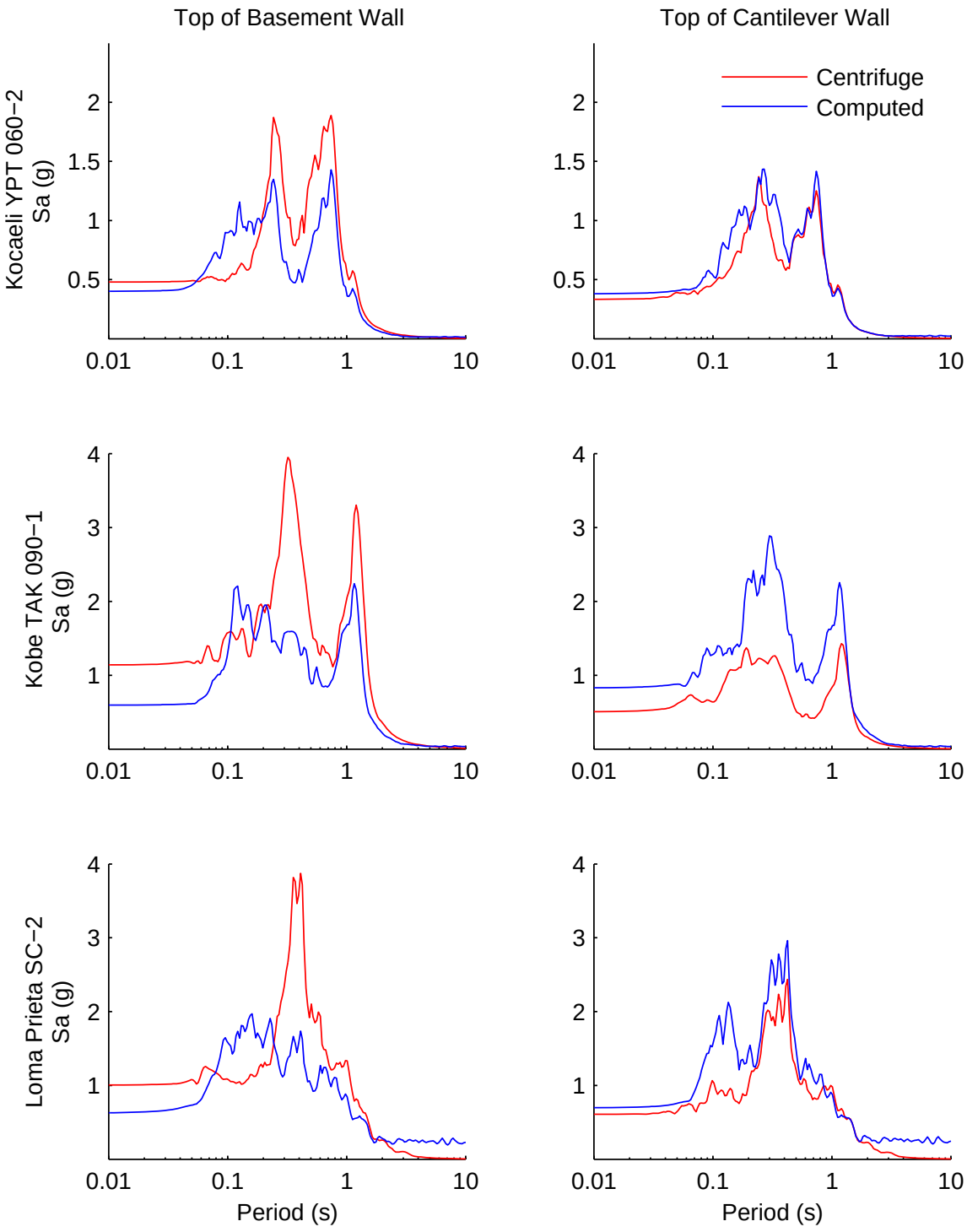

Figure C.18 Comparison of measured and computed acceleration response spectra at 5% damping at the top of basement and cantilever walls.

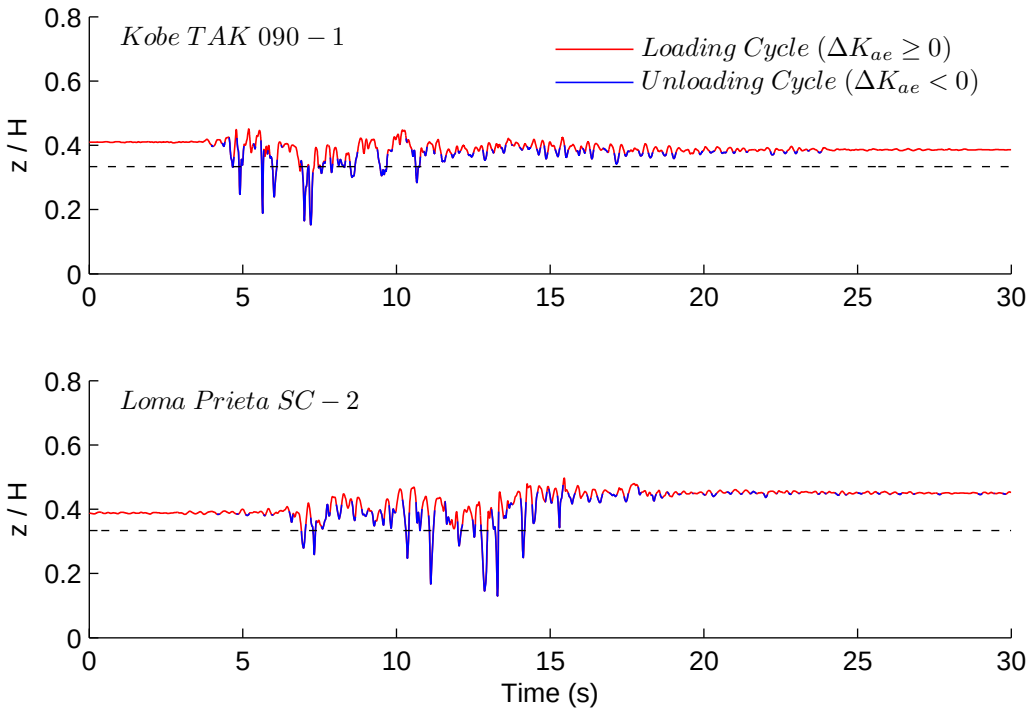

Figure C.19 Computed point of application of seismic earth pressures in the north basement wall.

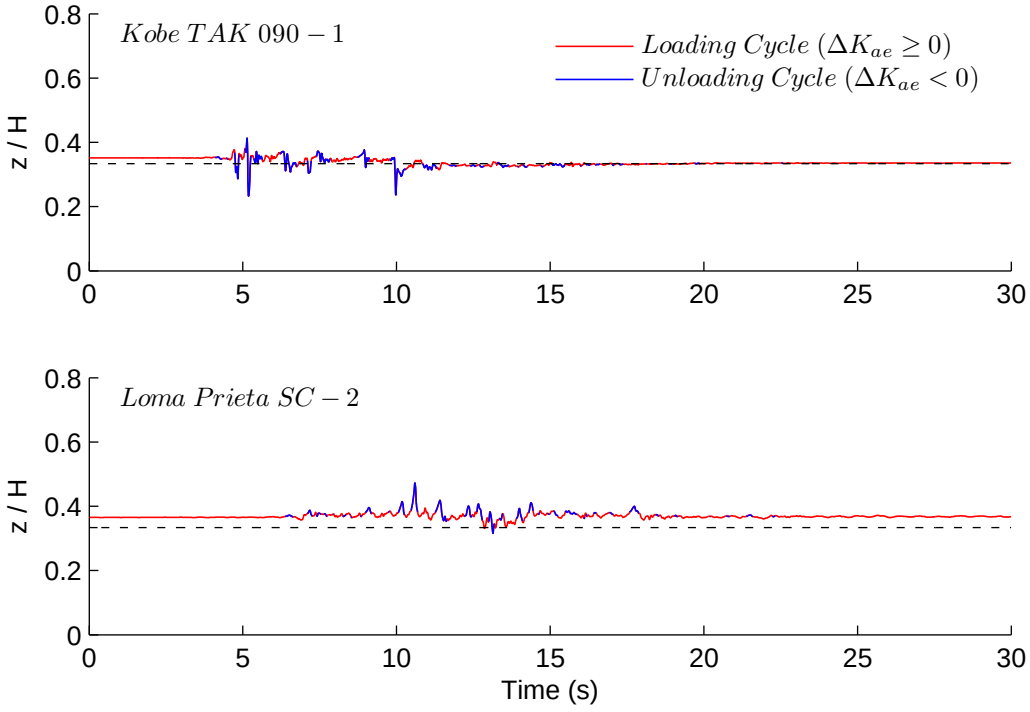

Figure C.20 Computed point of application of seismic earth pressures in the cantilever wall.

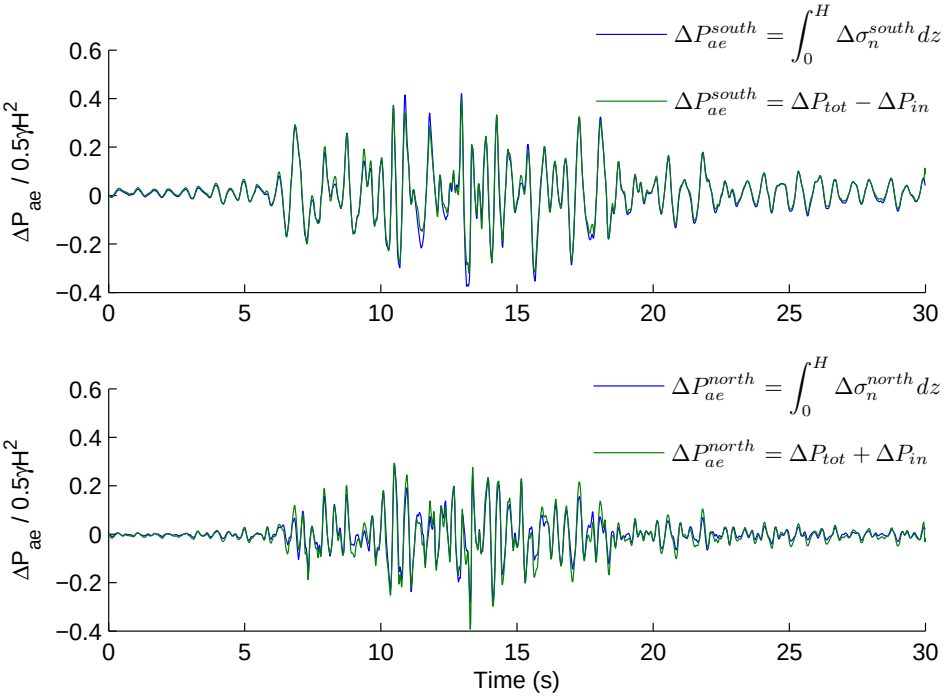

Figure C.21 Dynamic load increments during Loma Prieta based on the integration of interface elements and based on the simplified 1-D equation.

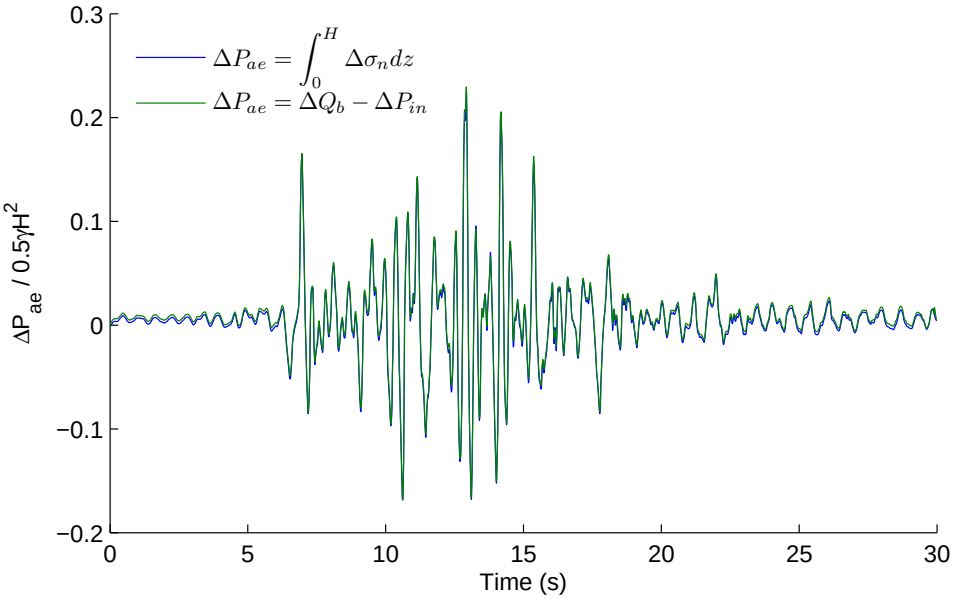

Figure C.22 Dynamic load increments during Loma Prieta based on the integration of interface elements and based on the simplified equation.

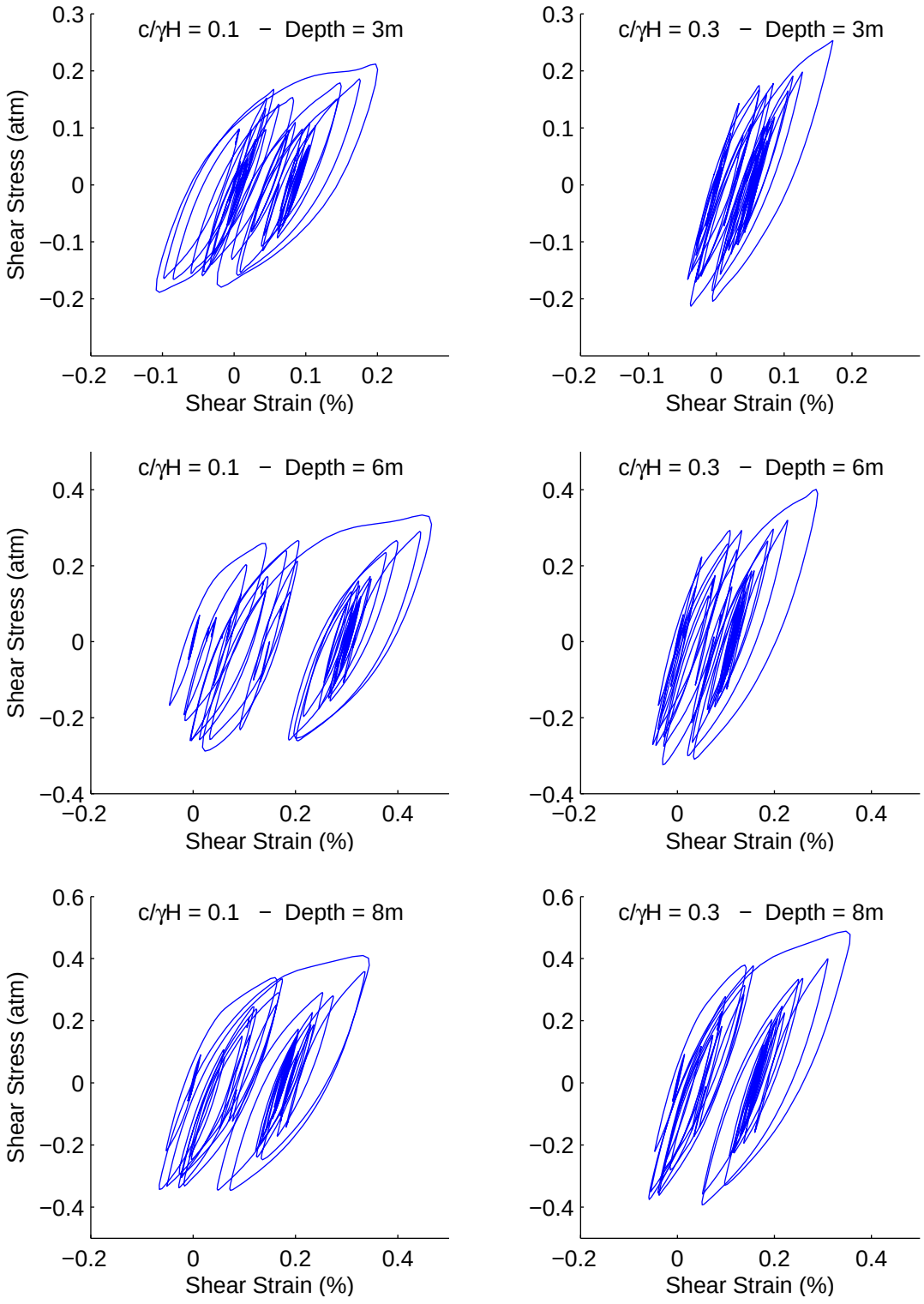

Figure C.23 Shear stress-strain cycles of UBCHYST elements during Loma Prieta SC-2 in the simplified basement model.

Appendix D: Additional tables and figures of sloping backfill experiment and numerical model GC02

Table D.1 Free field acceleration coefficients and cantilever wall loads measured in the sloping ground model GC02. Loads normalized by $0.5\gamma H^2$ = 405 kN/m

Experiment: GC02 Ground Motion	Base Input	Free Field	Slope Crest	Mid Slope	Top Ring N-S	Top Ring E-W	Top Ring UP
1) Kocali YPT060 - 1	0.12	0.18	0.16	0.15	0.25	0.16	0.16
2) Loma Prieta SC - 1	0.41	0.59	0.55	0.42	0.70	0.46	0.59
3) Kobe TAK090 - 1	0.72	0.73	0.66	0.59	1.31	0.40	1.66
4) Kocali YPT330 - 1	0.24	0.30	0.27	0.24	0.45	0.24	0.29
5) Kocali YPT060 - 2	0.40	0.62	0.55	0.48	0.88	0.34	0.61
6) Loma Prieta WVC270-1	0.57	0.65	0.59	0.46	0.79	0.26	0.98
7) Kobe TAK090 - 2	0.66	0.72	0.61	0.58	1.45	0.38	1.69
8) Loma Prieta SC - 2	0.58	0.72	0.65	0.46	1.15	0.53	0.81
9) Kobe TAK090 - 3	0.86	0.79	0.76	0.72	1.61	0.43	1.94
10) Kocali YPT330 - 2	0.36	0.50	0.47	0.41	0.74	0.35	0.58

Table D.2 Free field acceleration coefficients and cantilever wall loads measured in the sloping ground model GC02. Loads normalized by 0.5γH2 = 405 kN/m

Ground Motion	k_h active	k_h passive	Q_b	P_a	ΔP_{ae}	ΔP_{in}	$P_{ae}=Q_b-\Delta P_{in}$
1) Kocali YPT 060-1	0.16	0.18	-	0.67	-	0.000	-
2) Loma Prieta SC-1	0.59	0.51	-	0.67	-	0.000	-
3) Kobe TAK 090-1	0.71	0.71	1.13	0.67	0.50	-0.039	1.17
4) Kocali YPT 330-1	0.28	0.30	0.79	0.67	0.12	0.006	0.79
5) Kocali YPT 060-2	0.51	0.62	1.11	0.67	0.42	0.023	1.09
6) Loma Prieta WVC 270-1	0.66	0.45	0.94	0.67	0.25	0.019	0.92
7) Kobe TAK 090-2	0.72	0.68	1.14	0.67	0.52	-0.047	1.19
8) Loma Prieta SC-2	0.72	0.60	0.94	0.67	0.25	0.014	0.92
9) Kobe TAK 090-3	0.75	0.79	1.26	0.67	0.65	-0.055	1.32
10) Kocali YPT 330-2	0.50	0.46	0.92	0.67	0.23	0.011	0.91

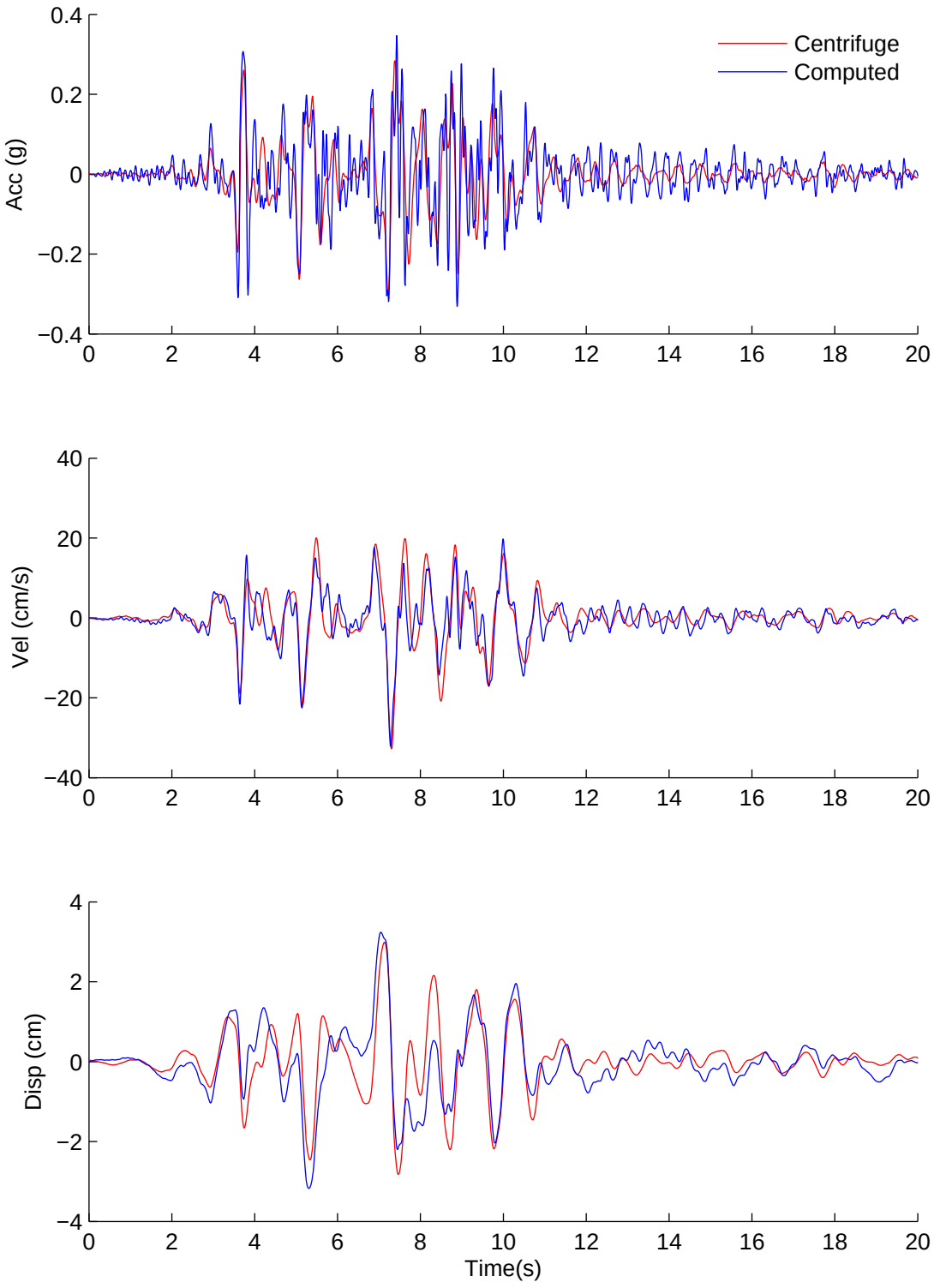

Figure D.1 Comparison of free field acceleration, velocity, and displacements during Kocaeli YPT 330-1 in sloping backfill model GC02.

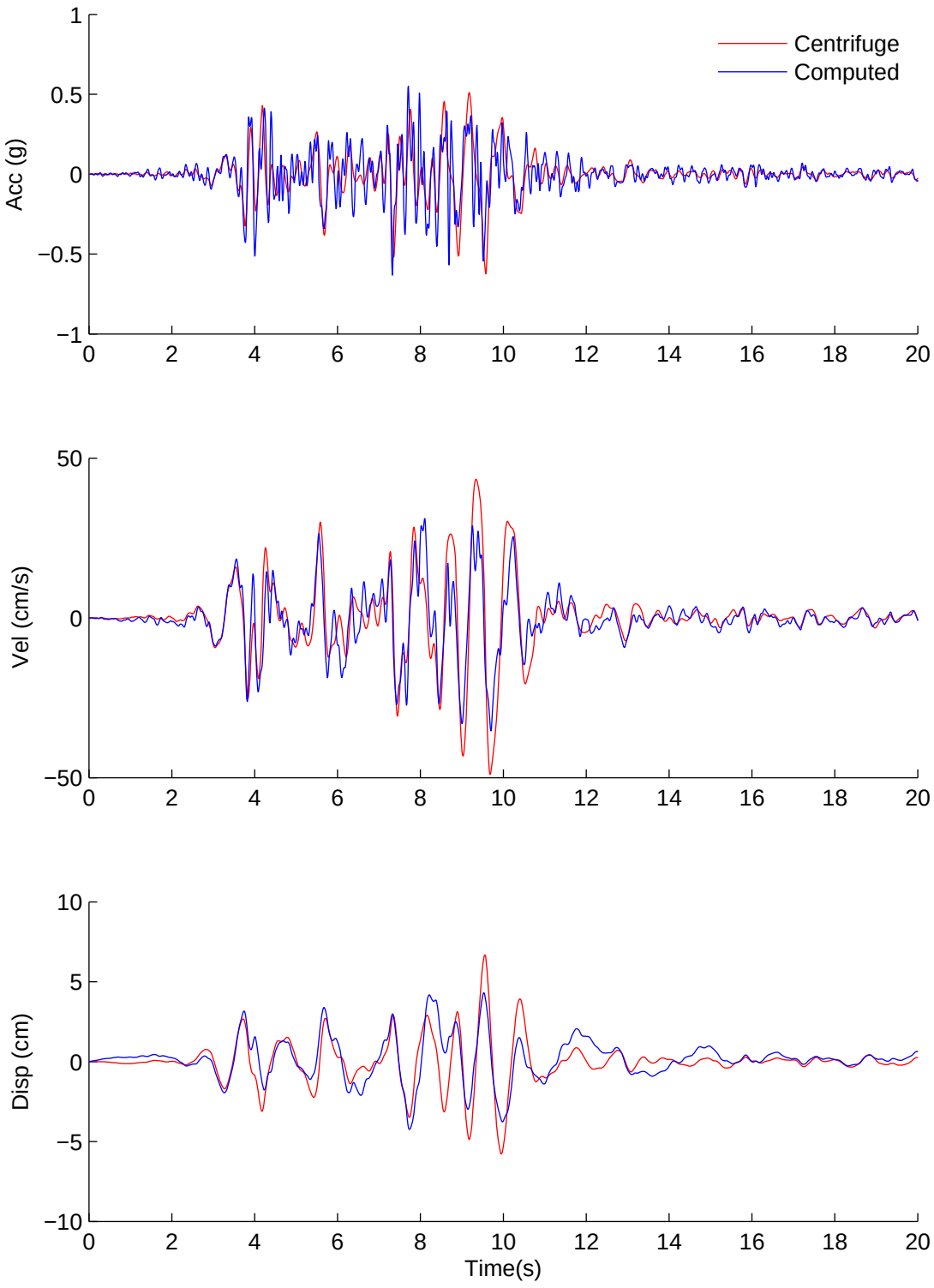

Figure D.2 Comparison of free field acceleration, velocity, and displacements during Kocaeli YPT 060-2 in sloping backfill model GC02.

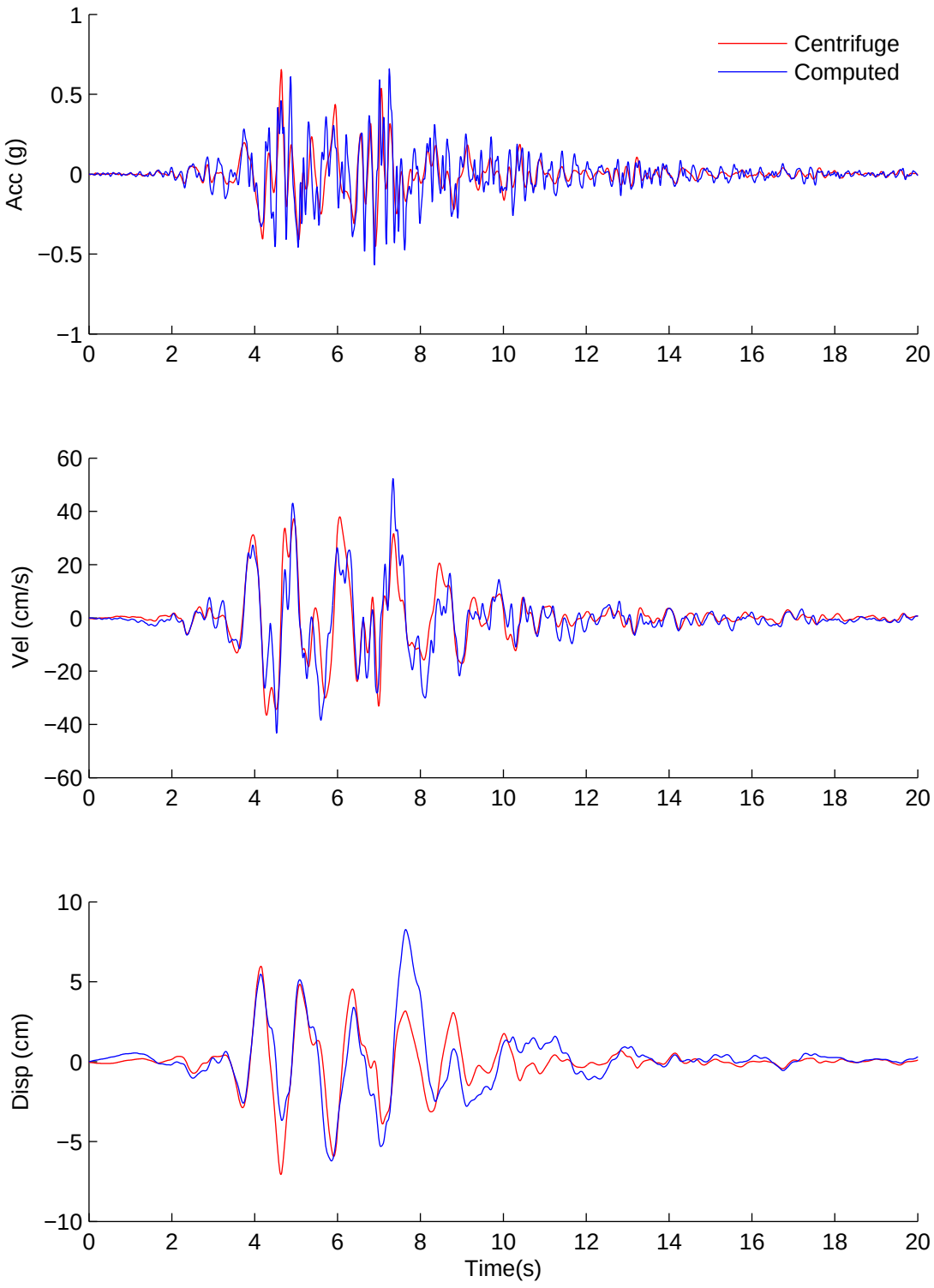

Figure D.3 Comparison of free field acceleration, velocity, and displacements during Loma Prieta WVC 270-1 in sloping backfill model GC02.

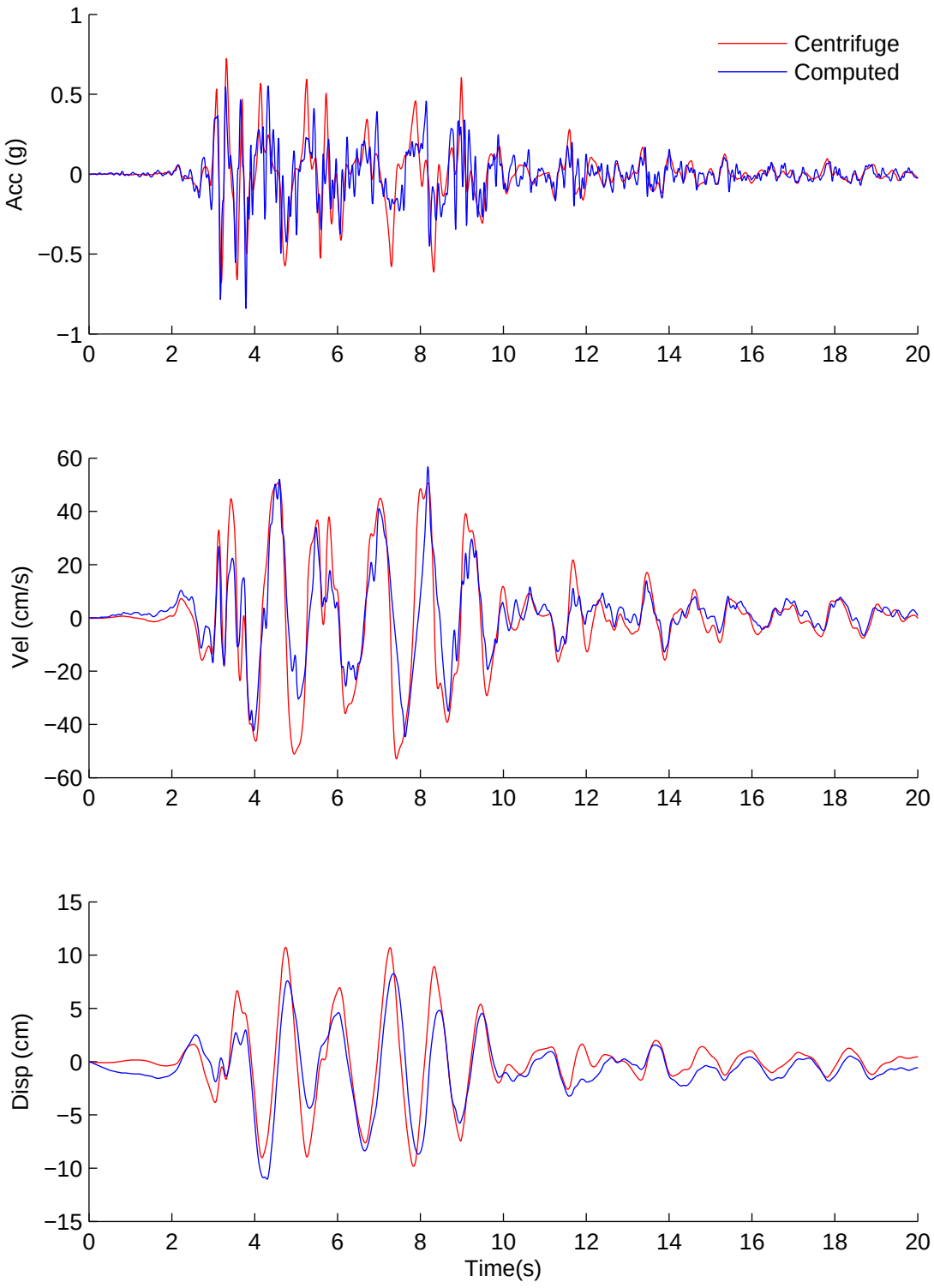

Figure D.4 Comparison of free field acceleration, velocity, and displacements during Kobe TAK 090-2 in sloping backfill model GC02.

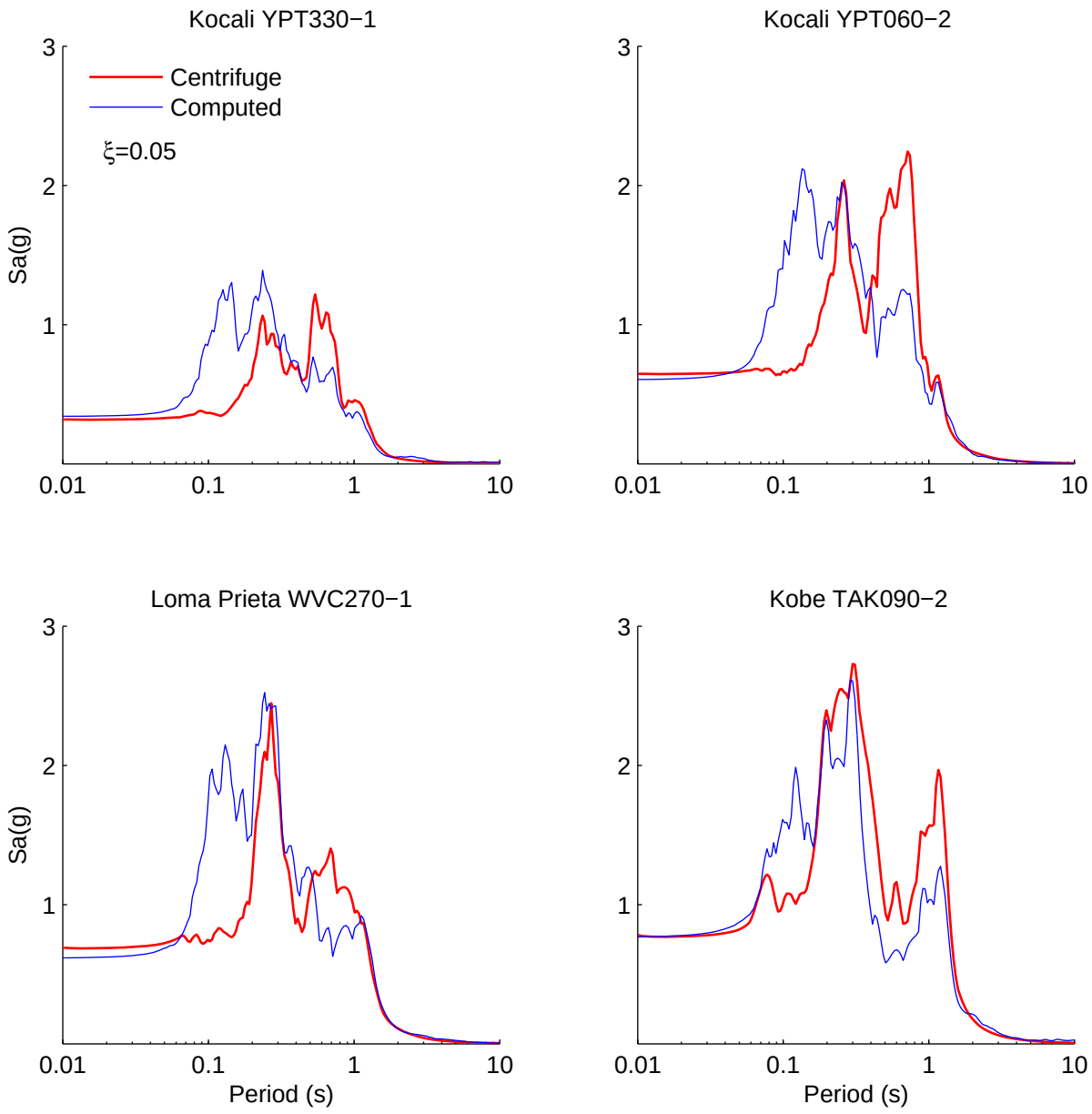

Figure D.5 Comparison of measured and computed acceleration response spectra with 5% damping at the surface of sloping backfill model GC02.

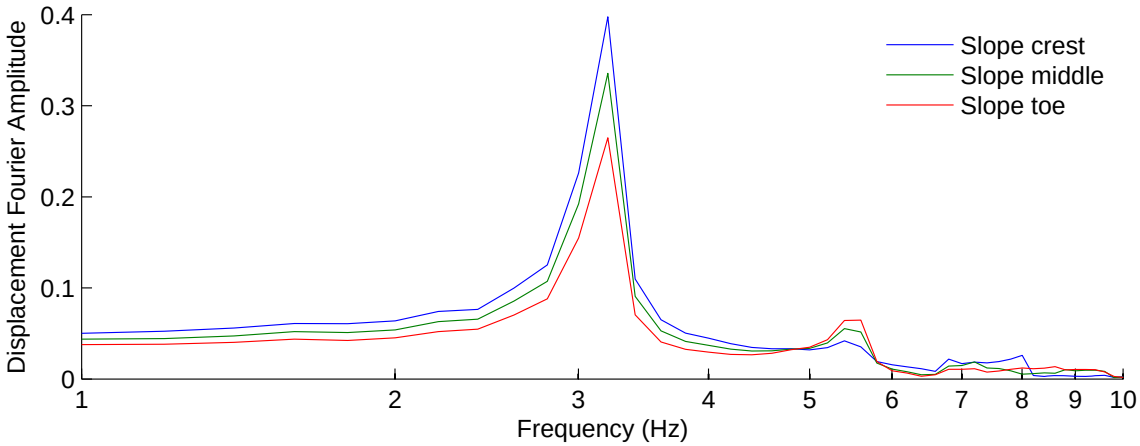

Figure D.6 Transfer function of horizontal slope displacements computed in the FLAC model of experiment GC02.

Appendix E: Review of Okabe's (1926) General Theory of earth pressures and derivation of a simplified closed form solution for the point of application of the seismic load.

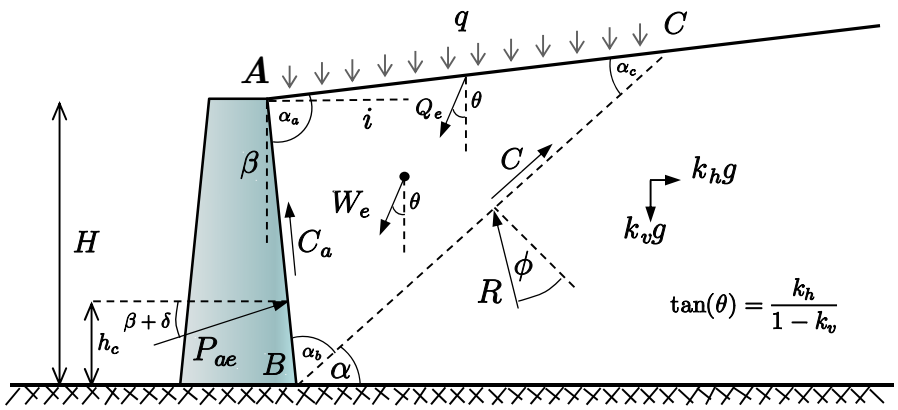

Figure E.1 Forces in Okabe analysis including adhesion

Wedge geometry: Internal wedge angles and side lengths

$$\alpha_{ab} = \pi/2 - +i - \beta \quad , \quad \alpha_{bc} = \pi/2 - \alpha + \beta \quad , \quad \alpha_{ac} = \alpha - i \tag{E.1}$$

$$l_{ab} = \frac{H}{\cos(\beta)} \quad , \quad l_{bc} = \frac{H\cos(\beta - i)}{\cos(\beta)\sin(\alpha - i)} \quad , \quad l_{ac} = \frac{H\cos(\alpha - \beta)}{\cos(\beta)\sin(\alpha - i)} \tag{E.2}$$

Weight and surcharge resultant

$$W = \frac{1}{2}\gamma H^2 \frac{\cos(\alpha - \beta)\cos(\beta - i)}{\cos^2\beta\ \sin(\alpha - i)} \qquad W_e = \frac{W}{\cos\theta} = \frac{1}{2}\gamma H^2 \frac{\cos(\alpha - \beta)\cos(\beta - i)}{\cos^2\beta\ \cos\theta\ \sin(\alpha - i)} \tag{E.3}$$

$$Q = \frac{\gamma H^2\ \tilde{q}\ \cos(\alpha - \beta)}{\cos\beta\ \sin(\alpha - i)} \quad Q_e = \frac{Q}{\cos\theta} = \frac{\gamma H^2\ \tilde{q}\ \cos(\alpha - \beta)}{\cos\beta\ \cos\theta\ \sin(\alpha - i)} \tag{E.4}$$

Cohesion and adhesion resultants

$$C = c \cdot l_{bc} = \frac{\gamma H^2 \tilde{c}\cos(\beta - i)}{\cos\beta\sin(\alpha - i)} \quad , \quad C_a = e\,c \cdot l_{ab} = \frac{\gamma H^2 \tilde{c}\, e}{\cos\beta} \tag{E.5}$$

Equilibrium Equations to determine P_{ae} and R

$$(W_e + Q_e)\sin\theta + R\sin(\alpha - \phi) + C_a \sin\beta = P_{ae}\cos(\delta + \beta) + C\cos\alpha$$
$$(W_e + Q_e)\cos\theta = R\cos(\alpha - \phi) + P_{ae}\sin(\delta + \beta) + C\sin\alpha + C_a\cos\beta \quad \text{(E.6)}$$

Solution of system of equations

$$P_{ae} = \frac{(W_e + Q_e)\sin(\alpha - \phi + \theta) - C\cos\phi - C_a\sin(\alpha - \beta - \phi)}{\cos(\alpha - \beta - \delta - \phi)} \quad \text{(E.7)}$$

$$R = \frac{(W_e + Q_e)\cos(\beta + \delta + \theta) - C\sin(\alpha - \beta - \delta) - C_a\cos\delta}{\cos(\alpha - \beta - \delta - \phi)}$$

Earth Pressure distribution on the wall

$$p_o = \frac{\partial P_{ae}}{\partial \eta}\cos\beta = \frac{(W_e 2\eta/H + Q_e)\sin(\alpha - \phi + \theta) - C\cos\phi - C_a\sin(\alpha - \beta - \phi)}{\cos(\alpha - \beta - \delta - \phi)}\frac{\cos\beta}{H} \quad \text{(E.8)}$$

Location of Earth Pressure Resultant

$$\frac{h_c}{H} = \frac{1}{2} - \frac{1}{6}\frac{W_e\sin(\alpha - \phi + \theta)}{(W_e + Q_e)\sin(\alpha - \phi + \theta) + C\cos\phi + C_a\sin(\alpha - \beta - \phi)} \quad \text{(E.9)}$$

For a vertical wall, level ground, no surcharge and no adhesion ($\beta = i = \tilde{q} = e = 0$)

$$\frac{h_c}{H} = \frac{1}{3} + \frac{\tilde{c}\cos(\phi)\cos(\theta)}{6\tilde{c}\cos(\phi)\cos(\theta) + 3\sin(\alpha - \phi + \theta)\cos(\alpha)} \quad \text{(E.10)}$$

Dividing by $\cos(\phi)\cos(\theta)$ the numerator and denominator of the second term of equation E.10 leads to

$$\frac{h_c}{H} = \frac{1}{3} + \frac{\tilde{c}}{6\tilde{c} + f(\phi, \tilde{c}, \alpha, \theta)} \quad \text{(E.11)}$$

where $f(\phi, \tilde{c}, \alpha, \theta)$ takes a value of $1.5(1 - \sin\phi)/\cos\phi$ for $k_h = 0$, and varies approximately linearly with the peak ground acceleration. Thus, the point of application of the seismic load for a cohesive soil with strength parameters c,ϕ can be approximated as

$$\frac{h_c}{H} = \frac{1}{3} + \frac{\tilde{c}}{6\tilde{c} + 2k_h + 1.5(1 - \sin\phi)/\cos(\phi)} \quad \text{(E.12)}$$

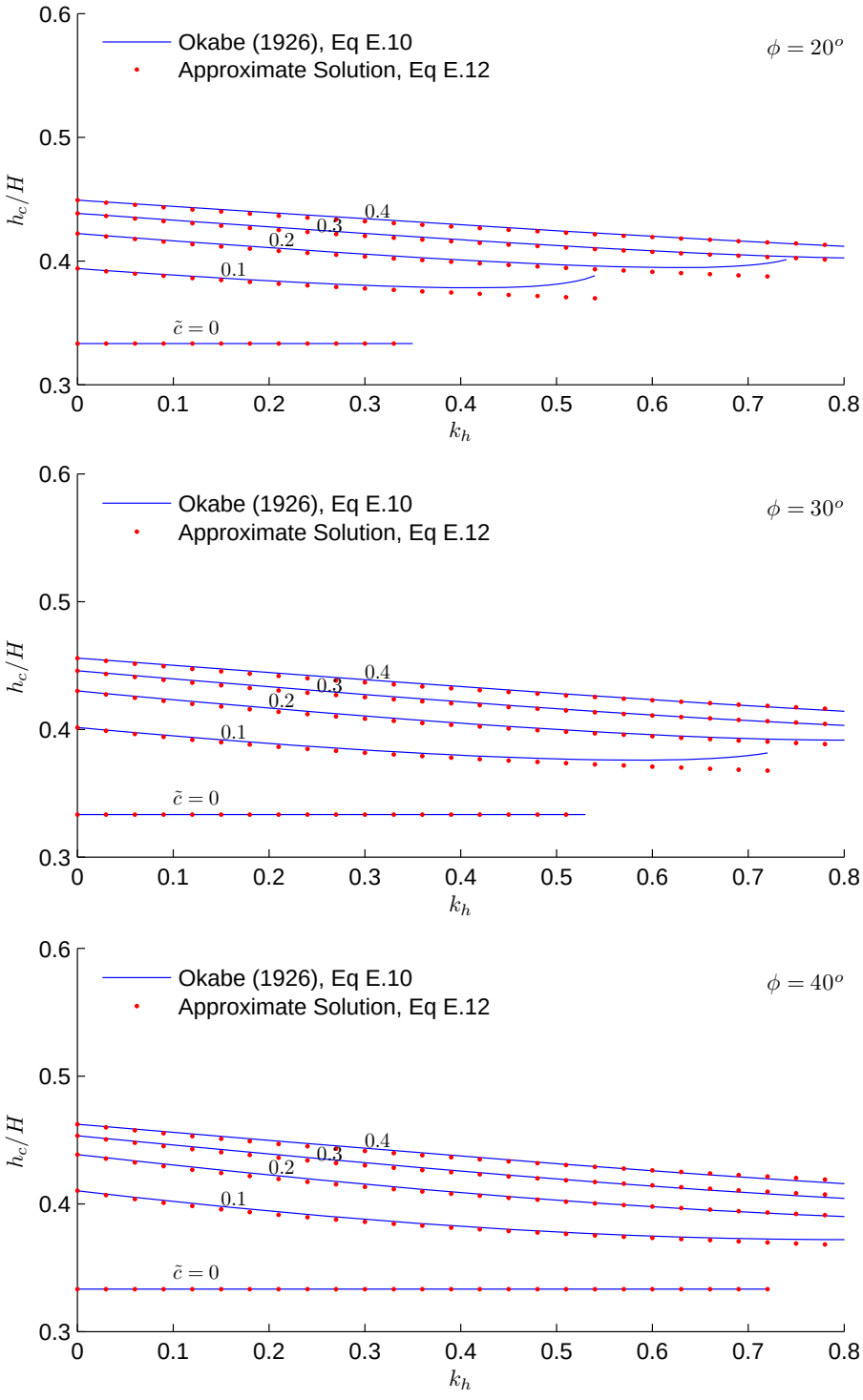

Figure E.2 Evaluation of simplified equation (Equation E.12) to compute the resultant of seismic earth pressures.